VOLUME 78 MARCH 14, 1974 NUMBER 6

JPCHAx

THE JOURNAL OF PHYSICAL CHEMISTRY

PUBLISHED BIWEEKLY BY THE AMERICAN CHEMICAL SOCIETY

THE JOURNAL OF

PHYSICAL CHEMISTRY

AMERICAN CHEMICAL SOCIETY, *1155 Sixteenth St., N.W., Washington, D. C. 20036*

Books and Journals Division

JOHN K CRUM *Director*
RUTH REYNARD *Assistant to the Director*

CHARLES R. BERTSCH *Head, Editorial Processing Department*
D. H. MICHAEL BOWEN *Head, Journals Department*
BACIL GUILEY *Head, Graphics and Production Department*
SELDON W. TERRANT *Head, Research and Development Department*

 Published biweekly by the American Chemical Society at 20th and Northampton Sts., Easton, Pa. 18042. Second-class postage paid at Washington, D. C., and at additional mailing offices.

All manuscripts should be sent to *The Journal of Physical Chemistry*, Department of Chemistry, University of Minnesota, Minneapolis, Minn. 55455.

Additions and Corrections are published once yearly in the final issue. See Volume 77, Number 26 for the proper form.

Extensive or unusual alterations in an article after it has been set in type are made at the author's expense, and it is understood that by requesting such alterations the author agrees to defray the cost thereof.

The American Chemical Society and the Editor of *The Journal of Physical Chemistry* assume no responsibility for the statements and opinions advanced by contributors.

Correspondence regarding accepted copy, proofs, and reprints should be directed to Editorial Processing Department, American Chemical Society, 20th and Northampton Sts., Easton, Pa. 18042. Head: CHARLES R. BERTSCH. Assistant Editor: EDWARD A. BORGER. Editorial Assistant: JOSEPH E. YURVATI.

Advertising Office: Centcom, Ltd., 142 East Avenue, Norwalk, Conn. 06851.

Business and Subscription Information

Send all new and renewal subscriptions *with payment* to: Office of the Controller, 1155 16th Street, N.W., Washington, D. C. 20036. Subscriptions should be renewed promptly to avoid a break in your series. All correspondence and telephone calls regarding changes of address, claims for missing issues, subscription service, the status of records, and accounts should be directed to Manager, Membership and Subscription Services, American Chemical Society, P.O. Box 3337, Columbus, Ohio 43210. Telephone (614) 421-7230.

On changes of address, include both old and new addresses with ZIP code numbers, accompanied by mailing label from a recent issue. Allow four weeks for change to become effective.

Claims for missing numbers will not be allowed (1) if loss was due to failure of notice of change in address to be received before the date specified, (2) if received more than sixty days from date of issue plus time normally required for postal delivery of journal and claim, or (3) if the reason for the claim is "issue missing from files."

Subscription rates (1974): members of the American Chemical Society, $20.00 for 1 year; to nonmembers, $60.00 for 1 year. Those interested in becoming members should write to the Admissions Department, American Chemical Society, 1155 Sixteenth St., N.W., Washington, D. C. 20036. Postage to Canada and countries in the Pan-American Union, $5.00; all other countries, $6.00. Air freight rates available on request. Single copies for current year: $3.00. Rates for back issues from Volume 56 to date are available from the Special Issues Sales Department, 1155 Sixteenth St., N.W., Washington, D. C. 20036.

Subscriptions to this and the other ACS periodical publications are available on microfilm. Supplementary material not printed in this journal is now available in microfiche form on a current subscription basis. For information on microfilm or microfiche subscriptions, write Special Issues Sales Department at the address above.

Notice to Authors last printed in the issue of December 6, 1973

THE JOURNAL OF

PHYSICAL CHEMISTRY

Volume 78, Number 6 March 14, 1974

JPCHAx 78 (6) 559–652 (1974)
ISSN 0022-3654

COMMUNICATIONS TO THE EDITOR

■ Supplementary material for this paper is available separately, in photocopy or microfiche form. Ordering information is given in the paper.

* In papers with more than one author, the asterisk indicates the name of the author to whom inquiries about the paper should be addressed.

AUTHOR INDEX

THE JOURNAL OF
PHYSICAL CHEMISTRY

VOLUME 78, NUMBER 6 MARCH 14, 1974

Hot Hydrogen Atom–Hydrocarbon Reactions. Dependence of Yields on Structure and Energy[1]

L. E. Compton, G. D. Beverly, and R. M. Martin*

Department of Chemistry, University of California, Santa Barbara, California 93106 (Received September 10, 1973)

The hot atom reactions of H atoms with C_2D_6, C_3D_8, and n-C_4D_{10}, and D atoms with C_2H_6, C_3H_8, n-C_4H_{10}, and n-C_6H_{14} have been studied over the hot atom initial energy range 1.1–2.9 eV, using HBr and DBr as photochemical sources. The steady-state treatment provides a consistent description of the data, giving ratios of the hot atom rate coefficients k_R/k_T, k_R/k_t, and k_M/k_t, where k_R is the hydrocarbon reaction coefficient, k_M the hydrocarbon moderation coefficient, k_t the hydrogen halide total interaction coefficient, and $k_T = k_R + k_M$. The integral reaction probability k_R/k_T is found to increase monotonically with energy for all systems, and increases strongly with n for the C_n compounds studied. k_R/k_t has a similar dependence on hydrocarbon structure, and a similar dependence on energy for the DBr–RH systems, but is nearly energy independent for the HBr–RD systems. k_M/k_t shows more variable behavior than the two k_R functions, but is approximately the same for different C_n compounds, and in general decreases about 50% for HBr–RD and 20% for DBr–RH from 1.1 to 2.9 eV, with an increase at intermediate energies for the DBr–RH systems. At 2.9 eV the k_M/k_t values are within 0.8 ± 0.1 for HBr–RD and 1.2 ± 0.1 for DBr–RH. The k_R/k_t values increase at this energy by half the C_2 value with each increase in n, and $(k_R/k_t)_{DBr-RH} = 4.8(k_R/k_t)_{HBr-RD}$. For HBr at 2.9 eV and HI at 185 nm (3.3–3.6 eV), $(k_t)_{HI}/(k_t)_{HBr}$ is only weakly dependent on the RD compound, with values in the range 1.7–2.0 from the k_R/k_t data and 1.8–2.1 from the k_M/k_t data. An average per bond yield formula is found to fit the integral reaction probability data in the 2–3 eV region, giving a secondary to primary bond yield ratio, Y_s/Y_p, of 2.4–2.6 for the C_2–C_4 cases. The composite isotope effect, $(k_R/k_T)_{D-RH}/(k_R/k_T)_{H-RD}$, is within 2.2 ± 0.3 for the C_2–C_4 hydrocarbons for initial hot atom energies of 1.1, 1.6, and 2.9 eV, and is consistent with the effect expected from inertial considerations. In general, it appears that the relative hot atom reaction yields in different RH compounds or RD compounds are primarily due to reactive effects rather than moderation effects, *i.e.*, to large differences in the primary and secondary bond reactivities.

Introduction

A number of studies on the reactions of photochemically generated hot H, D, and T atoms with hydrocarbons have been carried out since the first such work of Carter, Hamill, and Williams[2] with D atoms from the photolysis of DI. Objectives of these studies have included the determination of absolute and comparative reaction yields,[3-8] threshold energies,[9-11] isotope effects,[12,13] and reaction cross sections.[11] To date there has not been a comparative study of hot atom reaction yields in H–RD and D–RH systems as a function of initial hot atom energy and hydrocarbon structure. The present work was undertaken to investigate this behavior for a sufficient number of cases to obtain the general features of the yield dependence on initial energy, primary to secondary bond ratios, and isotopic system. The results show a high degree of consistency in these effects, which is discussed in terms of steady-state rate coefficients, and per bond yields and isotope effects. The underlying causes of the yield dependences observed here will need to be explored in further work, both experimental and theoretical.

Experimental Section

Reagents. HI and HBr were prepared from aqueous hydroiodic acid (Baker and Adamson ACS, 47% HI) and aqueous hydrobromic acid (Mallinckrodt analytical grade 48% HBr) by freezing an aliquot in a tube on the vacuum line, and allowing the solution to warm in the presence of excess P_2O_5. The HX gas evolved passed through a P_2O_5 drying tube, and was distilled between −115 and −196°

several times before being stored in the dark at −196°. Other deuterated reagents were Stohler Isotopes Chemical DBr (99% D) and Merck of Canada C_2D_6 (99% D), C_3D_8 (98% D), and C_4D_{10} (98% D). Hydrogenated hydrocarbons were Phillips research grade C_2H_6 and n-C_4H_{10}, Matheson instrument grade C_3H_8, and MCB spectroquality n-C_6H_{14}. Hydrogens used to calibrate the mass spectrometer were Matheson prepurified H_2, Isotopes Incorporated HD (Minimum 98% HD), and Matheson D_2 (99.5% D).

Infrared and visible spectra of the HI and HBr showed no detectable impurities in the HBr and only trace amounts of I_2 (less than ≈0.05%) in the HI. Corrections were made for HBr in the DBr by photolyzing DBr samples and determining an effective isotopic purity under photolysis conditions, as described later. The actual isotopic purity of the DBr in the photolysis cells was greater than 97% in all runs. Mass spectroscopic analysis of the deuterated hydrocarbons gave isotopic purities of 99.3% for the ethane, 98.9% for the propane, and 98.4% for the butane. HD was found to contain 1.6% H_2 and 0.4% D_2. Gas chromatography and ultraviolet spectrophotometry detected no impurities in the hydrogenated hydrocarbons or in the hydrogens.

Photolysis System and Procedure. Quartz photolysis cells of inner dimensions 2.40 cm diameter by 10.0 cm length fitted with Suprasil quartz windows and Pyrex stopcocks greased with Kel-F 90 were used for all photolyses. Low-pressure metal vapor lamps were used to obtain lines in the desired spectral range as follows: Hanovia Hg lamp with Suprasil quartz window (185.0 nm), Phillips Zn lamp (213.8 nm), Phillips Cd lamp (228.8 nm), and the Hanovia Hg or General Electric U tube Hg germicidal lamp (253.7 nm). The Zn and Cd sources emitted minor spectral lines at other wavelengths, which were not filtered out except in the experiments with n-C_4D_{10}. The 214-nm Zn source produced interfering lines at 206 and 203 nm (0.2 and 0.3 eV from the main line) amounting together to less than 10% of the intensity (quanta/sec) at 214 nm. The 229-nm Cd source produced an interfering line at 214 nm, 0.3 eV from the main line, which changed from 4 to 12% of the 229-nm intensity as the lamp aged. With the n-C_4D_{10} experiments, a 10 cm length of *cis*-2-butene at 10 Torr removed the 203- and 206-nm Zn lines, and an interference filter was used to block the 214-nm Cd line. For photolysis at 254 nm a Vycor filter was used to eliminate the 185-nm line. For photolysis at 185 nm, X-ray irradiated LiF crystals 1 mm thick were used with the Hanovia lamp to filter out the 254-nm line with all systems except H + n-C_4D_{10}. The 254-nm intensity was several times greater than the 185-nm intensity, and typical LiF absorbancies were 2.4 and 0.4 at the respective wavelengths. In the course of a 1-hr photolysis the absorbancies decreased approximately 10% and reexposure to X-rays after each experiment was required to return the filters to their initial characteristics. With the H + n-C_4D_{10} system hexafluoroacetone imine[14] was used as a 254-nm filter. A 10-cm cell with 50 Torr of the imine at room temperature gave absorbancies of 2.3 at 254 nm and 0.30 at 185 nm.

The initial hydrogen atom translational energies in electron volts may be calculated, assuming ground-state halide atom formation, from the relationship

$$E_i = \frac{m_X}{m_{AX}}\left[\frac{1239}{\lambda} + \bar{E}_{rot}(AX) - D_0°(AX)\right] \quad (1)$$

where m is the atomic or molecular mass, A is H or D, X is Br or I, λ is the photolysis wavelength, $D_0°$ is the dissociation energy from the ground state, and $\bar{E}_{rot}$ is the average rotational energy. All the photolyses were carried out at room temperature (23 ± 1°) where the average vibrational AX energy and A translational energy associated with AX motion are negligible. Taking $D_0°$ values of 3.75 eV for HBr and 3.80 eV for DBr,[15] the initial energies in eV for H atoms are 1.15, 1.67, 2.04, and 2.93 for 253.7, 228.8, 213.8, and 185.0 nm, and for D atoms are 1.08, 1.60, and 2.85 for 253.7, 228.8, and 185.0 nm, respectively.

Mixtures of HBr or HI with RD, or DBr with RH, were prepared on a mercury-free high-vacuum line, using calibrated diaphragm manometers for pressure measurement. Pressures of DBr were in the range 14–16 Torr except in the n-C_4D_{10} work, where the pressure was 11 Torr. Per cent decompositions were held to 0.5% or less for DBr and 0.8% or less for HBr and HI. Since previous work had indicated that dark run corrections were unnecessary, dark runs were only carried out intermittently as a precaution. No significant dark run yields were observed. Mass spectroscopic analyses of HD–D_2 or HD–H_2 product mixtures were performed on a quadrupole mass spectrometer with a Finnigan 1015 analyzer head and EAI Quad 250 electronics. The mass spectrometer was calibrated with HD–H_2 or HD–D_2 standards each time it was used for analysis.

Reaction System. The reactions which must be considered in the systems studied can be generalized for HX–RD as follows.

$$HX \xrightarrow{h\nu} H^* + X \quad (2)$$
$$H^* + HX \longrightarrow H_2 + X \quad (3)$$
$$H^* + HX \longrightarrow H + HX \quad (4)$$
$$H^* + RD \longrightarrow HD + R \quad (5)$$
$$H^* + RD \longrightarrow D + RH \quad (6)$$
$$H^* + RD \longrightarrow H + RD \quad (7)$$
$$H + HX \longrightarrow H_2 + X \quad (8)$$
$$D + HX \longrightarrow HD + X \quad (9)$$
$$R + HX \longrightarrow RH + X \quad (10)$$
$$X + X + M \longrightarrow X_2 + M \quad (11)$$
$$H + X_2 \longrightarrow HX + X \quad (12)$$
$$R + X_2 \longrightarrow RX + X \quad (13)$$
$$D + X_2 \longrightarrow DX + X \quad (14)$$

For DX–RH systems, the same set of reactions are involved with D and H exchanged, and the following discussion applies equally to both types of systems.

H* indicates a "hot" atom, which is defined as an atom with sufficient energy to react by (5), *i.e.*, in the present work essentially atoms with a laboratory energy greater than the threshold energy for (5), $E_5 \simeq 0.4$ eV.[10,11] At room temperature the average thermal atom energy is ~0.04 eV, which is also the realm of activation energies for "scavenging" reactions 8 and 12. Therefore the energy distribution of atoms with $E < E_5$ which are scavenged by HX or X_2 in such systems is in general expected to deviate significantly from thermal. This "quasithermal" distribution approaches thermal as the mole fraction of RD approaches unity.

In systems with thermal energy distributions, the steady-state treatment is usually applied to the reaction scheme to obtain the rate equation in terms of rate constants which are characteristic of the Maxwell–Boltzmann distribution and therefore temperature dependent, and in-

dependent of the molar composition of the reaction mixture. In a hot atom reaction system the situation is reversed: the atomic energy distribution is not Maxwellian, and in general is expected to be composition dependent rather than temperature dependent. However in spite of this *a priori* theoretical expectation, photochemical hot atom–hydrocarbon systems have been found to follow the behavior predicted by the steady-state treatment over a wide composition range. Close adherence to steady-state behavior has also been found for HX–RD–Xe hot atom systems when HX/RD is held constant and the product ratio determined as a function of Xe/RD.[11] Computer-simulated yield calculations on these systems have shown that wide variations in the reactive and non-reactive cross-section functions gave deviations from the steady-state equation of 2% or less over an RD mole fraction range of 1–0.01.

The close adherence of hot atom reaction yields to the linear steady-state equation permits a description of these reactions in terms of phenomenological hot atom rate coefficients, analogous to the usual thermal rate coefficients. For the reaction system given above, if the important reactions are reduced experimentally to (2–11) the steady-state treatment gives eq 15 for the product ratio as a function of reactant ratio.

$$\frac{(H_2)}{(HD)} = \frac{(k_3 + k_4)(HX)}{(k_5 + k_6)(RD)} + \frac{k_7}{k_5 + k_6} \qquad (15)$$

Results

For each photolysis wavelength and reaction system a series of photolyses were carried out at varying reactant ratios. The resulting product ratios were found to be linearly dependent on reactant ratios, and plots of the data were used to obtain the intercept I and slope S, as shown in Figures 1–7. For the DBr–RH systems, the D_2/HD ratios shown in Figures 4–6 have been corrected for DBr isotopic purity. The corrections were made by photolyzing a DBr sample, prepared at the same time as the DBr–RH mixture, to give an effective isotopic purity for DBr which was used to correct the D_2/HD ratio from the DBr–RH mixture photolysis. The corrections were approximately 0.8% at 185 and 229 nm and 2% at 254 nm. The larger correction at 254 nm was due mainly to the larger extinction coefficient ratio $\epsilon_{HBr}/\epsilon_{DBr}$ at this wavelength.[7] Corrections of up to 4% were also applied to the intercept values to account for the effect of minor photolysis lines, the magnitude of the corrections depending on both the lines involved and the value of the intercept. The effect of minor photolysis lines on the slopes was negligible. The slopes and corrected intercepts for the plots of Figures 1–7 are given in Table I. In this and subsequent tables, the precise initial energies E_1 given previously have been approximated to the nearest tenth of an eV.

The intercepts give the fraction of atoms reacting hot in the pure hydrocarbon prior to moderation below threshold, or "integral reaction probability," IRP = $(I + 1)^{-1}$. For simplicity, this quantity will also be referred to as the "yield" in the following discussion. The yields are given in Table II, and these values are also plotted in Figure 8 with the estimated error limits. The error limits shown are two-thirds of the difference between the maximum and minimum values of $(I + 1)^{-1}$ given by lines passing though the rectangular error range of the data points on the product ratio *vs.* reactant ratio plots. The Δx and Δy limits on the error rectangles were calculated as $[\Sigma_i \epsilon_i^2]^{1/2}$ where for Δx the ϵ_i are additive errors in the cell filling

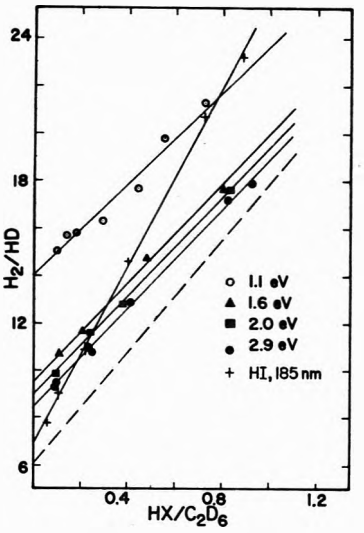

Figure 1. Yields for HBr and HI photolysis in C_2D_6: (– – –) data of Martin and Willard[3] for HBr–C_2D_6 at 2.9 eV.

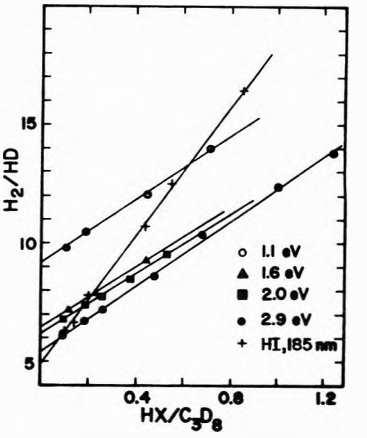

Figure 2. Yields for HBr and HI photolysis in C_3D_8.

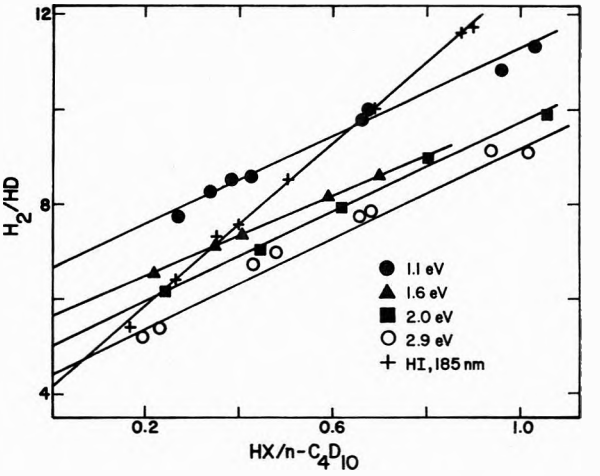

Figure 3. Yields for HBr and HI photolysis in n-C_4D_{10}.

procedure for a particular reactant ratio, and for Δy the ϵ_i are additive errors in the mass spectrometer calibration and product analysis, and in determination of the DBr isotopic purity. The graphical error determination for the intercepts was used for lack of an accurate linear regression analysis procedure when the error range on both the x and y axes is changing with each data point, as is the case

TABLE I: Slopes and Intercepts for the Product Ratio *Vs.* Reactant Ratio as a Function of Initial Energy (eV)

	1.1		1.6		2.0		2.9		HI, 185 nm	
	S	*I*	*S*	*I*	*S*	*I*	*S*	*I*	*S*	*I*
H-C_2D_6	10.0	14.15	10.2	9.53	10.4	9.00	10.5	7.84	18.9	6.94
H-C_3D_8	6.00	9.20	6.38	6.24	6.19	6.09	6.88	5.29	13.5	4.88
H-C_4D_{10}	4.64	6.63	4.24	5.62	4.68	5.02	5.05	4.38	8.55	4.15
D-C_2H_6	3.87	5.66	2.50	4.18			2.15	2.57		
D-C_3H_8	2.01	3.48	1.69	2.68			1.44	1.67		
D-C_4H_{10}	1.62	2.38	1.17	1.84			1.00	1.27		
D-C_6H_{14}	1.09	1.67	0.79	1.23			0.71	0.83		

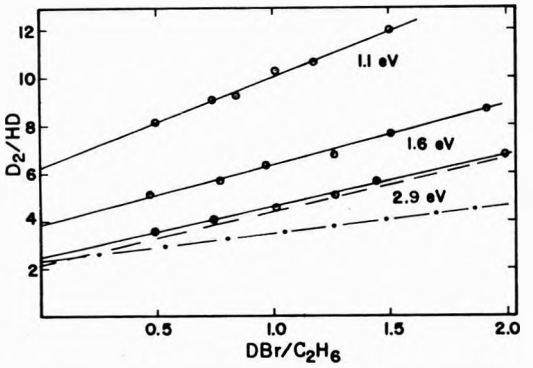

Figure 4. Yields for DBr photolysis in C_2H_6: (– – –) data of Martin and Willard[3] at 2.9 eV; (–•–•–) data of Fink, *et al.*,[6] at 2.0 eV.

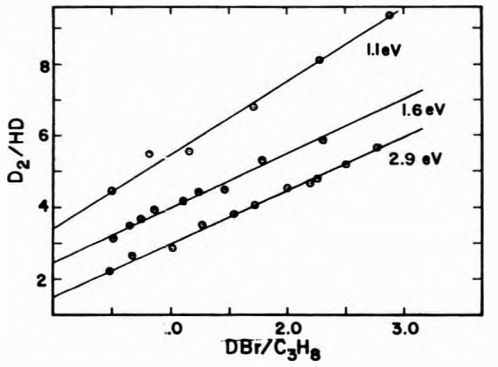

Figure 5. Yields for DBr photolysis in C_3H_8.

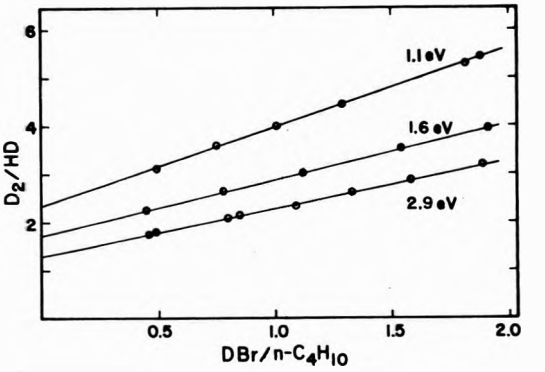

Figure 6. Yields for DBr photolysis in n-C_4H_{10}.

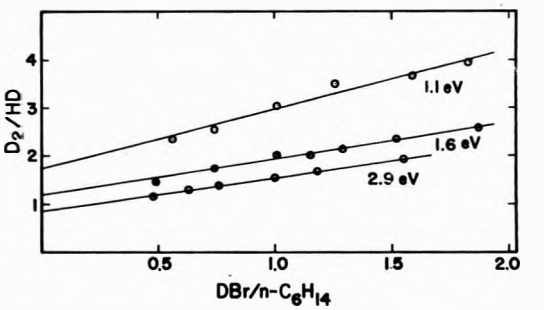

Figure 7. Yields for DBr photolysis in n-C_6H_{14}.

here. Since good linearity was observed in all of the plots in Figures 1–7, the graphical analysis of the intercept error range should be as good as a linear regression analysis with approximations. The differences between the graphical and calculated least-squares intercepts were well within the graphically determined error limits.

Competition between the hydrogen halide and the halogen photolysis product can cause significant errors in the intercepts. HBr decomposition of less than 0.8% appeared to suppress such scavenging errors below the indeterminate error level at all reactant ratios studied. However in preliminary work done with the DBr-C_3H_8 system at 185.0 nm significant negative deviations of product D_2/HD were found at DBr/C_3H_8 ratios below approximately 0.5 for per cent decomposition in the 0.5% range. At higher reactant ratios changes in per cent decomposition in the 0.5% range had no effect within experimental accuracy. The negative deviation for the DBr–RH systems under conditions where it is not observed for HBr–RD systems is probably due to $k_{17}/k_{16} > k_{12}/k_8$ as the mole fraction of

$$D + DX \longrightarrow D_2 + X \qquad (16)$$

$$D + X_2 \longrightarrow DX + X \qquad (17)$$

the hydrocarbon increases, moving the above ratios toward the thermal values. From the results of Fass, *et al.*,[16] and White and Su,[17] for X = Br the hot and thermal (25°) k_{17}/k_{16} ratios are 6 and 58, and the k_{12}/k_8 ratios are 5 and 23, respectively. The hot reaction coefficient ratios are only weakly dependent on hot atom initial energy above 1 eV. For the per cent decompositions used in the present work the average per cent of scavenged atoms scavenged by Br_2 is calculated to be 1.0–4.4% in competition with HBr and 0.7–7% in competition with DBr, where the range is for hot *vs.* thermal scavenging. The per cent decompositions and minimum reactant ratios were experimentally adjusted to give product ratios within 3% of the estimated 0% decomposition limit as estimated from studying the reactant ratios as a function of per cent decomposition. For DBr/RH ratios of 0.5 or greater the yield data indicate that more than half of the scavenging reactions are hot.

Several HBr-C_3D_8 and DBr-C_4H_{10} samples with HBr or DBr pressures of 1 Torr were photolyzed at 229 and 254 nm. Irreproducibility as high as ±25% in the product ratio was observed in the 0.1–1.0 reactant ratio range. Light stops which increased the distance from the light beam to

the cell wall did not solve this problem, which was not encountered at hydrogen halide pressures of 9–16 Torr.

A possible source of kinetic error is the reaction

$$Br + RD \longrightarrow DBr + R \qquad (18)$$

Although D atom abstraction by Br has an activation energy of ~0.5 eV, (18) could possibly compete with (19), which has an activation energy <0.04 eV[16] but is second order in radicals. Reaction 18 coupled with reaction 20 could form a chain producing enough DBr to compete with HBr in photodissociation. The resulting D* would react with HBr to give HD and with RD to give D_2, so that the net effect would be to increase the experimental yield HD/(HD + H_2). Hydrogen atom abstraction by Br atoms would also raise the experimental yield in DBr–RH systems. The evidence in the present work indicates that (18) did not compete with (19) in either type of system.

$$Br + Br + M \longrightarrow Br_2 + M \qquad (19)$$

$$R + HBr \longrightarrow RH + Br \qquad (20)$$

The analogous iodide abstraction reactions can be ruled out with activation energies >1 eV, and the HI photolysis results are found to be consistent with the HBr results (Figure 8). In addition, the product ratios in the HX–RD systems were observed to be independent of absorbed intensity over more than an order of magnitude variation, whereas the rate ratio of (18)/(19) would be intensity dependent. No comparisons of DI and DBr data are available for the DX–RH systems. However product analysis of D_2/HD/H_2 from the DBr–RH mixtures showed no significant amount of H_2 above that expected from the normal amount of HBr impurity in the initial DBr. It should be noted that the effect of HBr would be greatly enhanced at 254 nm, since at this wavelength the extinction coefficient ratio $\epsilon_{HBr}/\epsilon_{DBr}$ is about 6,[7] whereas it is close to unity at 185 nm. Also the absorbed light intensity at 254 nm was an order of magnitude lower than that at 229 nm, which would increase Br abstraction of H with respect to the biradical Br recombination reaction. However as shown in Figure 8, the 254-nm yields drop off consistently from the higher energy values and show no indication of being abnormally high.

The results for H + C_2D_6 and D + C_2H_6 at 2.9 eV are compared with those of Martin and Willard[3] (MW) in Figures 1 and 4. MW obtained yields of 0.14 and 0.31 respectively for H + C_2D_6 and D + C_2H_6, compared to the 0.11 and 0.28 of the present work. MW underestimated the error due to product Br_2 scavenging, and used per cent hydrogen bromide decompositions as high as 10%, giving average bromine/hydrogen bromide ratios up to 2.5%. Estimates of the Br_2 scavenging error in the MW work expected on the basis of recent data on the relative rates of hot and thermal hydrogen bromide and bromine reactions[16,17] are consistent with their higher yield values. The errors in the MW methane results were larger, as a result of the small yields for these cases. The H–CD_4 yield at 2.9 eV in the limit of low HBr per cent decomposition has been found to be 0.039[7] compared to the MW value of 0.062. MW found a yield for D–CH_4 of 0.17, which we estimate is approximately 25% above the true value. For large per cent decompositions halogen scavenging can cause significant negative deviations from linearity in the data for sufficiently small reactant ratios, and this was observed by MW with the HBr–CD_4, DBr–CH_4, and DBr–C_2H_6 reaction systems. More commonly halogen scavenging shifts the data toward increasingly large negative deviations with decreasing reactant ratios, while leaving it linear within experimental error. Therefore the linearity of photochemical hot atom data is not by itself evidence that the halogen scavenging effect is within experimental error. The shifting of the line is illustrated by comparison of the MW and present data in Figures 1 and 4. The lines approach each other at high reactant ratios because in this domain the halogen/hydrogen halide rate coefficient ratios approach the hot values given previously.

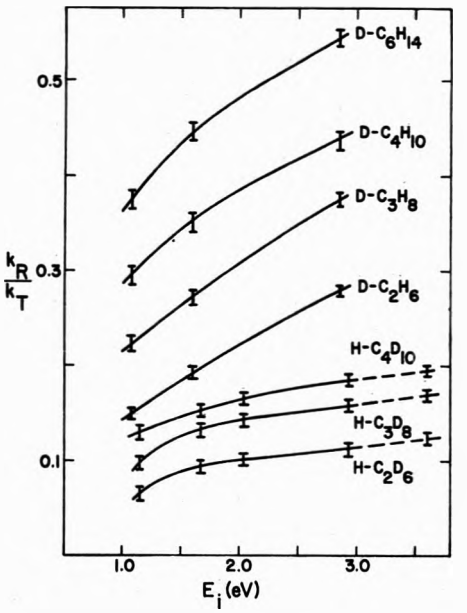

Figure 8. Hot atom reaction yields for hydrocarbon systems (eq 21a). E_i is the initial hot atom laboratory energy. The yields from the 185-nm photolysis of HI have been placed at the maximum H energy of 3.6 eV, although the average value may be somewhat lower (see text). The curves are all expected to pass close to the origin.

Nicholas, Bayrakceken, and Fink (NBF) have studied the yield *vs.* E_i for the D–C_2H_6 system.[6,10] The NBF product *vs.* reactant linear plot for E_i = 2.0 eV[6] is shown in Figure 4, and gives an intercept about 2/3 and a slope about 1/2 of that expected from the present work. They obtain a yield of 0.30 whereas the D–C_2H_6 plot in Figure 8 gives a value of 0.22 at 2.0 eV. In a subsequent publication[10] they have studied the yield from 0.28–1.95 eV, and found (from their Figure 1[10]) values of 0.19 at 1.1 eV and 0.27 at 1.6 eV, in contrast to the 0.15 and 0.19 found at these energies in the present work. The error bars shown in Figure 8 are approximately standard deviations (see previous discussion) based on the random errors in the cell-filling and analysis procedures, and are ±0.01 or less. Taking twice this (±0.02) as an estimate of the maximum error, which is the same as that quoted by NBF,[6] still leaves a significant discrepancy between our results and those of NBF for D–C_2H_6 at 1.6 and 2.0 eV. The cause of the discrepancy is unknown. The Br_2 scavenging error would cause a low intercept, but the NBF DBr decomposition was reported to be 1% or less, and the slope of the NBF line in Figure 4 is smaller than expected from the present work, whereas a high percentage decomposition would be expected to give a slope which is too large, as discussed above.

In earlier work from this laboratory,[18] the photodissociation energetics of HI were investigated using the H + n-C_4D_{10} yield as an energy calibration curve for H atoms

TABLE II: Dependence of the Integral Reaction Probability (k_R/k_T) on Hot Atom Initial Energy (eV)[a]

	1.1		1.6		2.0		2.9		HI, 185 nm	
H–C_2D_6	0.066	1.00	0.095	1.00	0.100	1.00	0.113	1.00	0.126	1.00
H–C_3D_8	0.098	1.48	0.138	1.45	0.141	1.41	0.159	1.41	0.170	1.35
H–C_4D_{10}	0.131	1.98	0.151	1.59	0.166	1.66	0.186	1.65	0.194	1.54
D–C_2H_6	0.150	1.00	0.193	1.00			0.280	1.00		
D–C_3H_8	0.223	1.49	0.272	1.41			0.375	1.34		
D–C_4H_{10}	0.296	1.97	0.352	1.82			0.441	1.57		
D–C_6H_{14}	0.375	2.50	0.447	2.32			0.545	1.95		

[a] The data on the right in each column are normalized to ethane.

generated from HI photolysis. The yields obtained in that work for HI and DBr at 1850 Å were too high, and have been corrected in the present work. It appears that the major cause of the previous error was again excess per cent HX decomposition, and possibly some spurious X_2, especially in the HI work, from thermal decomposition during cell-filling procedures. The new data on the H–C_4D_{10} system in the 3.0-eV region bring into question the earlier conclusions on the photodissociation energetics of HI. Previously the H atom energy from HI at 185 nm was found to be 3.6 eV. The data of Table II and Figure 8 are in agreement with this assignment, but the small slope of the curve does not permit a sensitive test of hot atom energy in the 3-eV region. The H–RD curves in Figure 8 show a consistent increase with energy from 1.6 to 2.9 eV, and using these curves and the error bars on the 185-nm HI yield data, a lower limit of 3.3 eV is obtained for the hydrogen atom energy from all three curves. The fact that the yields for all three HI–RD systems are as expected for 3.6-eV H atoms suggests that the average H atom energy from HI at 185 nm is closer to this upper limit than to 3.3 eV.

The previous H–C_4H_{10} data were also used to estimate the hot hydrogen atom energy from H_2S at 185 nm.[19] The value of 2.3 eV was in satisfactory agreement with the 2.6 eV found for D_2S at 185 nm,[20] using the present D–C_4H_{10} yield data. This and the fact that the H_2S yield was in an energy region where there is reasonable agreement between the present and former H–C_4D_{10} yield curves supports the previous findings regarding the H_2S photodissociation energetics.

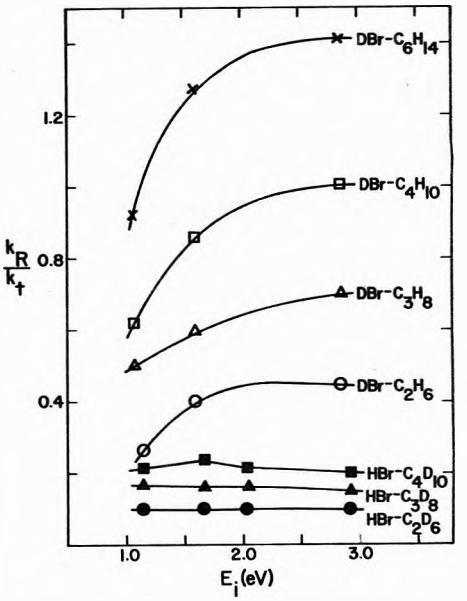

Figure 8. k_R/k_t (eq 21b) as a function of E_i. The curves are all expected to pass close to the origin.

Discussion

From the steady-state expression (15), the following hot atom rate coefficient ratios may be defined

$$(I + 1)^{-1} = \frac{k_5 + k_6}{k_5 + k_6 + k_7} = \frac{k_R}{k_T} \quad (21a)$$

$$S^{-1} = \frac{k_5 + k_6}{k_3 + k_4} = \frac{k_R}{k_t} \quad (21b)$$

$$I/S = \frac{k_7}{k_3 + k_4} = \frac{k_M}{k_t} \quad (21c)$$

$$(I + 1)/S = \frac{k_5 + k_6 + k_7}{k_3 + k_4} = \frac{k_T}{k_t} \quad (21d)$$

where k_R is the rate coefficient for reaction with the hydrocarbon, k_M is the hydrocarbon moderation rate coefficient, k_T is the total interaction rate coefficient for the hydrocarbon ($k_T = k_R + k_M$), and k_t is the total interaction rate coefficient for interaction with hydrogen halide. The functions 20a–d are plotted *vs.* initial hot atom energy in Figures 8–11.

Chou and Rowland[5b] found 22% substitution in reactions of T atoms with CH_4 at E_i = 2.8 eV, whereas with CD_4 the substitution yield was 6%,[9] and fell to <1% at 1.9 eV. It appears that the per cent substitution by tritium with the higher hydrocarbons is much lower than with methane in this energy region.[21] On the basis of this indirect evidence the yields of the present work are assumed to be due essentially to abstraction, *i.e.*, $k_6 \ll k_5$. Since the substitution thresholds for the H + RD and D + RH systems are expected to be similar to the T + CD_4 threshold, $k_6 \ll k_5$ should be an excellent approximation below 2 eV. If substitution contributes significantly at higher energies, the discussion and conclusions of this work apply to the total hot atom yield (abstraction + substitution) above 2 eV.

Comparison of Figures 8 and 9 shows a similarity in the trend of the k_R/k_T and k_R/k_t functions with respect to reaction system and energy. Both functions increase in the same order for the seven hydrocarbons studied although k_R/k_T involves only hydrocarbon coefficients, whereas k_R/k_t involves both hydrocarbon and hydrogen halide coefficients, and compares H + HBr with D + DBr. There is also a similarity in the energy dependence of the two functions over the initial energy range studied. k_R/k_T increases with E_i for all the hydrocarbons, rising more slowly for the H–RD systems than for D–RH. k_R/k_t is nearly independent of energy for the HBr–RD systems, and increases over the 1–3 eV range for D–RH, although it may reach a maximum in the 3-eV region.

As seen in Figure 10, the HBr–RD systems show a general decrease in k_M/k_t with increasing E_i, whereas for

TABLE III: Values of k_R/k_t and k_M/k_t Relative to Ethane, as a Function of Initial Energy (eV)

	1.1		1.6		2.0		2.9		HI, 185 nm	
	k_R/k_t	k_M/k_t	k_R/k_t	k_M/k_t	k_R/k_t	k_M/k_t	k_R/k_t	k_M/k_t	k_R/k_t	k_M/k_t
HBr–C_2D_6	1.00	1.00	1.00	1.00	1.00	1.00	1.00	1.00	1.00	1.00
HBr–C_3D_8	1.67	1.05	1.60	1.05	1.69	1.14	1.53	1.03	1.40	0.98
HBr–C_4D_{10}	2.15	0.99	2.40	1.41	2.23	1.24	2.08	1.16	2.21	1.32
DBr–C_2H_6	1.00	1.00	1.00	1.00			1.00	1.00		
DBr–C_3H_8	1.93	1.18	1.48	0.95			1.49	0.97		
DBr–C_4H_{10}	2.39	1.01	2.14	0.94			2.15	1.07		
DBr–C_6H_{14}	3.55	1.05	3.17	0.93			3.03	0.98		

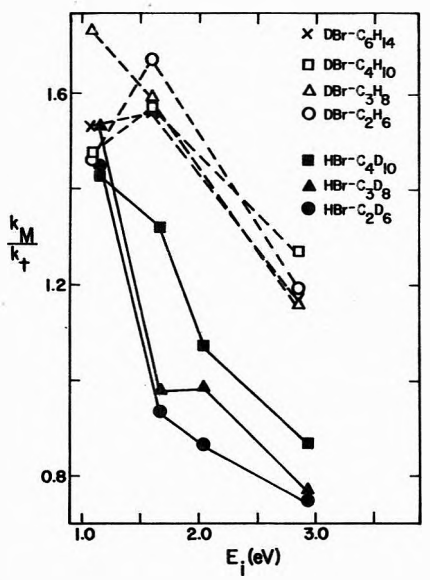

Figure 10. k_M/k_t (eq 21c) as a function of E_i.

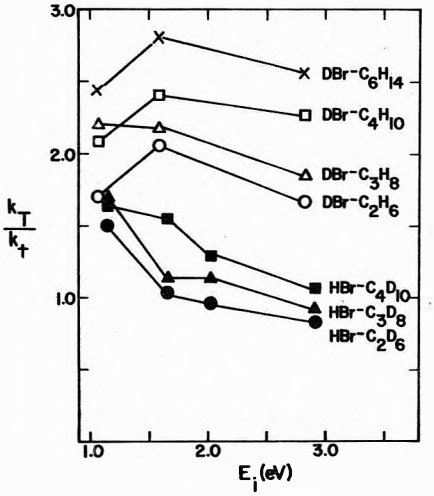

Figure 11. k_T/k_t (eq 21d) as a function of E_i.

DBr–RH k_M/k_t increases in the region 1.1–1.6 eV (except for DBr–C_3H_8) and then decreases in the region 1.6–2.9 eV. Although a few of the k_M/k_t points appear anomalous (*i.e.*, HBr–C_4D_{10} at 1.67 eV and DBr–C_3H_8 at 1.08 eV) the data are otherwise quite consistent within the HBr–RD and DBr–RH groupings. This is illustrated by giving the ± % range of experimental values: at 1.1 eV ±3% for all cases except DBr–C_3H_8, at 1.6 eV ±4% for DBr–RH, at 2.0 eV ±12% for HBr–RD, and at 2.9 eV ±8 and ±5% for HBr–RD and DBr–RH, respectively. It is of interest to compare the role of the slopes and intercepts in producing the anomalous points of Figure 10. In Figure 8 the value of $k_R/k_T = (I + 1)^{-1}$ for D–C_3H_8 at 1.1 eV is in accord with the other data, whereas the value of $k_R/k_t = S^{-1}$ for this system in Figure 9 is high with respect to the trend of the other D–RH data. There is a 10% decrease in the relative values of S^{-1}, normalized to ethane, in going from 1.1 to 1.6 eV, and if this trend is taken into account the data at the two energies can be used to obtain a "normal" value of S^{-1} for D–C_3H_8 at 1.1 eV of 0.43 instead of the experimental 0.50. This would bring the k_M/k_t point of Figure 10 down to 1.50, in agreement with the rest of the data, and shows that k_R/k_t is anomalously large for DBr–C_3H_8 at 1.1 eV. With HBr–C_4D_{10} at 1.67 eV, k_R/k_T appears to be slightly low, and k_R/k_t high with respect to the other data. Using "normal" values for these functions, k_M/k_t would be reduced from 1.32 to 1.18 (with 80% of the correction due to the lower k_R/k_t value) bringing the variation of k_M/k_t for HBr–RD within ±10% at 1.6 eV.

As shown in Figure 11, k_T/k_t reflects the variation in k_M/k_t at low energy, but at 2.9 eV the functions show a progression with change of hydrocarbon similar to that observed for k_R/k_t.

Table III gives the values of k_R/k_t and k_M/k_t relative to ethane. When the data are normalized in this way it is seen that k_M/k_t is similar for different hydrocarbons of the same isotopic type, especially the RH cases. With the exception of HBr–C_4D_{10} at 1.6 and 2.0 eV, and HI–C_4D_{10} at 185 nm, the k_M/k_t values are all within a range of ±10%, whereas the k_R/k_t values increase by more than a factor of 2 for the butanes and a factor of 3 for hexane, indicating that the relative yields in the different hydrocarbons are governed principally by differences in k_R.

The trends in the values of k_R/k_t and k_M/k_t are particularly consistent at the highest energy of 2.9 eV. The absolute k_M/k_t values are in the range 0.81 ± 0.06 for HBr–RD and 1.22 ± 0.06 for DBr–RH. In contrast k_R/k_t increases by 50% of the ethane value for every pair of secondary hydrogens (or deuteriums) added. This behavior can be summarized by the expression

$$k_R/k_t = \alpha(0.096 + 0.025n_s) \qquad (22)$$

where α is a factor of unity for HBr–RD and 4.8 for DBr–RH, and n_s is the number of secondary bonds. The data at 2.9 eV follow this expression to better than experimental error. When the HBr–RD data at 2.9 eV are compared with the HI–RD data at 185 nm (3.3–3.6 eV), values for $(k_t)_{HI}/(k_t)_{HBr}$ of 1.7–2.0 are obtained from k_R/k_t, and 1.8–2.1 from k_M/k_t, showing that the ratio of k_t values for HI and HBr is the same within experimental error when derived from the S^{-1} and I/S functions, and does not vary more than ±10% between the C_2D_6, C_3D_8, and C_4D_{10} substrates.

The high-energy values of k_R/k_T (Table II) correlate well with the total yield expression

$$Y_T = (n_p Y_p + n_s Y_s)/n \quad (23)$$

where Y_T is the total integral hot atom reaction probability in the hydrocarbon, given by k_R/k_T, n_p and n_s are the number of primary and secondary hydrocarbon bonds, Y_p and Y_s are the corresponding per bond yields, and $n = n_p + n_s$. The C_2–C_4 relative yields for H–RD at 2.0 and 2.9 eV correspond to $Y_s/Y_p = 2.6$, giving $C_2/C_3/C_4 = 1.00/1.40/1.64$, while the H–RD yields for HI at 185 nm and D–RH yields at 2.9 eV correspond to $Y_s/Y_p = 2.4$, giving $C_2/C_3/C_4 = 1.00/1.35/1.56$. The relative yield for C_6H_{14} at 2.9 eV corresponds to $Y_s/Y_p = 2.7$. At the lower energies the Y_s/Y_p values corresponding to the relative experimental yields increase with decreasing energy, and also with increasing n at a given energy, with the exception of the H–C_4D_{10} yield at 1.6 eV. For example, at 1.1 eV, the Y_s/Y_p values normalized to ethane are 2.9 and 3.4 for C_3D_8 and C_4D_{10}, and 3.0, 3.4, and 3.6 for C_3H_8, C_4H_{10}, and C_6H_{14}, respectively.

The Y_s/Y_p ratio has been determined for H–C_4D_{10} as a function of E_i in a Xe-moderated system, and found to be 2.5 ± 0.3 in the 1.6–2.0-eV E_i range.[8] All the C_2–C_4 H–RD yield data above 1.6 eV are therefore in accord with eq 23 and a Y_s/Y_p of 2.4–2.6, even though the data are for different reactants and moderators. The D–RH data at 2.9 eV for C_2–C_4 also give a Y_s/Y_p in this range. Therefore it appears that with the C_2–C_4 hydrocarbons, the yields relative to ethane in the 2–3-eV region are determined principally by the primary/secondary bond ratio, rather than the effects of different hot atom energy distributions due to different hydrocarbon, hydrogen halide, or Xe moderators.

The increasing spread in relative yields with decreasing E_i below 2 eV is in accord with the trend in Y_s/Y_p found for C_4D_{10} in Xe-moderated systems.[8] This trend may be attributed at least partially to the difference in the primary and secondary bond strengths, giving a lower threshold for abstraction in the secondary position. The threshold energy difference is 0.1–0.2 eV[11] and it is expected that the resulting yield difference will tend to be obscured by higher energy reactions for E_i an eV or more above the 0.5-eV threshold region. The deviation of the low-energy data from the per bond correlation formula might be ascribed to a decrease in secondary bond energies with increasing chain length, but such differences are unknown within experimental error.[22] Another structural effect which may increase the yield with increasing chain length above that expected on a per bond yield basis is internal scattering, *i.e.*, as the chain length is increased bent structures result, which can be expected to lead to a significant fraction of multiple collision trajectories on the potential energy surface. These could increase the reactive cross section due to energy or inertial effects. An example of an energy effect would be the excitation of an attacked atom on the initial collision, followed by the abstraction of the same atom by the attacking atom after rebounding from an adjacent potential in the molecule. Multiple collisions could also increase the number of abstraction captures by reducing the rate of rebound of the attacking atom from the attacked atom after the initial collision.

Table IV shows the total hot atom yield ratios Y_T(D–RH)/Y_T(H–RD) for three initial hot atom energies. This composite isotope effect, favoring H abstraction by D over D abstraction by H, is nearly independent of structure and initial energy in the 1–3-eV range, the nine values falling within 2.2 ± 0.3. The agreement at 1.1 and 2.9 eV is striking.

TABLE IV: Hot Atom Composite Isotope Effect, Y_T(D–RH)/Y_T(H–RD),[a] as a Function of Initial Energy (eV)

	1.1	1.6	2.9
C_2	2.27	2.03	2.48
C_3	2.27	1.97	2.36
C_4	2.26	2.33	2.37

[a] Y_T is the total hot atom reaction yield (*i.e.*, integral reaction probability) in the pure hydrocarbon, and is equal to k_R/k_T.

TABLE V: Hot Atom Per Cent Yields for Photochemical D Atoms and Recoil T Atoms with Hydrocarbons

		Recoil T[a]	
	D, E_i = 2.9 eV	Abstraction	Substitution
C_2H_6	28.0	33.1	19.7
C_3H_8	37.5	37.4	20.2
C_4H_{10}	44.1	39.2	21.8

[a] Data from ref 23.

The yields observed with photochemical D atoms at E_i = 2.9 eV are compared with those for recoil T atoms with hydrocarbons in Table V. The finding that the D photochemical yields are comparable to recoil T abstraction yields is not surprising, since displacement competes strongly with abstraction in the case of recoil T. Therefore the data of Table V cannot provide an indication of the energy range for recoil T abstraction. As discussed below, inertial effects are expected to favor H atom abstraction by T over D at the same energy.

The agreement between the Y_s/Y_p values from applying the per bond yield formula to the present ethane, propane, and butane data, and the ratio found for H–C_4D_{10} in a Xe-moderated system,[8] suggests that the relative yields are not a sensitive function of the moderating environment. The uniformity of the composite isotope effect is also consistent with this hypothesis, and is in accord with recoil tritium hot atom yields for which moderating isotope effects have been found to be of minor importance compared to reactive effects.[23] The structural independence of the Y_T(D–RH)/Y_T(H–RD) ratios of Table IV also suggests that these ratios are approximately the same for primary and secondary bonds. A reactive isotope effect of 1.3 has been found favoring H atom abstraction over D in recoil T atom reactions with methanes and ethanes.[23] This ratio appears to be insensitive to secondary effects from different substituents. The reactive isotope effect for E_i = 2.8 eV T atom abstraction reactions with methanes is 1.7 ± 0.3.[12] These data and the larger composite isotope effect observed for D + RH *vs.* H + RD abstraction are consistent with an interpretation based on inertial effects. Such effects were explored by Polanyi and coworkers[24] in three-atom model trajectory calculations on hot T atom reactions. At 2 eV it was found that the effect on the abstraction cross section of increasing the mass of the atom under attack was qualitatively the same as the effect of a decrease in the mass of the attacking atom; in both cases there was a decrease in the abstraction reaction cross section. For a given hot atom energy, when the mass of the attacking atom is decreased, the velocity is increased and this results in fewer abstraction captures, since the attacked atom is often not able to move rapidly enough to form the new bond. Increasing the mass of the attacked atom also results in fewer captures for the same reason.

In the photolysis of HI at 254 nm, giving H atoms with a maximum energy of 1.8 eV, Hong and Mains[13] have found per bond isotope effects favoring H over D abstraction of 8 for C_2D_5H and 5 for CHD_2CHD_2 and CH_3CD_3. These effects are larger than would be expected from applying simple inertial considerations to the present results, since the composite effect of switching masses of 1 and 2 amu as the attacking and attacked atom should be greater than the effect of switching these masses as the attacked atom only.

The present results cannot be compared quantitatively with theory until additional data are available on the reactive and nonreactive cross sections. Porter[25] has given a general formulation of hot atom rate theory using a stochastic approach, based on the Miller–Dodson formula for the integral reaction probability

$$Y(E) = \int_{E_0}^{\infty} n(E,E')p(E')\,dE' \qquad (24)$$

$n(E,E')$ is the collision density, defined in Porter's treatment as the average number of collisions per unit energy at E' if the first collision is at E, $p(E')$ is the reaction probability per collision at energy E', and E_0 is the threshold energy. The Miller–Dodson formula was transformed to give

$$Y(E) = p(E) + [1 - p(E)] \int_0^{\infty} P(E,E')Y(E')\,dE' \qquad (25)$$

where $P(E,E')$ is the probability distribution exclusive of reaction

$$P(E,E') = \sigma(E,E')/S_N(E) \qquad (26)$$

$\sigma(E,E')$ is the cross section for collisions in which the laboratory hot atom energy is changed from E to E', $S_N(E)$ is the total nonreactive cross section for hot atom laboratory energy E, and $Y(E')$ is the integral reaction probability starting with energy E' after the first collision. The first term on the right in expression 25 is the probability that reaction takes place on the first collision starting with an initial hot atom laboratory energy E, and the second term is the probability that the reaction occurs on a subsequent collision. The reaction probability per collision is given by $p(E) = S_R(E)/[S_N(E) + S_R(E)]$ where $S_R(E)$ is the total reactive cross section. Equation 25 can be solved by iteration, using $p(E)$ as a first approximation to $Y(E)$.

A calculation of the integral reaction probability requires a knowledge of the differential and total nonreactive scattering cross sections to obtain $P(E,E')$, as well as the total reactive cross section to obtain $p(E)$. If the nonreactive cross sections $\sigma(E,E')$ and $S_N(E)$ are known, then under certain favorable conditions $S_R(E)$ can be extracted from the data by unfolding the IRP integral. However Melton and Gordon[26] have shown that the unfolding of integral rate equations often involves large and unpredicted errors, and in general neither accurate nor unique solutions to the reaction cross section function can be expected from integral reaction probabilities.

Dubrin and coworkers[11] studied the reaction

$$H + n\text{-}C_4D_{10} \longrightarrow HD + C_4D_9(sec) \qquad (27)$$

in a Xe-moderated photochemical hot atom system and determined an $S_R(E)$ curve from the experimental $Y(E_i)$ data. The collision density was calculated using r^{-n} potentials for H–Xe, and the difference between adjacent yields, $\Delta Y(E_i,E_i') = Y(E_i') - Y(E_i)$, was then compared with theoretical ΔY values obtained using trial $S_R(E)$ functions. The final $S_R(E)$ curve was subject to large errors with increasing E, especially at 1 eV and above. The cumulative error could have been reduced by using $CH_3CD_2CD_2CH_3$ as the substrate, instead of taking the difference between $CD_3CH_2CH_2CD_3$ and n-C_4D_{10}.[11] However the method is inherently limited by the small rate of increase of the $Y(E_i)$ function above 1 eV, a trend which is seen both in the H–RD systems (Figure 8), and in the Xe-moderated H–C_4D_{10} system. This results in a large error in determining the $\Delta Y/\Delta E$ function, which is carried through to the $S(E)$ calculation. Therefore it appears that a major improvement in the accuracy of the inert-gas-moderated IRP method would be required to determine the reaction cross section $S_R(E)$ for these systems to useful accuracy for comparison with theory over the 1-3-eV range. This is particularly true in view of the uncertainties involved in IRP unfolding procedures.[26]

References and Notes

(1) This research was supported by the National Science Foundation, Grant No. GP-8579.
(2) R. L. Carter, W. H. Hamill, and R. R. Williams, *J. Amer. Chem. Soc.*, **77**, 6457 (1955).
(3) R. M. Martin and J. E. Willard, *J. Chem. Phys.*, **40**, 3007 (1964).
(4) J. C. Biordi, Y. Rousseau, and G. J. Mains, *J. Chem. Phys.*, **49**, 2642 (1968).
(5) (a) C. C. Chou, T. Smail, and F. S. Rowland, *J. Amer. Chem. Soc.*, **91**, 3104 (1969); (b) C. C. Chou and F. S. Rowland, *ibid.*, **88**, 2612 (1966).
(6) J. E. Nicholas, F. Bayrakceken, and R. D. Fink, *J. Phys. Chem.*, **75**, 841 (1971).
(7) J. A. Betts, Ph.D. Thesis, California Institute of Technology, 1971. Available from University Microfilms, Ann Arbor, Michigan.
(8) R. G. Gann, W. M. Ollison, and J. Dubrin, *J. Amer. Chem. Soc.*, **92**, 450 (1970).
(9) C. C. Chou and F. S. Rowland, *J. Chem. Phys.*, **50**, 2763 (1969).
(10) J. E. Nicholas, F. Bayrakceken, and R. D. Fink, *J. Chem. Phys.*, **56**, 1008 (1972).
(11) R. G. Gann, W. M. Ollison, and J. Dubrin, *J. Chem. Phys.*, **54**, 2304 (1971).
(12) C. C. Chou and F. S. Rowland, *J. Phys. Chem.*, **75**, 1283 (1971).
(13) K. Hong and G. J. Mains, *J. Phys. Chem.*, **76**, 3337 (1972).
(14) S. Toby and G. O. Pritchard, *J. Phys. Chem.*, **75**, 1326 (1971).
(15) B. de B. Darwent, *Nat. Ref. Data Ser., Nat. Bur. Stand.*, **No. 3**, (1970).
(16) (a) R. A. Fass, *J. Phys. Chem.*, **74**, 984 (1970); (b) R. A. Fass, J. W. Hoover, and L. M. Simpson, *ibid.*, **76**, 2801 (1972).
(17) J. M. White and H. Y. Su, *J. Chem. Phys.*, **57**, 2344 (1972).
(18) L. E. Compton and R. M. Martin, *J. Phys. Chem.*, **73**, 3474 (1969).
(19) L. E. Compton, J. L. Gole, and R. M. Martin, *J. Phys. Chem.*, **73**, 1158 (1969).
(20) L. E. Compton and R. M. Martin, *J. Chem. Phys.*, **52**, 1613 (1970).
(21) F. S. Rowland, private communication.
(22) J. W. Root, W. Breckenridge, and F. S. Rowland, *J. Chem. Phys.*, **43**, 3694 (1965).
(23) R. Wolfgang, *Progr. React. Kinet.*, **3**, 97 (1965).
(24) P. J. Kuntz, E. M. Nemeth, J. C. Polanyi, and W. H. Wong, *J. Chem. Phys.*, **52**, 4654 (1970).
(25) R. N. Porter, *J. Chem. Phys.*, **45**, 2284 (1966).
(26) L. A. Melton and R. G. Gordon, *J. Chem. Phys.*, **51**, 5449 (1969).

Comments on the Ultraviolet Spectrum and Photophysical Properties of Trimethylenecyclopropane

Ernest A. Dorko,

Department of Aeromechanical Engineering, Air Force Institute of Technology, Wright-Patterson Air Force Base, Ohio 45433

Richard Scheps, and Stuart A. Rice*

The Department of Chemistry and The James Franck Institute, The University of Chicago, Chicago, Illinois 60637
(Received October 12, 1973)

Publication costs assisted by the Air Force Office of Scientific Research

The spectrum and fluorescence of TMCP are analyzed with respect to possible photoproducts.

I. Introduction

Recent theoretical[1] and experimental[2-4] studies have considerably extended our understanding of photophysical radiationless processes in large aromatic molecules. In the best studied case, namely benzene[2] and several of its deuterated derivatives,[3,4] single vibronic level fluorescence lifetime data are in excellent agreement with theoretical calculations which emphasize the importance of frequency changes and shifts of origins of the CH and CC vibrational modes which serve as energy acceptors.[1] Thus far, however, the adequacy of the theory has been tested only in the prediction of relative rates of radiationless decay. The far more ambitious task of predicting the absolute rates of radiationless decay depends on accurate evaluation of the electronic matrix element connecting the zeroth-order manifolds $^1B_{2u}$ and $^3B_{1u}$, a calculation which is fraught with uncertainty because of the inaccuracies in currently available molecular wave functions.

As part of a study designed to contribute to the data base from which can be obtained information about the importance of different kinds of vibronic coupling for radiationless processes, we have examined the spectrum and fluorescence of trimethylenecyclopropane (TMCP). TMCP, the first member of the family of radialenes, is a stable isomer of benzene. In contrast with benzene, its lowest electronic transition is allowed and strong while the next two are forbidden. Furthermore, the photolysis of TMCP is expected to lead to fulvene and benzene, isomers more stable than TMCP hence accessible with the energy of excitation in the lowest allowed transition. Thus, a study of the photophysics of TMCP provides, in principle, an opportunity to examine the coupling between competing photochemical and photophysical decay channels, as well as the influence thereon of vibronic coupling.

We have been unable to detect fluorescence from TMCP and so have been unable to compare its decay processes with those of benzene. Nevertheless, the absence of fluorescence taken together with available molecular orbital calculations does permit some limited deductions to be made about radiationless decay in TMCP. A more positive outcome of our investigation is the observation of a set of Rydberg transitions from which the ionization potential of TMCP can be estimated.

II. Results

The uv absorption spectrum of TMCP is reproduced in Figure 1. Absorption begins near 3430 Å. An intense diffuse transition appears with a maximum at 2885 Å and shoulders at 2990 and possibly 3200 Å. Above 3100 Å the spectrum displayed shows some absorption due to unremoved second-order light. This contribution is small, however, and its effect may be gauged by the intensity of the structure near 3220 Å. In the unpurified compound a weak band was observed at 2515 Å, but this did not appear in the purified samples. A second broad transition of lower intensity is observed with a peak at 2235 Å and with a shoulder at 2295 Å. (This band was originally reported[5] to have greater intensity than the 2885-Å band. However, the earlier observation was not corrected to account for instrumental anomalies and does not reflect the true intensity relationships.) The absorption at higher energy suggests a Rydberg series with an ionization potential in the vicinity of 9 eV. The results of this spectroscopic investigation are summarized in Tables I and II. Our suggested classification of the Rydberg bands, shown in Table II, gives an ionization potential of 9.0 eV and quantum defect $\delta = 0.58$. The agreement between calculated and observed band positions is excellent, especially when the uncertainties in observed band positions (~ 100 cm^{-1}) are taken into account.

In order to determine if the broadening in the lower energy transitions can be attributed to hot band and sequence congestion an attempt was made to measure the absorption of TMCP at low temperature. Initially, we hoped to use a suitable matrix as a Shpolskii host,[6] but difficulty in handling TMCP prevented this and finally we recorded the spectrum of the pure solid at 77°K. The spectrum obtained was not noticeably less diffuse than that of the gas. Although interactions in the pure solid can lead to spectral broadening, and therefore this result is inconclusive, we believe the weight of evidence and conjecture supports the notion that the observed spectral broadening is a result of nonradiative processes.

The results of the fluorescence study place an upper limit on the quantum yield for fluorescence. We used λ_{exc} 2885 Å with relatively large bandpass (3.8 Å). After 4 hr of excitation at 5-kHz pulse repetition frequency no fluorescence was observed. Earlier work on chloroacetylene[7] has shown that quantum yields as low as 0.025 can be mea-

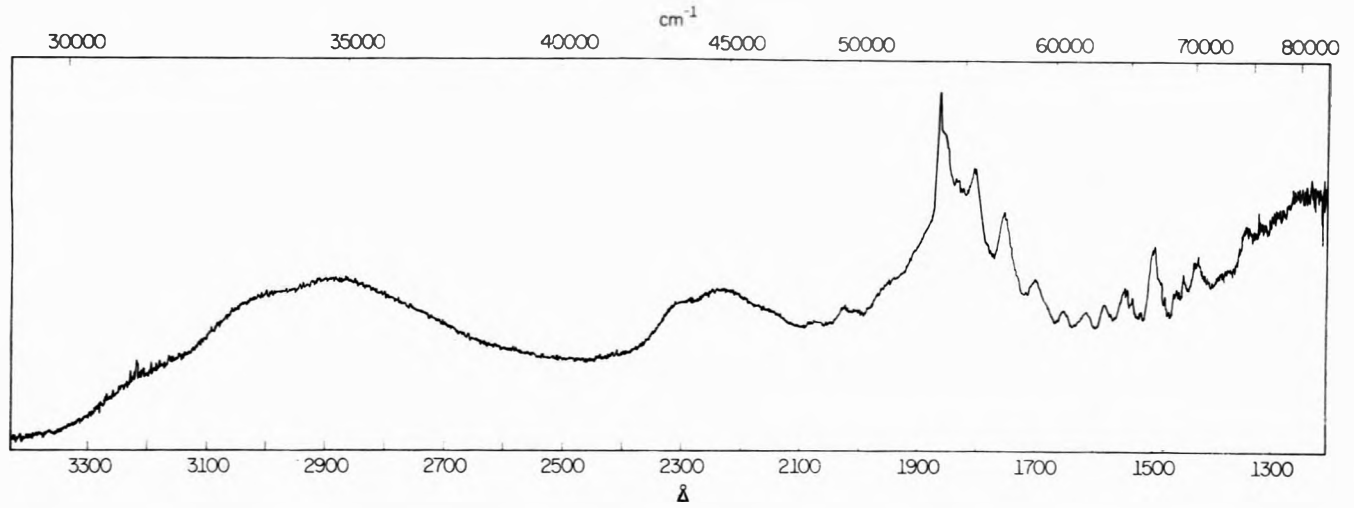

Figure 1. Absorption spectrum of TMCP vapor at ~1 Torr. The region between 1800 and 1900 Å was originally recorded on a reduced scale, and was expanded for this figure, hence the line shape in this region is not exact. The resolution is ~0.5 Å and the cell path length 10 cm.

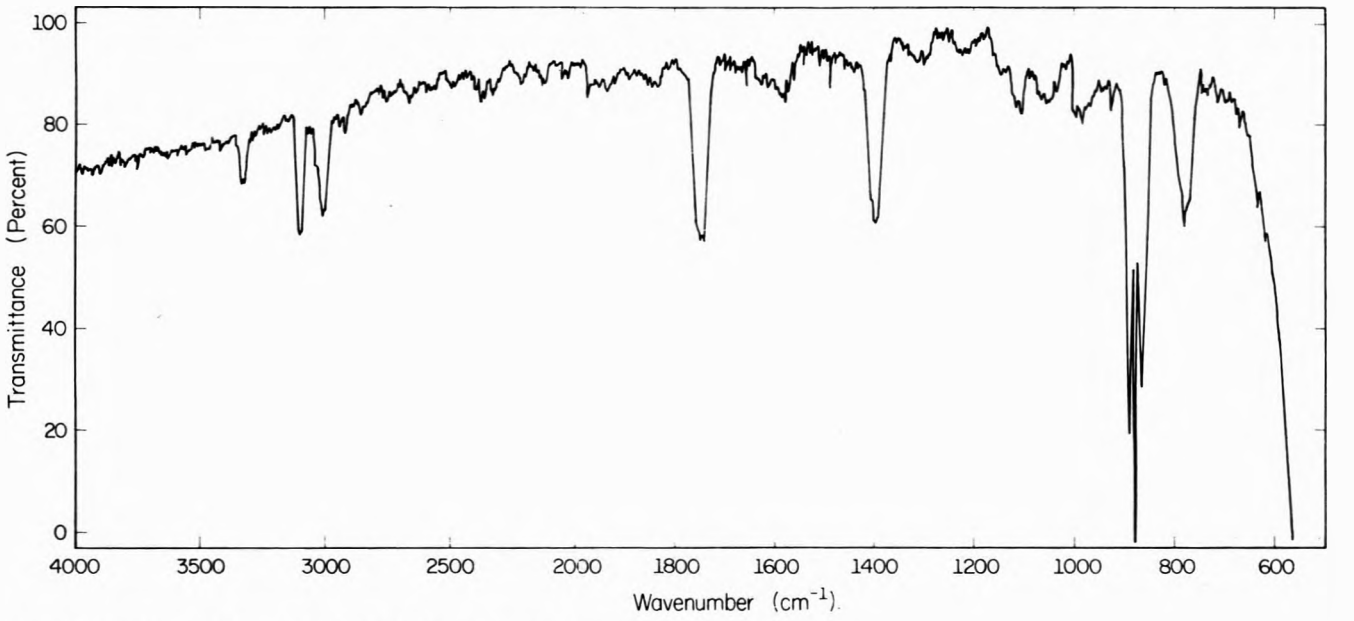

Figure 2. Infrared spectrum of TMCP vapor at ~1 mm, cell path 5 cm.

sured using our apparatus. We take this value as an upper limit to the quantum yield of TMCP, although it is reasonable to expect the actual value to be at least an order of magnitude lower.

The infrared absorption spectrum we have obtained is shown in Figure 2. The agreement with the work of Rhee and Miller[8] is excellent. We observe that the bands proposed by these authors to be impurity bands appear in our spectrum as well. It is interesting to note that although we and they used the same method of synthesis, our purification was more extensive. Yet these "impurity" bands appear with the same relative intensity in both spectra. One infers that these bands may not, after all, be due to impurity.

III. Discussion

The results of this work clearly show that TMCP in its lowest excited state is efficiently depopulated through nonradiative processes. Certainly one such process will be intersystem crossing. Two triplet manifolds can, in principle, play a role in this crossing. If the theoretical prediction[9] is accurate, T_1 and T_2 lie, respectively, ~18,000 and 1300 cm^{-1} below S_1. We expect that crossing to T_1 will be inefficient because the energy gap is half an order of magnitude larger than the highest frequency acceptor mode, and the Franck-Condon factor for the isoenergetic crossing must be very small. We also expect that crossing to T_2 will be only modestly efficient, probably less efficient than the $S_1 \rightsquigarrow T_1$ crossing in benzene. Here the limitation on the rate of crossing will be determined by the low density of acceptor modes because of the very small energy gap (the S_1-T_1 energy gap in benzene is ~8000 cm^{-1}). Thus, it seems unreasonable to us that crossing to either T_1 or T_2 can be so efficient that all fluorescence is quenched. Accordingly, we look elsewhere for an explanation of the low quantum yield of fluorescence of TMCP.

We expect that the excited state is effectively depopulated *via* a photochemical pathway. One possibility is

TABLE I: Transitions in TMCP

λ_{max}, Å[a]	Energy, cm^{-1}	Appearance	Assignment
2885	34,662 (4.3 eV)	Broad, intense shoulders at 2990 and 3200 Å	$^1E'$
2235	44,743 (5.5 eV)	Broad, weaker than 2885-Å system	
2075	48,193 (6.0 eV)	Weak bands	
2025	49,383		
2005	49,875		
1950	51,282 (6.4 eV)	Shoulders to continuum	$^1E'$
1900	52,632 (6.5 eV)		
1857	53,850 (6.7 eV)	Intense structured system superposed on continuum	Rydberg $n = 3$ (3R)
1850	54,054		
1835	54,494		$3R4_0^1$
1802	55,494		$3R2_0^1$
1775	56,338		$3R2_0^14_0^1$
1752	57,078		$3R2_0^24_0^1$
1730	57,803		$3R2_0^24_0^2$
1699	58,858		$3R2_0^3$
1675	59,701		$3R2_0^34_0^1$
1650	60,606		$3R2_0^4$
1610	62,112		$3R2_0^5$
1580	63,291 (7.8 eV)		4R
1572	63,613		$3R2_0^6$
1547	64,641		$4R3_0^1$ (?)
1542	64,851		$4R2_0^1$
1535	65,147		$3R2_0^7$
1520	65,789		$4R2_0^14_0^1$
1498	66,756 (8.3 eV)		5R; $3R2_0^8$; $4R2_0^2$
1485	67,340		$5R4_0^1$
1480	67,568		$4R2_0^24_0^1$
1472	67,934		$5R4_0^2$
1463	68,353		$5R2_0^1$
1457	68,634 (8.5 eV)		6R
1448	69,061		$5R2_0^14_0^1$
1432	69,830 (8.6 eV)		7R
1428	70,028		$5R2_0^2$
1423	70,274		$6R2_0^1$
1385	72,202	Broad bands	
1375	72,727		
1357	73,692		

[a] Bands are uncertain to ±2 Å due to diffuseness.

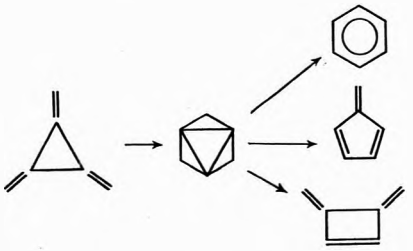

which leads to the formation of benzene, fulvene, and dimethylenecyclobutene. Angular momentum is easily conserved for the pictured photochemical intermediate despite the change in moments of inertia. It is at least possible that this mechanism dominates the decay of excited TMCP.

We consider now the absorption spectra of TMCP.

The ir spectrum is similar enough to that of Rhee and Miller[8] to eliminate the need for any further discussion of it.

The electronic absorption spectrum indicates four intravalence transitions and a Rydberg series. From the latter we obtain a first ionization potential of 9.0 eV. This agrees well with the value of 9.07 eV calculated by Simmons[9] (corrected to obtain optimum agreement for 1,3-butadiene and hence lower by 2.45 eV than the original calculation). The vibrational structure is quite pronounced, especially for ν_2, the totally symmetric C=C stretch. This is to be expected since the π electrons lie highest in energy, and ionization will be accompanied by a weakening and, hence, elongation of the C=C bond. The Rydberg series is allowed and is either of species E′ or A_2''. We note that transitions to all p orbitals and all d orbitals except d_{z^2} are allowed. The value of δ implies excitation to np orbitals, but we cannot distinguish between $np\pi$ and $np\sigma$ orbitals. The state of the ion is $^2E''$.

TABLE II: Rydberg Analysis

$$\tau = \text{IP} - \frac{109{,}737.1}{(n-\delta)^2}\ (\text{cm}^{-1})$$

n	Obsd, cm^{-1}	Calcd, cm^{-1}	Δ(obsd − calcd), cm^{-1}
3	53,850	53,774	−76
4	63,291	63,130	−161
5	66,756	66,895	+139
6	68,634	68,777	+143
7	69,830	69,850	+20
8	Not observed	70,519	

$\delta = 0.58$

IP = 72,512 ± 800 cm^{-1} (9.0 ± 0.1 eV)

Underlying the "sharp" (15-Å full-width at half-maximum) $n = 3$ Rydberg transition is a broad continuum, which we associate with the $S_0 \rightarrow S_4$ ($^1E'$) transition, calculated to lie at 7.1 eV and observed at ~6.4 eV. It is interesting to note that no interference effects arising from interaction between the Rydberg levels and the intravalence continuum are observed. This observation can be explained if there is only limited configuration interaction between the Rydberg and S_4 valence states, or by assuming the Rydberg state has symmetry A_2''. This latter suggestion leads to a classification of Rydberg states which bears strong analogy to benzene.[10]

We associate the low-energy intense transition with $S_0 \rightarrow S_1$ ($^1E'$), observed at 4.3 eV ($\hbar\omega_{max}$) and predicted to lie at 4.8 eV (origin). There is little doubt in this assignment.

We are left with two unassigned transitions, one at 5.5 eV ($\hbar\omega_{max}$), the other at 6.0 eV. Two states are predicted to lie in this region, both dipole forbidden and both at ~7.1 eV. It is possible that these bands obtain allowed character by vibronic mixing with the E′ states and we would then assign the band to the red as $^1A_2'(S_2)$ and the band to the blue as $^1A_1'(S_3)$. Unfortunately the band assigned $^1A_2'$ has no vibrational structure so that we cannot confirm the assignment.

The weaker system is also difficult to assign for the same reason, although we note that the spacing between the first two bands is roughly twice that between the second and third (within the error set by the diffuseness) and this corresponds roughly to the e′ vibration ν_{14} reported by Burr, *et al.*[11] Finally, we remark that several authors have assigned the bands at 5.5 and 6.0 eV to impurities and scattered light (instrumental limitations).[9,12] While we cannot conclusively rule out this possibility for the 5.5-eV band, we offer the following information. (1) The 5.5-eV band persisted, with roughly the same relative intensity, through repeated vacuum distillations, so that if

it were due to an impurity that impurity must have a vapor pressure similar to that of TMCP. The expected impurities do not satisfy this criterion. In particular, the impurity bands which appear in the ir spectrum are most likely due to the dimer, which of course will have a lower vapor pressure. (2) The spectra of the impurities expected to be present were taken and none produced the 2235-Å absorption band. (3) We did not observe any further absorption bands of the proposed impurity in the uv and vacuum uv. However, it remains difficult to satisfactorily explain the results of Waitkus, *et al.*,[11] who, using TMCP obtained *via* a different synthesis, did not observe the 5.5-eV band, and the theoretical predictions of Simmons,[9] who does not predict an allowed transition in this region.

The spectral assignments suggested and the nonradiative decay mechanism suggested cannot be considered established at the present time. Experimental work with perdeuteriotrimethylenecyclopropane, more sensitive fluorescence experiments, photochemical product analysis, and more accurate molecular orbital calculations are all necessary before the matter can be resolved. Further studies will be reported at a later time.

IV. Experimental Method

TMCP was prepared as previously described.[5] The sample was passed through a trap containing KOH to absorb H_2O and CO_2 and then was subjected to a bulb-to-bulb distillation at 250°K (P_{vap} = 0.85 Torr). A complicating factor in handling TMCP is its extreme tendency to polymerize. This called for special considerations in working with the compound throughout this project. The severest test of purity was the reproducibility of the absorption spectrum upon repeated fractionation of the TMCP. The vapor pressure of TMCP was determined at 256, 263, and 295°K to be 1.5, 2.5, and 23 Torr, respectively. From these data the heat of vaporization was determined to be 10.7 kcal/mol and the boiling point 367°K.

The sample cell was filled by connecting it to the reservoir containing TMCP. The reservoir was immersed in a slurry of appropriate temperature so that TMCP could vaporize into the test cell to the desired vapor pressure without excessive polymerization.

Sample cells used were (1) a 10-cm path length LiF windowed cell modified from the original McPherson design to include a stainless steel stopcock valve so the it could be filled on any vacuum line in the laboratory and moved to the spectrometer. The cover for the stainless steel dual beam sample chamber was modified to allow the entire cell assembly to be evacuated. (2) Modified 1- and 2-mm quartz curvets which fit into a liquid nitrogen optical dewar, (3) a fluorescence cell similar to that used in the previously reported studies of benzene, and (4) a 10-cm path length Perkin-Elmer infrared cell fitted with two KRS-5 windows.

The vapor absorption spectrum was taken on a McPherson 3.0-m coma-corrected vacuum monochromator. This system has been described previously.[13] A Hinterreger hydrogen glow discharge light source was operated at 350 W, and absorption was recorded directly using a dual-beam chopping system in conjunction with a logarithmic ratiometer. A 0.3-m predisperser was used to reduce stray light. The linear dispersion of the monochromator using a 1200 line/mm grating blazed at 1500 Å in first order is 2.7 Å/mm.

The spectrum of the solid at 77°K was taken on a Cary 14 using a Hanovia 150-W xenon arc lamp. The sample was placed in a crude dewar fitted with quartz windows and altered to fit in the Cary 14 sample compartment. The compartment was then made light tight and flushed with dry nitrogen to avoid condensation on the dewar windows.

The fluorescence work was carried out in a manner similar to that used for benzene and using an arrangement previously described.[3]

The infrared spectrum was taken on a standard Perkin-Elmer Model 180 infrared spectrometer.

Acknowledgments. One of us (E. A. D.) would like to thank the U. S. Air Force Systems Command for a summer Research Associateship at the University of Chicago under AFSC/AFIT funding. S. A. R. wishes to thank the Directorate of Chemical Sciences, Air Force Office of Scientific Research, for their support. We also acknowledge the general support of the Materials Research Laboratory at the University of Chicago by the National Science Foundation.

References and Notes

(1) D. F. Heller, K. F. Freed, and W. M. Gelbart, *J. Chem. Phys.*, **56**, 2309 (1972).
(2) C. S. Parmenter and M. W. Schuyler, *Chem. Phys. Lett.*, **6**, 339 (1970).
(3) K. G. Spears and S. A. Rice, *J. Chem. Phys.*, **55**, 5561 (1971); A. Abramson, K. G. Spears, and S. A. Rice, *ibid.*, **56**, 2291 (1972).
(4) C. Guttman and S. A. Rice, *J. Chem. Phys.*, in press.
(5) E. A. Dorko, *J. Amer. Chem. Soc.*, **87**, 5518 (1965).
(6) E. V. Shpolskii, *Usp. Fiz. Nank.*, **71**, 215 (1960). For a review see S. Leach, *Mem. Soc. Roy. Sci. Liege, Collect. 5°*, **20**, 179 (1970).
(7) K. Evans, R. Scheps, S. A. Rice, and D. Heller, *J. Chem. Soc., Faraday Trans. 2*, **69**, 856 (1973).
(8) K. H. Rhee and F. A. Miller, *Spectrochim. Acta, Part A*, **27**, 1 (1971).
(9) H. E. Simmons, *Progr. Phys. Org. Chem.*, **7**, 1 (1970).
(10) See R. Scheps, D. Florida, and S. A. Rice, *J. Chem. Phys.*, **56**, 295 (1972); *Chem. Phys. Lett.*, **15**, 490 (1972).
(11) J. C. Burr, Jr., E. A. Dorko, and J. A. Merritt, *J. Chem. Phys.*, **45**, 3877 (1966).
(12) P. A. Waitkus, E. B. Sanders, L. I. Peterson, and G. W. Griffin, *J. Amer. Chem. Soc.*, **89**, 6318 (1967).
(13) R. Scheps, Ph.D. Thesis, University of Chicago, 1973.

Wavelength Dependence of Nitropentaamminecobalt(III) Photochemistry. Charge Transfer and Ligand Field Excited-State Behavior

Franco Scandola,* Carlo Bartocci, and Maria Anita Scandola

Istituto Chimico dell'Università di Ferrara, Centro di Studio sulla Fotochimica e Reattività degli Stati Eccitati dei Composti di Coordinazione del C.N.R., 44100 Ferrara, Italy *(Received May 9, 1973; Revised Manuscript Received September 30, 1973)*

Publication costs assisted by Consiglio Nazionale delle Ricerche

The photochemistry of $Co(NH_3)_5NO_2^{2+}$ has been investigated in water–ethanol solvent using 11 different wavelengths of irradiation in the 254–530-nm range, covering the charge-transfer and ligand field regions of the spectrum. In agreement with previous reports, both redox decomposition and nitro–nitrito linkage isomerization photoreactions occurred with constant ratio at all of the irradiation wavelengths used. The redox quantum yields underwent a continuous decrease as the irradiation wavelength was increased within the charge-transfer region of the spectrum, showing definite variations within each charge-transfer absorption band. The quantum yield sharply decreased in going from the charge-transfer region to the ligand field one, but then it remained constant throughout the whole ligand field band. The results indicate that thermal equilibration prior to reaction is efficient in the singlet ligand field excited state but not in the charge-transfer singlet states. The reasons for this behavior are discussed on the basis of proposed potential energy surfaces for the singlet excited states involved.

The interpretation of the photoreaction mechanisms of organic molecules in solution has usually been based on the general assumption that both vibrational relaxation of the excited states and internal conversion from upper excited states to the lowest ones (typical rates of the order of 10^{13} and 10^{11} sec^{-1}, respectively) are exceedingly fast as compared with chemical reaction and/or light emission.[1,2] Experimentally, this assumption is supported by the common finding of wavelength independent quantum yields for photochemical reaction and emission of organic molecules in solution. From a mechanistic standpoint, the main implication of this assumption is that the sole precursors to both photochemistry and luminescence are the lowest thermally equilibrated excited states of any multiplicity.[3-5]

Many features of the photochemistry of coordination compounds[6] strongly suggest that such a simple generalization cannot apply to this class of compounds. The clearest example of this statement is afforded by the photochemical behavior of Co(III) complexes.[6-8] These complexes exhibit a very different photochemical behavior depending on whether they are irradiated into high-energy ligand-to-metal charge-transfer (CT) bands or in low-energy ligand field bands. In the first case, intramolecular redox decomposition reactions are observed with high quantum yields, while in the second one relatively low yields of ligand substitution reactions are only observed. Some noticeable exceptions to this typical behavior are known,[6] but the general experimental feature of the photochemistry of Co(III) complexes is definitely that of a strong wavelength dependence for both type and quantum yields of photochemical reactions. Thus, it must be concluded that in upper (CT) excited states of these complexes chemical reaction is fast enough as to compete efficiently with internal conversion to lower (ligand field) excited states. As to the possibility of chemical reaction competing with vibrational relaxation, it should be remarked that specific investigations on this aspect, which would require the use of several irradiation wavelengths within each absorption band, have seldom been carried out. From the available results it would appear, however, that photoreaction quantum yields do not vary much within single absorption bands, while the major changes seem to be associated with changes from one absorption band to another.[6-8] Hence, the photochemistry of Co(III) complexes is usually considered as the chemistry of distinct but thermally equilibrated excited electronic states.

The photochemistry of $Co(NH_3)_5NO_2^{2+}$ has previously been investigated by Balzani, *et al.*[9] The complex was shown to undergo simultaneous redox decomposition and nitro–nitrito linkage isomerization, regardless of whether CT or ligand field bands were irradiated. The quantum yields of the two processes decreased with increasing wavelength of irradiation, while their ratio remained appreciably constant. It was proposed that: (i) a $NO_2 \rightarrow Co$ CT excited state was eventually populated regardless of the type (CT or ligand field) of light absorption; (ii) a primary homolytic $Co-NO_2$ bond splitting occurring in this excited state was the precursor of both photoreactions; (iii) the quantum yield values of redox decomposition and linkage isomerization were determined by a dissociation–recombination mechanism of the following type

$$^{*}Co(NH_3)_5NO_2^{2+} \rightarrow \{Co(NH_3)_5^{2+}, NO_2\}_{\text{solvent cage}} \quad (1)$$

(bond homolysis in the reactive CT state)

$$\{Co(NH_3)_5^{2+}, NO_2\}_{\text{solvent cage}} \rightarrow Co(NH_3)_5NO_2^{2+} \quad (2)$$

(primary geminate recombination)

$$\{Co(NH_3)_5^{2+}, NO_2\}_{\text{solvent cage}} \rightarrow Co(NH_3)_5^{2+}, NO_2 \quad (3)$$

(diffusive cage escape)

$$Co(NH_3)_5^{2+}, NO_2 \rightarrow Co(NH_3)_5NO_2^{2+} \quad (4)$$

(secondary geminate recombination without isomerization)

$$Co(NH_3)_5^{2+}, NO_2 \rightarrow Co(NH_3)_5ONO^{2+} \quad (5)$$

(secondary geminate recombination with isomerization)

$$Co(NH_3)_5^{2+}, NO_2 \rightarrow Co^{2+} + 5NH_3 + NO_2 \quad (6)$$

(ultimate separation and decomposition)

where the overall quantum yield is determined by the competition between processes 2 and 3 (which depends on the initial kinetic energy content of the caged radical pair and, ultimately, on the irradiation wavelength), while the ratio between redox decomposition and linkage isomerization is determined by the competition between processes 5 and 6 (which is independent of the initial energy of the caged pair and of irradiation wavelength).[9]

According to point (i), a reactive CT state is to be populated following ligand field absorption. It should be noticed, however, that CT absorption occurs at considerably higher energies than ligand field absorption in the $Co(NH_3)_5NO_2^{2+}$ spectrum. This discrepancy was explained by Balzani, *et al.*,[9] by means of a very interesting hypothesis. They suggested that at least one of the CT states of the complex was dissociative in character, and that, owing to its strong distortion, it could extend in energy until below the ligand field state, although its absorption in this spectral region was negligible because of Franck–Condon restrictions.

This hypothesis was originally advanced on purely speculative grounds, but, if true, it could be of considerable general interest to the photochemistry of Co(III) complexes. Therefore, it seemed to us that some kind of experimental testing of this proposal would have been highly desirable. Actually, it is easily predictable that dissociative and bound excited states should differ sharply in their relaxation properties. Thus, some insight into this problem could be likely obtained by a thorough examination of the wavelength dependence of the photochemical quantum yields of $Co(NH_3)_5NO_2^{2+}$.

Experimental Section

Materials. $[Co(NH_3)_5NO_2](NO_3)_2$ was prepared by the method of Murman and Taube[10] and was twice recrystallized from water solution. All other chemicals were of reagent grade. Spectrograde ethanol was used.

Apparatus. Monochromatic light of 254 nm was obtained from a low-pressure mercury vapor lamp (Hanau NN 15/44) by means of a solution filter.[11] A narrow band of polychromatic radiation centered at 265 nm, with a half-width of 15 nm, was obtained from a 150-W Xenon lamp by means of a grating monochromator. Radiation consisting of several mercury lines in the range 280–313 nm was obtained from a medium pressure mercury vapor lamp (Hanau Q 400) by means of a Baird Atomic interference filter. The measured output (relative intensities) of this lamp-filter combination was: 275 nm, 2.5%; 280 nm, 19.7%; 286 nm, 2.2%; 289 nm, 22.7%; 292 nm, 3.8%; 297 nm, 18.3%; 302 nm, 18.0%; 313 nm, 12.8%. In this case, the photochemical quantum yields were corrected for the amount of reaction caused by the 313-nm component by using the independently determined 313-nm quantum yield (see below). The result was an average value of the quantum yield for radiations in the 280–302-nm range, thereafter referred to as 290-nm quantum yield. Monochromatic radiations of 313, 334, 365, 404, and 436 nm were obtained from a medium pressure mercury vapor lamp by means of Schott & Gen. or Ealing-TPF interference filters. Narrow bands of polychromatic light centered at 472, 506, and 530 nm were obtained from a 150-W tungsten incandescent lamp by using interference filters (472 nm: T_{max} = 33%, half-width = 10 nm; 506 nm: T_{max} = 36%, half-width = 15 nm; 530 nm: T_{max} = 45%; half-width = 12 nm).

The radiations were concentrated by means of quartz or glass lenses on the window of a thermostated cell holder containing the reaction cell (standard spectrophotometer cell, capacity 3 ml). The incident light intensity was measured by ferric oxalate actinometry[12] performed in the reaction cell before and after each experiment. The absorbed light intensity was calculated on the basis of the absorbance of the irradiated solution at the wavelength of excitation. Absorbed light intensities were in the range 1×10^{-8} to 2×10^{-7} $Nh\nu$/min, depending on the wavelength of irradiation used.

Spectrophotometric measurements were performed with Optica CF4 NI (double beam) and Shimadzu QV-50 (single beam) spectrophotometers.

Procedures. All of the experiments were carried out in 50% water–ethanol solvent mixtures.[13,14] The solutions were always made 10^{-2} M in $HClO_4$ in order to prevent air oxidation of the Co^{2+} released in the redox photoreaction (see below). After irradiation, the solutions were examined by both spectrophotometric analysis[15] and Co^{2+} determination.[16] The nitro–nitrito linkage isomerization was quantitatively measured by the difference between the experimental spectral variations and those which could be calculated on the basis of the measured extent of redox decomposition. Qualitative evidence for the occurrence of isomerization was obtained by observing the spectral variations which take place in the dark after irradiation, due to the thermal back nitrito–nitro isomerization process.[9] Quantum yield values for both redox decomposition and nitro–nitrito linkage isomerization were straightforwardly obtained by limiting the irradiation periods so as to remain within experimental zero-order photoreaction kinetics.

Results

The spectrum of $Co(NH_3)_5NO_2^{2+}$ in 50% water–ethanol is shown in Figure 1. It consists of two $NO_2 \rightarrow Co$ CT bands at 239 and 325 nm and one ligand field band ($^1A_{1g} \rightarrow {}^1T_{1g}$ in the octahedral approximation) at 458 nm. The second ligand field band ($^1A_{1g} \rightarrow {}^1T_{2g}$ in the octahedral approximation), which should lie at about 340 nm, is completely hidden by the intense CT transition at 325 nm.

The photochemical behavior of $Co(NH_3)_5NO_2^{2+}$ in 50% water–ethanol has been investigated using 11 different wavelengths of irradiation in the region of CT and ligand field transitions, namely, 254, 265, 290, 313, 334, 365, 404, 436, 472, 506, and 530 nm. From a qualitative standpoint the same results were obtained as those reported for aqueous solutions by Balzani, *et al.*[9] In fact, two simultaneous photochemical processes, namely, redox decomposition and nitro–nitrito linkage isomerization, were found to occur following each type (CT or ligand field) of excitation. Both redox and isomerization quantum yields were about 20% higher than those obtained, for corresponding wavelengths of excitation, in aqueous solution. As in aqueous solution, however, the ratio between the two reaction modes was essentially constant throughout the whole spectral region, with $\Phi_{redox}/\Phi_{isom} = 3 \pm 0.5$.

The wavelength dependence of the quantum yields of the photoredox decomposition of $Co(NH_3)_5NO_2^{2+}$ is shown in Figure 1. Preliminary experiments showed that quantum yields were independent of absorbed light intensity in the range 1×10^{-8} to 2×10^{-7} $Nh\nu$/min. Thus,

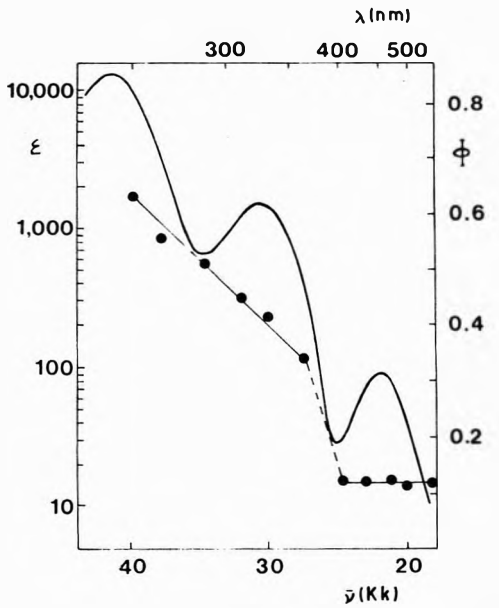

Figure 1. Electronic absorption spectrum (left scale) and photoredox quantum yields (right scale) of $Co(NH_3)_5NO_2^{2+}$

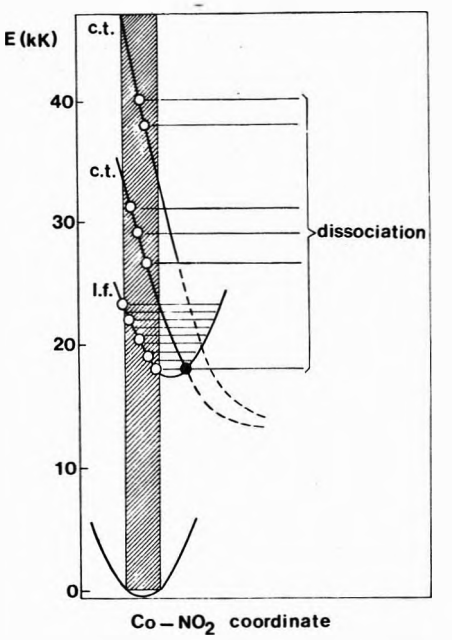

Figure 2. Potential energy diagram for the ligand field (l.f.) and charge transfer (c.t.) singlet excited states of $Co(NH_3)_5NO_2^{2+}$. Open circles represent Franck–Condon levels of the excited states corresponding to the various excitation wavelengths used (the 290-nm excitation has been omitted, due to the difficulty of assigning it to one or another of the CT states). The full circle indicates the crossing point at which internal conversion from the equilibrated ligand field state to the reactive charge-transfer state occurs.

variations in light intensity from one exciting wavelength to another are of no consequence, and the changes in the quantum yield values shown in Figure 1 are the result of wavelength effects only.

Discussion

The discussion of the experimental results of this work must be based on two rather straightforward preliminary considerations. First, the common primary photochemical process giving rise to both redox decomposition and linkage isomerization is a Co–NO_2 homolytic bond splitting.[9,17] Secondly, a primary process of this kind can neither originate in a ligand field excited state nor in the ground state, but only in excited states of CT character.[6]

One of the most interesting features of Figure 1 is the definite decrease of the quantum yield *within* each of the two CT absorption bands. Although reports of wavelength dependence of redox quantum yields are not uncommon in the photochemistry of Co(III) complexes,[6-8] this seems to be the first case in which significant quantum yield variations are observed within the wavelength range of single nonoverlapping[18] CT bands. The important implication of this experimental result is that *in both of the singlet CT states of* $Co(NH_3)_5NO_2^{2+}$ *physical events leading to chemical reaction are fast enough to prevent thermal equilibration of the excited state.* In principle, the occurrence of homolytic bond splitting following CT excitation could be described by one of the following models. (i) The singlet CT states reached by light absorption are not reactive by themselves but they undergo intersystem crossing to a reactive CT state of triplet multiplicity.[19-22] (ii) The singlet CT states reached by light absorption can undergo reaction in competition with deactivating internal conversion to ligand field states (in this hypothsis, the role of the hidden second ligand field state[18] could be a very important one). (iii) The singlet CT states reached by light absorption are essentially dissociative with regard to the Co–NO_2 coordinate and undergo prompt homolytic dissociation as the only primary process.

As far as models i and ii are concerned, the main difficulty is to find convincing explanations for both the exceedingly high rate of radiationless transition to other states (which would be required in order to account for the observed lack of thermal equilibration) and for the regular variation of radiationless transition efficiency with vibronic energy of the CT states (which would be required in order to fit the observed wavelength dependence).[23] Model iii, on the contrary, straightforwardly predicts the lack of vibrational equilibration of the CT states prior to reaction, and it offers a simple qualitative explanation of the observed wavelength dependence, based on the effect of the initial Franck–Condon energy of the singlet CT states on the efficiency of a primary cage recombination.[9] Hence, we believe that the observed behavior following CT excitation is the result of prompt dissociation of the singlet CT states reached by light absorption. The proposed CT excited state behavior is sketched in the upper part of Figure 2. It might be of some interest to note that no appreciable discontinuity is observed to occur in the quantum yield variation (Figure 1) when the irradiation wavelength changes from one to another of the two CT bands. This might indicate that no significant energy difference exists between the dissociation products of the two CT singlet states.

In Figure 1, a sharp difference in behavior can be observed to occur between the CT and ligand field regions of the spectrum. In fact, the quantum yield values undergo a sharp decrease when the excitation energy is changed from the lowest CT band to the ligand field one, but then they remain appreciably constant throughout the entire ligand field band. This difference is indicative of a substantial difference in the CT and ligand field singlet excited state behavior. On the basis of the experimental evidence, in fact, it is to be concluded that, contrary to what happens in CT singlet states, *vibrational relaxation of the lowest singlet ligand field excited state is much faster*

than any other important photophysical or photochemical process of this state. This conclusion agrees with the usual considerations about relative rates of vibrational relaxation and chemical reaction of excited states, and is consistent with a picture of the lowest ligand field singlet of $Co(NH_3)_5NO_2^{2+}$ as having a bound potential energy surface.

As said previously, the reaction mode observed following ligand field excitation is characteristic of an excited state of CT type. Thus, a CT excited state must cross the ligand field state in the proximity of its zero vibrational level, so as to be populated with appreciable efficiency from the equilibrated ligand field state. In this regard, it may be worthwhile to note that in Figure 1 the quantum yields seem to depend linearly on the excitation energy within the CT region. We are not presently attempting to suggest any quantitative interpretation of this feature within the context of the dissociation cage-recombination mechanism.[9] We may note, however, that the quantum yield value which is obtained at the origin of the ligand field band (wavelength of irradiation, 530 nm) is of the same size as would have been anticipated by a rough extrapolation of the quantum yields of the CT region down to the corresponding energy value. In other words, ligand field excitation seems to be equivalent to the excitation of the complex to a nonspectroscopic (Franck–Condon forbidden) level of the lowest singlet CT state of the same energy as the equilibrated ligand field singlet. Thus the results are best explained assuming that the lowest CT singlet state has a potential energy surface which crosses the lowest ligand field state near to its zero vibrational level. According to this picture, the lowest CT singlet state can even be populated with high efficiency following ligand field excitation. This excited state situation is sketched in Figure 2.

It has often been argued[6,24] that the main reason for the very low photoreaction quantum yields generally obtained following ligand field excitation of Co(III) complexes was the deactivation of the ligand field states by fast internal conversion to the ground state. In the present case, these radiationless deactivations do not appear to be fast enough as to prevent efficient conversion of the ligand field singlet to the reactive CT state.

Finally, it should be emphasized that the above sketched situation is not meant to be a general one for Co(III) complexes. As has previously been pointed out,[6-9] the possibility of charge transfer excited states extending down in energy until below the ligand field states is certainly associated with the strongly reducing nature of the NO_2^- ligand. There are a number of other Co(III) complexes containing reducing ligands and showing redox behavior in ligand field bands.[6-8] In only a few cases have detailed wavelength dependence studies been performed, and in most of them band overlap is a major factor determining the results. In one case ($Co(ox)_3^{3-}$) the behavior seems to be definitely different from that of $Co(NH_3)_5NO_2^{2+}$, since a pronounced decrease in the redox quantum yields was observed within a pure ligand field band.[25]

Acknowledgment. The authors are indebted to Professor V. Carassiti and to Professor V. Balzani for stimulating discussions and helpful criticism.

References and Notes

(1) N. J. Turro, "Molecular Photochemistry," W. A. Benjamin, New York, N. Y., 1965, p 19.
(2) P. A. Leermakers in "Energy Transfer and Organic Photochemistry," P. A. Leermakers and A. Weissberger, Ed., Interscience, New York, N. Y., 1969, p 5.
(3) Actually, an increasing number of possible exceptions to the lowest-excited-state rule is being discovered (see, for example, the discussion in ref 4). Also, chemical processes have been found in some cases that efficiently compete with vibrational relaxation of the excited states (see, for example, ref 5).
(4) N. J. Turro, *Mol. Photochem.*, **1**, 147 (1969).
(5) M. Luria and G. Stein, *J. Phys. Chem.*, **76**, 165 (1972).
(6) V. Balzani and V. Carassiti, "Photochemistry of Coorcination Compounds," Academic Press, New York, N. Y., 1970.
(7) V. Balzani, L. Moggi, F. Scandola, and V. Carassiti, *Inorg. Chim. Acta Rev.*, **1**, 7 (1967).
(8) A. W. Adamson, W. L. Waltz, E. Zinato, D. W. Watts, P. D. Fleischauer, and R. Lindholm, *Chem. Rev.*, **68**, 541 (1968).
(9) V. Balzani, R. Ballardini, N. Sabbatini, and L. Moggi, *Inorg. Chem.*, **7**, 1398 (1968).
(10) R. K. Murman and H. Taube, *J. Amer. Chem. Soc.*, **78**, 4886 (1956).
(11) V. Balzani, V. Carassiti, L. Moggi, and F. Scandola, *Inorg. Chem.*, **4**, 1243 (1965).
(12) C. G. Hatchard and C. A. Parker, *Proc. Roy. Soc., Ser. A*, **253**, 518 (1956).
(13) Simultaneous to the present work, a photosensitization study of $Co(NH_3)_5NO_2^{2+}$ using organic donors was in progress in this laboratory[14] which required the use of 50% water–ethanol solvent. This solvent system has also been used in the present work for purposes of comparison.
(14) M. A. Scandola, C. Bartocci, F. Scandola, and V. Carassiti, manuscript in preparation.
(15) Spectrophotometric analyses were based on the product spectra of ref 9.
(16) F. Vydra and R. Pribil, *Talanta*, **5**, 44 (1960).
(17) F. Scandola, C. Bartocci, and H. A. Scandola, *J. Amer. Chem. Soc.*, **95**, 7898 (1973).
(18) It might be noticed that a second ligand field band exists which is hidden below the 325-nm CT band. However, the great difference in extinction coefficients between CT and ligand field bands makes the effect of such ligand field absorption negligible when compared with the experimental quantum yield variations.
(19) The importance of CT excited states of triplet multiplicity in the photochemistry of various Co(III) complexes has been demonstrated in recent years by the use of photosensitization techniques.[20-22]
(20) M. A. Scandola and F. Scandola, *J. Amer. Chem. Soc.*, **92**, 7278 (1970).
(21) H. D. Gafney and A. W. Adamson, *J. Phys. Chem.*, **76**, 1105 (1972).
(22) P. Natarajan and J. F. Endicott, *J. Amer. Chem. Soc.*, **94**, 3635 (1972).
(23) While mechanism i seems to be unlikely for the above stated reasons, a definite answer on it should only come from a sensitization study using sensitizers of various triplet energies. A study of this kind is in progress in this laboratory.[14]
(24) T. L. Kelly and J. F. Endicott, *J. Amer. Chem. Soc.*, **94**, 1797 (1972).
(25) G. B. Porter, J. G. W. Doering, and S. Karanka, *J. Amer. Chem. Soc.*, **84**, 4027 (1962).

Radicals Formed during the Radiolysis of a Range of Oxysulfur and Oxyphosphorus Compounds

S. P. Mishra, K. V. S. Rao, and M. C. R. Symons*

Department of Chemistry, The University, Leicester LE1 7RH, England *(Received November 20, 1972; Revised Manuscript Received November 2, 1973)*

Exposure of the following compounds, both pure and in various solvents, to ^{60}Co γ rays at 77 K gave esr spectra which have been interpreted in terms of the radicals indicated in parentheses, either directly, or after annealing: chlorosulfonic acid ($\dot{H}SO_3$, $\dot{H}SO_3Cl^-$, $\dot{O}_3SCl$, $\dot{O}S(OH)Cl^+$); thiophosphoryl chloride ($\dot{S}PCl_3^-$, $\dot{S}PCl_2$, $\dot{S}PCl_3^+$); thionyl chloride ($\dot{O}SCl_2^-$, $\dot{C}lSO_2$); and sulfur chloride ($\dot{S}_2Cl_2^-$). In addition, thiophosphoryl bromide gave $\dot{S}PBr_3^-$ and $\dot{S}PBr_2$ radicals. The mechanisms of the reactions involved and the structures of the radicals are discussed. Attention is drawn to the observation of two species with properties characteristic of $\dot{P}X_4$ radicals formed from thiophosphoryl chloride in glassy methanol. One, which had only one strongly interacting chloride ligand, gave way to the more stable, with two strongly interacting chloride ligands, on slight warming. It is suggested that the former is the thermodynamically unstable isomer of $\dot{S}PCl_3^-$ having sulfur and chloride in the axial positions rather than two chloride ligands.

Introduction

Although a wide range of oxyphosphorus and alkyloxyphosphous radicals have now been studied by esr spectroscopy,[1] relatively little work has been done on corresponding halogen derivatives. Following the discovery of $\dot{P}F_4$ by Morton,[2] and the important fact that this radical contains two pairs of nonequivalent fluoride ligands,[3] Kokoszka and Brinckman[4] prepared $\dot{P}Cl_4$ which also contained two quite different pairs of chloride ligands. They also studied $\dot{P}Cl_2$ and a species thought to be $CH_3\dot{P}Cl_3$ in these studies.

We obtained species thought to be $\dot{O}PCl_3^-$ and $\dot{O}PCl_2$ radicals in γ-irradiated phosphoryl chloride,[5] and Kerr and Williams[6] also reported $\dot{O}PCl_3^-$ radicals in this system. Very recently, these authors have reported their detailed esr studies of irradiated sulfuryl chloride,[7] both pure and in various solvents. They obtained good evidence for the anion $\dot{S}O_2Cl_2^-$ which, in aprotic solvents, tended to dissociate to give Cl_2^- and possibly $\dot{S}O_2^-$. On photolysis of the irradiated solutions, $\dot{S}O_2^-$ was clearly formed. A few related fluorine-containing radicals have been reported, including $\dot{P}O_2F^-$,[8] $\dot{O}_3PF^-$, and $\dot{O}_2PF_2$.[9] The aim of the present work was to extend our knowledge of such radicals to include radicals containing sulfur and bromine ligands.

Experimental Section

Thiophosphoryl chloride and bromide (Albright and Wilson Mfg. Ltd.), thionyl chloride (Hopkin and Williams Ltd.), disulfur chloride (BDH), carbon disulfide (M and B), and chlorosulfonic acid (Fisons) were all of reagent grade and were used without further purification. Solvents were all of the highest commercial grade and were outgassed immediately prior to use. After degassing, liquids and solutions were rapidly frozen in liquid nitrogen in the form of small glassy beads. Solid samples were ground to very fine powders which showed no orientational effects in their esr spectra after irradiation. No crystallization effects were observed during the annealing process. The irradiations were carried out for 2 hr at 77 K in a Vickrad ^{60}Co source, having a nominal dose rate of 4 Mrads hr^{-1}.

Esr spectra were run at 77 K on a Varian E.3 spectrometer at X-band and on a Q-band superheterodyne spectrometer described elsewhere.[10] Samples were annealed by controlled warming in the dewar insert with continuous monitoring of the spectra. As soon as significant changes were observed, they were recooled to 77 K for measurement.

As a result of γ-irradiation, thiophosphoryl chloride, thionyl chloride, sulfur chloride, and chlorosulfonic acid gave purple, violet, black, and brown colored beads, respectively. On annealing, thiophosphoryl chloride, thionyl chloride, and chlorosulfonic acid became colorless, whereas sulfur chloride changed to green colored beads.

Results and Discussion

Quadrupole Effects. For many of these chlorine-containing radicals, a severe limitation is placed on the interpretation of their powder esr spectra by the effect of the relatively large quadrupole moment of the ^{35}Cl and ^{37}Cl nuclei It has been our experience for many chlorine-containing radicals, such as Cl_2^-, whose magnetic parameters are accurately known from single crystal esr studies, that the powder spectra give the parallel g and A values with high accuracy, but that the perpendicular components are far more difficult to extract. This arises because, for these radicals, the parallel axis coincides with the major quadrupole axis, so that for this direction there is no competition between magnetic and electrical effects and the spectra are normal. Competition does occur, however, for other directions. If the quadrupole interaction energy, $\frac{1}{2}e^2Qq_z$ (where z is the X–Cl bond direction), is appreciably smaller than the x or y hyperfine interaction energy, then the normal four components are still observed (together with weaker forbidden lines), but they are noticeably shifted such that the splitting between the $\pm 1/2$ lines is greater than that between the $+3/2$ and $+1/2$ or $-1/2$ and $-3/2$ lines. If, however, $\frac{1}{2}e^2Qq_z$ is greater than the hyperfine energy, then the spectrum takes on the form of a triplet (from the $\pm 1/2$ lines and a combined central "forbidden" line) flanked on each side by a pair of far weaker lines.[11,12] Fortunately, the splitting between the

TABLE I: Esr Data for Various Radicals in Irradiated Chlorosulfonic Acid, Thiophosphoryl Chloride, Sulfur Chloride, Thionyl Chloride, and Thiophosphoryl Bromide

Host	Radical	Nucleus	Hyperfine tensor components, G[a] ‖	Hyperfine tensor components, G[a] ⊥	g tensor components[a] ‖	g tensor components[a] ⊥
HSO_3Cl	$O_2\dot{S}OH$	^{33}S	140	*ca.* 118 G		
		^{1}H	20 ± 1	20 ± 1	2.0060	2.010
HSO_3Cl	O_3SCl^-	^{35}Cl	$a_{av} \div 1.5 \pm 0.5$		$g_{av} = 2.0064$	
	$HOSO_2Cl^-$	^{35}Cl	(iso) 48.7			
$SPCl_3$	$SPCl_3^-$	^{31}P	$a_{av} = 1274 \pm 10$		$g_{av} = 2.0158$	
		^{35}Cl	$a_{av}(Cl_1) = 0 \pm 10$; $a_{av}(Cl_2) = 50 \pm 2$			
$SPCl_3$	$S\dot{P}Cl_2$	^{31}P		~670	$g_{av} = 1.997$	
		^{35}Cl	15			
$SPCl_3$	$SPCl_3^+$	^{31}P		~30[c]	2.00	2.04
		^{35}Cl	10 ± 1	6.5 ± 1		
$OSCl_2$	$OSCl_2^-$	^{35}Cl	53[b]	*c*	2.00	
$OSCl_2$	O_2SCl	^{35}Cl	12 ± 1	10 ± 2	1.998	2.009, 2.010
		^{33}S	*ca.* 160	*ca.* 130		
S_2Cl_2	$S_2Cl_2^-$	^{35}Cl	45 ± 1[b]	*ca.* 10	2.007	2.079
$SPBr_3$	$S\dot{P}Br_3^-$	^{31}P	$a_{av} = 1230 \pm 10$		g_{av} 2.02	
		^{81}Br	$a_{av} = 190 \pm 10$			
	$S\dot{P}Br_2$	^{31}P	$a_{av} = 590$		g_{av} 2.00	
		^{81}Br	$a_{av} = 70$			

[a] Corrected using the full Breit-Rabi equation wher. necessary. [b] These are not the correct components, but the values for which both chlorine atoms are equivalent. [c] No clear perpendicular features.

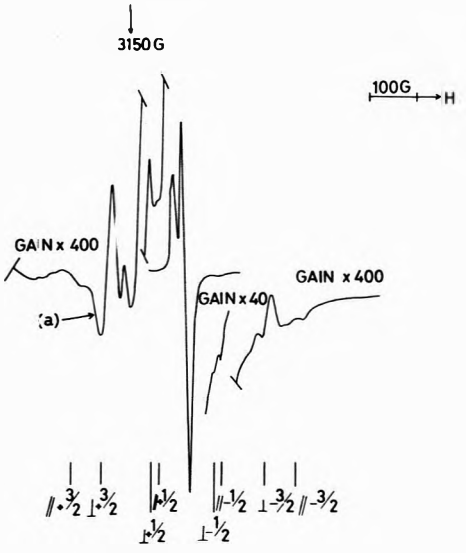

Figure 1. First derivative X-band esr spectrum for chlorosulfonic acid after exposure to γ rays at 77 K showing features assigned to HSO_3 radicals: (a) unidentified lines which distort +3/2 ^{33}S component.

components of the intense triplet is equal to the hyperfine coupling, and it has been this fact that has enabled us to derive the correct A values from such spectra.

One important diagnostic factor derives from these effects. Thus, for example, the largest coupling for the radical thought to be O_3SCl^- is an evenly spaced quartet of 48.7-G separation. Had this been a π radical, X-Cl, with the major coupling perpendicular to the X-Cl bond, the spacing would have been markedly uneven, as is indeed the case for R_2C-Cl radicals.[13] We conclude that the direction for this large coupling must be along or close to the S-Cl bond direction, which is certainly possible for O_3SCl^- radicals since the powder spectra are dominated by the chlorine interactions, and these radicals are expected to experience mainly σ delocalization. This is less likely for O_2SCl radicals, which tend to confer spin onto the ligands mainly by a pseudo π mechanism.[14]

Figure 2. First derivative X-band esr spectrum for chlorosulfonic acid after exposure to γ rays at 77 K after annealing to remove HSO_3, showing features assigned to HSO_3Cl^- (or O_2SCl) and O_3SCl radicals.

As indicated in some of the figures, we have interpreted the smaller couplings to chlorine in the "perpendicular" regions in terms of triplets rather than quartets. This certainly gives a better fit, and in the case of the HSO_3Cl^- radicals, extra wing features tie in well with the expected outer weak lines[11,12] (Figure 2). A more detailed discussion of the effects of nuclear quadrupole interactions for chlorine-, bromine-, and iodine-containing radicals will be presented at a later date.[15] However, in many instances resolution in the perpendicular regions was poor, and only an overall range could be derived. We stress that although

Figure 3. First derivative X-band esr spectrum for thiophosphoryl chloride ($SPCl_3$) after exposure to γ rays at 77 K showing $\pm 1/2$ ^{31}P lines assigned to $SPCl_3^-$ and $SPCl_2$ radicals.

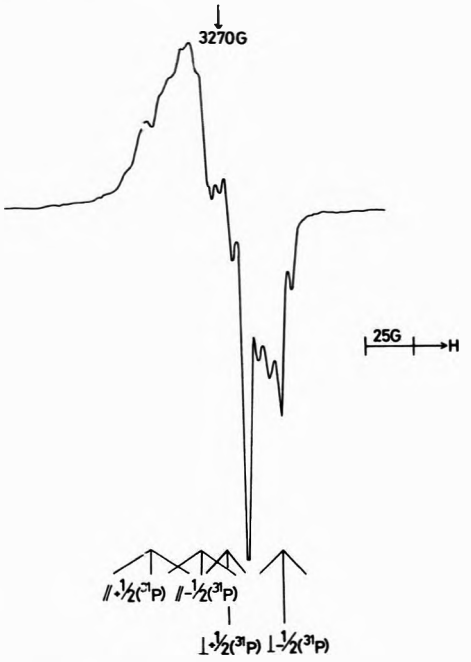

Figure 4. First derivative X-band esr spectrum for thiophosphoryl chloride ($SPCl_3$) after exposure to γ rays at 77 K showing central region assigned to $SPCl_3^+$ radicals.

some assignments may seem somewhat arbitrary in the figures, they all check well with the Q-band spectra, which gives us confidence in their validity. We have found that measurements at two wavelengths serve as an important check on possible powder spectra reconstructions.

Chlorosulfonic Acid. The strongest feature observed directly after irradiation of the pure material at 77 K was an asymmetric doublet of 20-G separation, which could either be caused by a hyperfine interaction with a nuclear spin of 1/2, or by an axial g tensor. The Q-band spectrum also comprised a 20-G doublet which rules out the latter possibility. The asymmetry arises because of overlap of the high-field component with the line due to O_3SCl radicals (see below). At high gain, ^{33}S satellites can be seen (Figure 1) together with several features due to other radicals. The results (Table I) and derived orbital populations[1a] (Table II) are very similar indeed to the results for SO_3^- radicals[16] and we assign these features to $O_2\dot{S}(OH)$ radicals.

TABLE II: Approximate Orbital Populations Derived from the Hyperfine Coupling Data in Table I

Radical	Nucleus	a_s^2, %[a]	a_p^2, %[a]
$O_2\dot{S}OH$	^{33}S	11.0	50
$O_3\dot{S}Cl^{2-}$	^{35}Cl	1.6	22.5
$S\dot{P}Cl_3^-$	^{31}P	35	
$S\dot{P}Cl_2$	^{31}P	16.5	
$SPBr_3^-$	^{31}P	33.8	
	^{81}Br	2.3	
$SPBr_2$	^{31}P	16.2	
	^{81}Br	0.84	

[a] $A_{\parallel}$ and $A_{\perp}$ taken as positive, other sign combinations gave physically unacceptable results.

After annealing, these lines were lost irreversibly, leaving hyperfine lines and a strong central line (Figure 2). The central component comprises four broad overlapping lines which we assign to a hyperfine coupling to chlorine nuclei. This species is almost certainly either the positive hole center, $HS\dot{O}_3Cl^+$, or, more reasonably, O_3SCl, with $A(Cl) \approx 1.5$ G. An explanation of the very low spin density on chlorine for this species is offered in the section on 31 electron AB_4 radicals, below.

The remaining lines are due to a radical having one strongly interacting chlorine nucleus (A = 48.7 G). This is most reasonably assigned to the parent radical anion $(HO)SO_2Cl^-$, or possibly to $O_2\dot{S}Cl$. The former assignment is strongly supported by analogy with the large chlorine hyperfine coupling found for isostructural species such as $\dot{P}Cl_4$,[4] $O\dot{P}Cl_3$,[5,6] and $O_2SCl_2^-$, while the latter is

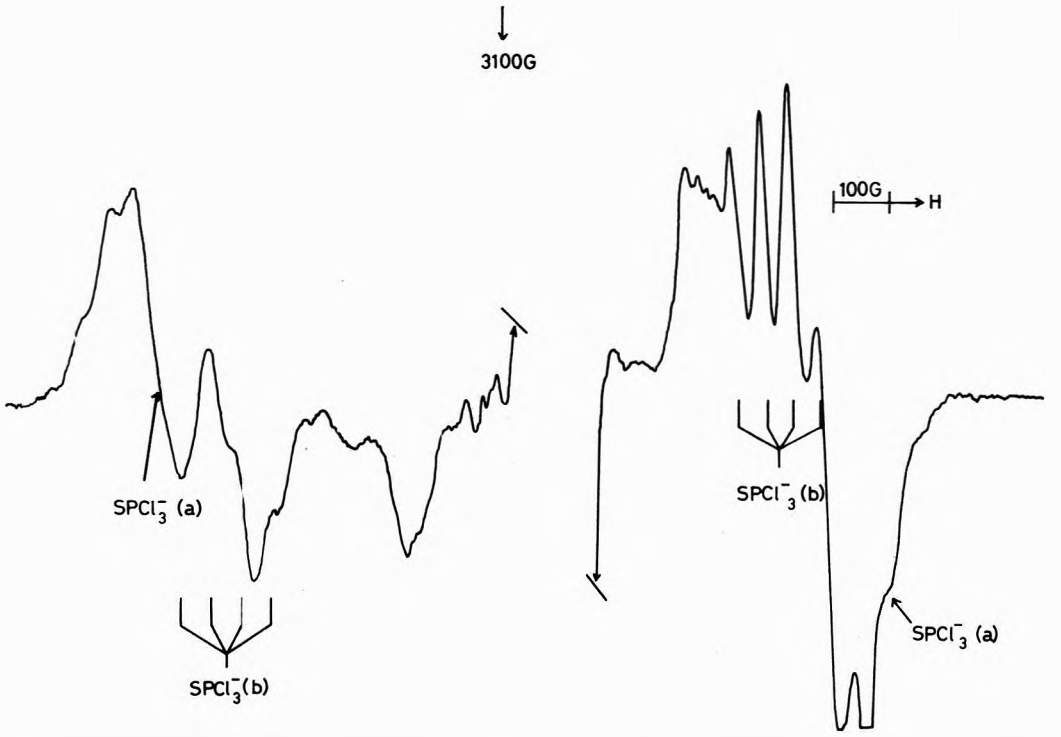

Figure 5. First derivative X-band esr spectrum for thiophosphoryl chloride ($SPCl_3$) after exposure to γ rays at 77 K in the solvent methanol-d_4 showing extra features (Figure 4) assigned to $SPCl_3^-$ radicals in a conformation different from normal (Figure 3). On warming features (Figure 4) were selectively lost.

not supported by analogy with the chlorine coupling from isostructural radicals such as $OPCl_2$,[5] which has $A(^{35}Cl)$ = 18 G. Furthermore, a species identified below as the isostructural radical $SPCl_2$ has $A(Cl) \simeq 10$ G.

In order to shed more light on this species we studied dilute solutions in sulfuric acid in which chlorosulfonic acid dissolves without change. After annealing, features due to Cl_2^- radicals were well defined, and a new set of lines comprising a doublet (5 G) of doublets (39 G) appeared (Figure 2). When perdeuteriosulfuric acid was used, the 5-G splitting was lost, and extra features were resolved in the regions expected for the $M_I = \pm 1/2$ lines of a quartet. We suggest that this species is HOSOCl, whose formation from the parent anion is encouraged by the action of the sulfuric acid host. Unfortunately, neither the $HOSO_2Cl^-$ nor the HOSOCl radical were formed in sufficient concentration to enable us to detect satellites from species containing ^{33}S. A reasonable mechanism for the formation of these radicals is

$$HSO_3Cl \longrightarrow HSO_3Cl^+ + e^-$$

$$HSO_3Cl + e^- \longrightarrow HSO_3Cl^- \longrightarrow HSO_3 + Cl^-$$

$$2H_2SO_4 + HSO_3Cl^- \longrightarrow H_2O + 2HSO_4^- + HSO_2Cl$$

$$HSO_3Cl \longrightarrow (H^+) + O_3SCl$$

Thiophosphoryl Chloride ($SPCl_3$). Clear $M_I = \pm 1/2$ (^{31}P) lines for two radicals can be seen in Figures 3–5. Those with a large ^{31}P hyperfine splitting are sets of seven nearly isotropic lines which we assign to hyperfine interaction with two equivalent chlorine atoms. Possible radicals are $SPCl_2$ and $SPCl_3^-$. The ^{31}P isotropic coupling of 1274 G (after correction) is, we believe, impossibly large for any pyramidal 25-electron PX_3 radicals such as $SPCl_2$, but is close to the coupling observed for several 33-electron PX_4 radicals such as PF_4 (1330 G[2]), PCl_4 (1206 G,[5] 1248 G[4]), and $POCl_3^-$ (1359 G[5]), which strongly favors

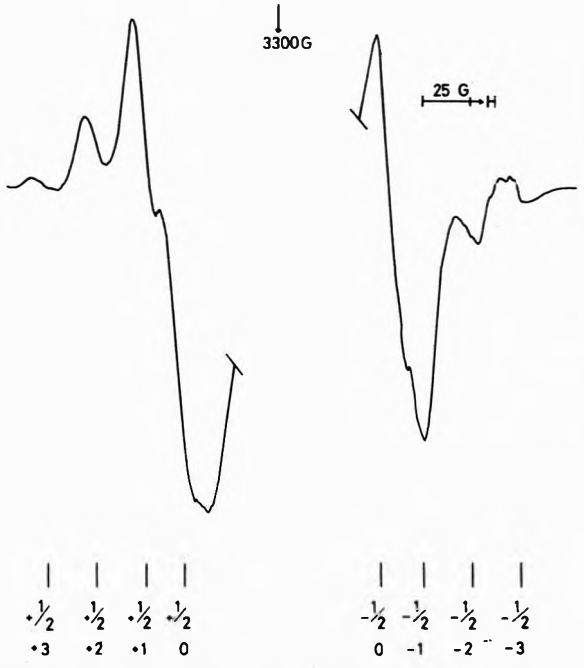

Figure 6. First derivative X-band esr spectra for thiophosphoryl bromide ($SPBr_3$) after exposure to γ rays at 77 K showing outer features assigned to $SPBr_3^-$. The inner lines for $SPBr_3^-$ are hidden under those for $SPBr_2$ and $(SPBr_3)^+$ radicals.

the $SPCl_3^-$ assignment. The fact that only two chlorine nuclei gave resolved hyperfine lines is reasonable, since these radicals are all found to distort from the tetrahedral geometry of the parent molecules in a manner that gives two strongly coupled ligands and two weakly coupled ligands. Thus PCl_4 had two chlorines with A = 62 G and two with A = 7 G, while $OPCl_3^-$ had two with A = 67 G and

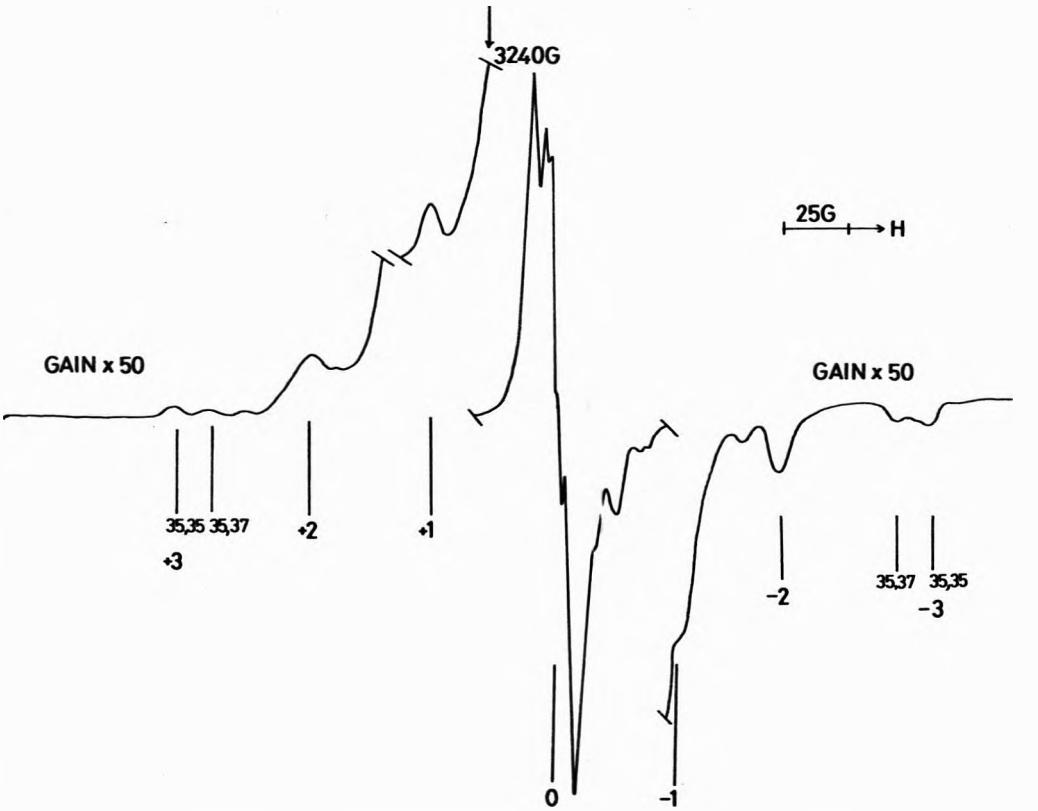

Figure 7. First derivative X-band esr spectrum for thionyl chloride ($SOCl_2$) after exposure to γ rays at 77 K showing features assigned to $\dot{S}OCl_2^-$

one with A = 15 G. We conclude that the radical responsible for the outer features in Figure 3 is $\dot{S}PCl_3^-$, the coupling to the third chlorine ligand being less than *ca.* 10 G.

Solutions of $SPCl_3$ in methyl cyanide or 2-methyltetrahydrofuran also gave this species, with very similar hyperfine coupling constants. However, methanolic solutions gave two species with large ^{31}P hyperfine coupling constants (Figure 5), the outer lines being almost identical with those assigned to $\dot{S}PCl_3^-$ radicals. The second set have $A(^{31}P) \doteqdot 1000$ G, and a coupling of about 50 G to a single chlorine nucleus. These results can, in our view, only be accommodated by the postulate that this species is also $\dot{S}PCl_3^-$, but having sulfur and one chlorine in the strongly interacting near-axial positions, the remaining two chlorine atoms being in the equatorial positions.

This isomer is less stable than that with two axial chlorine atoms, and in accordance with this, annealing to *ca.* 100 K resulted in a rapid loss of the one-chlorine species in favor of the normal two-chlorine species. It seems that initial electron addition can give either isomer, the choice probably depending upon fortuitous distortions present in the parent molecules, and on fortuitous constraints from the medium. The reason why this effect was only detected for methanolic solutions is then because this forms a very constrained and rigid glass, so that the equilibration process requires a higher temperature than in the looser solids formed by the parent material and the aprotic solvents.

The doublet with components separated by *ca.* 670 G (Figures 3 and 5) has several subcomponents separated by *ca.* 15 G and some anisotropy, which could not be properly estimated because of overlapping lines. We suggest that the species responsible is $\dot{S}PCl_2$, since this should have two equivalent chlorine ligands with a coupling in the region of 10–20 G and a ^{31}P isotropic hyperfine coupling close to those for other isostructural 24-electron AB_3 radicals (*cf.* PO_3^{2-}, 698 G[17] and $O\dot{P}Cl_2$, 759 G[5]).

The strong central features in Figure 4 are assigned, as usual, to the positive hole center, in this case to $SPCl_3^+$ radicals. The hyperfine constants given in Table I afford the best fit for this spectrum, but various alternatives were also found to fit reasonably well. The results are certainly reasonable for such a radical, and can be compared with the values $A_\perp(^{31}P)$ = 43 G and $A_\parallel$ = 45 G assigned to PO_2Cl_2,[5] and 43.8 G assigned to PO_2F_2.[9] Also the coupling constants to ^{35}Cl of *ca.* 10 ($A_\parallel$) and 6.5 G ($A_\perp$) are close to the values found for PO_2Cl_2.[15] Reasonable reactions which explain these results are

$$SPCl_3 \longrightarrow SPCl_3^+ + e^-$$

$$SPCl_3 + e^- \longrightarrow \dot{S}PCl_3^- \longrightarrow \dot{S}PCl_2 + Cl^-$$

Thiophosphoryl Bromide. This material damaged only with difficulty, and prolonged irradiations were required to give reasonable esr signals (Figure 6). Two species with large ^{31}P hyperfine coupling constants were obtained, that with a coupling in the region of 1230 G being assigned to $\dot{S}PBr_3^-$ radicals by analogy with the very similar results for $\dot{S}PCl_3^-$ radicals, and that with a coupling of *ca.* 590 G being assigned to $\dot{S}PBr_2$ radicals. On annealing, the outer features were lost in favor of those assigned to $\dot{S}PBr_2$ radicals, in accord with expectation for these species.

So far as we are aware, radicals of either class containing bromine ligands have not previously been prepared. As expected in terms of electronegativity trends, there has been a slight fall in $A_{iso}(^{31}P)$ on replacing chlorine by bromine for each class of radical. The coupling to bromine in $SPBr_3^-$, although very large, is in fact quite comparable

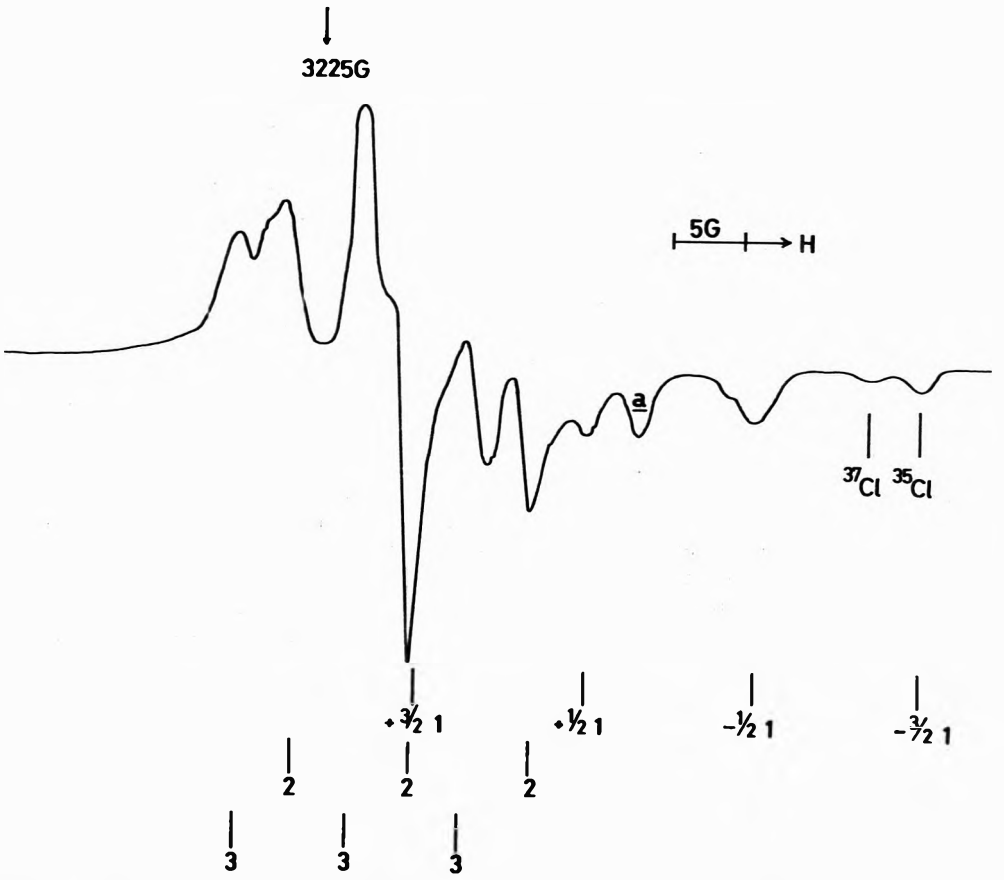

Figure 8. First derivative X-band esr spectrum for thionyl chloride ($SOCl_2$) after exposure to γ rays at 77 K after annealing, showing features for a monochloro radical. (a) Features from other radicals.

to that for chlorine when allowance is made for the much larger nuclear magnetic moments for the bromine isotopes. Again, the coupling for bromine in $SPBr_2$ is very close to that for chlorine in $SPCl_2$ when this allowance is made (*cf.* the estimated spin densities given in Table II).

Thionyl Chloride ($OSCl_2$). Again, the major species detected at 77 K contains two equivalent coupled chlorine nuclei (Figure 7). This could most reasonably be assigned the structures $OSCl_2^-$ or $OSCl_2^+$. The former is a 27-electron tetraatomic radical, only two of which are known (ClO_2^{2-} [18] and O_2IF^- [19]), while the latter is a 25-electron tetraatomic radical isoelectronic with SO_3^-.

We favor the former assignment for the following reasons. (i) The seven-line spectrum was not obtained for solutions in various solvents, but strong features for Cl_2^- were obtained (see below). This suggests a solvent facilitation of the reaction

$$SOCl_2^- \longrightarrow SO + Cl_2^-(solv)$$

(ii) The observed hyperfine coupling to $^{35,37}Cl$ of *ca.* 53 G is fairly close to the coupling for $SO_2Cl_2^-$.[7] It is considerably larger than that expected for $SOCl_2^+$.

After further annealing, all these features were lost, leaving central components (Figure 8) which we have tentatively analyzed in terms of the radical O_2SCl. These radicals, also identified as a radiolysis product for chlorosulfonic acid above, would be formed readily from any HOSOCl present and this is a very probable impurity.

Sulfur Chloride (S_2Cl_2). The main species formed at 77 K contains two equivalent chlorine atoms (Figure 9) but unfortunately we were unable to obtain this species in sufficient concentration to enable us to see the expected ^{33}S

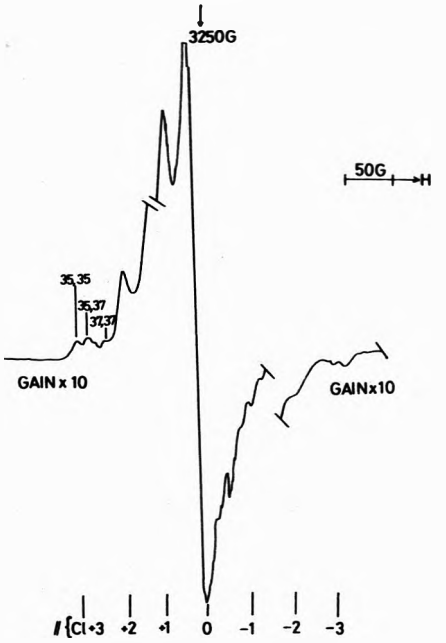

Figure 9. First derivative X-band esr spectrum for sulfur chloride (S_2Cl_2) after exposure to γ rays at 77 K showing featuers assigned to $S_2Cl_2^-$ radicals.

satellites. The results seem to be reasonable for the anion $S_2Cl_2^-$, but since no such species has previously been studied by esr spectroscopy (so far as we are aware), we cannot argue by analogy. The cation $S_2Cl_2^+$ is also quite

possible but for reasons given below, we think this is less likely.

A second species, containing one coupled chlorine nucleus was obtained after annealing. This spectrum was similar to that obtained for ClOO radicals in irradiated potassium chlorate[20] and from photolyzed chlorine dioxide,[21] and is probably due to ClSS radicals. Since this study was completed, an excellent spectrum for ClSS has been published, and a very complete analysis of the chlorine hyperfine coupling described.[12] Our very much poorer results accord reasonably well with these. A reasonable reaction sequence is

$$S_2Cl_2 \longrightarrow S_2Cl_2^+ + e^-,\ S_2Cl_2 + e^- \longrightarrow S_2Cl_2^- \longrightarrow ClS_2 + Cl^-$$

Attempts to obtain clearer results using various solvents were unsuccessful. For methanolic solutions, features for Cl_2^- radicals completely dominated the spectra, which suggests that the radical anions can also break down by the alternative route, $S_2Cl_2^- \rightarrow S_2 + Cl_2^-$.

Irradiation in Solvents. Whenever possible, solutions involving a range of solvents which form good glasses were used in addition to the pure materials, since this often helps in the task of identification by favoring electron capture or electron loss processes. The solvents available were limited because of the reactivity of the substrates, but this tendency was minimized by dissolution at low temperature followed immediately by immersion in liquid nitrogen.

The most significant solvent-induced modification was the formation of Cl_2^- ions from $SOCl_2$ and S_2Cl_2, both in methyl cyanide (CD_3CN) and methanol (CD_3OD). The species identified as the negative ions in the pure solvents were not formed under these circumstances. This result is simlar to that obtained by Kerr and Williams for SO_2Cl_2,[6] and means that loss of Cl_2^- from dichloro species may not be as structurally significant as was inferred.

Electronic Structures. In several instances, the esr data, while being quite satisfactory for purposes of identification, do not warrant detailed analysis. In those cases where analysis was fairly clear, we have computed approximate orbital populations in the usual way,[10] and these are listed in Table II.

25-Electron AB_3 Radicals. The proton coupling for HSO_3 radicals is small, as expected for an OH proton, and the effect of protonation has not modified the ^{33}S coupling, relative to that for SO_3^- radicals, by an important amount. This is, in fact, a general conclusion that can be drawn for oxygen protonation or alkylation of XO_2 or XO_3 and related radicals, the effect of protonation being a small increase in spin density on the central atom in a manner quite comparable with that found for changes in environment.[14]

The other 25-electron AB_3 radicals, $SPCl_2$ and $SPBr_2$, seem to be quite normal with respect to the central atom and ligand hyperfine tensor components, and the data fit in quite well with various linear correlations previously observed for such radicals.[1a,17]

31-Electron AB_4 Radicals. The radicals $SPCl_3^+$ and O_3SCl^- are isostructural with radicals such as PO_4^{2-}, which have their unpaired electrons confined to ligand orbitals that are nonbonding with respect to the central atom.[1a] For O_3SCl^- the very small coupling to the chlorine atom is reminiscent of that to fluorine in O_3PF^-,[9] and we conclude that the magnetic electron is in the a_2 orbital which is confined to the three oxygen ligands. For $SPCl_3^+$ if the electron was in a similar orbital of a_2 symmetry it would be confined to the chlorine atoms. Although the spin density on chlorine, as gauged from the considerably larger hyperfine coupling, is quite high, it would be somewhat surprising, in view of the lower electronegativity of the sulfur atom, for the spin to be so confined. We suggest that the preferred orbital in this case is one of e symmetry, with both sulfur and chlorine contributions.

33-Electron AB_4 Radicals. These radicals normally have their excess electron in an antibonding orbital centered largely on the central atom, the ligands being distorted from the near tetrahedral arrangement of the parent molecules so as to reduce the antibonding effect. The radical $SPCl_3^-$ is quite normal in its properties. The rule that the more electronegative ligands couple most strongly is clearly followed, and the replacement of oxygen by sulfur on going from $OPCl_3^{2-}$ to $SPCl_3^-$ has only a minor effect on the magnetic properties.

The radical $HOSO_2Cl^-$ also has a comparable, but somewhat smaller, coupling to chlorine, but in the absence of good ^{33}S data, we cannot deduce very much about this species.

The $S_2Cl_2^-$ Radical. These radicals are quite different from those previously discussed, in that there is no single "central" atom. To a first approximation, the structure of $S_2Cl_2^-$ could be pictured in terms of an electron in a σ^* orbital largely confined to sulfur. The extent to which this delocalizes onto chlorine will depend upon the distortion that occurs from the shape of the parent molecule, which has an "open-book" structure similar to that of hydrogen peroxide, with a Cl–S–S angle of 103°. If our results are properly assigned to this radical, then we deduce that as much as 40% of the spin is delocalized onto chlorine so that, in fact, the σ^* orbital is strongly delocalized through the whole molecule. The form of the g tensor also fits this σ^* description satisfactorily. The fact that Cl_2^- can be readily formed from this anion accords with the high spin density on chlorine.

The alternative formulation, $S_2Cl_2^+$, for this center should also be considered, because the unpaired electron will now be a π^* orbital, again delocalized across the molecule, with considerable spin density on chlorine. In the absence of ^{33}S hyperfine data and clear anisotropic coupling constants, it is not possible to make a clear distinction at this stage.

Acknowledgment. We thank the Commonwealth Scholarship Commission in the United Kingdom for a fellowship to S. P. M., the S. R. C. for a grant to K. V. S. R., Mr. J. A. Brivati for experimental assistance, and the referees for helpful advice.

References and Notes

(1) (a) P. W. Atkins and M. C. R. Symons, "The Structure of Inorganic Radicals," Elsevier, Amsterdam, 1967; (b) P. J. Krusic, W. Mahler, and J. K. Kochi, *J. Amer. Chem. Soc.*, **94**, 6033 (1972); (c) A. G. Davies, D. Griller, and B. P. Roberts, *Angew. Chem., Int. Ed. Engl.*, **10**, 738 (1971).
(2) J. R. Morton, *Can. J. Phys.*, **41**, 706 (1963); see also P. W. Atkins and M. C. R. Symons, *J. Chem. Soc.*, 4363 (1964).
(3) R. W. Fessenden and R. H. Schuler, *J. Chem. Phys.*, **45**, 1845 (1966).
(4) G. F. Kokoszka and F. E. Brinckman, *J. Amer. Chem. Soc.*, **92**, 1199 (1970).
(5) A. Begum and M. C. R. Symons, *J. Chem. Soc. A*, 2065 (1971).
(6) C. M. L. Kerr and F. Williams, *J. Phys. Chem.*, **75**, 3023 (1971).
(7) C. M. L. Kerr and F. Williams, *J. Amer. Chem. Soc.*, **94**, 5212 (1972).
(8) A. Begum, S. Subramanian, and M. C. R. Symons, *J. Chem. Soc. A*, 700 (1971).
(9) A. Begum, S. Subramanian, and M. C. R. Symons, *J. Chem. Soc. A*, 1323 (1970).

(10) J. A. Brivati, J. M. Gross, M. C. R. Symons, and D. J. A. Tinling, *J. Chem. Soc.*, 6504 (1965).
(11) F. J. Adrian, E. L. Cochran, and V. A. Bowers, *J. Chem. Phys.*, **36**, 1938 (1962).
(12) F. G. Herring, C. A. McDowell, and J. C. Tait, *J. Chem. Phys.*, **57**, 4564 (1972).
(13) S. P. Mishra, G. W. Neilson, and M. C. R. Symons, *J. Amer. Chem. Soc.*, **95**, 605 (1973).
(14) H. Bower, M. C. R. Symons, and D. J. A. Tinling, "Radical Ions," E. T. Kaiser and L. Kevan, Ed., Interscience, London, 1968.
(15) G. W. Neilson, unpublished calculations.
(16) G. W. Chantry, A. Horsfield, J. R. Morton, and D. H. Whiffen, *Mol. Phys.*, **5**, 233 (1962).
(17) M. C. R. Symons, *J. Chem. Soc. A*, 1998 (1970).
(18) R. S. Eachus and M. C. R. Symons, *J. Chem. Soc. A*, 2433 (1968).
(19) S. Subramanian and M. T. Rogers, *J. Phys. Chem.*, **75**, 3479 (1971).
(20) R. S. Eachus, P. R. Edwards, S. Subramanian, and M. C. R. Symons, *J. Chem. Soc. A*, 1704 (1968).
(21) P. W. Atkins, J. A. Brivati, N. Keen, M. C. R. Symons, and P. A. Trevalion, *J. Chem. Soc.*, 4785 (1962).

Radiochemical Study of Active Sites on Palladium. Behavior of Preadsorbed [^{14}C]Acetylene and [^{14}C]Carbon Monoxide in Acetylene Hydrogenation

Iwao Yasumori,* Toshiaki Kabe, and Yasunobu Inoue

Department of Chemistry, Tokyo Institute of Technology, Ookayama, Meguro-ku, Tokyo, Japan *(Received December 31, 1970; Revised Manuscript Received October 1, 1973)*

Publication costs assisted by Tokyo Institute of Technology

The nature of active sites on palladium foil for the hydrogenation of acetylene was investigated with the radiochemical technique using acetylene and carbon monoxide labeled with ^{14}C. From the behavior of preadsorbed acetylene, the adsorbed acetylene was classified into four species. One of them was found to be removed during hydrogenation leaving an effective site for the reaction. The density and distribution of the sites were evaluated for the cold-worked foil annealed at temperatures from 200 to 800°, and two kinds of sites with different activities were found to appear depending on the annealing temperature. The sites, which have a high specific activity, 9×10^2 molecules min^{-1} site^{-1}, and which are isolatedly distributed, exist only in the foil activated or annealed below 200°. The other sites of a lower activity, $(1.5 \pm 0.2) \times 10^2$ molecules min^{-1} site^{-1}, appear in the treatment above 300° and increase in number with increasing temperature of annealing. The effects of CO poisoning on these sites were different; the former was unaffected by the adsorbed CO up to 5% of surface palladium atoms whereas the depression of the latter activity was linear with increasing amount of adsorbed CO. Argon and helium ion bombardments proved to increase the catalytic activity of the foil and the enhanced activities showed similar change on annealing to that of the cold-worked foil. Thus a close correlation between vacancies and highly active sites was verified. The relationships between surface structure and these sites are discussed and plausible models of the active sites are proposed.

Introduction

As reported previously on the study on the cold-worked palladium foil, a drastic decrease in the catalytic activity for acetylene hydrogenation was found when the foil was annealed in the temperature range 200–300°. The activity reduced in this way was partly recovered after annealing above 600°.[1] Palladium foils annealed at 200 and 800° were taken as typical catalysts having different nature and kinetic studies, such as pressure jump and isotope replacement techniques, were applied to reactions on them. It was then revealed that the difference in reaction mechanism is due to whether the major reactive intermediate is hydrogen associatively adsorbed or surface hydrogen equilibrated with hydrogen dissolved in the bulk of the metal.[2] This difference in mechanism can be understood on the basis of surface structures of these palladium foils. In addition to the activity due to the lattice plane, the importance of lattice imperfections on catalysis has been pointed out during the last decades.[3,4] The observed change in activity with annealing leads us to the assumption that the activity of Pd foil annealed below 200° is correlated with lattice imperfections whereas that of Pd annealed above 600° is attributed to a preferentially developed lattice plane. The purpose of this paper is to report more fully on this work as well as on some additional results. The palladium foil was activated by various procedures such as cold working, or argon or helium ion bombardment, and the effect of annealing on the activity was investigated for acetylene hydrogenation. The structural change with annealing was inspected by means of electron microscopy and electron and X-ray diffraction.

In order to follow the precise behavior of active sites during the course of a reaction, a radio tracer method[5,6] was extensively applied to the present study by using acetylene labeled with ^{14}C. The surface density of the effective sites was evaluated from the amount of desorbed acetylene during hydrogenation and the specific activity per site estimated. The distribution of active sites on the surface and its change with annealing were also examined. Carbon monoxide labeled with ^{14}C was used as a poison in

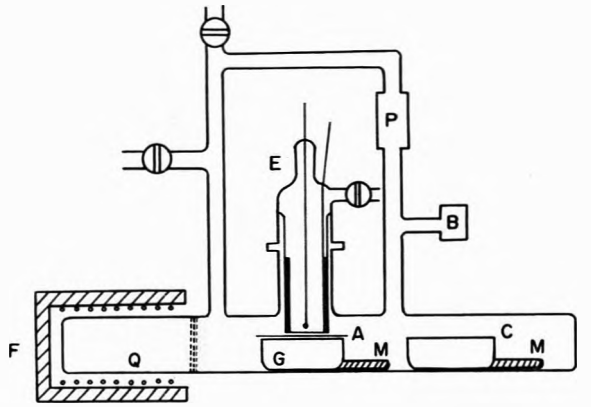

Figure 1. Apparatus used for tracer study: A, palladium foil; B, Bourdon gauge, C, reference boat; E, G.M. counter; F, furnace; G, glass boat; Q, quartz end; M, magnet; P, circulating pump.

order to determine the nature of interactions among adsorbed species.

On the basis of these results, plausible models of active sites are proposed.

Experimental Section

Apparatus and Procedure. A glass vessel used in the radiochemical study, as shown in Figure 1, was incorporated with a G.M. counter, which was similar to that used by Thomson, *et al.*[5] The present apparatus was improved to follow the reaction, by combining the vessel with a circulating pump, a glass Bourdon gauge, and a gas chromatograph for product analysis. The end-window type G.M. tube involved a stainless steel cylinder 40 mm long and 22 mm in diameter as a cathode and 0.15 mm o.d. tungsten wire as an anode. A thin mica sheet of 2.5 mg/cm^2 was attached on a glass crosspiece of the window. The counter was filled with a quenching gas, a mixture of argon (60 Torr) with ethylene (20 Torr), and had a plateau of slope 5% per 100 V over the range of applied voltages 1150–1400 V. A radiation scaler, Riken Keiki Model RSC-2T1, was used. The catalyst foil was mounted on a quartz boat which can be moved by an outside magnet. After being annealed and reduced with hydrogen in the quartz end of the vessel, the foil was set below the counter.

In the preadsorption experiments, the foil was exposed to radioactive [^{14}C]acetylene at a pressure of 5×10^{-3} Torr for several minutes at 27°. The acetylene was then pumped out and a reaction mixture of nonradioactive acetylene and hydrogen, 1:2 molar ratio, was admitted at a total pressure of 20 Torr. The surface concentration of preadsorbed [^{14}C]acetylene and the rate of hydrogenation were simultaneously followed during the course of the reaction.

In the poisoning experiments a clean catalyst surface was exposed to [^{14}C]carbon monoxide ranging from 10^{-2} to 10^{-3} Torr and, without evacuation, the reaction mixture was added. The change in the amount of adsorbed CO was followed during hydrogenation. The count rate of radioactive species on the surface was estimated from the difference between the total and the gas-phase count rates. The latter was evaluated from the count rate when the catalyst foil was replaced by a glass plate. [^{14}C]Acetylene and [^{14}C]carbon monoxide obtained from Radiochemical Center, Amersham, were of the activity 19.5 and 32.4 mC/mM, respectively. The surface densities of acetylene and carbon monoxide per cpm were estimated as 2.2 and 1.4×10^{11} molecules cm^{-2}, respectively.

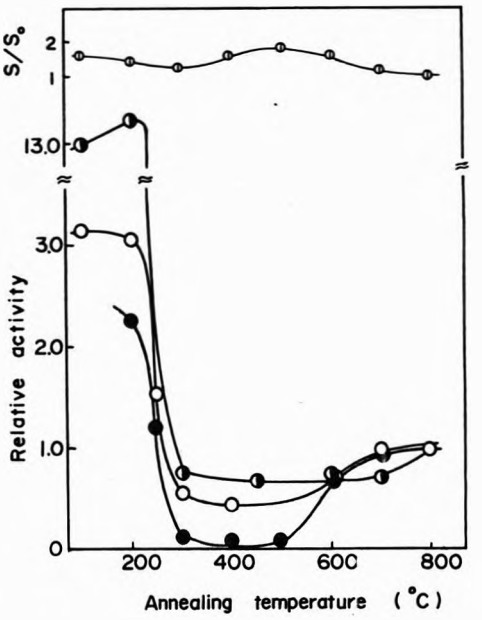

Figure 2. Changes in enhanced activities with annealing: ●, cold-worked foil (from ref 1); ○, foil bombarded with argon ions at 500 V; ◑, foil bombarded with helium ions at 3000 V. Activities are normalized to those of the 800° annealed foil: ⊖, change in the roughness factor, S/S_0, for the cold-worked foil (from ref 8).

Palladium foil (more than 99.99% pure) was obtained from Johnson Matthey and Co., Ltd., and was used in the form of a foil 20 mm in width and 0.2 mm in thickness. After being washed with acetone and distilled water, the foil was annealed once at 800° for several hours under vacuum in order to remove its structural history and then it was newly modified with one of the following treatments: cold-working, successive rolling was carried out in one direction at room temperature; ion bombardment, bombarding was carried out with argon ions accelerated to 500 V at 100 μA cm^{-2} for 30 min or with helium ions of 110 μA cm^{-2} at 3000 V for 10 min. Modified foils were reduced with hydrogen at 50 Torr and 150° and then the catalytic activity and its change with annealing were examined. Annealing was performed by heating the foil in the vessel at various temperatures between 200 and 800° under vacuum below 10^{-6} Torr for 1 hr. Prior to each kinetic run, the annealed foil was again reduced with hydrogen at 150° and evacuated at the same temperature.

In the ion-bombardment experiments a separate grease free apparatus was used which can be pumped to below 10^{-8} Torr. This apparatus consisted of the bombardment and reaction cells, which were separated from each other by a greaseless valve. The foil activated in the bombardment cell was transferred to the reaction cell prior to reaction by an outside magnet.

Repeated runs proved that the activity was reproduced with a fluctuation smaller than 10% in every case.

Results

Enhanced Activity and Its Change with Annealing. As reported previously,[1,2] the catalytic activity of the annealed foil was increased by cold working and this enhanced activity changed with annealing at temperatures from 200 to 800° as shown in Figure 2. The selectivity, defined as the ratio of ethylene to ethane produced, was higher than 10 but it increased to above 30 for the foil annealed at 800°.

It was found that the activation by argon ion bombardment had a threshold energy of 300 V and that the catalytic activity of the foil was enhanced by a factor of 3 after 10 min of bombardment at 500 V. In the case of helium ion bombardment at 3000 V, the catalytic activity was found to be greater by a factor of 13 than the original activity. These enhanced activities decreased markedly by annealing around 300°. However, the decreased activities approached that of the 800° annealed foil and did not show the activity minimum which was observed in the cold-worked foil. A preliminary study using inert gas ions showed that both the orders of threshold voltage for activation and of the enhanced steady activity are He > Ne > Ar > Kr.[7] It is noted that the decrease in activity occurs by annealing at the same temperature region in every case of the modified foils.

Structural Change of the Cold-Worked Foil with Annealing. The surface structure of the foil annealed at 200, 400, and 800° was examined by means of electron microscopy and the texture of these foils was analyzed by using X-ray pole figure of the (111) diffraction. The obtained pole figure showed that the (110) plane was exposed in parallel with the rolled surface after cold working. A number of etch pits were observed along the direction of rolling on the foil treated with concentrated HNO_3 and these etch pits disappeared when the foil was annealed at 400° but the orientation of the texture still remained. After annealing at 800°, the surface became smoother than those annealed at 200° and the peculiar orientation disappeared.

Electron diffraction showed a halo-like pattern on the foil annealed at 200° which indicates the presence of irregular structure on the surface. With the treatment at 400°, a strong ring due to (220) and a weak one due to (111) and (222) appeared. X-Ray diffraction also provided corresponding results; with annealing at 500–800°, the ring due to (220) vanished and then that due to (222) became stronger. These findings indicate that the crystal growth and the atom arrangement proceed extensively by heating around 800° and that the (111) plane is mainly exposed. This annealing also brought a narrower diffraction peak and completely separated Cu-Kα doublet. After bombardment with argon ions, the surface was covered with a large number of craters, *ca.* 200 Å in diameter.

Behavior of Preadsorbed Acetylene. Figure 3 shows the behavior of preadsorbed radioactive acetylene on the 800° annealed foil. About 44% of the surface acetylene was removed rapidly on evacuation and the successive introduction of the nonradioactive reaction mixture caused a slower decrease of the remaining acetylene concurrently with the progress of the hydrogenation. In the second run, however, the concentration of the acetylene decreased rapidly to the lowest level previously reached and the increase of the reaction rate to a steady value also became much faster than that in the first run. After the reaction, a definite amount of the radioactive species was found to remain on the surface. A similar behavior of preadsorbed acetylene was also observed in the 200° annealed foil.

The acetylene preadsorbed on a clean surface was classified into the following four species: A, which desorbed on evacuation prior to the reaction; B, which was removed from the surface during the course of reaction; C, which was removed by reduction with hydrogen at 150°; and D, which remained on the surface after the reduction. The surface concentrations of respective species were estimated for the foil annealed at various temperatures up to 800°. The amounts of species A and D remained unchanged for the annealed surfaces while those of species B and C showed a minimum in the temperature range 400–500°.

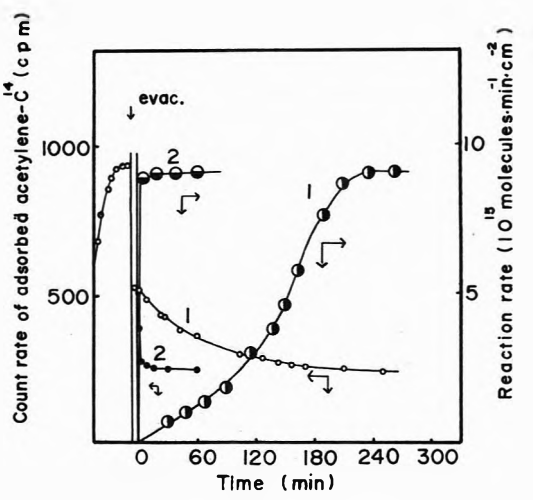

Figure 3. Changes in the amount of adsorbed [^{14}C]acetylene and reaction rate: (1) first run; (2) second run after evacuation.

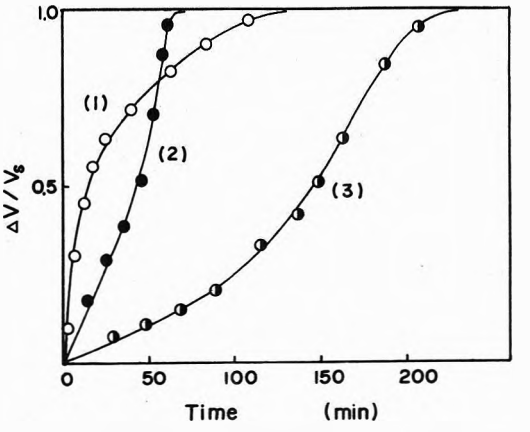

Figure 4. Behavior of rate increase in the induction period and after the pressure jump of hydrogen: curve 1, the pressure jump on the 800° annealed foil (ΔV is represented as the difference of rates before and after the jump); curve 2, the induction period on the 200° annealed foil; curve 3, the induction period on the 800° annealed foil. The rate increase (ΔV) is respectively normalized to the rate (V_s) at the reaction steady states.

The rate increase in the initial stage of the first run was compared to the rate increase after the hydrogen pressure jump. The results are shown in Figure 4. The pressure jump was carried out by a sudden increase of hydrogen pressure to about three times the previous value when the hydrogenation proceeded at a steady rate. Thus curve 1 is evidently different from curves 2 and 3 of the induction period. When hydrogen was admitted on the 800° annealed foil, the amount of hydrogen absorbed was found to increase in a way analogous to curve 1. This supports the conclusion that the rate increase upon the hydrogen jump depended on the amount of hydrogen absorbed, as described previously.[2] On the other hand, Figure 3 showed that the reaction became stationary when the concentration of acetylene on the surface attained a steady value. Therefore, the induction period is considered to be the interval in which the moderately bound acetylene (species B) is removed to form a vacant site effective for the reaction. This assumption enables us to estimate the activity per the site. A high value, 9×10^2 molecules min^{-1}

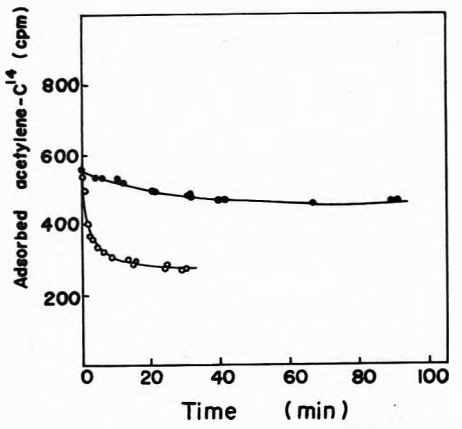

Figure 5. Exchange of adsorbed acetylene with gaseous acetylene at 27° on the 800° annealed foil: ●, fresh surface; O, used surface. Acetylene pressure = 7 Torr.

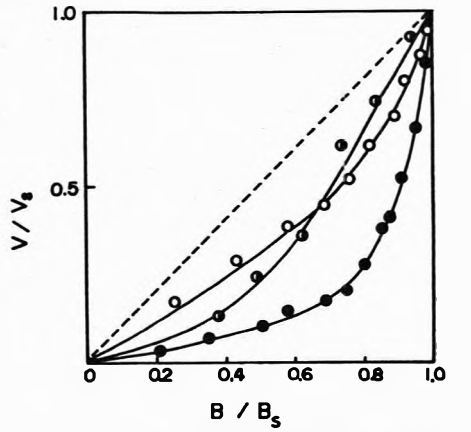

Figure 6. Correlation between the rate of the removal of species B and the activity increase in the initial phase of the reaction: B/B_s, fraction of removed species B; V/V_s, fraction of activity increase; O, 200° annealed foil; ●, 800° annealed foil; ◑, 800° annealed foil poisoned by CO.

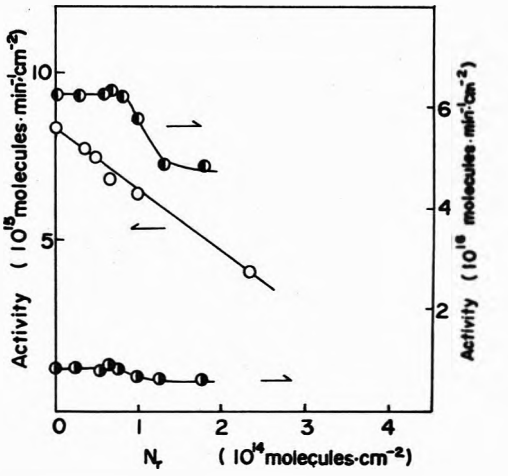

Figure 7. Effects of poisoning by CO: (a) 800° annealed foil; O, activity of ethylene formation at 27°, (b) 200° annealed foil; ◐, activity of ethylene formation at 40°; ◑, activity of ethane formation at 40°

site^{-1}, was obtained for the foil annealed at 200° while a lower constant value, (1.5 ± 0.2) × 10^2 molecules min^{-1} site^{-1}, was observed after the annealing above 300°. This result indicates that there are two kinds of sites having different specific activities. The recovery of total activity with annealing above 600° is attributed to the increase in the number of the latter site. Figure 5 shows the different behavior of adsorbed acetylene on the fresh surface (the first run) and on the used surface (the second run). About 83% of preadsorbed acetylene on the fresh surface was not exchanged with gaseous acetylene of 7 Torr and, further, 60% of the remaining acetylene was removed slowly by introducing hydrogen at 10 Torr. The concentration of surface acetylene after the hydrogen treatment corresponded to the sum of species C and D in Figure 3. Hydrogen is, therefore, mainly responsible for the removal of preadsorbed acetylene. On the other hand, the acetylene on the used surface was easily replaced by gaseous acetylene, as is also shown in Figure 5.

Figure 6 shows the correlation between the rate of removal of species B and the activity increase during the initial phase of reaction on fresh catalyst. The deviation from diagonal suggests that the active site of reaction is an aggregate of the vacant site. Though the curve for the 800° annealed foil deviates from the diagonal more markedly than that for the 200° annealed foil, the former approaches the latter when the surface was covered with CO of 2.6 × 10^{14} molecules cm^{-2}, that is, 15% of surface Pd atoms.

Effects of CO Poisoning. The amount of adsorbed CO on the foil annealed at 800° remained constant during an induction period. As the hydrogenation started, the amount increased slightly and attained a steady value. Figure 7 shows that the rate of hydrogenation decreases linearly with increasing amount of surface CO and zero activity is brought about at CO of 5 × 10^{14} molecules cm^{-2}, 30% of surface Pd atoms, as evaluated by extrapolation. On the other hand, in the case of the foil annealed at 200°, the rate of hydrogenation is unaffected by adsorbed CO up to 5% of surface Pd atoms and is decreased stepwise by further adsorption of CO, as shown in Figure 7.

From a study of adsorbed CO on the 200° annealed foil, it was found that the amount of CO was increased by 70% in the presence of hydrogen at 27°. On the contrary, the addition of acetylene decreased about 30% of the originally adsorbed CO and the introduction of the reaction mixture at 20 Torr decreased it an additional 30%. For the 800° annealed foil, the replacement of CO occurred to a similar extent, about 45%, by both acetylene and the mixture.

Discussion

The catalytic activity of palladium shows several modes of behavior depending on the annealing temperature. The highest activity exists after annealing below 200° but it decreases markedly with annealing at 250–300°. Such a decrease in activity with annealing was observed in a similar temperature range on cold-worked nickel in the dehydrogenation of ethanol and the para–ortho hydrogen conversion.[4] The minimum in activity appears with annealing at 400–500° and a moderate activity with high selectivity is recovered with treatments above 600°. A similar change of activity was also observed on platinum foil, though the recovery of the activity occurred by the treatment above 700°.

This decrease in the activity is due to neither the oxidation nor contamination of the surface; the annealed foil was always reduced with hydrogen at 150° prior to each kinetic run and a similar change in activity was also observed in the He bombarded foil kept in a grease-free sys-

tem. By the use of Xe adsorption at 77 K, the surface area of the foil and its change with annealing were estimated and the roughness factor,[8] defined as the ratio of real surface area S to geometric surface S_0, was found to change from 1.1 to 1.8, as shown in Figure 2. Since no parallelism is held between these change in activity and surface area, it is evident that the activity is very sensitive to the fine structure of surface.

Structure of Active Sites. When Pd foil is subjected to cold working or is bombarded with massive particles of high energy, imperfections involving vacancies and dislocations are formed in the bulk and the surface of the metal. On the other hand, point defects consisting of vacancies and interstitial atoms are mainly produced when the foil was irradiated with high-energy electrons or light particles such as He.[9] The interstitial atoms produced in the bulk of Pd diffuse onto the surface and disappear by heating above 100° whereas vacancies vanish by heating at 200–250°.[10] Recent LEED studies also showed that the damage on the Pd (100) surface caused by argon ion bombardment was annealed out in this temperature range.[11] The fact that vacancies can be formed by all activation procedures used in the present study and that, of various defects present, only the vacancies disappear in the temperature range where the catalytic activity decreases markedly lead to the conclusion that the structure of active sites on the 200° annealed foil is closely correlated with the surface vacancies. A higher activity of the bombarded surface than that of cold-worked foil may be due to higher density of the produced vacancies. The fine structure of the surface around a vacancy and its role in catalysis are well understood on the basis of the so-called B_n model, as an assembly of n exposed atoms, proposed by van Hardeveld and van Montfoort[12] and Bond.[13] The vacancy on the (110) plane forms a "B_7" site where two t_{2g} and e_g orbitals of each atom in the first layer lie parallel to the plane and emerge at 45° respectively, four t_{2g} orbitals from the second layer atom emerge at 30°, and one t_{2g} of the third layer atom is normal to the plane. A schematic representation is given in Figure 8a and all these orbitals are, as dangling bonds, available for the adsorption of acetylene. A hydrogen molecule can be held on a position close to the adsorbed acetylene by unused e_g or t_{2g} orbitals of the site. On the (100) and (111) planes, a monovacancy can not act as the adsorption site because of the shorter interatomic distance across the atomic hole. However, the clusters of vacancies readily create effective sites for adsorption and reaction. It is, therefore, probable that the bombarded surface is composed of these vacancies because of sufficient density of bombarding. The edge or corner atoms of the crystal grains may constitute structures available for the adsorption of acetylene or hydrogen but both species are hardly accessible to each other on these sites.

It is not probable that the minimum activity is due to carbon contaminant diffused from the bulk of the foil; as is apparent from the preadsorption experiment, species D cannot be removed by reduction and is always present as a carbonaceous residue during the course of reaction. Further, the annealing of the foil bombarded by helium or argon ion does not cause as low an activity as that observed in the cold-worked foil, though species D is still present on surface. This indicates that the low activity is not due to the contamination but is peculiar to the cold-worked surface which needs further investigation.

The annealing above 600° promoted the exposure of

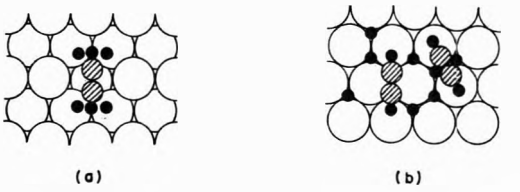

Figure 8. Schematic representation of active sites: C, palladium atom; ⊘, carbon atom; ●, hydrogen atom; (a) B_7 site on the 200° annealed foil; (b) B_2 and B_4 sites on the 800° annealed foil.

(111) planes as the result of recrystallization. This fact was also confirmed from the LEED study on platinum crystals annealed at temperatures higher than 700°.[14] These results suggest that the active sites on the 800° annealed foil are strongly correlated with the (111) plane or facet. The finding that the annealing at 600° and above increases the number of the active sites, leaving the specific activity per site unchanged, conforms with the preferential growth of the plane. The recent LEED study showed that steps on the Pt (111) surface interacted more strongly with hydrogen and oxygen than the (111) face and dissociated ethylene and carbon monoxide into carbon residue.[15] However, acetylene and ethylene were chemisorbed easily on the (111) surface with an ordered structure.[16] The (111) face seems, therefore, to be effective for the reaction by forming B_2 and B_4 sites, though the participation of steps in hydrogenation is not completely ruled out. The previous study on kinetics[2] revealed that hydrogenation on this surface occurred between adsorbed acetylene and surface hydrogen which is equilibrated with dissolved hydrogen. It is, therefore, reasonable to suppose that the acetylene reacts readily with the hydrogen coming up through the hole among Pd atoms from the inside of metal (Figure 8b).

States of Adsorbed Acetylene. The states of adsorbed acetylene can be distinguished according to their relative stabilities on the surface. Since species A was easily pumped out at room temperature, it may be physically adsorbed or reversibly chemisorbed acetylene. An ir study has shown that absorption bands were observed around 2900 cm^{-1} when the reaction mixture was admitted on a fresh Pd surface but no appreciable bands appear by the admission of acetylene only.[17,18] Acetylene on the used surface, however, provided a weak band near 3030 cm^{-1} and the thermal desorption peak of acetylene near 20° corresponded to this species.[19] These results show that acetylene first interacts with the fresh Pd surface so that the surface is covered with the moderately bound acetylene (species B) and surface polymerizates (species C and D). In the second run, the active sites are formed by the removal of species B and are stabilized by the surrounding polymerizates. The polymerizates may make the adsorption bond of acetylene weak. This idea is supported by the stabilizing effect of preadsorbed acetylene on the activity of ethylene hydrogenation[18] and by the fact that the rate of exchange between the adsorbed and gaseous acetylenes is increased on the used surface as shown in Figure 5.

In the 200° annealed foil, it was found that the amount of hydrogen dissolved during hydrogenation was negligibly small and, further, the previously dissolved hydrogen was not effective for the hydrogenation.[2] However, in the second run of the 800° annealed foil, there was a large amount of the dissolved hydrogen, and the rate of hydrogenation was found to be proportional to the amount.[2] These results lead to the conclusion that the charged hy-

drogen contributes partly to the second run, in addition to the effect of the surface polymerizates.

The results of Figure 6 show that the active sites on the 200° annealed Pd are distributed rather independently whereas those on the 800° annealed Pd are correlated with each other and this correlation becomes weak in the presence of adsorbed CO. This suggests that CO adsorbed randomly on the whole surface isolates the active sites. Complete understanding of these phenomena will be obtained by the topographic analysis of the well-defined surface as attempted by Rideal and Herington.[20] It is evident that the active sites which are present on a surface annealed at 800° scarcely contribute to the activity of the 200° annealed catalyst, because its activity is not affected by CO adsorption as shown in Figure 7.

Carbon Monoxide Poisoning. The effect of CO poisoning on the 800° annealed foil indicates that the active sites are homogeneously distributed on the whole surface or that CO is randomly adsorbed at some subgroup of active sites. On the foil annealed at 200° a larger fraction of the adsorbed CO was removed by the reaction mixture than that removed by acetylene, though the introduction of only hydrogen enhanced moderately the adsorption of CO. This result clearly indicates that the interaction between hydrogen and acetylene on active sites is much stronger than that between hydrogen and carbon monoxide. This view is supported by the fact that the reaction was not poisoned by CO and that there was no time lag in the response of the rate on pressure jump or on isotope replacement and further by the high yield of ethane, as seen in the previous study.[2]

References and Notes

(1) Y. Inoue and I. Yasumori, *J. Phys. Chem.*, **73**, 1618 (1969).
(2) Y. Inoue and I. Yasumori, *J. Phys. Chem.*, **75**, 880 (1971).
(3) H. E. Farnsworth and R. F. Woodcock, *Advan. Catal.*, **9**, 123 (1957); J. Tuul and H. E. Farnsworth, *J. Amer. Chem. Soc.*, **83**, 2247, 2253 (1961).
(4) I. Jhara, Y. Numata, H. Hamada, and Y. Kageyama, *J. Phys. Chem.*, **66**, 1374 (1962); I. Uhara, S. Kishimoto, T. Hikino, H. Hamada, and Y. Numata, *J. Phys. Chem.*, **67**, 996 (1963).
(5) D. Cormack, S. J. Thomson, and G. Webb, *J. Catal.*, **5**, 224 (1966).
(6) A. Lawson, *J. Catal.*, **11**, 283, 295 (1968).
(7) To be submitted for publication.
(8) T. Kabe, T. Mizuno, and I. Yasumori, *Bull. Chem. Soc. Jap.*, **40**, 2047 (1967).
(9) E. H. Taylor, *Advan. Catal.*, **18**, 111 (1968).
(10) L. M. Clarebrough, M. E. Hargreaves, and G. W. West, *Proc. Roy. Soc., Ser. A*, **232**, 252 (1955); *Phil. Mag.*, **1**, 528 (1956); *Acta Met.*, **8**, 797 (1960).
(11) R. L. Park and H. H. Madden, Jr., *Surface Sci.*, **11**, 188 (1968).
(12) R. van Hardeveld and A. van Montfoort, *Surface Sci.*, **4**, 396 (1966); **15**, 189 (1969); **17**, 90 (1969).
(13) G. C. Bond, *Proc. Int. Congr. Catal., 4th, 1968*, **2**, 266 (1969).
(14) H. B. Lyon and G. A. Somorjai, *J. Chem. Phys.*, **46**, 2539 (1967).
(15) B. Lang, R. W. Joyner, and G. A. Somorjai, *Surface Sci.*, **30**, 440, 454 (1972).
(16) A. E. Morgan and G. A. Somorjai, *J. Chem. Phys.*, **51**, 3309 (1968).
(17) L. H. Little, N. Sheppard, and D. J. C. Yates, *Proc. Roy. Soc., Ser. A*, **259**, 242 (1960).
(18) I. Yasumori, N. Shinohara, and Y. Inoue, Catalysis; *Proc. Int. Congr. Catal., 5th, 1972*, 771 (1973).
(19) To be submitted for publication.
(20) E. F. G. Herington and E. K. Rideal, *Trans. Faraday Soc.*, **40**, 505 (1944).

Infrared Study of Nitric Oxide and Carbon Monoxide Adsorbed on Chromia/Alumina[1]

J. B. Peri

Research and Development Department, Amoco Oil Company, Whiting, Indiana 46394

(Received October 29, 1973)

Publication costs assisted by Amoco Oil Company

Infrared study was made of NO and CO adsorbed on chromia/γ-alumina catalysts to elucidate the nature and distribution of exposed Cr ions. The catalysts, prepared in several ways, contained from 0.3 to 5.0% Cr. Depending on sample pretreatment, adsorbed NO gave eight or more bands in the spectral region from 1700 to 2300 cm^{-1}, evidently representing adsorbed species ranging from $(NO)_2$ dimer to adsorbed NO^- ions. Adsorbed CO gave at least three bands in the 2150–2250-cm^{-1} region. Variations in relative intensities of the bands with gas pressure, sample pretreatment, and Cr concentration were investigated to permit assignment of these bands to CO, NO, or $(NO)_2$ dimer on exposed cations, principally Cr^{2+} and Cr^{3+}. Preadsorption of NH_3 and simultaneous adsorption of CO and NO were also studied. Some exposed Cr ions had two or more vacant coordination positions, others only one. Exposed Cr^{2+} ions, which predominated after high-temperature reduction, or after simple evacuation at high temperatures of oxidized chromia/alumina, are probably the sites of greatest catalytic importance. Paired Cr^{2+} may be needed for hydrocarbon dehydrogenation and dehydrocyclization, while single Cr^{2+} ions with two vacant coordination positions may catalyze olefin polymerization.

Introduction

Chromia catalysts are of interest in several important areas. Chromia is an active catalyst for hydrogenation–dehydrogenation and was the first dehydrocyclization catalyst discovered.[2] Oxide-supported chromia has been used commercially for naphtha reforming,[3] for production of butadiene from butane,[4] and, in the Phillips process, for polymerization of olefins.[5,6] Chromia catalysts cata-

lyze CO oxidation + NO reduction reactions that may be important in cleaning up automotive emissions.[7]

Good review articles cover the chemisorptive and catalytic behavior of chromia[8] and the physical-chemical properties of chromia/alumina catalysts.[9] Chromia catalysts have been studied intensively, because the electronic configuration of chromium makes it suitable for investigation by a variety of physical-chemical techniques, particularly the conventional adsorption methods,[10-12] magnetic susceptibility,[13] esr,[13-16] and infrared studies of adsorbed "probe" molecules.[17,18] Each method has yielded some useful information, but none has provided more than a fragmentary picture of the complex surface chemistry of chromia catalysts.

Infrared spectroscopic study of adsorbed probe molecules offers some advantages over most other methods, because it "sees" only those chromium atoms actually exposed on the surface. It has been applied to adsorption of CO and CO_2 on α-chromia,[19] chromia/silica,[20] and chromia/alumina.[21] Adsorbed H_2O, N_2O, O_2, and pyridine have also been studied on α-chromia.[22] Rather surprisingly, however, no infrared study of the adsorption of NO on chromia or supported chromia seems to have been reported since the pioneering work of Terenin and Roev.[23] Nitric oxide is particularly interesting as a probe molecule because of the variety of possible adsorbed forms, ranging from NO^+ to NO^-, readily distinguishable spectroscopically, which may provide information about the Cr atoms exposed on the surface.

The importance of the surface chemistry of chromia catalysts, plus the prospect that improved spectrometers and techniques would provide better data than in earlier studies, prompted reinvestigation of the adsorption of NO and CO on chromia/alumina. Chromia/silica was briefly studied for comparison.

Experimental Section

Apparatus and Procedures. The apparatus and procedures have been described.[24] A Beckman IR-9 spectrometer was used, as before, in single-beam operation. Infrared study was limited to the spectral region from 1200 to 4000 cm^{-1}. Disks for infrared study were normally prepared by pressing 0.25 or 0.30 g of powdered catalyst in a steel die, 1.25 in. in diameter, usually at 5 ton/in.^{2}, but in some cases up to 50% higher to obtain suitable disks. Unless otherwise specified, reduction of catalysts in H_2 was for 1 hr at a pressure of 50 Torr. Repeated reduction in fresh H_2 at a given temperature produced little change in subsequent NO spectra. Spectra of adsorbed NO were typically initially recorded with 5–6 Torr of NO in the cell and then again after 5-min evacuation.

Materials. Chemicals used in catalyst preparation were reagent grade. Catalysts were made by impregnation of alumina or silica gel with a solution of CrO_3, ammonium dichromate, or $CrCl_3$ in sufficient water to just moisten the gel (typically about 7.5 ml/10 g of alumina).

Two alumina supports were used. Alumina A was an aerogel, prepared from alcogel as previously described,[25] lightly ground to a powder, and calcined in air for 16 hr at 600°. (Surface area by N_2 adsorption was approximately 300 m^2/g.) Alumina B was prepared by drying, in a vacuum oven, an aqueous alumina sol similar to that used in preparation of the aerogel, then calcining in air for 16 hr at 500° (surface area = 230 m^2/g). Silica was Davison Grade 62 (surface area = 297 m^2/g). Surface areas determined by N_2 adsorption on three of the final alumina-supported catalysts, containing up to 10% CrO_3, all fell in the range 230–252 m^2/g. The 10% CrO_3/silica catalyst had an area of 268 m^2/g.

Nitric oxide, supplied by Linde Co., was purified by bulb-to-bulb distillation. Carbon monoxide was Airco or Linde-Assayed reagent. Hydrogen was purified by diffusion through palladium-silver alloy.

Results

Spectra of Chromia/Alumina. General Features. The spectral features of chromia/alumina were approximately those expected for similarly pretreated alumina. In particular, hydroxyl-stretching bands in the 3600–3800-cm^{-1} region and "carbonate" and/or "carboxylate" bands in the 1300–1700-cm^{-1} region together with a "trapped CO_2" band at 2350 cm^{-1} were evident in the spectra.[26-28] Minor differences that might have resulted from the presence of chromium were not systematically studied. The carbonate and carboxylate bands should be expected, because they are not completely removed from alumina spectra except by evacuation at 800°, and not always then if closed pores are present.[26-28]

Adsorption of NO on Chromia/Alumina. Spectra for adsorbed NO generally showed a complicated set of seven or more bands between 1700 and 1950 cm^{-1} with an additional band, or bands, near 2260 cm^{-1}. The relative intensities of these bands depended on NO pressure and sample pretreatment.

Figure 1a shows spectra for adsorbed NO on a catalyst prepared by addition of 10 wt % CrO_3 in aqueous solution to alumina B (~5% Cr/Al_2O_3 on reduced catalyst) and prereduced in H_2 at 400°. Spectra were obtained with NO at 5–6 Torr pressure and again after 5-min evacuation at 40°. Prereduction in H_2 at progressively higher temperatures, as shown in Figure 1b and 1c, increased the relative intensities of bands near 1880 and 1755 cm^{-1} (A and B) produced by strongly held NO. It decreased and ultimately eliminated bands near 1905 and 1775 cm^{-1} (C and D) due to strongly held NO, and bands near 1940, 1875, and 1820 cm^{-1} (E, F, and G) due to weakly held NO. The positions of some of these bands, especially in the 1750–1790-cm^{-1} region, apparently shift by 10 cm^{-1} or more, depending on pretreatment and amount of adsorption.

Figure 2 shows spectra for NO on three catalysts prepared by impregnation of alumina A with 6.0, 2.0, and 0.6% CrO_3 (3, 1, and 0.3% Cr/Al_2O_3 on reduced catalyst) and prereduced in H_2 at 600°. A striking feature is the relative constancy of the intensities of the E, F, and G bands over a tenfold variation of Cr concentration. The alumina support, whether merely dried or reduced in H_2, showed no trace of these bands when NO was added. These bands, especially E and G, disappeared at roughly equal rates as the NO pressure was reduced (spectra not shown). They were typically mostly removed by 5-min evacuation at 40°, although complete removal was not always evident, particularly for the F band which overlaps the A band.

The intensities of the A, B, C, and D bands appeared to be more nearly proportional to the Cr concentrations at similar NO equilibrium pressures (similarly numbered spectra in Figure 2), but correlation of intensities with Cr concentration was not exact for individual bands. Figure 3 shows plots of the approximate peak band intensities after evacuation as indicated *vs.* Cr concentration. Intensities were estimated by graphical resolution of the incompletely resolved bands, assuming that after evacuation at 40°

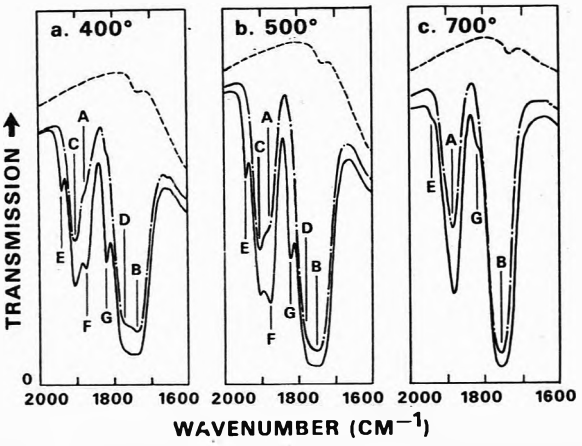

Figure 1. Spectra of adsorbed NO on 10% CrO_3/Al_2O_3, prereduced in H_2 at temperatures indicated (°C): (- - -) after reduction; (——) after addition of ~6 Torr of NO; (—·—) after evacuation.

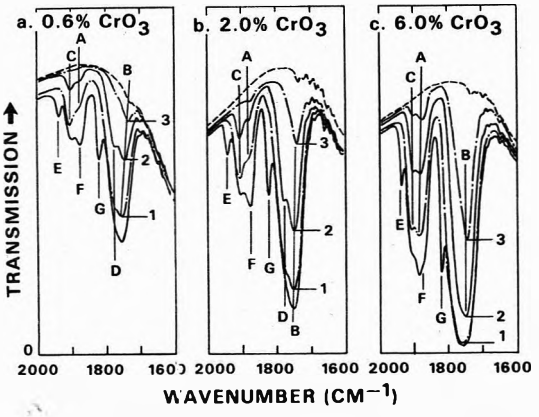

Figure 2. Spectra of adsorbed NO on CrO_3/Al_2O_3 catalysts prereduced in H_2 at 600°. CrO_3 concentrations (wt %) on original catalysts as indicated: (- - -) after reduction; (lower ——) after addition of NO; remaining spectra after evacuation at (1) 40, (2) 100, and (3) 150°.

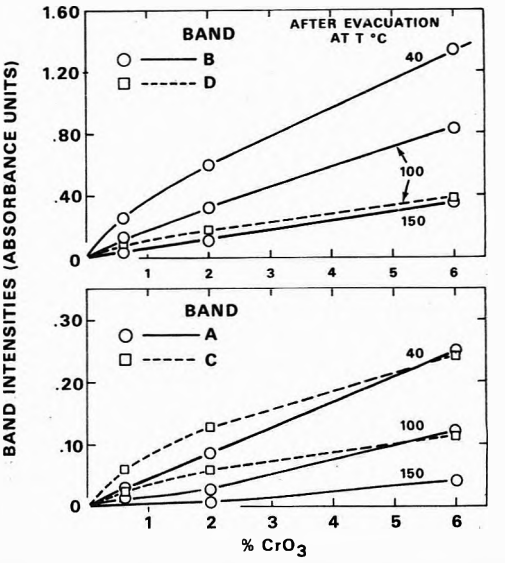

Figure 3. Band intensities for NO on CrO_3/Al_2O_3 prereduced at 600°.

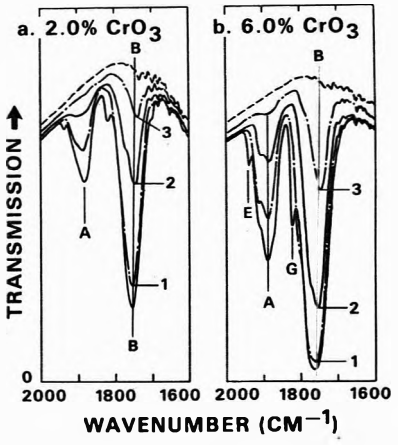

Figure 4. Spectra of adsorbed NO on CrO_3/Al_2O_3 prereduced at 700°: (---) after reduction; (lower ——) after addition of NO; remaining spectra after evacuation at (1) 40, (2) 100, and (3) 150°.

or higher only four bands remained. This assumption is probably not completely valid, because there is a shoulder near 1805 cm^{-1} in some of the spectra. The intensities of the D band are also fairly uncertain at higher Cr concentrations. Nevertheless, the plots show significant differences in the behavior of the bands.

The roughly parallel changes in the intensities of the C and D bands on samples of increasing Cr content suggest that these bands could arise from a single type of NO adsorption. The A and B bands also increase in roughly the same way with increasing Cr content, but closer observation indicates that they change significantly in relative intensity with either changing Cr concentration or as NO is progressively desorbed. The ratio of absorbances (A/B) of the two bands, after evacuation at 40°, for example, changes from 0.19 for 3% Cr to 0.14 for 1% Cr and to 0.12 for 0.3% Cr, suggesting that different types of adsorption sites are involved for the two bands. Similar changes in A/B ratios as NO is desorbed are also consistent with two different types of sites, although such behavior could also suggest two types of adsorption on similar types of sites. The poor resolution of the D band in many of the spectra precludes similar observations regarding the C and D bands.

Figure 4 shows spectra for NO on two of the catalysts of Figure 2 prereduced at 700°. The differences from those shown in Figure 2 are about as expected from consideration of the changes in Figure 1 after 600 and 700° reduction. Some differences, however, especially the greater persistence of the weakly held bands, E, F, and G and of the C and D bands after 700° reduction, may arise from variation in surface properties of the alumina support or Cr concentration.

Figure 5 shows spectra of NO on the three catalysts after prereduction at 500°. These spectra emphasize the E, F, and G bands which, as before, change relatively little in intensity with Cr concentration, and may also cast some doubt on a possible close relationship between the C and D bands. The C/D ratio seems slightly lower (0.24 *vs.* 0.30–0.32) than in Figure 2. The shoulder near 1805 cm^{-1} is particularly prominent after evacuation at 40°, but is suppressed or shifted to a lower frequency at higher NO pressures.

Figure 6 shows spectra for NO on 1% Cr/Al_2O_3, prepared from alumina B and $CrCl_3$, both before (Figure 6a) and after (Figure 6b) prereduction in H_2 at 500°. Three bands (E, F, and G) corresponding to weakly held NO, similar to those in Figure 5, are evident. For the unreduced catalyst other major bands corresponding to strong-

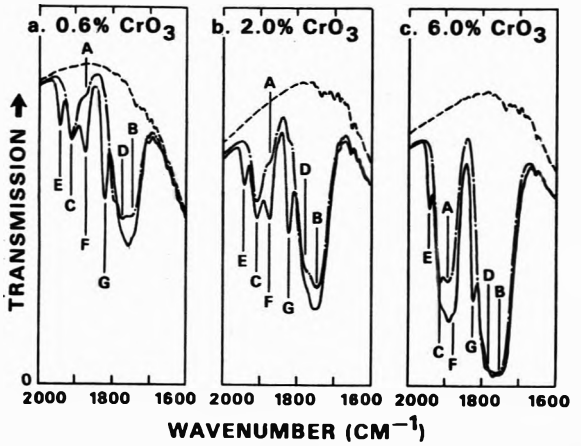

Figure 5. Spectra of adsorbed NO on CrO_3/Al_2O_3 catalysts prereduced at 500°. CrO_3 concentrations (wt %) on original catalysts as indicated: (– – –) after reduction; (——) after addition of NO; (—·—) after 5-min evacuation.

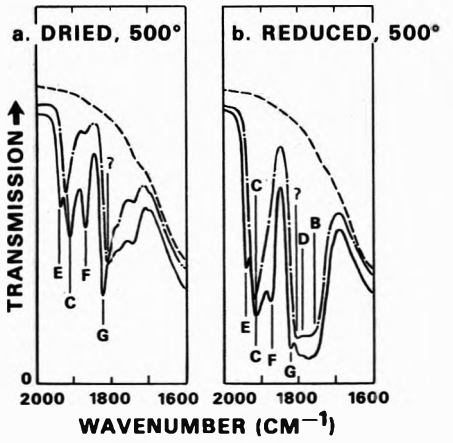

Figure 6. Spectra of adsorbed NO on $CrCl_3/Al_2O_3$ (a) predried by evacuation at 500° and (b) prereduced at 500°: (– – –) after evacuation or reduction; (——) after addition of NO; (—·—) after 5-min evacuation.

ly held NO appear near 1920 and 1810 cm^{-1}. Prereduction markedly increases the intensity of the 1920-cm^{-1} band, and produces strong bands in the 1750–1800-cm^{-1} region and a possible shoulder near 1885 cm^{-1} on the 1920-cm^{-1} band. The spectra of NO on unreduced Cr/Al_2O_3 suggest either that the E, F, and G bands all represent NO held by Cr^{3+} ions, or that adsorption of Cr^{3+} on alumina leads to stabilization of higher and lower oxidation states ($2Cr^{3+} \rightarrow Cr^{2+} + Cr^{4+}$) which can also hold NO.

Coadsorption of NO and CO. Further evidence on the possible origin of the E, F, and G bands is provided in Figure 7. Figure 7a shows the effects of adding CO to a 1% Cr/Al_2O_3 sample (2% CrO_3) which had been exposed to NO and then evacuated for 5 min at 40°. Adsorption of CO in the absence of NO gave no bands in this region. The addition of CO caused the bands near 1930 and 1820 cm^{-1}, evidently E and G, to reappear (both had previously disappeared on removal of weakly held NO by evacuation), and decreased the intensities of other bands, particularly at 1910 cm^{-1} (presumably the C band). Figure 7b shows the spectral changes produced in the 2100–2300-cm^{-1} region when the CO was adsorbed. Comparison with spectra obtained in the absence of preadsorbed NO (shown below in Figure 9) reveals that the 2185-cm^{-1} band would not normally have appeared. These results indicate that

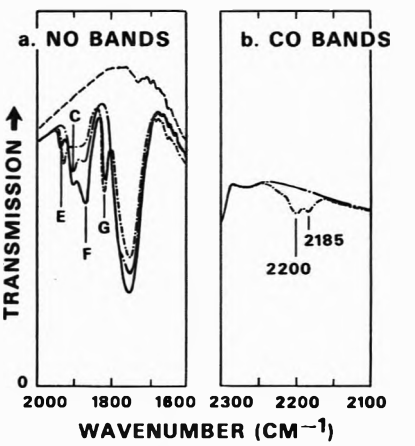

Figure 7. Spectra of adsorbed NO + CO on 2% CrO_3/Al_2O_3 prereduced at 600°: (– – –) after reduction; (——) after addition of NO; (—·—) after 5-min evacuation; (·····) after addition of CO.

adsorption of CO on a Cr^{3+} ion already holding NO restores the E and G bands. In the absence of CO, these two bands evidently arise from NO on Cr^{3+} ions which hold two NO molecules.

Preadsorption of NH_3. Preadsorption of NH_3 changes the spectra of NO adsorbed subsequently. After adsorption of NH_3 at 40°, desorption at 100 or 150°, and addition of NO, the NO bands are significantly shifted to lower frequencies, probably reflecting the influence of neighboring NH_3 molecules or hydroxyl groups. As the NH_3 was progressively desorbed at higher temperatures, the NO bands usually seen after NO addition were restored and shifted to higher frequencies. First to reappear were bands at 1868 and 1733 cm^{-1} (presumably shifted A and B bands). After desorption of NH_3 at 300°, adsorption of NO produced all seven of the major bands normally seen in this region. The C band appeared to have especially increased, but the E and G bands were less intense than normal. After desorption of NH_3 at 500° all the NO bands were restored to approximately normal intensities.

NO Bands on Cr/Al_2O_3 from Ammonium Dichromate. A sample of 2% Cr/Al_2O_3 prepared by impregnation of alumina B with ammonium dichromate + NH_4OH solution (pH 8) exhibited, after evacuation above 400°, reduction in hydrogen, and exposure to NO, the same set of NO bands with approximately the same relative intensities, as did the samples prepared from CrO_3.

NO Bands on "Oxidized" CrO_3/Al_2O_3. When fresh CrO_3/Al_2O_3 was heated in O_2 and dried by evacuation at 500 or 600° without subsequent reduction, the bands seen on addition of NO were as shown in Figure 8a. Rather surprisingly, these closely resemble those typically most prominent after prereduction at 600 or 700° in H_2. Progressive reduction of such "oxidized" CrO_3/Al_2O_3 in H_2 at 300 and 400°, as shown in Figure 8b and 8c, gradually restored the other NO bands typically seen on reduced samples after NO readdition, ultimately to approximately the same relative intensities previously observed on CrO_3/Al_2O_3 reduced at 400–500°. The E and G bands were somewhat weaker than usual, however.

Effect of Potassium "Promoter" on NO Bands. Alkali metal "promoters" are commonly used with CrO_3/Al_2O_3 catalysts. They are assumed to aid catalyst performance by either (a) destroying the acidity of the alumina, (b) promoting redispersion of CrO_3 during regeneration, or (c) stabilizing higher oxidation states of Cr against reduction.

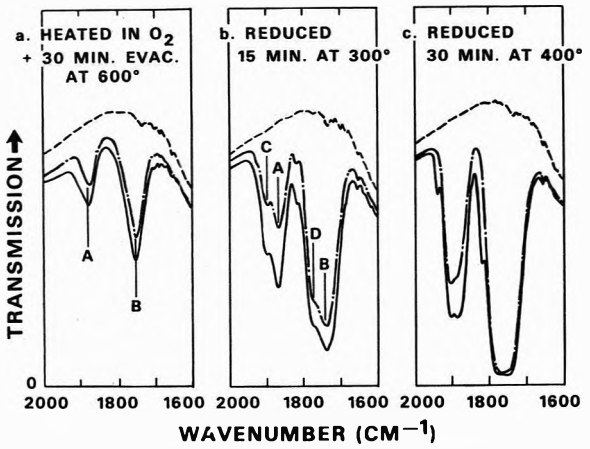

Figure 8. Spectra of adsorbed NO on 6.0% CrO_3/Al_2O_3 preheated in O_2: (– – –) after pretreatment as indicated; (——) after addition of NO; (—•—) after 5-min evacuation.

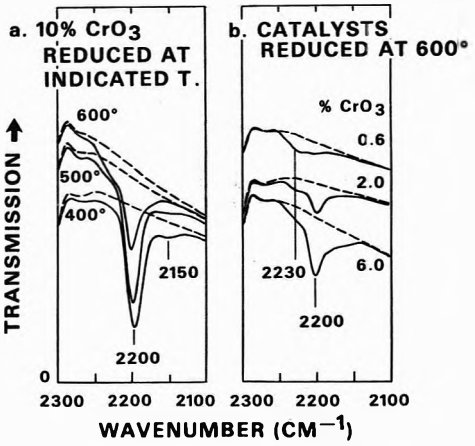

Figure 9. Spectra of adsorbed CO on CrO_3 prereduced at various temperature: (---) after reduction; (———) after addition of CO.

Spectra (not shown) of NO adsorbed on a catalyst of original composition 1% K_2O + 9.8% Cr_2O_3 + 89.2% Al_2O_3, prereduced in H_2 at 500° (or higher), closely resembled the spectra obtained after prereduction at 700° for NO on 10% Cr_2O_3/Al_2O_3 (see Figure 1). Two major bands were present near 1880 and 1750 cm^{-1}, but no trace of E, F, or G bands was seen. Rather than stabilizing higher oxidation states of Cr, the K appears to aid the reduction of Cr.

CO Adsorption on, and CO Reduction of, Cr/Al_2O_3. Figure 9 shows typical bands observed when CO was adsorbed on Cr/Al_2O_3, variously pretreated. The major band was near 2200 cm^{-1}, as found by others for CO on chromia/alumina,[21] chromia/silica,[20] or on amorphous chromia.[19] Small bands, varying in intensity with sample pretreatment and CO pressure, appear near 2150 and 2230 cm^{-1}. The intensity of the 2200-cm^{-1} band is roughly proportional to, while that of the 2230-cm^{-1} band is independent of, the Cr concentration. When the catalysts were prereduced above 500°, the intensity of the 2200-cm^{-1} band decreased, and a low-frequency "tail" appeared, indicating an underlying band, or bands, centered around 2180 cm^{-1}. Except for the band at 2230 cm^{-1}, these bands are generally similar to those reported for CO on chromia/silica[20] reduced at 400°, or on amorphous chromia[19] after surface dehydration, which have been attributed to CO on Cr^{3+} ions. The major band at 2200 cm^{-1} should be assigned to CO on Cr^{3+}. The "tail" on the 2200-cm^{-1} band, most prominent on the most thoroughly reduced samples, may arise from CO on Cr^{2+} ions. It seems probable, however, that CO is held much less strongly by Cr^{2+} than by Cr^{3+} ions. The 2230-cm^{-1} band arises mainly from CO on Al^{3+} ions in "α sites"[26] but adsorption on Cr ions in the Al_2O_3 surface may also be involved. The nature of the Cr ion sites responsible for the 2150-cm^{-1} CO band is uncertain, but these sites do not contain Cr^{2+} ions.[19]

The adsorption of CO also produced "carbonate" bands on incompletely reduced samples.[21] Progressive reduction of the sample by heating in CO and evacuation at progressively higher temperature gradually eliminated these carbonate bands and enhanced the bands in the 2200-cm^{-1} region. CO reduction gave approximately the same final reduced states as H_2 reduction, as shown by spectra of adsorbed NO or CO.

NO Adsorbed on Chromia/Silica. Chromia/silica catalysts were studied only briefly, but further work might yield important new insight on the Cr sites important in olefin polymerization. Spectra (not shown) of NO adsorbed on 10% CrO_3/silica showed that variation in pretreatment can greatly affect the surface Cr sites. After prereduction at 400° in H_2, addition of NO produced strong bands near 1880 and 1750 cm^{-1} with a small band near 1815 cm^{-1}, all rather similar to bands typically seen for NO adsorbed on 10% CrO_3/Al_2O_3 prereduced at 600 or 700°. After heating in O_2 at 600°, evacuation and reduction in H_2 at 500°, and evacuation at 300°, adsorption of NO gave a major band near 1815 cm^{-1}, while the other bands were greatly reduced in intensity. The 1815-cm^{-1} band appeared to be produced by NO held somewhat more strongly than that responsible for the G band on Cr/Al_2O_3. Different types of adsorption sites are probably responsible for these bands on the two catalysts. If similar sites are involved, they must be far more numerous on the Cr/silica catalyst after pretreatment as described. Because such pretreatment is generally similar to that used in the activation of chromia/silica polymerization catalysts, such sites could be those most active for polymerization.

Discussion

The complexity of the NO bands reveals a wide variety of adsorption sites on Cr_2O_3/Al_2O_3. This is hardly surprising, in the light of previous studies. The probable nature of the binding of NO has been adequately discussed elsewhere.[18] The differences between the present spectra and those of Terenin and Roev (TR)[23] are striking. The bands reported in the 2000–2100-cm^{-1} region by TR for NO on Cr (whether metal, oxide, or salt) were never seen in the present study. The three bands typically found by TR in the 1700–2000-cm^{-1} region (invariably one near 1735 cm^{-1} and others variously at 1830, 1842, 1905, or 1920 cm^{-1}) do not correspond well to the bands in this region in the present study. (The 1735-cm^{-1} band was also observed by TR for NO on Fe and Ni samples.) The NO bands reported by TR below 1700 cm^{-1}, attributed to adsorption on the supporting gel, were also not seen here. These discrepancies demand some explanation. Although Cr^0, produced by decomposition of Cr carbonyl might (through "coordinative ionic" or ionic bonding as described by TR), give bands above 2000 cm^{-1}, adsorption of Cr^0 can hardly explain such bands on Cr oxide or sulfate (as recognized by TR). The use of Cr and other car-

TABLE I: Assignments for Adsorbed NO on Chromia/Alumina

Band, cm^{-1}	Adsorption sites	Open coordination Positions/Cr	Adsorbed Species
A (1880)	Cr^{2+}	1	NO
C (1905)	Cr^{2+}	1	NO
B (1755)	Cr^{2+}-Cr^{2+} or Cr^{2+}-Cr^{3+} pairs	1	$(NO)_2$ dimer
D (1775)	Cr^{3+}-Cr^{3+} pairs	1	$(NO)_2$ dimer
E (1940)	Cr^{3+} in Al_2O_3 surface	2	ON NO / Cr^{3+}
G (1820)	Cr^{3+} in Al_2O_3 surface	2	
F (1875)	Cr^{3+} in Al_2O_3 surface	1	NO
2260	Al^{3+}-O^{2-}	1	NO^+

bonyls suggests another explanation. Traces of undecomposed carbonyls left as contaminants in the vacuum system could produce bands in the 2000–2100-cm^{-1} region, and react with NO to form mixed nitrosyl carbonyls, which could account for other bands observed by TR but not found here. The failure of TR to observe major bands reported here must then be attributed to lower sensitivity in their studies, possibly reflecting poorer dispersion of Cr on the alumina support.

Assuming that the present spectra correctly reflect the state of dispersion and oxidation of Cr on alumina, the problem of assigning the bands remains formidable. A summary of proposed assignments is given in Table I. Although any assignment must be tentative, certain conclusions seem warranted. The A and B bands (1885 and 1755 cm^{-1}) corresponding to strongly held NO, which increase on reduction at high temperatures, and predominate after reduction at 700° (Figure 1c), can reasonably be attributed to NO on Cr^{2+} ions, because reduction of chromia/alumina leads to extensive formation of Cr^{2+} on the surface.[7,15] The variation in the A/B ratio as NO is gradually desorbed indicates that the two bands either represent NO on two different types of sites or NO held differently on similar sites. The similarity in the relative intensities and frequencies of these bands and those reported for NO dimer and monomer adsorbed on alkali halide films[29,30] at low temperatures suggests that such compounds may be involved here, although held more strongly than on the alkali halides. The B band and possibly some of the A band could arise from NO dimer held on two closely spaced Cr^{2+} ions (or even on one Cr^{2+} ion). The A band probably mainly reflects NO monomer held on single Cr^{2+} ions. Other assignments, of course, are possible. For example, neutral complexes of Cr which hold two NO molecules per Cr atom typically show bands in the 1670–1825-cm^{-1} region.[31]

The persistance of the C and D bands (strongly held NO) after reduction at moderately high temperatures, together with their gradual elimination as the A and B bands increase, indicates that these bands show NO adsorbed on Cr^{3+} ions. This conclusion is apparently supported by the results obtained on $CrCl_3$-impregnated alumina before and after reduction, although a frequency shift of about 20 cm^{-1} must, in this case, be ascribed to the influence of chloride. The A, B, C, and D bands all probably arise from NO on exposed Cr ions on (rather than in) the Al_2O_3 surface, and/or in two dimensional chromia islands or on the surface of chromia crystallites.

The weakly held NO which causes the E, F, and G bands also seems, from the results with $CrCl_3$-impregnated Al_2O_3 (Figure 6), to be held by Cr^{3+} ions. The fact that the number of sites holding the NO responsible for the bands does not increase greatly with increasing Cr concentration suggests that these Cr^{3+} ions are held in special sites *in* the surface of the alumina support, rather than in small chromia "islands" or on the surface of a separate chromia phase. Bands E and G evidently arise from NO on exposed Cr^{3+} ions which hold a second NO molecule, as indicated by the spectra of Figure 7. The F band then probably arises from NO held weakly by Cr^{3+} ions in sites in the Al_2O_3 surface where only one NO molecule can be held per Cr^{3+} ions.

A less likely alternative explanation is that the E, F, and G bands reflect disproportionation of Cr^{3+} on special sites to form Cr^{2+} and Cr^{4+} ions. The weakly held NO responsible for the E and G bands could, on this basis, be held by Cr^{4+} ions. The sites responsible for the E and G bands are those which hold NH_3 most strongly, as would be expected for Cr^{4+} ions, and Cr^{4+} sites would probably also show weak binding of NO, because back-bonding from Cr^{4+} ions to adsorbed NO should be less than from Cr^{3+} or Cr^{2+} ions. Stronger binding of NH_3 and weaker binding of a second NO ligand also fit the explanation that exposed Cr^{3+} ions with two open coordination positions are responsible for the E and G bands, however. The F band, regarded as arising from Cr^{3+} in the Al_2O_3 surface where only one coordination position is open, presents no problems because, when NH_3 is desorbed, it is restored more readily than the other two bands.

The band (or bands) near 2260 cm^{-1} for NO adsorbed on highly dried (or highly reduced) chromia/alumina, which is not substantially different from that seen for NO on highly dried alumina, is attributed to NO^+ ions formed by interaction of NO with Al^{3+} in α sites on the surface of highly dried Al_2O_3.[32] Careful study was not made of the detailed variations of intensity and shape of this band, but the numbers and nature of the Al^{3+} sites holding NO^+ may be altered somewhat by the presence of Cr ions. Small amounts of adsorbed N_2O might also give rise to a band in this region.

The most surprising finding is the nature of the NO bands on "oxidized" CrO_3/Al_2O_3 after preevacuation at 500 or 600°. On the basis of the assignments given above, these bands appear to show Cr^{2+} ions rather than, as might be expected, Cr^{4+} or Cr^{5+} ions. Although reference spectra for NO held by Cr^{4+} or Cr^{5+} are lacking, the close resemblance to the bands obtained on H_2-reduced samples, plus the similar behavior of the sites causing these bands when NH_3 is preadsorbed and progressively desorbed strongly suggest that NO on Cr^{2+} ions is indeed responsible for these bands.

If this is so, some further explanation is needed. The studies of O'Reilly, Van Reijen, Kazanski, and others have shown that some Cr^{5+} exists on similar Cr/Al_2O_3 samples, and Cr^{4+} is thought to be present in significant amounts. The Cr^{4+} ions are not necessarily exposed on the catalyst surface, however. When CrO_3/Al_2O_3 is heated in air, it goes in part to Cr_2O_3. Studies of the electrical conductivity of chromia/alumina have led to the postulate[33] that the equilibrium $2Cr^{3+} = Cr^{2+} + Cr^{4+}$ is important at high temperatures. If both Cr^{2+} and Cr^{4+} ions are produced in the surface, it seems probable that the Cr^{2+} ions would, because of their larger ionic radii, be preferentially exposed, while Cr^{4+}, Cr^{5+}, or Cr^{6+} ions

which readily fit in octahedral interstices in an oxide lattice would remain fully coordinated with oxide ions. Only Cr^{2+} ions would, therefore, be available to adsorb NO, until reduction with CO or H_2 exposed other Cr ions, principally Cr^{3+}

Possible Catalytic Implications. In dehydrogenation and dehydrocyclization of hydrocarbons at elevated temperatures and pressures a strongly reducing atmosphere exists, and the catalytically active sites are probably either exposed Cr^{3+} or Cr^{2+} ions.[9,11] Various mechanisms have been offered for the hydrogenation of hydrocarbons.[4] Chemisorption of the reactant molecule is thought to initially complete the octahedral coordination of an exposed Cr ion. In one proposed mechanism, chemisorption occurs through transfer of a proton to an adjacent oxide ion, leaving a carbanion which is then attached to a surface Cr^{3+} ion. In another mechanism, Cr^{2+} sites donate electrons to hydrocarbon radical fragments, while hydrogen atoms shift to closely adjoining Cr ions. In either case, an alkyl group becomes attached to a chromium ion and loses H, and an olefin molecule is desorbed.

Although no Cr^{2+} was found by Weller and Voltz on reduced chromia/alumina,[11] later work[7,15] has provided good evidence that most surface Cr atoms can be reduced to Cr^{2+}. The results of the present study support this conclusion. The active sites thus probably contain exposed Cr^{2+} ions, but perhaps only those which closely adjoin other exposed Cr^{2+} or Cr^{3+} ions can catalyze dehydrogenation and dehydrocyclization of hydrocarbons. It would be desirable to check such a possibility by comparing the catalytic activities of catalysts with widely differing ratios of "single" to paired Cr ion sites (as shown by infrared spectra of adsorbed NO), and also differing Cr^{3+} to Cr^{2+} ratios. Unfortunately the attempts made in this study to alter the single/pair ratio by varying Cr concentrations or using different pH apparently did not produce large alterations. This ratio seems to be determined in large part by specific interactions with the surface of the support. Different supports and/or impregnation with Cr in the presence of complexing agents, such as oxalic acid, may be more effective in changing this ratio.

For catalysis of olefin polymerization, sites different from those most effective for dehydrogenation are evidently involved. Chromia/silica or chromia/silica–alumina catalysts are substantially more active than chromia/alumina catalysts.[5] The active sites have been postulated by Van Reijen and Cossee and by Kazanski[16] to be Cr^{5+} ions initially in a distorted tetrahedral coordination. In the presence of the olefin this changes to a distorted octahedral configuration, in which two of the six coordination positions are available for olefin or the polymerizing polymer chain. There seems to be general agreement that the active sites have two available coordination positions on the Cr ion.

Recent evidence[6,34] indicates that the active sites on chromia/silica polymerization catalysts are exposed Cr^{2+} ions, produced initially either by reduction of the catalyst with monomeric olefin or in a separate reduction step, which can hold two or more ligands. The present study indicates that exposed Cr^{3+} ions capable of holding two extra ligands exist on partially reduced chromia/alumina, and also that exposed Cr^{2+} ions can be formed by merely evacuating CrO_3/Al_2O_3 at high temperatures. There is no clear evidence for Cr^{2+} ions capable of holding more than one ligand, but such ions could be present. On chromia/silica, the sites responsible for the 1815-cm^{-1} band might be exposed Cr^{2+} ions capable of holding two or more extra ligands; further study is needed to settle this question.

References and Notes

(1) Presented at 165th National Meeting of The American Chemical Society, Dallas, Tex., Apr 1973.
(2) B. L. Moldavskii and H. Kamusher, C. *R. Acad. Sci. USSR*, **1**, 355 (1936).
(3) F. G. Ciapetta, R. M. Dobres, and R. W. Baker, "Catalysis" Vol. VI, P. H. Emmett, Ed., Reinhold, New York, N. Y., 1958, Chapter 6, p 495.
(4) S. Carra and L. Forni, *Catal. Rev.*, **5**, 159 (1971).
(5) A. Clark, *Catal. Rev.*, **3**, 145 (1969).
(6) J. P. Hogan, *J. Polym. Sci.*, **8**, 2637 (1970).
(7) M. Shelef, K. Otto, and H. Gandhi, *J. Catal.*, **12**, 361 (1968).
(8) R. L. Burwell, Jr., G. L. Haller, K. C. Taylor, and J. F. Read, *Advan. Catal.*, **20**, 1 (1969).
(9) C. P. Poole and D. S. MacIver, *Advan. Catal.*, **17**, 223 (1966).
(10) S. W. Weller and S. E. Voltz, *J. Amer. Chem. Soc.*, **76**, 4695 (1954).
(11) S. W. Weller and S. E. Voltz, *J. Amer. Chem. Soc.*, **76**, 4701 (1954).
(12) K. Otto and M. Shelef, *J. Catal.*, **14**, 226 (1969).
(13) A. Ellison, J. O. V. Oubridge, and K. S. W. Sing, *Trans. Faraday Soc.*, **66**, 1004 (1970).
(14) D. E. O'Reilly and D. S. McIver, *J. Phys. Chem.*, **66**, 276 (1962).
(15) L. L. Van Reijen, W. M. H. Sachtler, P. Cossee, and D. M. Brouwer, *Proc. Int. Congr. Catal., 3rd, 1964*, **2**, 829 (1965).
(16) V. B. Kazanski and J. Turkevich, *J. Catal.*, **8**, 231 (1967).
(17) M. L. Hair, "Infrared Spectroscopy in Surface Chemistry," Marcel Dekker, New York, N. Y., 1967.
(18) L. H. Little, "Infrared Spectra of Adsorbed Species," Academic Press, New York, N. Y., 1966.
(19) A. Zecchina, S. Coluccia, E. Guglielminotti, and G. Ghiotti, *J. Phys. Chem.*, **75**, 2774, 2790 (1971).
(20) E. Borello, A. Zecchina, C. Morterra, and G. Ghiotti, *J. Phys. Chem.*, **73**, 1286, 1292 (1969).
(21) L. H. Little and C. H. Amberg, *Can. J. Chem.*, **40**, 1997 (1962).
(22) A. Zecchina, E. Guglielminotti, L. Cerruti, and S. Coluccia, *J. Phys. Chem.*, **76**, 571 (1972).
(23) A. Terenin and L. Roev, *Spectrochim. Acta*, **15**, 274, 946 (1959); *Actes Congr. Int. Catal., 2nd, 1960*, **2**, 2183 (1961).
(24) J. B. Peri, *Discuss. Faraday Soc.*, **41**, 121 (1966).
(25) J. B. Peri, *J. Phys. Chem.*, **69**, 211 (1965).
(26) J. B. Peri, *J. Phys. Chem.*, **70**, 3168 (1966).
(27) N. D. Parkyns, *J. Chem. Soc. A*, 1910 (1967); 696 (1969).
(28) N. D. Parkyns, *J. Catal.*, **27**, 34 (1972).
(29) A. Lubezky and M. Folman, *Trans. Faraday Soc.*, **67**, 3110 (1971).
(30) A. J. Woodward and N. Jonathan, *J. Phys. Chem.*, **75**, 2930 (1971).
(31) J. Lewis, J. Irving, and G. Wilkinson, *J. Inorg. Nucl. Chem.*, **7**, 32 (1958).
(32) G. Kortüm and H. Quabeck, *Ber. Bunsenges. Phys. Chem.*, **73**, 1020 (1969).
(33) G. Lorenz and W. Fischer, *Z. Phys. Chem. (Frankfurt am Main)*, **18**, 265 (1958).
(34) H. L. Krauss, *Proc. Int. Cong. Catal., 5th, 1972*, **1**, 207 (1973).

Coordination of Cadmium(II) with Chloride Ions in Molten Potassium Tetrachloroaluminate. A Raman Spectral Study

J. H. R. Clarke*[1] and P. J. Hartley

Chemistry Department, University of Southampton, Southampton SO9 5NH, England *(Received August 20, 1973)*

Raman spectra were determined at 550° for various solutions of Cd^{2+} and Cl^- ions in molten potassium tetrachloroaluminate. The variation of intensity with Cl^-/Cd^{2+} ratio was studied for (a) the symmetric stretching band of the cadmium–chloro complex at 265 cm^{-1} and (b) the ~300-cm^{-1} band of $Al_2Cl_7^-$. The latter species is formed in small quantities in the pure solvent according to the equilibrium $2AlCl_4^- \rightleftarrows Al_2Cl_7^- + Cl^-$. This equilibrium is displaced to the right in the presence of free Cd^{2+} ions. It is concluded that $CdCl_4^{2-}$ is the most important cadmium complex formed in this solvent with an association constant of $4(\pm 3) \times 10^5$ in mole fraction units. The results are compared with previous studies using molten sodium potassium nitrate as solvent, in which the predominant complex contains chloride and cadmium in the ratio 3:1. Intensity measurements as a function of concentration for solutions of K_4CdCl_6 in molten potassium tetrachloroaluminate indicate that $CdCl_4^{2-}$ also predominates in pure K_4CdCl_6.

Introduction

In previous articles[2,3] we have discussed the Raman spectra of cadmium–halide complexes in various molten salt media. Despite the probable polyatomic nature of these complexes, only the symmetric stretching modes are well defined in the Raman spectra. For a particular halide ligand the symmetric stretching frequencies also appear to be relatively insensitive to stoichiometry.[3] For these reasons it is difficult to deduce the structures of complexes from the frequency spectra alone. However, it has been shown that information regarding the stoichiometry of the complexes can be obtained from Raman intensity measurements.[2]

Using molten sodium potassium nitrate as solvent[2] it was found that both chloride and bromide ions form highly stable complexes with Cd^{2+}. However, while $CdBr_4^{2-}$ is readily formed (with some evidence for stepwise formation of lower complexes) the results indicated that the predominant chloro complex over a wide composition range contains Cl and Cd in the ratio 3:1. Since four coordination is most characteristic of Cd^{2+} in ionic and polar solvents, one explanation for this observation is that there is solvation to give a complex such as $[CdCl_3(NO_3)]^{2-}$ and that this solvation is sufficiently strong to prevent the stabilization of a fourth chloride ligand. This would be consistent with the behavior of Cd^{2+} dissolved in pure molten alkali metal halides for which it was shown[3] that four coordination was most stable for both chloride and bromide ligands.

The present investigation was undertaken for two reasons. First, it was of interest to study the formation of cadmium–chloro complexes in alternative ionic solvents of low basicity. Potassium tetrachloroaluminate satisfies this condition[4] and the chloride-donor solvent ligand, $AlCl_4^-$, provides a contrast to the NO_3^- ion of the sodium potassium nitrate. Furthermore solutions of $CdCl_2$ with KCl in molten potassium tetrachloroaluminate are stable to decomposition and phase separation over a wide concentration range (at 750°, for instance, K_4CdCl_6 is miscible with $KAlCl_4$ up to a concentration of 50 mol %). It was possible therefore to monitor any changes in the spectra and hence the structure and distribution of cadmium–chloro complexes in going from a dilute solution to a pure halide melt of the type K_4CdCl_6.

Part of the Raman spectrum of a representative solution of Cd^{2+} and Cl^- ions in potassium tetrachloroaluminate at 550° is shown in Figure 1. Most of the scattering intensity is due to the solvent as can be seen from a comparison with the pure solvent spectrum. The gross features of the spectrum correspond to the Raman spectrum of the tetrahedral $AlCl_4^-$ ion and have been discussed elsewhere.[5,6] Only one band, at 265 cm^{-1}, can be assigned to a cadmium complex in the solution spectrum. However, this frequency is quite similar to that observed for the symmetric stretching frequency in molten sodium potassium nitrate (264 cm^{-1}). Another important feature in the solution spectrum is a weak band at approximately 300 cm^{-1} which also occurs, but with a diminished intensity, for the pure solvent. A similar weak band has been observed in previous studies of molten KCl–$AlCl_3$ mixtures and assigned[5,6] to a vibration of the species $Al_2Cl_7^-$, formed by the equilibrium

$$2AlCl_4^- \rightleftarrows Cl^- + Al_2Cl_7^- \qquad (1)$$

(Although the peak frequency is given as 313 cm^{-1} for this band,[5] the discrepancy with the value quoted above probably merely reflects the difficulty in measuring the exact peak frequency for the composition $KAlCl_4$, for which the band occurs only as a shoulder on the side of the intense 350-cm^{-1} band (Figure 1).) The formation of $Al_2Cl_7^-$ is promoted by increasing the temperature but at 550° the concentration still amounts to less than 1% of the $AlCl_4^-$ concentration. It is not difficult to account for the enhanced intensity of this band for solutions containing cadmium ions (Figures 1 and 2) if we assume that the formation of a cadmium–chloro complex results in the removal of chloride ions from the solvent. In all the recorded spectra of the pure solvent used for these experiments there was no evidence of the band at 270 cm^{-1} reported previously[6] for molten $NaAlCl_4$.

Experimental Section

Potassium tetrachloroaluminate was prepared by fusing together at 400° equimolar quantities of dried potassium

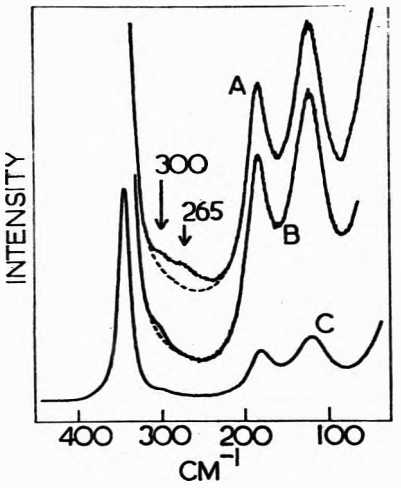

Figure 1. Raman spectra of (A) a solution of 3.6 mol % $CdCl_2$ in molten $KAlCl_4$ at 550°, (B) pure $KAlCl_4$ at 550° with identical instrumental conditions as for spectrum A, (C) solvent spectrum obtained with low instrumental sensitivity.

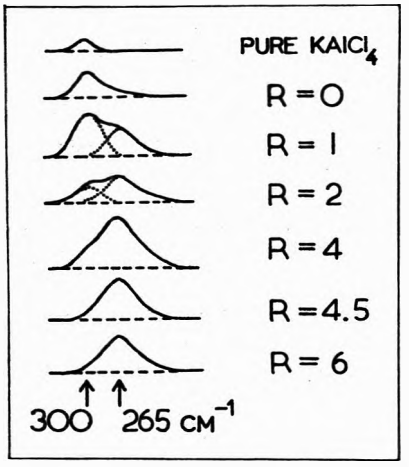

Figure 2. Raman scattering in the frequency region 200–350 cm^{-1} for solutions of Cd^{2+} and Cl^- in $KAlCl_4$ at 550°. Background scattering has been subtracted. R is the ratio of added chloride to cadmium. Spectra correspond to the solutions listed in Table I.

chloride and anhydrous aluminum chloride (Fluka, "iron free"). The product was kept molten for 72 hr in a dry atmosphere (30 ppm of H_2O) and the water-clear melt filtered from carbonaceous deposit, cooled, and stored in a sealed tube. Analysis for chloride was performed by Volhard's method and for aluminum by precipitation of the 9-hydroxyquinoline complex. The ratio of Cl/Al was found to be 4 ± 0.02 over four separate determinations. The same stock sample of potassium tetrachloroaluminate was used for all the experiments. Cadmium tetrachloroaluminate was prepared by controlled fusion in appropriate proportions of cadmium chloride, mercuric chloride, and powdered aluminum in an evacuated ampoule. The strongly exothermic reaction is

$$CdCl_2 + 3HgCl_2 + Al \longrightarrow Cd(AlCl_4)_2 + 3Hg$$

The product was maintained at 400° for 48 hr to give a clear liquid, which was solidified and separated from the metallic mercury. The required solutions were made up by fusion of weighed quantities of $Cd(AlCl_4)_2$, $KAlCl_4$, KCl, and $CdCl_2$. For solutions containing added potassium chloride the total concentration of cadmium plus added chloride was, in each case, 20 mol %. For solutions richer in cadmium it was necessary to use lower total concentrations in order to achieve complete miscibility.

Since the Raman spectrum of the solvent dominates the solution spectra, meaningful intensity measurements on the 264-cm^{-1} band of the cadmium complex required great care. For instance, the background scattering and solvent band shapes were very sensitive to changes in temperature. The Raman spectrometer and high-temperature sample cell have been described previously.[3] Final preparation of samples was carried out under a dry atmosphere (30 ppm of H_2O). There was no observable decomposition or deterioration of any of the samples throughout the experiments. Intensities of the 265-cm^{-1} band were measured by comparing each solution spectrum with a spectrum of the pure solvent obtained using identical instrumental conditions (slit width 2 cm^{-1}). The spectral sensitivity (as measured on the chart paper) was adjusted so that for each solution the shapes and intensities of all the main solvent bands as well as the background scattering between 150 and 400 cm^{-1} were identical (within the limits of the signal-to-noise ratio) with those obtained for the pure solvent spectrum. The solvent spectra (less the 300-cm^{-1} band) were subtracted from the solution spectra and two bands at 265 and 300 cm^{-1} were fitted to the residual intensity profile using a Du Pont curve resolver. Intensities (I_R) were measured relative to the 350-cm^{-1} band of $AlCl_4^-$ (ν_1) and corrected to a common relative intensity scale[2] by multiplication with the mole fraction of $AlCl_4^-$.

Results and Discussion

Relevant spectra transferred to a horizontal baseline are shown in Figure 2 for selection of solutions containing various ratios, R, of added chloride to cadmium ions (exclusive of the chloride ions in $KAlCl_4$). The complete results are summarized in Table I. The bands were resolved on the basis that the individual peak frequencies and band widths at half-height were constant to within 5% over the entire concentration range.

Two changes are observed to occur as R is increased; the 300-cm^{-1} band decreases in intensity and the 265 cm^{-1} increases in intensity in accordance with the formation of a cadmium-chloro complex. A comparison of band intensities on the spectra of Figures 1 and 2 shows that the addition of Cd^{2+} ions alone (in the form of $Cd(AlCl_4)_2$) promotes the formation of $Al_2Cl_7^-$, so that the cadmium complex evidently is highly stable. This competition for chloride ions between Cd^{2+} and $Al_2Cl_7^-$ complicates the analysis of intensity measurements but, as we shall see, provides extra evidence for the final conclusions. The intensity of the 265-cm^{-1} band per mole of cadmium ions is plotted in Figure 3 as a function of R. As expected the plot initially increases with R and finally reaches a limiting value when all the cadmium is taken up in the chloro complex. The sizes of the circles around each point are indicative of the reproducibility of measurement over four separate spectra.

The plot shows striking differences from that obtained using sodium potassium nitrate as solvent.[2] First, the intercept of the average slope for $R < 3$ and the limiting slope occurs at $R = 4$ indicating that the ratio of chloride to cadmium in the complex is four and not three as in the case of sodium potassium nitrate solutions. Second, the intensity is appreciable when $R = 0$ as a result of chloride ions being furnished from equilibrium 1. For the entire

TABLE I: Raman Intensity Data for Solutions of Cd^{2+} and Cl^- in Molten $KAlCl_4$ at 550°[a]

Temp, °C	Ion fraction of Cd(II) × 10^2	R	265-cm^{-1} band (cadmium complex) Frequency, cm^{-1}	Half-width, cm^{-1}	Intensity, arbitrary units	300 cm^{-1} ($Al_2Cl_7^-$) Intensity, arbitrary units
550	2.6	0	266	48	3.5	12.0
550	5.4	1.0	266	48	14.2	21.5
550	3.6	2.0	266	49	12.5	9.0
550	6.4	2.5	266	52	26.0	12.5
550	5.7	3.0	265	52	26.0	8.5
550	5.6	3.5	265	49	27.5	6.0
550	4.6	4.0	265	49	23.0	5.0
550	4.4	4.5	265	44	20.5	0.0
550	3.9	5.0	265	47	21.0	0.0
550	3.4	6.0	265	44	18.0	0.0
Pure solvent 550						5.5

[a] *R* is the ratio of *added* chloride to cadmium.

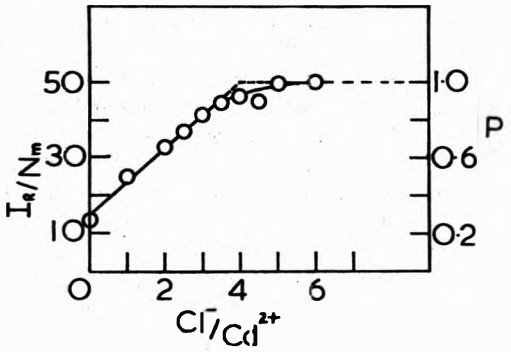

Figure 3. The intensity per mole of cadmium ions (I_R/N) of the 265-cm^{-1} band as a function of the ratio of added chloride to cadmium for the solutions listed in Table I.

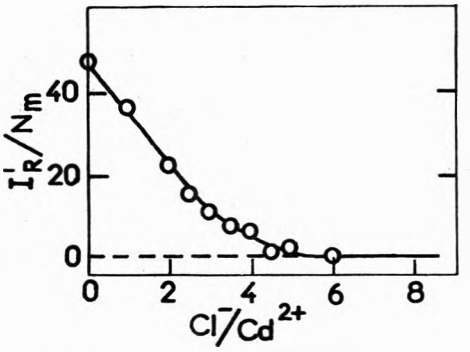

Figure 4. The intensity per mole of cadmium ions (I_R'/N) of the 300-cm^{-1} band as a function of the ratio of added chloride to cadmium for the solutions listed in Table I.

composition range in which the cadmium–chloro complex is incompletely formed, this effect gives rise to a larger concentration of the complex than expected in the absence of equilibrium 1. The effect of such additional equilibria on the reliability of the Yoe and Jones method of determining complex stoichiometry has been fully discussed by other authors.[7] In this particular example the effect should lead to the intersection of initial and limiting slopes being displaced to a slightly *lower* value of *R* than corresponds to the true complex stoichiometry.[7] (In the limiting case of a cadmium complex of infinitely high stability the intersection would be at $R = 0$.) The uncertainty introduced by equilibrium 1 does not therefore affect the conclusion that $CdCl_4^{2-}$ rather than $CdCl_3^-$ (solvated by $AlCl_4^-$) is the predominant complex. From previous work[3] we do not expect the formation of higher complexes than $CdCl_4^{2-}$ in ionic solvents. Another effect of the competing equilibrium may be to obscure fine details of the Yoe and Jones plot which might be indicative of the stepwise formation of lower chloro complexes, as exemplified by bromide coordination with Cd^{2+} in sodium potassium nitrate solvent.[2] However, there was no evidence for the formation of 1:1 or 1:2 cadmium–chloro complexes in the latter solvent, so that in the present case it seems justifiable to write the overall equilibrium

$$Cd^{2+}(solv) + 4Cl^- \rightleftharpoons CdCl_4^{2-} \qquad (2)$$

in which $Cd^{2+}(solv)$ is a solvated cadmium ion, although no bands were found which might characterize the solvation of Cd^{2+} by $AlCl_4^-$ ions.

The above conclusions gain support from an analysis of intensities of the 300-cm^{-1} band of $Al_2Cl_7^-$, a species whose concentration is progressively suppressed as extra chloride is added to the solution. The results are listed in Table I. In Figure 4, the intensities per mole of cadmium ions are plotted as a function of *R*. As might be expected the plot is of opposite form to that in Figure 3, showing a monotonic decrease of intensity until $R \approx 4$. An important feature is that at a value of $R = 4$ the 300-cm^{-1} band intensity (Table I) is closest to that observed for the *pure* solvent, a situation which should arise only when all the cadmium is in the form of the chloro complex and when there is *no excess* of added chloride ions. For values of $R > 4$ the added excess of chloride ions suppresses formation of $Al_2Cl_7^-$ below the level found for the pure solvent.

It is possible to check the internal consistency of the data in Table I and plotted in Figures 3 and 4, by calculating values of the formation quotient Q_2 defined by equilibrium 2. Writing this dissociation quotient of equilibrium 1 as Q_1 and knowing that the chloride concentration is common to both equilibria, then

$$\frac{Q_2(n - [CdCl_4^{2-}])}{[CdCl_4^{2-}]} = \left\{\frac{[Al_2Cl_7^-]}{[AlCl_4^-]^2 Q_1}\right\}^4$$

in which *n* is the total concentration of cadmium. We note that $[CdCl_4^{2-}]/n = P$, the fraction of complexed cadmium, which can be determined from Figure 3. Since the concentration of $Al_2Cl_7^-$ is proportional to the 300-cm^{-1} band intensity, we may write $[Al_2Cl_7^-]/[AlCl_4^-] = I_R'$ (I_R' is the intensity relative to ν_1 of $AlCl_4^-$ and *k* is a proportionality constant). In order to determine *k* it is necessary to have independent quantitative data on equilibrium 1. The dissociation constant (K_1) has been measured[8] over a range of temperatures (*T*) between 275 and 400°. There is an approximately linear relationship be-

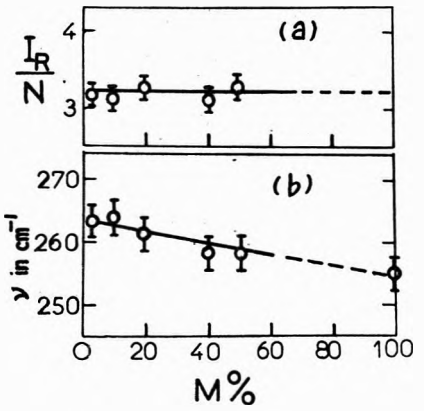

Figure 5. The intensity (a) and peak frequency (b) of the Cd–Cl symmetric stretching band as a function of the concentration of K_4CdCl_6 in molten $KAlCl_4$ at 750°.

tween log K_1 and $1/T$, leading to an estimated value of 0.4×10^{-4} for K_1 at 550° which was the temperature of our experiments. Assuming that $Q_2 = K_2$, a value of 0.44 was obtained for the intensity-concentration proportionality constant k as defined above. Finally, assuming that $[AlCl_4^-] = 1$ for the solutions under study, the calculated values of Q_2 were found to be constant, $4 \pm 3 \times 10^5$ in mole fraction units, for $0 < R < 4$. As expected this value is considerably larger than the stability quotient of $CdCl_3^-$ in sodium potassium nitrate[2] ($4 \pm 2 \times 10^4$).

It was of interest to measure the intensity of the 265-cm^{-1} band of $CdCl_4^{2-}$ as a function of concentration for solutions of K_4CdCl_6 in potassium tetrachloroaluminate. From spectra of cadmium chloride dissolved in pure alkali metal halides it was concluded[3] that the symmetric stretching frequencies of $CdCl_3^-$ and $CdCl_4^{2-}$ were quite similar. Meaningful intensity measurements also were difficult to perform for these solutions so that it was not possible to show conclusively if $CdCl_4^{2-}$ or $CdCl_3^-$ predominated in pure alkali metal chloride melts. The intensities of the 265-cm^{-1} band per mole of cadmium for various solutions of K_4CdCl_6 in potassium tetrachloroaluminate are shown in Figure 5. For all these solutions, as well as for pure K_4CdCl_6 we expect the cadmium-chloro complex to be completely formed. Assuming that the molar *intensities* for the symmetric stretching modes of different cadmium-chloro complexes do differ appreciably then the invariance of the observed intensities over the concentration range 3.4–50 mol % indicates that there is no change in the complex stoichiometry and suggests that the most stable complex in pure K_4CdCl_6 probably is $CdCl_4^{2-}$, in agreement with previous conclusions.[3] The band peak frequency is plotted also in Figure 5 and is seen to extrapolate linearly to the value[3] for the pure melt. The band half-width increases only slightly over the entire composition range (44–48 cm^{-1}). This is consistent with previous findings that the symmetric stretching frequency is as much a function of the general ionic environment as of the complex stoichiometry (Figure 5, ref 3).

Conclusions

Raman intensity measurements suggest that the major cadmium-chloro complex formed in molten potassium tetrachloroaluminate at 550° is $CdCl_4^{2-}$. The results can be compared with the conclusions of a similar study[2] using sodium potassium nitrate as solvent at 320 and 420°, in which it was found that the predominant complex had a Cl/Cd ratio of 3. The measurements do not exclude, however, the formation of minor quantities of other chloro complexes.

The different results can be explained on the assumption of different basicities of the two solvents toward Cd^{2+} in the nitrate solvent, $CdCl_3^-$ probably is four coordinate with NO_3^- acting as the fourth ligand. This interaction is evidently sufficiently strong to inhibit substitution by a fourth chloride ion but weak compared with the interaction[9] of NO_3^- with free Cd^{2+}. Bromide evidently is a much stronger ligand toward cadmium since the complex $CdBr_4^{2-}$ is readily formed in the nitrate solvent. Potassium tetrachloroaluminate is much less basic, allowing complete coordination of Cd^{2+} even by chloride ions.

The ability of solvents to dictate the stoichiometry of cadmium-halo complexes has also been studied for CdI_2–AI (A = alkali metal) systems dissolved in various organic solvents.[10] Stabilization of CdI_3^- was correlated with the ability of the solvent molecules to coordinate with Cd^{2+}. The four-coordinate complex was formed in solvents less able to neutralize the charge on Cd^{2+}.

Acknowledgments. The authors express thanks to the U. K. Central Electricity Generating Board for financial support.

References and Notes

(1) Present address, Chemistry Department, University of Manchester Institute of Science and Technology, Manchester M60 1QD, England.
(2) J. H. R. Clarke, P. J. Hartley, and Y. Kuroda, *Inorg. Chem.*, **11**, 29 (1972).
(3) J. H. R. Clarke, P. J. Hartley, and Y. Kuroda, *J. Phys. Chem.*, **76**, 1831 (1972).
(4) J. H. R. Clarke and G. J. Hills, *Chem. Brit.*, 9, 12 (1973).
(5) G. Torsi, G. Mamantov, and G. H. Begun, *Inorg. Nucl. Chem. Lett.*, **66**, 553 (1970).
(6) H. A. Oye, E. Rytter, P. Klaeboe, and S. J. Cyvin, *Acta Chem. Scand.*, **25**, 559 (1971).
(7) L. I. Katsin and E. Gebert, *J. Amer. Chem. Soc.*, **72**, 5455 (1950).
(8) G. Torsi and G. Mamantov, *Inorg. Chem.*, **11**, 1439 (1972).
(9) P. J. Hartley, Ph.D. Thesis, Southampton, 1973.
(10) E. Ya. Gorenbein, V. M. Shevchenko, and A. K. Trofunichuk, *Russ. J. Phys. Chem.*, **45**, 1743 (1971).

Thermochemistry of Carbonyl Addition Reactions. II. Enthalpy of Addition of Dimethylamine to Formaldehyde[1]

F. E. Rogers* and R. J. Rapiejko

Department of Chemistry, University of Dayton, Dayton, Ohio 45469 *(Received January 5, 1973; Revised Manuscript Received September 22, 1973)*

Dimethylamine and formaldehyde react under varying conditions to give dimethylaminomethanol and bis(dimethylamino)methane. The enthalpies of reaction for this system have been determined by solution calorimetry. Corrections for the enthalpies of solution and vaporization gave the enthalpies for the gas-phase reactions at 25°. Implications of these results are discussed.

Introduction

Amines are known to react readily with formaldehyde to form carbinolamines (1), bisaminomethanes (2), and heterocyclic compounds (3) among other products.[2,3] The

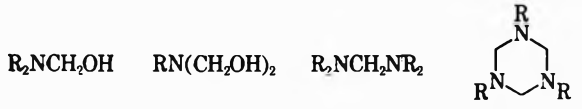

1 1 2 3

nature of the product depends on the type of amine used, the pH, the reaction stoichiometry, and equilibrium constant. While compounds 1, 2, and 3 are reported to play an important role in the Mannich Reaction[4] and formol titrations of amino acids and proteins[5] there are few thermochemical data for these addition reactions. Le Henaff and Feraud[6] derived enthalpy data from the temperature dependence of the equilibrium constants for the reaction of formaldehyde and several amino acids. We wish to report the enthalpy of addition of dimethylamine (A) to aqueous formaldehyde (F) to give the following products: $(CH_3)_2NCH_2OH$ (AF), $(CH_3)_2NCH_2N(CH_3)_2$ (A_2F). In addition, the enthalpy of formolysis of A_2F to form AF in aqueous formaldehyde was also determined. Corrections for the enthalpies of solution and vaporization gave the enthalpies of reaction in the solution and gas phase. These enthalpy data, the reported equilibrium constants,[7,8] and entropy estimates based on the method of Benson[9] permitted a detailed thermodynamic description of the dimethylamine–formaldehyde system. Finally, an equation is presented which relates the thermodynamic parameters for a gas-phase reaction with those in solution.

Experimental Results

Materials. Paraformaldehyde and an ethereal solution of excess dimethylamine react readily to form bis(dimethylamino)methane, bp 84.2°,[10] nmr spectra (neat), δ 1.60, s, CH_2–$(N)_2$; δ 1.14, s, CH_3–N. This compound was purified by preparative glpc immediately before using. Formaldehyde (36–38%, Matheson Coleman and Bell, ACS Reagent) was analyzed by the sodium sulfite method (ref 3, p 486). The carbinolamine, 2-(dimethylamino)ethanol, is commercially available and was purified by preparative glpc immediately before using. Anhydrous dimethylamine (Matheson; 99.0% minimum purity) was used directly; the concentration of its aqueous solutions was determined by titration with HCl using a Methyl Red indicator.

Calorimetric Procedures. The differential isoperibol calorimeter employed in this study has been described in detail elsewhere.[11] The reactions were carried out by injecting 50–100 μl of one component into an excess of the other at 25 ± 0.5°. The relative amounts were chosen in accordance with the reported equilibrium studies for dimethylamine–formaldehyde:[7,8] $(AF)/(A)(F) = 1150$, $(A_2F)/(AF)(A) \doteq 100$, and $(A_2F)/(A)^2(F) \doteq 1.2 \times 10^5$.

For the three series of experiments, molar ratios of A/F = 300, F/A = 600, and F/A_2F = 670 assured greater than 99.5% conversion to A_2F, AF, and AF, respectively. To measure the heat of reaction leading to bis(dimethylamino)methane (A_2F), 50 μl of 37% formaldehyde were added to 200 ml of 1.1 *M* dimethylamine. Just prior to the run, analysis of 200-μl aliquots of 37% formaldehyde by the sodium sulfite method gave the concentration as 0.6758 ± 0.0015 mmol of H_2CO/50 μl of solution. The heats of solution of the amine components of the reaction, A and A_2F, were also determined in 1.1 *M* dimethylamine. A gas-tight syringe whose barrel was lightly lubricated with mineral oil was used to transfer 20-cc samples of gaseous dimethylamine to the calorimeter. Similar samples injected into distilled water were titrated with HCl using a Methyl Red indicator. The heat of dilution of A_2F was measured by injecting 50-μl (0.03800 ± 0.00020 g) samples into 1.1 *M* dimethylamine (200 ml). Finally, we assumed that the heat of dilution of 37% formaldehyde in water is the same as in 1.1 *M* dimethylamine. To determine the heat of dilution of 37% formaldehyde to more concentrated ranges a variation of the usual technique was employed. Into a 5-ml plastic syringe 0.2 ml of 37% formaldehyde was injected. A fine needle was attached and with the syringe held vertically, all the air was forced out except for a column in the needle. This column of air prevented premature mixing when the syringe was equilibrated in the calorimeter. To make a measurement, the plunger is quickly withdrawn to a predetermined mark and solvent is drawn up into the barrel. The final liquid level in the syringe should be well below the solvent level in the calorimeter to minimize heat leak. Thermal equilibrium is quickly reestablished before diffusion through the fine needle becomes a problem. (If the final volume is known with some certainty the solution may be subsequently ejected into the calorimeter solvent for a high dilution heat estimate.) These heat of dilution values of aqueous formaldehyde were used to adjust the reported molar heat of hydration of gaseous formaldehyde to the concentration levels required in this study.

The heat of reaction leading to dimethylaminomethanol (AF) was measured by injecting 90 μl of 4.02 *M* dimethylamine into 200 ml of 3.7% formaldehyde previously adjusted to pH 8.2 with *ca.* 180 μl of 4.02 *M* dimethylamine. During three subsequent experimental runs the pH increased by about 0.5 unit to 8.7. The heat of dilution of 4.02 *M* dimethylamine in water was considered the same as in 3.7% formaldehyde. The dilution measurements were made with the method devised for formaldehyde. Dimethylaminomethanol is unstable. Therefore heats of solution were determined on its homolog, dimethylaminoethanol. There is no clear cut linear relationship between heat of solution and chain length in a homologous series of amines or alcohols.[12,13] However, the data on four carbon secondary amines[12] and alcohols[13] show that the addition of a CH_2 group changes the heat of solution by −0.10 and +0.22 kcal/mol, respectively. Since aminoalcohols are bifunctional, the experimental heat of solution of dimethylaminoethanol should closely approximate that value for dimethylaminomethanol. It is assumed that the heats of solution of formaldehyde in water and in dilute formaldehyde (3.7%) are nearly equal.

The heat of formolysis of the bisaminomethane (A_2F) to the carbinolamine (AF) was measured by the successive additions of 50 μl (0.03800 ± 0.00020 g) of A_2F to 200 ml of 3.7% aqueous formaldehyde previously neutralized to pH 8.3 with the reactant. Neutralization usually required no more than 40–60 μl of amine. Three successive experimental runs increased the pH from 8.3 to about 8.9. An nmr study showed that the resonance of the CH_2-$(N)_2$ protons (δ 1.60) disappeared as expected upon the addition of excess formaldehyde.

To correct these reactions to the gas phase, enthalpies of vaporization were required. The value for the bisaminomethane was determined directly, while that for the unstable dimethylaminomethanol was inferred by analogy with amines and alcohols. The heats of vaporization were determined as follows. A test tube (1.2 × 7 cm) fitted with a 14/20 male joint was secured in the calorimeter cap so that the bottom of the tube was 2–3 cm below the liquid level inside and the joint just extended above the Teflon cap. The tube was carefully connected to a vacuum system by the female joint. Evacuation of the tube was endothermic by 0.148 ± 0.007 cal and the experimental quantities were corrected by this amount. To make a measurement 30–100 μl of the compound at 25 ± 1° was injected into the tube taking care not to touch the tube with the syringe needle. The cap was set in place and the tube evacuated. Vaporization began immediately and was generally complete within 2 min. Presumably, most of the small sample disappeared when the total pressure reached the saturation vapor pressure of the liquid at 25°. Morawetz[14,15] and Sunner[14] found that the experimental heats of vaporization ($\Delta H_v'$) determined at reduced pressure are low by 0.0–0.6 kcal/mol depending on the compound and the system geometry. The maximum deviation (0.6 kcal/mol) occurs when no pressure-volume work is done and $\Delta H_v' = \Delta E_v$. Since direct comparison with our method is not possible, we have calibrated the apparatus with benzene and *o*-xylene. The experimental and literature values of $\Delta H_v°$ (25°) are benzene, 8.03 (8.09)[16] kcal/mol and *o*-xylene, 10.24 (10.38)[16] kcal/mol. For A_2F, the experimental heat of vaporization was 7.9 kcal/mol. The analogous hydrocarbon, 2,4-dimethylpentane, has a similar bp, 80.5°, and $\Delta H_v°$, 7.86 kcal/mol,[16] suggesting that the replacement of a tertiary carbon by a tertiary nitrogen causes no large change in boiling point and $\Delta H_v°$. Similarly, the boiling point and $\Delta H_v°$ of triethylamine and triethylmethane are 89.5°, 8.46 kcal/mol[16] and 93.5°, 8.42 kcal/mol,[16] respectively. The carbinolamine, AF, is not stable but the above observations suggested isobutyl alcohol ($\Delta H_v°$ = 12.15 kcal/mol) as a model for AF. Therefore, we assign $\Delta H_v°$(AF) = 12.0 kcal/mol. The data are collected in Tables I and II.

Discussion

Depending on reaction stoichiometry, the dimethylamine–formaldehyde system gave the carbinolamine (AF) or bisaminomethane (A_2F); a large excess of formaldehyde gave the former and an excess of amine the latter. In the presence of a large excess of formaldehyde, the bisaminomethane is hydrolyzed to the carbinolamine, AF. Therefore, control of relative concentrations and mode of addition allowed the determination of the heats for the following aqueous reactions.

$$(CH_3)_2NH + CH_2O \rightleftharpoons (CH_3)_2NCH_2OH \qquad \Delta H_r°(aq) = -8.44 \text{ kcal/mol} \quad (1)$$

$$2(CH_3)_2NH + CH_2O \rightleftharpoons (CH_3)_2NCH_2N(CH_3)_2 + H_2O \qquad \Delta H_r°(aq) = -13.5 \text{ kcal/mol} \quad (2)$$

$$(CH_3)_2NCH_2N(CH_3)_2 + CH_2(OH)_2 \rightleftharpoons 2(CH_3)_2NCH_2OH \qquad \Delta H_r°(aq) = -2.0 \text{ kcal/mol} \quad (3)$$

Subtracting reaction 1 from 2 gave the heat of reaction starting with the carbinolamine.

$$(CH_3)_2NH + (CH_3)_2NCH_2OH \rightleftharpoons (CH_3)_2NCH_2N(CH_3)_2 + HOH \qquad \Delta H_r° = -5.07 \text{ kcal/mol} \quad (4)$$

Reactions 1 and 2 are transferred to the gas state by correcting for the enthalpies of solution and vaporization of the amine components (A, AF, and A_2F) and formaldehyde. The gas-phase enthalpy for reaction 4 is again determined by difference. The instability of methanediol made it impossible to transfer reaction 3 to the gas phase and small errors in any approximations would have a disproportionately large effect on the small heat for the aqueous reaction. The resulting enthalpies for the gas-phase reaction appear in Table II.

The data clearly show that the addition of the first equivalent of amine to formaldehyde in any phase is much more exothermic than the addition of the second equivalent. Since two different reaction types are involved it is not unexpected that the enthalpies differ. The first mole of amine adds to a carbonyl group and the second involves substitution of an amine for a hydroxyl group. The partial (to AF and A) or complete (to 2A and F) hydrolysis of bis(dimethylamino)methane (A_2F) is an endothermic reaction with not quite equal amounts of enthalpy required for each step. On the other hand, the formolysis of A_2F is exothermic by 2 kcal/mol. We may use these data to reexamine some previous calorimetric work on the secondary amine–formaldehyde system. Fernandez and Butler[17] found that the temperature rise on the addition of 1 mol of formaldehyde to 2 mol of morpholine in water was much larger than that observed on the addition of a second mole of formaldehyde. If the first mole of formaldehyde gave rise to the carbinolamine 4 then the addition of a second mole of formaldehyde would cause an equivalent temperature rise. On the other hand, if the first mole of formaldehyde formed the methylenebis(morpholine) 5, the second mole of formaldehyde would cause little or no tem-

TABLE I: Enthalpies of Dilution, Solution, and Vaporization (25°, kcal/mol)

Process (solvent)[a]	ΔH_s	ΔH_{diln}	$\Delta H_v°$	$\Delta H_h°$[d]
	Formaldehyde (F)			−15.09 ± 0.03
F(g) → 2.7% F (W)	−14.8[b]			
37% F → 3.7% F (W)		−0.39 ± 0.02		
37% F → 0.02% F (W)		0.68 ± 0.01		
	Dimethylamine (A)			−12.82 ± 0.02
A(g) → 4.3% A (W)	−12.47[b]			
A(g) → 0.25% A (W)	−12.77[b]			
A(g) → 0.02% A (5% A)	−12.82 ± 0.02			
16% A(aq) → 0.08% A (W)		−0.86 ± 0.02		
16% A(aq) → 0.08% A (0.45% A)		−0.89 ± 0.01		
	Bis(dimethylamino)methane (A_2F)		7.9 ± 0.1	−16.51 ± 0.18
A_2F(l) → 0.02% A_2F(5% A)	−8.63 ± 0.10			
	Dimethylaminomethanol (AF)[c]		12.0	−18.15 ± 0.28
AF(l) → 0.02% AF (W)	−6.15 ± 0.04			

[a] (W) = distilled deionized water. [b] D. D. Wagman, W. H. Evans, V. B. Parker, W. M. Bailey, and R. H. Schumm, *Nat. Bur. Stand., Techn. Note*, No. 570-3 (1968). [c] Dimethylaminoethanol used as a model. See text. [d] The energy liberated when one mole of the gas forms a very dilute aqueous solution. *i.e.*, $\Delta H_h = \Delta H_s - \Delta H_v$.

TABLE II: Enthalpies of Reaction (25°, kcal/mol)

Reaction	ΔH_r (exptl)[c]	$\Delta H_r°$ (soln)	$\Delta H_r°$[b]	$\Delta H_r°$(g)
A[a] + F ⇌ AF + W	−9.33 ± 0.03	−8.44 ± 0.06	−30.2 ± 0.2	−18.2 ± 0.4
2A + F[a] ⇌ A_2F + 2W	−14.19 ± 0.02	−13.51 ± 0.03	−45.6 ± 0.2	−27.2 ± 0.3
A_2F[a] + F ⇌ 2AF	−10.61 ± 0.02	−2.0 ± 0.1		
AF + A ⇌ A_2F + W		−5.07 ± 0.1		

[a] Reaction initiated by adding this component to excess of the other. [b] Heat of reaction for components in their standard states. Gas phase chosen as standard state of formaldehyde. [c] Refer to the text for experimental conditions.

perature change. The relative magnitudes of the temperature rises led to the conclusion that the preponderant product in these solutions is the methylenebis(morpholine) **5**.

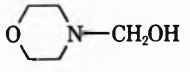

4

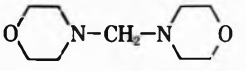

5

If this system bears an energetic similarity to the dimethylamine–formaldehyde reaction then the first mole of formaldehyde could give complete conversion to the bisaminomethane (**5**) with the liberation of −13.5 kcal/mol and the second mole of formaldehyde could cause complete formolysis to the carbinolamine (**4**) and only liberate 2 kcal (reaction 3). In solution, the actual situation is apparently not so extreme, as Kallen and Jencks[7] have reported that the first mole of formaldehyde gives 75% **5** and the second mole of formaldehyde 72% **4**.

The components of these reactions are unusual in that they have nitrogen and/or oxygen atoms bound to the same carbon atom. Radom, Hehre, and Pople[18] have reported that such arrangements in saturated molecules result in an appreciable stabilizing interaction between the nonbonded atoms. This interaction was termed the bond separation energy and would be zero if a bond additivity hypothesis were truly valid. The disproportionation reaction 3 is a particularly interesting example involving all possible binary combinations of the nitrogen–oxygen interaction; *i.e.*, oxygen–oxygen (O-C-O) and nitrogen–nitrogen (N-C-N) interactions are transformed to two nitrogen–oxygen interactions (N-C-O). We may calculate the enthalpy for reaction 3 from the appropriate bond separation energies[18] on the assumption that the driving force is the reorganization of the pairwise interactions. The predicted enthalpy, −2.5 kcal/mol, is in good agreement with the experimental value, −2.0 kcal/mol. The relative order of decreasing energy for these binary interactions is then O-C-O > O-C-N ≫ N-C-N.

The inadequacy of bond energy schemes for predicting the heat of formation of compounds has led to many alternate methods. In the group increment approach, the contribution of interactions between nonbonded atoms is included in the assigned group value. Thus, the contribution of an $X-CH_2-Y$ group to the heat of formation depends on the nature and interaction of X and Y. The group increment value where both X and Y are oxygen is known and our work permits the calculation of the corresponding values where one or both oxygens are replaced by nitrogen. The gas-phase enthalpies of reaction may be expressed in terms of group increment contributions to the heat of formation.[19] Substitution of the heats of formation of water and formaldehyde[16] and cancelling those group increments common to both sides gives the following equations.

$$(CH_3)_2NH\ (g) + CH_2O\ (g) \rightleftharpoons (CH_3)_2NCH_2OH\ (g) \quad (1)$$
$$\Delta H_r°(g) = -3.20 + [C-(H)_2N,O]$$

$$2(CH_3)_2NH\ (g) + CH_2O\ (g) \rightleftharpoons (CH_3)_2NCH_2N(CH_3)_2\ (g) + H_2O\ (g) \quad (2)$$
$$\Delta H_r°(g) = -14.45 + [C-(H)_2(N)_2]$$

From the respective values of $\Delta H_r°(g)$ (Table II), we calculated $[C-(H)_2N,O] = -14.98$ and $[C-(H)_2(N)_2] = -12.75$ kcal/mol. These group increments are smaller by

Scheme I

	$\Delta H_r°$[a]	$\Delta S_r°$[a]	$\Delta G_r°$[a]
Reaction 1			
A (g) + F (g) $\rightleftharpoons$ AF (g)	−18.2	−37.0	−7.1
hydration ↓	9.75	30.6	0.6
A (aq) + F (aq) $\rightleftharpoons$ AF (aq) + W	−8.44	−6.4	−6.5
Reaction 2			
AF (g) + A (g) $\rightleftharpoons$ A_2F (g) + W (g)	−9.02	−7.1	−7.1
hydration ↓	3.95	(7.1)[b]	(2.0)[b]
AF (aq) + A (aq) $\rightleftharpoons$ A_2F (aq) + W	−5.07	($\geq$0)[b]	($\leq$−5.1)[b]

[a] In kcal/mol except for $\Delta S_r°$ in cal/deg mol. [b] These estimates are based on an approximate equilibrium constant (ref 8).

0.45 and 2.7 kcal/mol respectively than the value for a methylene between two oxygens, [C-(H)$_2$,(O)$_2$], −15.43 kcal/mol, which reflects the decreased nonbonded interaction energy when either or both of the oxygens are replaced by nitrogen.

To complete the thermodynamic definition of these reactions it was desirable to compute the free-energy and entropy changes for the gas and solution reactions. The free-energy and entropy changes for reactions 1 and 4 were computed from the available equilibrium constants[7,8] which are better established for the former reaction. The entropies of the gas-phase reactants, A and F, are known and values for the products AF and A_2F were estimated after the method of Benson.[9] The free-energy, entropy, and enthalpy of hydration were calculated as the value for the solution reaction less the gas reaction value, *i.e.*, $\Delta H_r°_h(25°) = \Delta H_r°(aq) - \Delta H_r°(g)$, etc. These values are attached to the reactions shown in Scheme I. In the gas phase, the free-energy change is the same for the addition of the first (reaction 1) and second (reaction 4) mole of amine to formaldehyde, even though the enthalpies and entropies differ widely. Reaction 1, unlike reaction 4, proceeds with a decrease in the number of molecules and hence the loss of translational entropy. This unfavorable entropy change offsets the rather large enthalpy change in reaction 1. In aqueous solution, the free-energy difference between reaction 1 and 4 is about 1.4 kcal.

In both reactions, the enthalpy change is more favorable and the entropy change less favorable in the gas phase. This difference, as expressed in energies of hydration, is smaller in reaction 4. The enthalpies of hydration of the reactants are more endothermic than the products (Table I) and this fact explains the positive enthalpies of hydration $\Delta H_r°_h$, in both reactions. The relatively larger values of $\Delta H_r°_h$ and $\Delta S_r°_h$ in reaction 1 are attributable, in part, to the behavior of formaldehyde. In water, formaldehyde is completely hydrated to methanediol and the energy required to convert this species to the "free" formaldehyde necessary for reaction with amines[20] (reactions 1 and 2) makes the heat of reaction in solution less than in the gas phase.

$$CH_2O\ (g) \overset{+H_2O}{\rightleftharpoons} CH_2(OH)_2\ (aq) \overset{-H_2O}{\rightleftharpoons} CH_2O\ (aq) \overset{(CH_3)NH}{\rightleftharpoons} AF\ (aq)$$

Also, the significant entropy decrease accompanying the conversion of gaseous formaldehyde to methanediol partly explains the relative magnitude of $\Delta S_r°_h$ in reaction 1. In reaction 4, a change in functionality from carbonyl to glycol upon hydration is not involved so that $\Delta H_r°_h$ and $\Delta S_r°_h$ are smaller.

Empirical methods for the estimation of the thermodynamic parameters[21] for gas-phase reactions have become quite sophisticated but no adequate methods exist for dealing with reactions in solution where much of the research is done. The above schemes show that the difference between the gas and solution reactions is given by the enthalpy and entropy of solvation. It has been shown that for many classes of solutes and solvents a linear relationship exists between the enthalpy and entropy of solvation.[12,22] For alcohols, amines, and certain other solutes such as acetone, hydration enthalpies and entropies correlate well with the line given by[23]

$$\Delta S_h°\ (\text{cal/deg mol}) = 3.65 \times 10^{-3}\,\Delta H_h°\ (\text{cal/mol}) + 5.90 \quad (I)$$

For gas-phase reactions between species covered by this line the entropy of hydration for the reaction is

$$\Delta S_r°_h = 3.65 \times 10^{-3}\,\Delta H_r°_h + \Delta n\,5.90$$

where $\Delta H_r°_h = \Sigma\Delta H_h°(\text{products}) - \Sigma\Delta H_h°(\text{reactants})$ and Δn is the change in the number of moles in the reaction, *i.e.*, reaction 1 $n = -1$, reaction 4 $n = 0$. The solution of this equation for reactions 1 and 4 gives $\Delta S_r°_h$ (1) = 29.7 and (4) = 14.4 eu. Combining these values with the entropy change for the gas-phase reactions gives the values for the aqueous reaction $\Delta S_r°(aq)$ (1) = −7.3[−6.4] and (4) = +7.3[0] where bracketed numbers are those derived from the reported equilibrium constants[7,8] and our enthalpy data. The agreement is good and the method in the present stage of refinement provides an approach to a quantitative estimation of thermodynamic parameters for certain solution reactions when sufficient enthalpy of solvation data are available.

The method may be applied to the simple hydration reactions of carbonyl compounds to gain an insight into entropy changes from enthalpy data alone. Acetaldehyde provides such an example. The solvation of gaseous acetaldehyde is given by the following equation.

$$CH_3CHO\ (g) \overset{a}{\rightleftharpoons} \underset{\mathbf{6}}{CH_3CHO\ (aq)} \overset{b}{\rightleftharpoons} \underset{\mathbf{7}}{CH_3CH(OH)_2}$$

The first step is the dissolution of the gas followed by partial conversion of the solvated species (**6**) to the hydrated form (**7**). From literature data[24] and eq I, we calculate $\Delta S°$ (step a) = −22.78 and $\Delta S°$ (step a + b) = −32.89 cal/deg mol. The difference, −10.11 cal/deg mol, is the entropy change accompanying partial conversion to the

hydrated species (7). At equilibrium acetaldehyde is 51% hydrated so that on a mole basis the entropy change for step b is −19.8 compared to the experimental value of −18.7 cal/deg mol.[25] The agreement is quite good and lends further encouragement to the overall approach.

References and Notes

(1) Part I. F. E. Rogers and R. J. Rapie ko, *J. Amer. Chem. Soc.*, **93**, 4596 (1971).
(2) A. P. Terentev, E. G. Rukhadze, and S. F. Zaposkalova in "Problemy Organicheskogo Sinteza," S. N. Danilov, Ed., Academy of Science of the USSR, Moscow, 1965, pp 120–124.
(3) J. F. Walker, "Formaldehyde," ACS Monograph No. 159, 3d ed, Reinhold, New York, N. Y., 1964, pp 359–373.
(4) E. C. Wagner, *J. Org. Chem.*, **19**, 1862 (1954); H. Heilman and G. Optiz, "α-Aminoalkylierung," Verlag Chemie, Weinheim, Germany, 1966; G. Reichert, "Die Mannich-Reaction," Springer-Verlag, Berlin, 1959.
(5) D. French and J. T. Edsall, *Advan. Protein Chem.*, **2**, 277 (1945).
(6) P. F. Feraud and P. Le Henaff, *Bull. Soc. Chim. Fr.*, **5**, 1968 (1966).
(7) R. G. Kallen and W. P. Jencks, *J. Biol. Chem.*, **241**, 5864 (1966).
(8) P. Le Henaff, *Bull. Soc. Chim. Fr.*, **11**, 3113 (1965).
(9) S. W. Benson, "Thermochemical Kinetics," Wiley, New York, N. Y., 1968.
(10) J. E. Fernandez and R. Sutor, *J. Org. Chem.*, **32**, 477 (1967).
(11) F. E. Rogers, *J. Phys. Chem.*, **75**, 1734 (1971).
(12) F. Franks and B. Watson, *Trans. Faraday Soc.*, **65**, 2339 (1969).
(13) R. Aveyard and R. W. Mitchell, *Trans. Faraday Soc.*, **64**, 1756 (1968).
(14) E. Morawetz and S. Sunner, *Acta Chem. Scand.*, **17**, 473 (1963).
(15) E. Morawetz, *Acta Chem. Scand.*, **22**, 1509 (1968).
(16) J. D. Cox and G. Pilcher, "Thermochemistry of Organic and Organometallic Compounds," Academic Press, New York, N. Y., 1970.
(17) J. E. Fernandez and G. B. Butler, *J. Org. Chem.*, **28**, 3258 (1963).
(18) L. Radom, W. J. Hehre, and J. A. Pople, *J. Amer. Chem. Soc.*, **93**, 289 (1971).
(19) Reference 16, p 590.
(20) P. LeHenaff, *C. R. Acad. Sci. U. S.*, **256**, 1752 (1963).
(21) G. Janz, "Thermodynamic Properties of Organic Compounds," Revised Edition, Academic Press, New York, N. Y., 1967.
(22) I. M. Barclay and J. A. V. Butler, *Trans. Faraday Soc.*, **34**, 1445 (1938).
(23) The equation is applicable only to "infinitely" dilute solutions (<0.08 *M*).
(24) See footnote *b*, Table I.
(25) J. L. Kurtz, *J. Amer. Chem. Soc.*, **89**, 3524 (1967).

Gaseous Phosphorus Compounds. X. Mass Spectrometric Determination of the Dissociation Energies of Arsenic and Bismuth Monophosphides

K. A. Gingerich,* D. L. Cocke, and J. Kordis

Department of Chemistry, Texas A & M University, College Station, Texas 77843

(*Received August 6, 1973*)

The gaseous equilibria AsP = As + P, AsP = As + 0.5P_2, and Bi_2 + P_2 = 2BiP have been investigated by Knudsen cell mass spectrometry. The respective third-law reaction enthalpies, $\Delta H°_{298}$, were measured as 432.2 ± 2.5, 190.8 ± 1.7, and 125.5 ± 2.1 kJ, where the error terms are standard deviations. These reaction enthalpies have been combined with the appropriate literature data, to obtain the dissociation energies, $D°_0$, and standard heats of formation, $\Delta H_f°_{298}$ of the molecules AsP and BiP: for AsP $D°_0$ = 429.7 ± 12.6 kJ mol^{-1} and $\Delta H_f°_{298}$ = 187.0 ± 12.6 kJ mol^{-1}; for BiP $D°_0$ = 278 ± 13 $\Delta H_f°_{298}$ = 262 ± 13. The trends in the dissociation energies of the diatomic group V phosphides have been discussed in relation to other diatomic intergroup V molecules.

Introduction

All the diatomic intergroup V molecules with phosphorus have been observed by optical spectroscopy, except BiP.[1-5] Determinations of the dissociation energies of PN[6-8] and SbP[9,10] have been reported. Mass spectrometric observations of gaseous arsenic phosphides have been reported by Gutbier and by Carlson, *et al.*, but no thermodynamic evaluation of these molecules was presented.[11] The ion AsP^+ observed by Gutbier was attributed partially to fragmentation from such molecules as AsP_3, As_2P_2, and As_3P. The extent of this fragmentation could not be quantitatively determined.

In the present work, AsP^+ and BiP^+ were observed under experimental conditions which favored their production as parent-molecule ions. Consequently, the dissociation energies of the molecules AsP and BiP are reported here.

Experimental Section

The design features of the high-temperature mass spectrometer as well as the experimental procedures used have been described previously.[12,13]

The AsP and BiP molecules were each observed in separate investigations that had other principle objectives. In one set of experiments, the ions As^+, AsP^+, P^+, and P_2^+ were observed in the effusing vapor from a graphite-lined tantalum Knudsen cell which contained a 1:1.5 molar ratio mixture of rhodium powder and TiP powder. The measurements reported here correspond to the same series of experiments as the investigation of the carbon-phosphorus molecules. Experimental details can be found in the report of the latter investigation,[14] since As and AsP were observed over the mentioned condensed system, simultaneously with the C–P species, and during the earlier stages of the investigation. The observation of the ions

TABLE I: Ion Currents, A, for P_2^+, P^+, As^+, and AsP^+[a]

T, K	$I(P_2^+)$	$I(P^+)$	$I(As^+)$	$I(AsP^+)$
1936	2.31×10^{-8}	1.90×10^{-9}	9.8×10^{-12}	8.4×10^{-13}
1967	2.41×10^{-8}	2.41×10^{-9}	2.50×10^{-12}	2.10×10^{-12}
2040	5.32×10^{-8}	7.47×10^{-9}	4.15×10^{-12}	3.08×10^{-12}
2140	7.33×10^{-8}	1.38×10^{-8}	4.45×10^{-12}	2.66×10^{-12}
2086	4.11×10^{-8}	7.16×10^{-9}	1.50×10^{-12}	9.4×10^{-13}

[a] The values given for P^+ and P_2^+ have been corrected for fragmentation. $P_i = 0.14 I_i T_i \sigma_{Ag} \gamma_{Ag} E_i/(\sigma_i \gamma_i)$ in atmospheres.

TABLE II: Ion Currents, A, for Bi_2^+, P_2^+, and BiP^+

T, K	$I(Bi_2^+)$	$I(P_2^+)$	$I(BiP^+)$
811.3	7.98×10^{-10}	1.03×10^{-10}	7.7×10^{-14}
826.4	1.05×10^{-9}	8.07×10^{-11}	6.5×10^{-14}
839.9	1.60×10^{-9}	8.16×10^{-11}	1.1×10^{-13}
854.5	2.43×10^{-9}	4.49×10^{-11}	1.4×10^{-13}

TABLE III: Free-Energy Functions

Species	$-(G°_T - H°_{298})/T$, J mol^{-1} K^{-1}				
	T 1800	2000	2200	800	900
P[a]	183.13	184.97	186.68		
P_2[a]	251.78	255.02	258.01		
As[b]	194.14	196.02	197.74		
AsP[c]	269.41	272.67	275.64		
Bi_2[c]				285.77	288.49
BiP[d]				265.06	267.86

[a] Reference 19. [b] Reference 20. [c] Rigid-rotator, harmonic-oscillator approximation based on available molecular parameters.[4,21,22] [d] Rigid-rotator, harmonic-oscillator approximation based on estimated molecular parameters: force constant = 2.30 mdyn Å^{-1};[1-5] internuclear distance = 2.32 Å;[22] vibrational frequency = 380 cm^{-1}; ground state, $^1\Sigma$.

As$^+$ and AsP$^+$ was apparently due to an arsenic impurity in the condensed sample, presumably TiP.

Identification of the ions pertinent to the study of the AsP molecule was obtained by their mass-to-charge ratios, shutter effects, and ionization efficiency curves. The appearance potentials for As$^+$, AsP$^+$, P$^+$, and P_2^+ were determined by the linear extrapolation method as 9.9 ± 0.5, 10.5 ± 0.6, 10.2 ± 0.3, and 10.3 ± 0.5 eV, respectively. Here the ionization potential of silver (7.57 eV) was used as the standard.[15] Considering the larger ionization potential for As over that of Sb, the appearance potential for AsP$^+$ compares well to that reported[9] for SbP$^+$ of 9.9 ± 0.3 eV.

The ion currents for As$^+$, AsP$^+$, P$^+$, and P_2^+ are presented in Table I. Those for $^{106}AsP^+$ have been corrected for $^{106}Pd^+$ that was simultaneously observed. The ion currents for P$^+$ and P_2^+ have been corrected for 1% fragmentation of P_2. Assuming the same percentage of fragmentation of AsP into As$^+$ as was observed for P_2, the fragment correction applied to As$^+$ would only be approximately one tenth of that shown for P$^+$, which is negligible within the accuracy of measurement.

The partial pressures, P_i, were obtained from the measured ion currents, I_i^+, by the relations $P_i = k_i I_i^+ T_i$ and $k_i = k_{Ag}\sigma_{Ag}\gamma_{Ag}E_i/(\sigma_i\gamma_i)$. The value of $k_{Ag} = 0.14$ atm A^{-1} K^{-1} was obtained by means of an integral silver calibration.[14] The relative cross sections, σ_i, for Ag(5.05), P(4.45), and As(5.02) were taken from Mann.[16] Those for P_2(6.68) and AsP(7.10) were estimated by multiplying the sum of Mann's atomic cross sections by 0.75.[17] The relative multiplier gains γ_i/γ_{Ag} were measured[14] for P(2.07) and P_2(2.32). That for As(1.76) was taken from Pottie, *et al.*[18] The value for AsP(1.92) was estimated by assuming $\gamma_{AsP} = (\gamma_{As} + \gamma_P)/2$. The empirical factors, $E_i = (I_{max}/I_{15})$, of Ag = 1.00, P = 1.16, P_2 = 1.00, As = 1.1, and AsP = 1.0 were applied to correct the measured ion currents at 15 eV, I_{15}, to maximum intensity. The resulting calibration constants, k_i, in atm A^{-1} K^{-1} were 0.146, 0.074_8, 0.144, and 0.085 for P, P_2, As, and AsP, respectively.

TABLE IV: Third-Law Enthalpies for Reaction 1

T, K	K_p	$-\Delta[(G°_T - H°_{298})/T]$, J K^{-1}	$\Delta H°_{298}$, kJ
1936	1.061×10^{-6}	108.16	431.0
1967	1.398×10^{-6}	108.24	433.5
2040	5.077×10^{-6}	108.41	428.0
2140	1.224×10^{-5}	108.62	433.9
2086	5.863×10^{-6}	108.49	435.1
		Av	432.2 ± 2.5

TABLE V: Third-Law Enthalpies for Reaction 2

T, K	K_p	$-\Delta[(G°_T - H°_{298})/T]$, J K^{-1}	$\Delta H°_{298}$, kJ
1936	3.617×10^{-3}	50.79	188.7
1967	3.801×10^{-3}	50.84	191.2
2040	6.506×10^{-3}	50.92	189.1
2140	9.710×10^{-3}	51.04	191.6
2086	6.811×10^{-3}	50.96	192.9
		Av	190.8 ± 1.7

TABLE VI: Third-Law Enthalpies for Reaction 3

T, K	K_{eq}	$-\Delta[(G°_T - H°_{298})/T]$, J K^{-1}	$\Delta H°_{298}$, kJ
811.3	5.861×10^{-8}	14.11	123.8
826.3	4.083×10^{-8}	14.12	128.4
839.9	7.728×10^{-8}	14.14	126.4
854.5	1.578×10^{-7}	14.15	123.4
		Av	125.5 ± 2.1

In the second investigation which had the principal objective of measuring thermodynamic properties of polyatomic phosphorus molecules, red phosphorus was evaporated in the presence of a Bi–Sn alloy from a graphite Knudsen effusion cell. Temperatures of the Knudsen cell were measured with a Pt–10Rh *vs.* Pt thermocouple that was calibrated *in situ* against the freezing points of Zn and Cu.

A near eutectic composition of Bi–Sn had been added to the Knudsen cell with the intention that this would serve as a liquid metal catalyst for the phosphorus vaporization. Apparently this alloy partially reacted with the red phosphorus. After the bulk of the red phosphorus had been evaporated, the phosphorus that was bound in the alloy was given off gradually upon further heating. This led to favorable conditions for the observation of primary BiP$^+$. During the early stages of the experiment at a temperature of 698 K and just prior to the time when the red phosphorus was completely evaporated, P_4 was the dominant molecular species in the vapor and its ion intensity was quite high, being 1.23×10^{-7} A. At this point BiP$^+$ was first observed at a very low ion current of 5.4×10^{-13}

TABLE VII: Summary of Dissociation Energies, $D°_0$(kJ mol^{-1}), of the Intergroup V Diatomic Molecules[a]

Group V atoms	N	P	As	Sb	Bi
	N_2				
N	941.4 ± 8.4 (19, 22)				
	PN	P_2			
P	613.4 ± 20.9 (8)	485.8 ± 0.4 (10, 19, 24)			
	AsN	AsP	As_2		
As	481 ± 96 (28)	429.7 ± 12.6 (*b*)	379.1 ± 9.6 (29)		
	SbN	SbP	SbAs	Sb_2	
Sb	297 ± 50 (28)	355.2 ± 3.8 (9, 10)	367 ± 10 (30)	297.9 ± 4.2 (10)	
Bi	BiN	BiP	BiAs	BiSb	Bi_2
		278 ± 13 (*b*)	299 ± 10 (30)	248.9 ± 3.8 (31)	196.6 ± 7.5 (27)

[a] References are given in parentheses. [b] This investigation.

A. From its ionization efficiency curve, the appearance potential of this ion was determined as 11.4 ± 0.6 eV by the linear extrapolation method. This high value shows that this ion probably resulted from fragmentation of some more complex Bi–P molecules which were most likely present due to the high P_4 concentration in the vapor. On the next higher temperature of 721.8 K the BiP^+ fragment was again observed. However at this temperature the P_4^+ ion intensity rapidly decreased as the red phosphorus was being completely evaporated. BiP^+ was not observed again until 811.3 K at which time P_4^+ was no longer measurable. Analogy to the Sb–P systems[9,10] in which P_4 was not observed leads one to project that in the absence of P_4 the mixed Bi–P species which could contribute to the BiP^+ ion intensity by fragmentation would be of much lower concentration in the vapor than BiP. This analogy supports BiP^+ being a parent molecule ion at this time in the experiment.

As the temperature was increased higher than 854.6 K the BiP molecule became obscured by the simultaneous presence of gaseous Sn_2, the ion intensity of which increased more rapidly with temperature than that of BiP.

The ions in this experiment were also identified by their mass to charge ratios, shutter effects, and ionization efficiency curves. The appearance potentials, AP, for P_2^+ and Bi_2^+ relative to Bi (IP = 7.3 eV)[15] were determined by the linear extrapolation method as 10.8 ± 0.5 and 7.3 ± 0.5 eV, respectively. The AP for BiP^+ could not be measured because of the small ion intensities. The ion currents for Bi_2^+, P_2^+, and BiP^+ are presented in Table II.

No pressure calibration was performed since a pressure-independent reaction was studied. However, ionization cross sections and mutiplier gains were considered. The relative ionization cross sections, σ_i, for Bi_2, P_2, and BiP were estimated as 12.18, 6.68, and 9.43, respectively, by multiplying the sum of Mann's[16] atomic cross sections by 0.75.[17] The multiplier gains, γ_i, were measured as $\gamma_{P_2} = 6.32 \times 10^5$ and $\gamma_{Bi_2} = 2.29 \times 10^5$ by use of a Faraday cup. γ_{BiP} was estimated as $\gamma_{BiP} = (\gamma_{Bi} + \gamma_P)/2 = 4.02 \times 10^5$. The empirical factors, E_i, were measured as $E_{Bi_2} = 1.00$, $E_{P_2} = 1.25$, and $E_{BiP} = 1.12$. The ion intensities, I_i^+, were corrected by multiplying by $E_i/\sigma_i\gamma_i$ before being used to calculate the equilibrium constants, K_{eq}.

Results and Discussion

The third law enthalpy changes, $\Delta H°_{298}$, for the equilibria

$$AsP(g) = As(g) + P(g) \quad (1)$$

$$AsP(g) = As(g) + 0.5P_2(g) \quad (2)$$

and

$$Bi_2(g) + P_2(g) = 2BiP(g) \quad (3)$$

were obtained from the standard relationship $\Delta H°_{298}/T = -4.576 \log Kp - \Delta[(G°_T - H°_{298})/T]$, using the free-energy functions shown in Table III.

In Tables IV and V, the third-law enthalpies for reactions 1 and 2 are presented together with the values for the corresponding equilibrium constants, K_p, and the free-energy function changes. $\Delta H°_{298}(1) = 432.2 \pm 2.5$ kJ represents directly $D°_{298}$(AsP). Combining the value for $D°_{298}(P_2) = 487.0 \pm 4.2$ kJ mol^{-1} [14] obtained from more numerous data sets over the temperature range 1888–2625 K in the same investigation with $\Delta H°_{298}(2)$, the dissociation energy of gaseous AsP results as $D°_{298}$(AsP) = 434.3 ± 2.5 kJ mol^{-1}. Using the literature value, $D°_{298}(P_2) = 489.1 \pm 0.4$[19,24] kJ mol^{-1}, $D°_{298}$(AsP) becomes 435.1 ± 1.7 kJ mol^{-1}.

In the final selection of $D°_{298}$(AsP) = 433.0 ± 12.6 kJ mol^{-1} more weight is given to the direct determination. With recourse to appropriate literature data and with $H°_{298} - H°_0 = 9.08$ kJ mol^{-1} for gaseous AsP, the following additional thermodynamic quantities for gaseous AsP are calculated: $D°_0 = 429.7 \pm 12.6$ kJ mol^{-1} and $\Delta H_f°_{298} = 187.0 \pm 12.6$ kJ mol^{-1}. Here, the literature values for the standard heats of sublimation of the monatomic gases of arsenic (286.2 ± 1.7 kJ mol^{-1})[25,26] and phosphorus (333.9 ± 0.4 kJ mol^{-1})[19] were used to arrive at the standard heat of formation for gaseous AsP.

In Table VI, the third-law enthalpies for reaction 3 are presented along with the equilibrium constants, K_{eq}, and the free-energy function changes. The average third-law enthalpy change, $\Delta H°_{298}$, was determined as 125.5 ± 2.1 kJ. This value in appropriate combination with the dissociation energy, $D°_{298}$, in kJ mol^{-1} of gaseous Bi_2[27] (198.7 ± 7.5) and P_2(489.1 ± 0.4)[19,24] yields the dissociation energy, $D°_{298}$, of BiP(g) as 281 ± 13 or $D°_0$ as 278 ± 13 kJ mol^{-1}.

The standard heat of formation of BiP(g) is derived as $\Delta H_f°_{298} = 262 \pm 13$ kJ mol^{-1} using heat of formation, $\Delta H_f°_{298}$, of Bi(g) (209.6 ± 2.1 kJ mol^{-1}).[25]

The error limits on the average third-law values given in Tables IV–VI are standard deviations. Error limits on all final values include estimated uncertainties in free-energy functions, ionization cross sections, multiplier

gains, ion intensity measurements, and temperatures. Multiplier gain and ionization cross section assumptions based on experience with the Sb–P system[9,10] results in less than 50% error in the equilibrium constants which corresponds to an uncertainty of less than 6 and 3 kJ mol^{-1} in the dissociation energy of AsP and BiP, respectively. The error resulting from the small ion intensities of AsP and BiP was taken as 1.5 times the standard deviations. Uncertainties in the free-energy functions and temperatures are liberally accounted for in the remainder.

The determination of the dissociation energies of AsP and BiP completes the first of the diatomic intergroup V series, the monophosphides. Table VII, which is essential to the discussion that is to follow, summarizes the presently known diatomic pnictide dissociation energies. Those for the homonuclear species are all known and are seen to decrease down the group. A similar decrease is observed for the diatomic phosphides.

It has been noted[31] that the dissociation energy of BiSb is closely represented by the average (247.3 kJ mol^{-1}) of the bond dissociation energies of the component homonuclear diatomic molecules. Similarly, the average (432.6 kJ mol^{-1}) of the dissociation energies of P_2 and As_2 is in good agreement with the value, 429.7 ± 12.6 kJ mol^{-1}, determined for AsP in this work. Taking these observations as a basis, the dissociation energy of SbAs is predicted to be 339 ± 21 kJ mol^{-1}. However, this is seen to be less than the experimental value[30] given in Table VII.

Applying the same procedure to the BiP molecule gives a value 341 kJ mol^{-1}, which far exceeds the value, 278 ± 13 kJ mol^{-1}, determined in the present study. This is not unexpected, since the same procedure applied to the SbP molecule gives a value 392 kJ mol^{-1}, which is larger than the experimental value of 354.4 ± 4.2 kJ mol^{-1}. It appears that this averaging procedure gives reasonable results only when the component atoms are adjacent in the group.

An alternative estimative procedure is the averaging of the dissociation energies of adjacent diatomic molecules in Table VII. By this procedure, the dissociation energy of SbP determined from AsP and BiP is 354 kJ mol^{-1}, in good agreement with the experimental value.[9,10] Extension of this approach to the BiAs molecule, and making use of the dissociation energies of BiP and BiSb, allows the $D°_0$(BiAs) to be predicted as 264 ± 25 kJ mol^{-1} which is again smaller than the experimental value.[30]

Nitrogen-containing species are excluded from the above considerations because of the exceptionally strong bonding in N_2 and the lack of knowledge of reliable bond energies of the diatomic nitrides.

The applicability of the empirical correlations used illustrates the bonding similarities among the intergroup V molecules.

Acknowledgment. The authors wish to acknowledge the continued support of the Robert A. Welch Foundation under Grant No. A-387.

References and Notes

(1) J. Curry, L. Herzberg, and G. Herzberg, *J. Chem. Phys.*, **1**, 749 (1933).
(2) J. Curry, L. Herzberg, and G. Herzberg, *Z. Phys.*, **86**, 348 (1933).
(3) K. K. Yee and W. E. Jones, *Chem. Commun.*, 586 (1969).
(4) L. Harding, W. E. Jones, and K. K. Yee, *Can. J. Phys.*, **48**, 2842 (1970).
(5) K. K. Yee and W. E. Jones, *J. Mol. Spectrosc.*, **33**, 119 (1970).
(6) E. O. Huffman, G. Tarbutton, K. L. Elmore, W. E. Cate, H. K. Walters, Jr., and G. V. Elmore, *J. Amer. Chem. Soc.*, **76**, 6239 (1954).
(7) O. M. Uy, F. J. Kohl, and K. D. Carlson, *J. Phys. Chem.*, **72**, 1611 (1968).
(8) K. A. Gingerich, *J. Phys. Chem.*, **73**, 2734 (1969).
(9) J. Kordis and K. A. Gingerich, *J. Phys. Chem.*, **76**, 2336 (1972).
(10) J. Kordis and K. A. Gingerich, *J. Chem. Phys.*, **58**, 5141 (1973).
(11) (a) H. Gutbier, *Z. Naturforsch. A*, **16**, 268 (1961); (b) K. D. Carlson, F. J. Kohl, and O. M. Uy, *Advan. Chem. Ser.*, **No. 72**, 245 (1968).
(12) K. A. Gingerich, *J. Chem. Phys.*, **49**, 14 (1968).
(13) D. L. Cocke and K. A. Gingerich, *J. Phys. Chem.*, **75**, 3264 (1971).
(14) J. Kordis and K. A. Gingerich, *J. Chem. Phys.*, **58**, 5058 (1973).
(15) C. E. Moore, *Nat. Bur. Stand. (U. S.), Circ.*, 467 (1958).
(16) J. B. Mann, *Recent Develop. Mass Spectrosc., Proc. Int. Con. Mass Spectrosc., 1969*, 814 (1970).
(17) J. Drowart and P. Goldfinger, *Angew. Chem.*, **79**, 589 (1967); *Angew. Chem., Int. Ed. Engl.*, **6**, 581 (1967).
(18) R. F. Pottie, D. L. Cocke, and K. A. Gingerich, *J. Mass Spectrom. Ion Phys.*, **11**, 41 (1973).
(19) "JANAF Thermochemical Tables," Dow Chemical Co., Midland, Mich., 1965.
(20) D. R. Stull and G. C. Sinke, *Advan. Chem. Ser.*, **No. 18**, (1965).
(21) N. Aslund, R. F. Barrow, W. G. Richards, and D. N. Travis, *Ark. Fys.*, **30**, 171 (1965).
(22) G. Herzberg, "Molecular Spectra and Molecular Structure, I, Spectra of Diatomic Molecules," 2nd ed, Van Nostrand-Reinhold, New York, N. Y., 1950.
(23) D. R. Herschbach and V. W. Laurie, *J. Chem. Phys.*, **35**, 458 (1931).
(24) G. Herzberg, *Ann. Phys.*, **15**, 677 (1932).
(25) R. Hultgren, R. L. Orr, and K. K. Kelley, "Supplement to Selected Values of Thermodynamic Properties of Metals and Alloys," University of California, Berkeley, Calif., Bi (1968) and As (1970).
(26) J. L. Murray, C. Pupp, and R. F. Pottie, *J. Chem. Phys.*, **58**, 2569 (1973).
(27) L. Rovner, A. Drowart, and J. Drowart, *Trans. Faraday Soc.*, **63**, 2906 (1967).
(28) A. G. Gaydon, "Dissociation Energies and Spectra of Diatomic Molecules," 3rd ed, Chapman and Hall, London, 1968.
(29) J. Kordis and K. A. Gingerich, *J. Chem. Eng. Data*, **18**, 135 (1973).
(30) J. E. Prusaczyk, *Diss. Abstr. Int.*, **32**, 1489B (1971).
(31) F. J. Kohl and K. D. Carlson, *J. Amer. Chem. Soc.*, **90**, 4814 (1968).

Thermodynamics of Polycarboxylate Aqueous Solutions. I. Dilatometry and Calorimetry of Protonation and Copper(II) Binding

V. Crescenzi,* F. Delben, S. Paoletti, and J. Škerjanc[1]

Institute of Chemistry, University of Trieste, Trieste, Italy *(Received March 28, 1973; Revised Manuscript Received October 29, 1973)*

Publication costs assisted by the Italian CNR

Protonation and copper(II) binding data for three maleic acid (MA) copolymers in 0.05 *M* $(CH_3)_4NClO_4$ at 25° obtained by means of dilatometric and of calorimetric measurements are reported. The copolymers studied are MA–ethylene (MAE), MA–propylene (MAP), and MA–isobutene (MAiB). The results of the protonation experiments, carried out over the entire range of the degree of dissociation of the polycarboxylates, show that the differential volume as well as the entropy of protonation assume two distinct values for $0 < \alpha < 1$ and $1 < \alpha < 2$ which are, respectively, quite similar for MAE, MAP, and MAiB. On the contrary, the enthalpy of protonation depends both on α and on the nature of the copolymer. The results of the copper(II) binding experiments show that while the differential enthalpy (always a positive quantity) is nearly the same for MAE, MAP, and MAiB at $\alpha = 1.0$ and 1.2 (α = degree of neutralization with $(CH_3)_4NOH$), the differential volume of binding depends on α and on the nature of the polyelectrolyte. The high values for such differential volumes evaluated in some cases would reflect an extensive desolvation of interacting Cu^{2+} ions and vicinal pairs of carboxylate groups, which would also perturb the solvation layers of neighboring chain elements.

Introduction

In previous papers from these laboratories the results of calorimetric and potentiometric measurements on the dissociation of different polycarboxylates in aqueous solution have been reported.[2]

Similar experiments have also been carried out to characterize the specific interaction of Li^+ ions as compared to Na^+ and $(CH_3)_4N^+$ ions with poly(maleic acid) in water.[3] In an extension of this type of investigations we have more recently aimed at the obtainment of a comparative thermodynamic picture of the protonation of different maleic acid copolymers (over the entire range of the degree of protonation) and of the binding of divalent metal ions by the same partially ionized polycarboxylates in dilute aqueous solution.

We wish to report here the results obtained by means of calorimetric and dilatometric measurements on the protonation of, and Cu^{2+} ions binding by, the following three maleic acid (MA) copolymers: MA–ethylene(MAE), MA–propylene (MAP), and MA–isobutene (MAiB) (in 0.05 *M* $(CH_3)_4NClO_4$ at 25°).

The measurements of volume and enthalpy changes accompanying the interaction of the polycarboxylates with protons and with copper ions, respectively, seem particularly suitable to disclose interesting features of such interactions connected with both diverse changes in the water structure close to the interacting ionic species[4] and with the energetics of chelate formation in polyelectrolyte solutions, about which so little is known.[5,6]

Experimental Section

(*a*) *Materials.* Maleic acid–ethylene copolymer, MAE, maleic acid–propylene copolymer, MAP, and maleic acid–isobutene copolymer, MAiB samples, all of the 1:1 alternating type, were received from the Monsanto Chemical Co. ($M_v \sim 10^5$). Stock solutions of the three polyacids were prepared as previously described.[2]

Titrations and partial neutralization of the polyelectrolytes were made using standardized 0.1 *N* $(CH_3)_4NOH$. The value $\alpha = 2$ corresponds to complete neutralization of the polydicarboxylic acids.

Copper perchlorate was prepared by reaction of the carbonate with warm aqueous $HClO_4$. The resultant solution was filtered and cooled. The metal perchlorate precipitated slowly; it was collected and recrystallized twice from water.

The titre of the copper perchlorate solutions was determined using EDTA.[7]

Pure $(CH_3)_4NClO_4$ was prepared by neutralization of ice cold aqueous $(CH_3)_4NOH$ with $HClO_4$. The white precipitate was collected, washed with cold water, then with methanol, and finally dried under vacuum. The purity of tetramethylammonium perchlorate and of copper perchlorate samples was checked by elemental analysis.

In all cases deionized, doubly distilled water was used.

(*b*) *Methods.* The calorimetric experiments were carried out at 25° using a LKB 10700-1 flow microcalorimeter, following closely a procedure already described.[2] Experimental heats of protonation and of binding, Q (μcal/sec), were normalized by the rate of flow of the polyelectrolyte, *i.e.*, $\Delta H = (Q/f_a a) \times 10^{-6}$, a being the polymer concentration in monomoles/liter and f_a the flow rate of the polymer solution in liter/sec.[8] The ΔH values of protonation were plotted against α, and a few representative values of the differential enthalpy of protonation ($\Delta \bar{H}_P$, in kcal/mol of bound H^+ ions) evaluated by interpolation as $(\Delta H_P)_\alpha = -(d\Delta H/d\alpha)_\alpha$ (see Table I).

The ΔH values for the binding of copper ions are directly reported in Figure 3 (ΔH_T, in kcal/monomol).

Linderstrom-Lang dilatometers were used to measure volume changes following a procedure similar to that applied by Begala and Strauss.[4] All measurements were carried out at 25°, with the bath temperature held constant to 0.001°. The pH of the solutions was lower than about 10

(α = 1.5), so that complications due to neutralization of free hydroxyl ions in the protonation experiments or to the possible formation of hydroxyl complexes in the copper(II) binding experiments were avoided.

The experimental volume changes, ΔV_T of Figures 1 and 3, are given in ml/monomol of polyelectrolyte.

In all calorimetric and dilatometric experiments, corrections for effects due to dilution on mixing were made but in most cases they were found to be negligible.

The equilibrium dialysis experiments were carried out using cellulose tubings (Kalle AG, Wiesbaden). Prior to use, these tubings were treated with acetic anhydride, repeatedly washed with hot dilute solutions of EDTA and $NaHCO_3$, respectively, then with ethanol, and finally rinsed throughly with twice distilled water. In each case dialysis equilibrium was reached in about 2 days (25°) and the copper(II) concentrations in the polyelectrolyte containing "internal" solutions and in the polyelectrolyte free "external" solution were determined by atomic absorption spectrometry (Perkin-Elmer 290-B). The final uncertainty in the calculated fraction of bound Cu^{2+} ions should not exceed 2%.[8]

Potentiometric titrations were performed at 25° using a Radiometer PHM4d pH meter with Radiometer "combination" electrodes GK-2301C.

Results and Discussion

Interaction with Hydrogen Ions. The volume changes observed upon mixing aqueous perchloric acid with the tetramethylammonium salts of MAE, MAP, and MAiB in 0.05 *M* $(CH_3)_4NClO_4$ are shown in Figure 1. The ordinate is the total volume change, ΔV_P, given in ml/monomol of polyacid and the abscissa, α, is the degree of neutralization.

It is seen that ΔV_P rises linearly with α but with two distinct slopes for $1 < \alpha < 2$ and for $0 < \alpha < 1$. For each polyelectrolyte, therefore, the differential volumes of protonation, $\Delta \bar{V}_P = -d\Delta V_P/d\alpha$ (ml/mole of protons bound), corresponding to the reactions

$$A^{2-} + H^+ \longrightarrow HA^- \quad (1)$$

and

$$HA^- + H^+ \longrightarrow H_2A \quad (2)^9$$

are constant, within experimental errors, *i.e.*, essentially independent of the charge density along the chains.

This fact, which clearly differentiates the behavior of the polydicarboxylic acids from that of other polyelectrolytes, such as, for example, poly(acrylic acid),[4] has been already disclosed for MAE in 0.2 *M* $(CH_3)_4NCl$ at 30° by Begala and Strauss whose dilatometric results, although for different experimental conditions, are in agreement with ours.

The ΔV_P values calculated from the plots of Figure 1 are given in the first two columns of Table I. The data show that passing from MAE to MAP and to MAiB there is only a slight increase in $\Delta \bar{V}_P^1$ (*i.e.*, the molar volume change for reaction 1) while $\Delta \bar{V}_P^2$, taking into account the estimated uncertainties in the final $\Delta \bar{V}_P$ figure, may be considered independent of chain backbone chemical constitution.

It thus seems logical also to adopt for MAP and MAiB the point of view of Begala and Strauss, which deserves repetition in view of other dilatometric data to be discussed in the following section. According to these authors a large $\Delta \bar{V}_P^2$ value for the maleic acid copolymers upon addition of the first proton is due to the disruption of

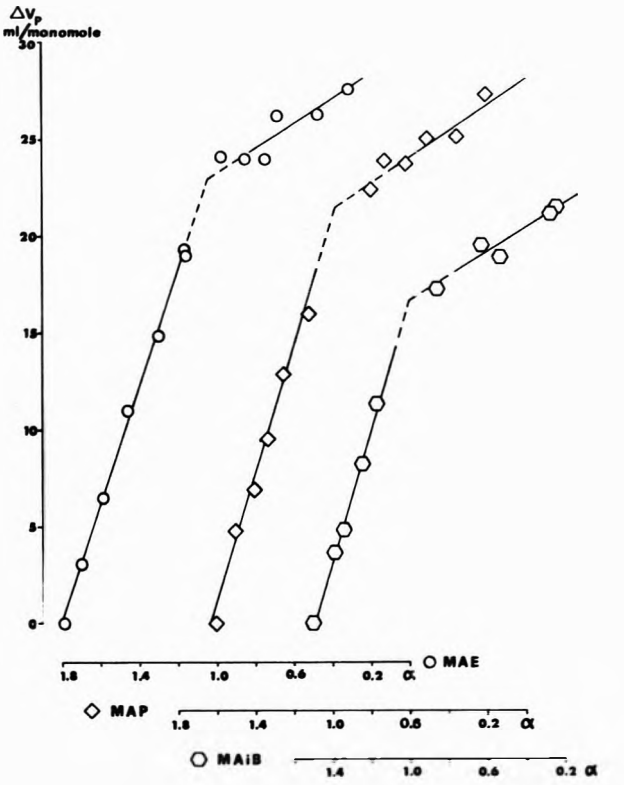

Figure 1. Volume change on the addition of perchloric acid to tetramethylammonium polycarboxylates in 0.05 *M* $(CH_3)_4NClO_4$ at 25°. The abscissa, α, denotes the state of neutralization of the polyacid. The ordinate, ΔV_p, gives the volume change in millilites/monomole of total polyacid: initial polyelectrolyte concentration 1×10^{-2} monomol/l.

water structure around the dianions, A^{2-}, and to the formation of a very stable chelate in which the proton is bound to both carboxylate groups. The resulting structure of each repeating unit largely prevailing at α = 1.0 for the copolymers would be less hydrated than if a full unit negative charge were located on one of the two carboxylated groups. Consequently, further protonation is characterized by a low differential volume change, abnormally small compared to those observed for monomeric carboxylic acids.[4]

In Table I a few results of our calorimetric and potentiometric measurements are also reported.

The sharp transition in the $\Delta \bar{V}_P$ values going from $1 < \alpha < 2$ to $0 < \alpha < 1$ is reflected also in the pH behavior of the three polyacids for which there is a difference in pK_a (K_a, the apparent ionization constant, is calculated from potentiometric titration data according to ref 10) of about 3.2 (MAE), 4.7 (MAP), and 6.7 (MAiB) units, respectively, between the first and the second ionization steps. Our data also show that, with the notable exception of MAP, the differential enthalpy of protonation, $\Delta \bar{H}_P$, undergoes a marked change going from reaction 1 to reaction 2, under the experimental conditions employed in this study. These data finally permit evaluation of the entropy of protonation, ΔS_p. From Table I it is seen that protonation of a dianion A^{2-} is accompanied by an increase in entropy approximately twice that for protonation of a HA^- group. This is qualitatively in agreement with the dilatometric data, in the light of the interpretation given by Begala and Strauss. That ΔV_P and ΔS_p cannot simply be proportional to each other may be due to entropy changes contributed by the chains, in addition to the

TABLE I: Dilatometric, Calorimetric, and Potentiometric Data for the Protonation of Maleic Acid Copolymers[a]

	α	$\Delta\bar{V}_P^1$, ml/mol of H^+	$\Delta\bar{V}_P^2$, ml/mol of H^+	$\Delta\bar{H}_P$, kcal/mol of H^+	pK_a	$-\Delta G_p$, kcal/mol of H^+	ΔS_p, cal/mol °K
MAE	0.70		6.4 ± 0.5	0.0	4.26	5.81	19.5
	0.80			0.21	4.31	5.88	20.4
	1.20	30 ± 1		1.65	7.47	10.19	39.7
	1.30			1.65	7.66	10.45	40.6
MAP	0.70		6.7 ± 0.3	0.09	4.02	5.48	18.7
	0.80			0.09	4.06	5.54	18.9
	1.20	33 ± 1		0.09	8.60	11.73	39.7
	1.30			0.09	8.83	12.04	40.7
MAiB	0.70		6.3 ± 0.3	0.98	3.29	4.49	18.3
	0.80			0.76	3.33	4.54	17.8
	1.20	34 ± 1		−1.66	9.91	13.55	39.9
	1.30			−1.66	10.10	13.77	40.6

[a] Solvent 0.05 *M* $TMAClO_4$; temperature 25°.

main source of the entropy increase residing in losses of water of hydration. Protonation of A^{2-} groups would in fact lead to rigid local structures of the repeating units (with a negative contribution to ΔS); reducing α below unity these structures are disrupted with an increase in the conformational entropy of the chains. Concerning the differences in acid strength between the three maleic acid copolymers considered by us, it appears that from a thermodynamic standpoint, these are controlled by differences in the enthalpy of dissociation. Data of Table I show, for instance, that the second ionization constants of MAE and MAiB differ by two orders of magnitude essentially because the enthalpy of dissociation of a half-neutralized repeating unit of MAE is more favorable with respect to the same reaction for MAiB by *ca.* 3.3 kcal.

Interaction with Cu^{2+} Ions. (*a*) *Dilatometric Data.* The changes in volume on mixing dilute solutions of $Cu(ClO_4)_2$ and of each of the three maleic acid copolymers for different α values (ΔV_T, in ml/monomol of polyelectrolyte) are plotted in Figure 2 as a function of $R(Cu^{2+})$, the ratio of moles of Cu^{2+} ions bound per monomole of polyelectrolyte. The $R(Cu^{2+})$ values were obtained from a series of equilibrium dialysis measurements carried out under experimental conditions very close to those used in the dilatometric experiments. The dialysis measurements have shown that, under these conditions, from 90 to 99% of added Cu^{2+} ions were bound by the polycarboxylates. In practice, at α = 1.2 and 1.5, Cu^{2+} binding resulted nearly quantitative, within the limits of experimental errors.

The dilatometric data of Figure 2 clearly show that ΔV_T depends on the nature of the polyelectrolyte and, for each given $R(Cu^{2+})$ value, varies with α, at least in the limited range of α values considered. With increasing $R(Cu^{2+})$ all the plots exhibit in fact a more or less marked curvature. In the Cu^{2+} binding process therefore, as opposed to protonation, the differential volume of binding varies continuously with the amount of counterions being linked to the polycarboxylate chains. Limiting values of such differential volumes, $\Delta\bar{V}_B$, may be directly evaluated from the initial slopes of the plots of Figure 2.

The resulting figures, which are somewhat uncertain due to the curvature of the plots and the relatively limited number of experimental points, are the following (in ml/mol of Cu^{2+} bound and for α = 1.0, 1.2, and 1.5, respectively): MAE 32, 41, and 52; MAP 26 and 52;[11] MAiB 31, 85, and 85. The $\Delta\bar{V}_B$ values, for $\alpha > 1$, are quite high indeed, particularly in the case of the MAiB copolymer. These values point out that extensive dehydration of carboxylated groups and Cu^{2+} ions takes place upon complex formation.

Our findings have, qualitatively speaking, certain analogies with those reported by Begala and Strauss for the binding of Mg^{2+} ions by the $(CH_3)_4N^+$ salt of the MAE copolymer.[4] In this case ionic binding of Mg^{2+} varying in strength with the overall charge of the polyions was taken as being responsible for the limited dehydration of interacting carboxylate and Mg^{2+} ions and for the decrease of $\Delta\bar{V}_B$ with increasing $R(Mg^{2+})$ ($\Delta\bar{V}_B$ from about 25 to 16 ml/mol of Mg^{2+} for $R(Mg^{2+})$ increasing from 0 to about 0.5). In our case, unless other types of experimental approaches will demonstrate to the contrary, we assume that chelation of Cu^{2+} involves formation of a CuA species only,[6] whose intrinsic stability would not strongly depend on $R(Cu^{2+})$. To explain our high $\Delta\bar{V}_B$ values, corresponding in some cases to a release of a number of water molecules of solvation greater than that explanable on the basis of the molar hydrations of Cu^{2+}[12] and of A^{2-} ions,[4] we would propose the following. At α values above unity, the formation of a CuA chelate very likely perturbes also the hydration layers of neighboring repeating units not directly involved in chelation. At higher $R(Cu^{2+})$ values this cooperative desolvation would be progressively smoothed out because of the diminished overall hydration and charge density of the chains.

At α = 1.0 the lowest $\Delta\bar{V}_B$ values are observed. This may due to a lack of interference between the hydration sheaths of neighboring repeating units so that copper binding could not lead to the cooperative effect assumed above for $\alpha > 1$. With the half-neutralized copolymers, however, it has to be pointed out that binding of Cu^{2+} ions, always under the hypothesis that only CuA species are formed, involves also an exchange of protons (from and to the HA^- groups along the chains) so that processes at $\alpha > 1$ and α = 1.0 cannot be directly compared. The same applies to the calorimetric data presented in the following paragraph.

(*b*) *Calorimetric Data.* The release of water molecules from the solvation spheres of interacting Cu^{2+} and A^{2-} species must involve an increase in entropy.

As a matter of fact, binding of Cu^{2+} ions by the maleic acid copolymers, a process occurring nearly quantitatively under the experimental conditions used, is entirely entropy driven. This is demonstrated by the enthalpy data reported in Figure 3 according to which both at α = 1.0 and 1.2 the interaction of Cu^{2+} ions with the three copolymers considered is endothermic. In Figure 3 ΔH_T is given in kcal/monomole of polyacid.

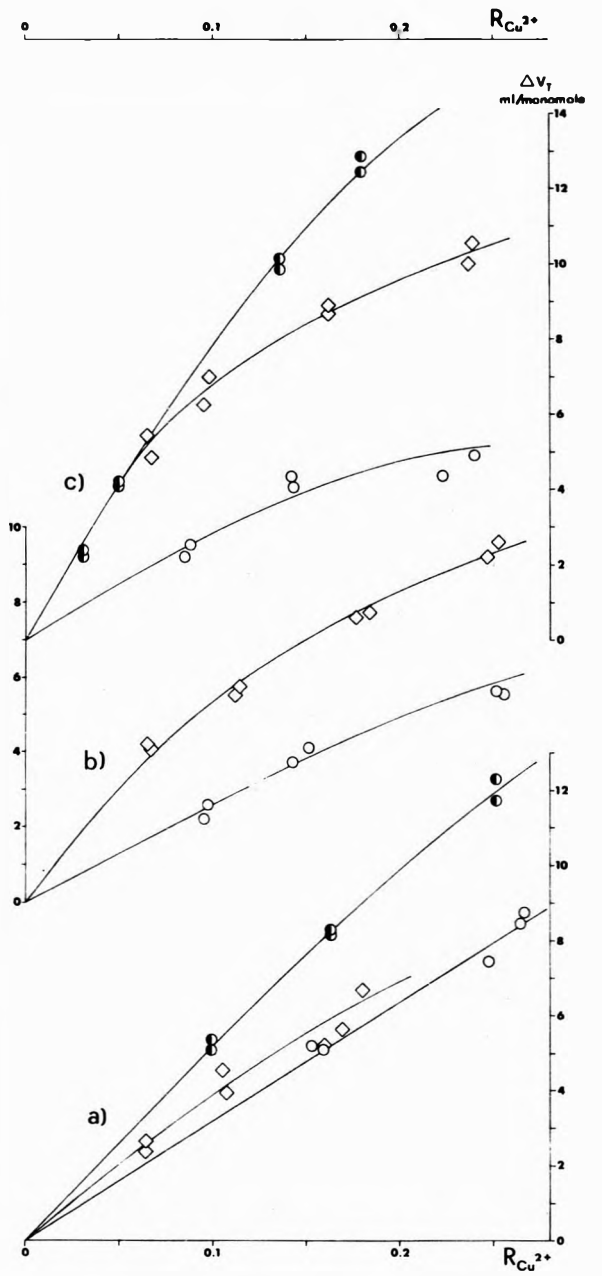

Figure 2. Volume change on the addition of $Cu(ClO_4)_2$ to tetramethylammonium polycarboxylates at various degrees of neutralization, α, in 0.05 M $(CH_3)_4NClO_4$ at 25°. The abscissa, $R(Cu^{2+})$, denotes the moles of added Cu^{2+} bound per monomole of total polyacid. The ordinate, ΔV_T, gives the volume change in milliliters per monomole of total polyacid: initial polyelectrolyte concentrations 1×10^{-2} monomole/l.; (a) MAE; (b) MAP; (c) MAiB; O, $\alpha = 1.00$; ◊, $\alpha = 1.20$; ◐, $\alpha = 1.50$.

In analogy with the treatment of the dilatometric data, we simply take for the differential enthalpy of binding, $\Delta\bar{H}_B$, the initial slopes of the plots of Figure 3. Evaluated in this way, ΔH_B (kcal/mol of copper bound) does not change passing from $\alpha = 1.0$ to 1.2 and assumes values which are quite similar for the three polyelectrolytes, *i.e.*, 4.4 for MAE and 4.0 for both MAP and MAiB. In all cases evidently the rupture of ion–dipole (solvent) bonds would be uncompensated by the formation of fewer bonds between fixed charges on the macroions and counterions, which may be itself an endothermic process.[13]

This situation is quite similar to that prevailing in the case of various monomeric dicarboxylic ligands and a few

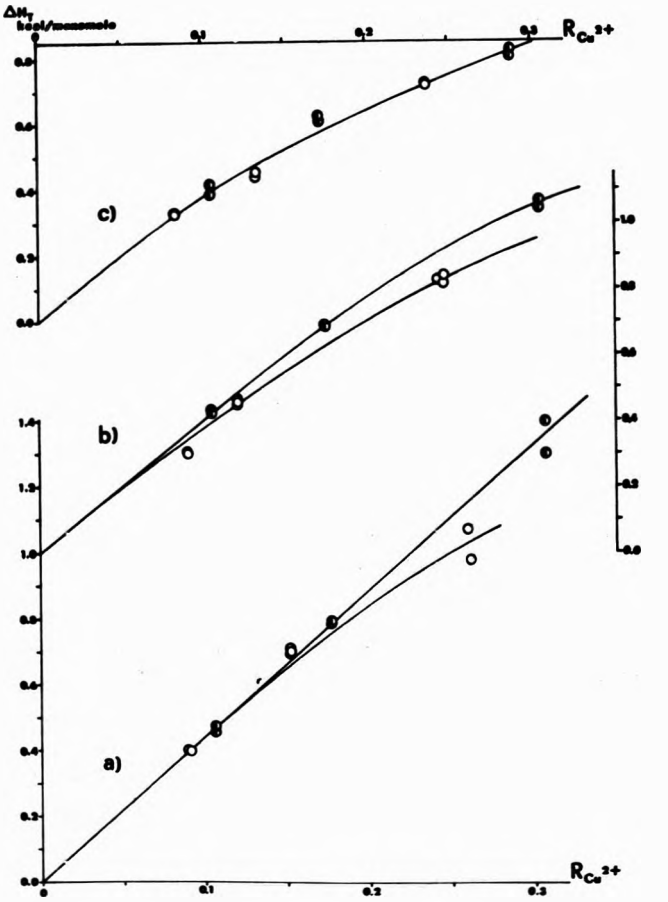

Figure 3. Enthalpy changes on the addition of $Cu(ClO_4)_2$ to tetramethylammonium polycarboxylates at various degrees of neutralization, α, in 0.05 M $(CH_3)_4NClO_4$ at 25°. The abscissa, $R(Cu^{2+})$, denotes the moles of added Cu^{2+} bound per monomoles of total polyacid. The ordinate, ΔH_T, gives the enthalpy change in kcal/monomole of total polyacid: initial polyelectrolyte concentration 1×10^{-2} monomole/l.; (a) MAE; (b) MAP; (c) MAiB; O, $\alpha = 1.00$; ◐, $\alpha = 1.20$.

transition metal ions.[14] Our calorimetric results are in qualitative agreement with those reported by Felber and Purdie[6] obtained working with MAE at $\alpha = 0.5$ in water ($\Delta\bar{H}_B = 3.6$ kcal/mol of Cu^{2+} bound at 25°), and happen to be quite close to those for the Cu^{2-}–succinate system (4.56 kcal/mol).

Comparison of the dilatometric and calorimetric data reveals that while $\Delta\bar{V}_B$ may change strongly with varying α or, at a given α value, passing from one polycarboxylate to the other, $\Delta\bar{H}_B$ would be on the contrary nearly a constant.

If $\Delta\bar{V}_B$ is in all cases simply proportional to the number of water molecules liberated in the Cu^{2+} binding process, which would in turn involve a proportional increase in the heat content of the system, the observed constancy of $\Delta\bar{H}_B$ should be the result of a compensation effect.[15] This effect could stem from a difference in the relative weights of the covalent and electrostatic contributions (likely of opposite sign)[16] to the Cu–carboxylate bonding energy, depending on α and/or the chemical structure of the polyelectrolyte chain backbones.

Similarly if the overall entropy of chelation increases with $\Delta\bar{V}_B$, then the free energy of binding would also depend on the last two factors mentioned above.

More data are evidently needed to better clarify these points. To this end, for a reliable partitioning of the observed changes in thermodynamic state functions in terms

of covalent and electrostatic contribution, it is particularly important to dispose of accurate values of formation constants for the Cu-polycarboxylate systems.

The entropy of Cu^{2+} ions binding might be in fact immediately calculated and permit a more direct, rational comparison with the $\Delta\bar{V}_B$ values already accumulated. For the moment relying upon the equilibrium dialysis data mentioned in the outset (see also the Experimental Section), we can only conclude that at $\alpha = 1.2$ and for small $R(Cu^{2+})$ values formation constants for the three copper(II)-maleic acid copolymer pairs must be higher than 10^5 (M^{-1}).[17] According to Felber and Purdie[6] the formation constant for the Cu-MAE system would be as high as 10^9 M^{-1}, on the basis of their elaboration of potentiometric titration data for MAE in aqueous $Cu(ClO_4)_2$ solution.

The free energy of binding is thus certainly greater than 7 kcal/mol of Cu^{2+} bound and the entropy will exceed 40 cal/mol °K. Both figures are, of course, higher than those reported for monomeric dicarboxylate complexes of transition metal ions.[14] The larger entropy of Cu^{2+} fixation by a pair of vicinal carboxylate groups along a polycarboxylate chain is, in our opinion, the result of the contribution due to a disruption of the overlapping hydration sheaths of repeating units neighboring to that directly involved in chelate formation. Finally, it is worth pointing out that even if as far as stoichiometry is concerned only one type of chelate is formed (CuA) with the three polyelectrolytes at all α and $R(Cu^{2+})$ values, more should be learned about the geometry of attack and the degree of penetration of the carboxylate ligands into the first coordination sphere of copper ions going from one copolymer to another. To this end and in order to make further steps in the interpretation of the thermodynamic data, spectroscopic measurements seem particularly valuable.

Work is in progress in our laboratories to get a better insight of the systems partially characterized in this paper, and we will report soon on the potentimetric and uv spectral results being accumulated.

Acknowledgments. This work has been carried out with financial support of the Italian Consiglio Nazionale delle Ricerche, CNR, Rome.

Supplementary Material Available. A complete list of dilatomeric and dialysis equilibrium experimental data will appear following these pages in the microfilm edition of this volume of the journal. Photocopies of the supplementary material from this paper only or microfiche (105 × 148 mm, 24× reduction, negatives) containing all of the supplementary material for the papers in this issue may be obtained from the Journals Department, American Chemical Society, 1155 16th St., N.W., Washington, D. C. 20036. Remit check or money order for $3.00 for photocopy or $2.00 for microfiche, referring to code number JPC-74-607.

References and Notes

(1) Department of Chemistry, University of Ljubljana, Ljubljana, Jugoslavia.
(2) V. Crescenzi, F. Delben, F. Quadrifoglio, and D. Dolar, *J. Phys. Chem.*, **77**, 539 (1973).
(3) F. Quadrifoglio, V. Crescenzi, and F. Delben, *Macromolecules*, **6**, 301 (1973).
(4) A. J. Begala and U. P. Strauss, *J. Phys. Chem.*, **76**, 254 (1972).
(5) E. M. Loebl, L. B. Luttinger, and H. P. Gregor, *J. Phys. Chem.*, **59**, 559 (1955).
(6) B. J. Felber and N. Purdie, *J. Phys. Chem.*, **75**, 1136 (1971).
(7) H. Flaschka, *Mikrochemie*, **39**, 38 (1952).
(8) See paragraph at end of paper regarding supplementary material.
(9) A^{2-}, HA^-, and H_2A represent a fully ionized, half ion zed, and fully protonated maleic acid copolymer repeating unit, respectively.
(10) P. L. Dubin and U. P. Strauss, *J. Phys. Chem.*, **74**, 2842 (1970).
(11) The value for $\alpha = 1.5$ has not been determined.
(12) R. Zana and E. Yeager, *J. Phys. Chem.*, **71**, 521 (1967).
(13) G. H. Nancollas, *Quart. Rev., Chem. Soc.*, **14**, 402 (1960).
(14) A. McAuley, G. H. Nancollas, and K. Torrance, *Inorg. Chem.*, **6**, 136 (1967).
(15) Also in this case, as with the dilatometric data, comparison should be safely made only among ΔH_B values for $\alpha = 1.2$ which are connected with the simple process $Cu^{2+} + A^{2-} \rightarrow CuA$, at least for very low $R(Cu^{2+})$ values.
(16) G. Degischer and G. Nancollas, *J. Chem. Soc. A*, 1125 (1970).
(17) This is easily seen writing an apparent formation constant as $[CuA]/[Cu^{2+}][A^{2-}]$, and considering on a simple stoichiometric basis that $[CuA]/[Cu^{2+}] \sim 98/2$ and $[A^{2-}] \sim 10^{-4}$ *M*, for $\alpha = 1.2$, for both MAP and MAiB according to equilibrium dialysis and potentiometric data.

Behavior of Collisional Efficiencies in External Activation Systems

W. P. Carter and D. C. Tardy*

University of Iowa, Department of Chemistry, Iowa City, Iowa 52242 *(Received February 14, 1973; Revised Manuscript Received December 13, 1973)*

The efficiencies of a weak collider in inhibiting reaction in external activation systems, which can be defined either relative to the decomposition yields, the stabilization yields, or the apparent rate constant ($k_a = \omega(D/S)$), are calculated from stochastic energy transfer models for several prototype systems in order to examine their dependence on the pressure, the level of excitation (E^+), the temperature, and the decomposition rate constants. The relationships between the efficiencies and the steady-state populations are studied for the first time. At low pressure the efficiency is most sensitive to the details of the energy transfer model, and is in general small and decreases markedly with increasing E^+. At high pressure the efficiencies are less sensitive to E^+, but do have a maximum at some E^+; the location of that maximum being farther out at higher temperatures or in systems that have looser activated complexes. This suppression of the high-pressure efficiencies at low E^+ is due to "up" transitions which are most important in this region. The sensitivity of various experimental regions (pressure and temperature variable) to energy transfer parameters is discussed.

Introduction

The nature of energy transfer *via* bimolecular collision processes in the gas phase can be studied by examining external activation systems[1] where excited species are formed with known excitation energies by chemical[2] or photochemical activation, electron impact, etc. Such information is obtained by examining the relative efficiency of bath gases in removing the excess energy above that required for some unimolecular process (such as decomposition, isomerization, or fluorescence). The most efficient bath gases in deactivating, which tend to be the larger molecules, are designated as "strong colliders;" where each collision removes at least enough excitation energy so that the unimolecular process is quenched.[3] Less efficient gases (generally smaller molecules or atoms) are called "weak colliders;" and, for these compounds, efficiencies are defined relative to strong colliders. In this paper, we shall discuss what is meant by the efficiency of a weak collider, and how it depends upon the energy transfer model, the collision rate (ω), the excitation energy above threshold (E_0, the minimum energy necessary for decomposition), the decomposition rate constants, and the bath gas temperature. From the above characteristics experiments can be chosen which are either dependent or independent of energy transfer parameters.

Conventionally, in external activation systems, the relative efficiency, β_ω^{ka},[3] is defined by eq 1 in terms of the apparent rate constant $k_a = \omega(D/S)$[4] (where D is the fraction of the total activated species which "decompose," *i.e.*, undergo the unimolecular process, and S is the fraction that are eventually stabilized). Here "weak" and "strong" refer to experiments with different deactivating gases, but with the same ω and activation conditions. The efficiency can also be defined by $\beta_\omega^{ka} = \beta_\omega^D \beta_\omega^S$, $\beta_\omega^D = D^{strong}/D^{weak}$, $\beta_\omega^S = S^{weak}/S^{strong}$ where β_ω^D is the efficiency relative to inhibiting decomposition, and can be measured by looking only at relative decomposition yields, while β_ω^S, the efficiency relative to stabilization, can be measured by looking at only the yields of stabilization products. In some cases, β_ω^D or β_ω^S may be easier to measure than β_ω^{ka}, and, as the next section will show, they are theoretically more elementary concepts.

$$\beta_\omega^{ka} = k_a^{strong}/k_a^{weak} \qquad (1)$$

Calculation Technique

Consider the activated species as having a number of discrete energy levels, indexed by i or j. The following terminology is used: k_i^m = rate of unimolecular process m when the activated species is in state i; $k_i^{tot} = \Sigma_m k_i^m$ = total rate of all possible unimolecular decompositions from state i (Note $k_i^{tot} = k_i$ if only one process occurs); f_i = input flux due to external activation forming energized species in state i; n_i = steady-state population of state i Upon collision with a bath gas molecule, the excited species in state i can either be stabilized, with probability s_i, or be transferred into state j, with probability p_{ji}. The energy transfer model is described completely by the matrix whose elements are p_{ji}; since something must happen upon collision, $s_i + \Sigma_j p_{ji} = 1$. The method of calculating these elements for a given model has been described previously[1,5] and is briefly discussed in the Appendix.

The total amount of stabilization, given by $S = \Sigma_i \omega s_i n_i$, is used to calculate β_ω^S.

The total decomposition *via* process m is given by $D^m = \Sigma_i k_i^m r_i$; and for each process a β_ω^D can be calculated. In this paper, we shall drop the superscript m on D^m and k_i^m, it being understood that these refer to the particular process considered in calculating β_ω^D. If other unimolecular processes are possible in a given activation system (*i.e.*, $k_i^{tot} \neq k_i$), it is necessary to specify which of the processes we are considering in calculating the β_ω^D's.

In order to calculate β_ω^D and β_ω^S, we need to know the steady-state populations for both the weak and strong collision case. If the steady-state approximation is assumed for each state i, where input flux equals output flux, we have (for each i)

$$f_i + \omega \sum_{j \neq i} p_{ij} n_j = k_i^{tot} n_i + \omega(1 - p_{ii}) n_i \qquad (2)$$

(p_{ii} is the probability of *not* leaving state i upon collision.) For strong colliders, all collisions cause stabilization (s_i = 1) and all $p_{ji} = 0$; so

$$n_i^{\text{strong}} = f_i/(\omega + k_i^{\text{tot}}) \quad (3)$$

For weak colliders, the problem is made much more tractable by adding $p_{ii}n_i$ to both sides of eq 2 and rearranging

$$f_i = \sum_j [\delta_{ij}k_i^{\text{tot}} + \omega(\delta_{ij} - p_{ij})]n_j$$

This is suitable for matrix notation

$$\vec{f} = [\mathbf{k}^D + \omega(\mathbf{I} - \mathbf{P})]\vec{n}$$

where $k_{ij}^D = \delta_{ij}k_i^{\text{tot}}$. The steady-state populations are obtained by conventional matrix techniques as shown by Rabinovitch and Hoare[6]

$$\vec{n} = [\mathbf{k}^D + \omega(\mathbf{I} - \mathbf{P})]^{-1}\vec{f}$$

or

$$n_i^{\text{weak}} = \sum_j [\mathbf{k}^D + \omega(\mathbf{I} - \mathbf{P})]_{ij}^{-1} f_j \quad (4)$$

Thus we can obtain the efficiencies

$$\beta_\omega^D = \frac{D^{\text{strong}}}{D^{\text{weak}}} = \frac{\sum_i k_i n_i^{\text{strong}}}{\sum_i k_i n_i^{\text{weak}}} =$$

$$\sum_i \frac{k_i f_i}{\omega + k_i^{\text{tot}}} \Big/ \left\{ \sum_i k_i \sum_j [\mathbf{k}^D + \omega(\mathbf{I} - \mathbf{P})]_{ij}^{-1} f_j \right\} \quad (5)$$

$$\beta_\omega^S = \frac{S^{\text{weak}}}{S^{\text{strong}}} = \frac{\sum_i \omega s_i n_i^{\text{weak}}}{\sum_i \omega n_i^{\text{strong}}} =$$

$$\left\{ \sum_i s_i \sum_j [\mathbf{k}^D + \omega(\mathbf{I} - \mathbf{P})]_{ij}^{-1} f_j \right\} \Big/ \sum_i \frac{f_i}{\omega + k_i^{\text{tot}}} \quad (6)$$

if we define

$$R_{ji} = [k^D + \omega(I - P)]_{ji}^{-1}(\omega + k_i^{\text{tot}}) = \frac{[k^D + \omega(I - P)]_{ji}}{n_i^{\text{strong}}} \quad (7)$$

rearrangement of eq 5 and 6 yields

$$\beta_\omega^D = \frac{\sum_i k_i n_i^{\text{strong}}}{\sum_i \left(\sum_j k_j R_{ji} \right) k_i n_i^{\text{strong}}} = 1 \Big/ \left\langle \sum_j \frac{k_j}{k_i} R_{ji} \right\rangle_{k_i n_i^{\text{strong}}} \quad (8)$$

$$\beta_\omega^S = \frac{\sum_i \left(\sum_j s_j R_{ji} \right) n_i^{\text{strong}}}{\Sigma n_i^{\text{strong}}} = \left\langle \sum_j s_j R_{ji} \right\rangle_{n_i^{\text{strong}}} \quad (9)$$

(Equation 8 is valid only if all input occurs above the critical energy.) The quantities R_{ji} can be thought of as relative steady-state distributions of populations resulting from input into level i. R_{ji} is the population of level j in the weak collision case divided by the total population in the strong collision case (which is n_i^{strong}) when, in both cases, the external input is into level i only (*i.e.*, $f_j = \delta_{ij}$). The above equations therefore show that β_ω^D is the reciprocal of an average of the total relative decomposition resulting from input at the various levels, weighed by the fraction of species that decompose from that level in the strong collision case. Similarly, β_ω^S is an average of the total relative stabilization resulting from the inputs, weighed, in this case, by the steady-state strong collision populations. In both cases, the averages, weighed by easy-to-calculate strong collision distributions, are only over levels where input actually occurs, even though weak colliders populate other levels. Probably the clearest interpretation of β_ω^{ka} in this context is simply to note that it always is the product of the other two efficiencies.

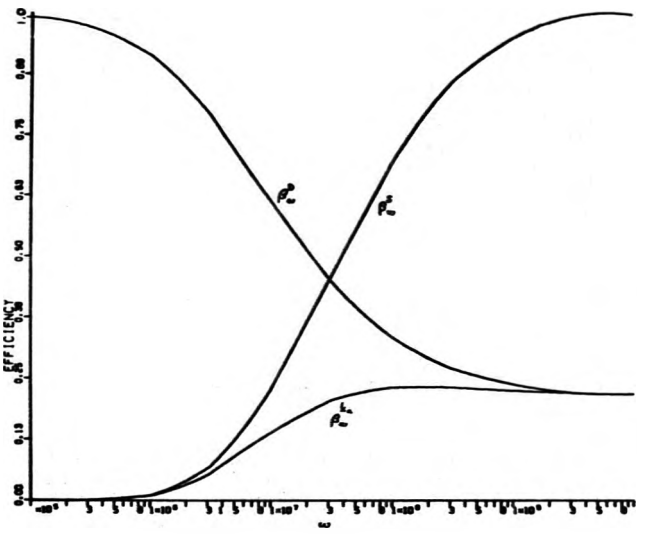

Figure 1. Dependence of β_ω^D, β_ω^S, and β_ω^{ka} on ω for the butyl-2 system, using a step-ladder model (step size = 400 cm^{-1} (1.14 kcal), T = 300°K).

Results

Pressure Dependence. Figure 1 shows the pressure dependence of β_ω^D, β_ω^S, and β_ω^{ka} calculated using a step ladder model for the butyl-2 chemical activation system. (Activated butyl-2 radicals are formed with a minimum of 41 kcal/mol of vibrational energy at 300°K by the biomolecular reaction of H + *cis*-2-butene;[7] butyl-2 can decompose forming methyl + propylene with a critical energy of 33 kcal/mol.) The pressure dependence shown in Figure 1 is typical, and is not qualitatively affected when different transfer models or activation systems are used, as shown earlier by Rabinovitch and coworkers.[1,8] Both β_ω^D and β_ω^S are monotonic functions of ω; $\beta_\omega^D = 1$ at zero pressure (since everything decomposes, regardless of collider (*i.e.*, $D^{\text{weak}} = D^{\text{strong}} = 1$)), and it decreases to a nonzero limit as pressure increases. Likewise, $\beta_\omega^S = 1$ at high pressure (where everything is stabilized, regardless of collider) and decreases as the pressure decreases. Both β_ω^D and β_ω^S change most rapidly in the region where ω is the same order of magnitude as the k_i^{tot}'s. In cases examined here, $k_i^{\text{tot}} = k_i$, where there is only one unimolecular process, however, with more than one process the total decomposition rate determines the steady-state populations, and thus the pressure dependence of the efficiencies, not the particular rate of the decompositions being studied. β_ω^{ka} may have a maximum in the moderate pressure region, but generally does not change too rapidly except in the low-pressure region.

In order to isolate influences on the efficiency other than the pressure (*i.e.*, ω), we shall examine the efficiencies in the low- and the high-pressure limits.

Low-Pressure Region. In this region, since $\beta_0^D = 1$ and $\beta_0^{ka} = \beta_0^S$, it is the efficiency of stabilization that is of interest. If in eq 2 terms with ω are neglected, considerable simplification occurs as the steady-state populations no longer depend on the collision models

$$n_i = n_i^{\text{weak}} = n_i^{\text{strong}} = f_i/k_i^{\text{tot}}$$

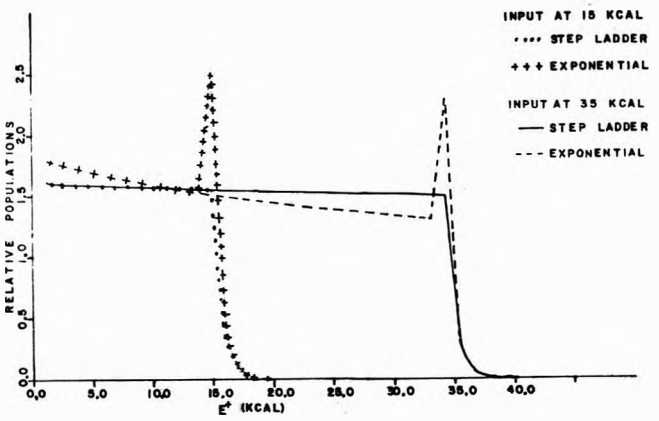

Figure 2. High-pressure relative steady-state populations resulting from monoenergetic inputs for the butyl-2 system at 300°K using step-ladder model (step size = 400 cm^{-1} (1.14 kcal)) with input at 15 kcal (. . . .), at 35 kcal (——), and using an exponential model (average energy = 550 cm^{-1} (1.57 kcal)) with input at 15 kcal (+ + +) and at 35 kcal (— — —).

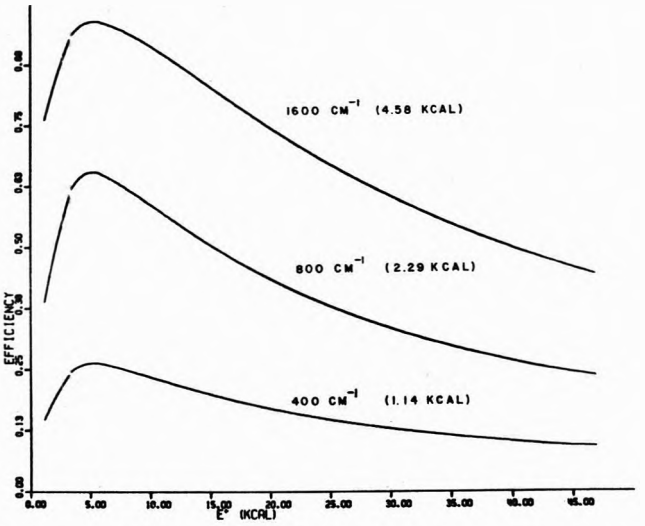

Figure 3. Dependence of β_ω^D on E^+ for the butyl-2 system for step-ladder models at 300°K with various step sizes shown. A similar set of curves result from an exponential model.

This gives $R_{ji} = \delta_{ji}$, so $\beta_0^{ka} = \beta_0^S = \langle s_i \rangle_{n_i}$. As ω approaches zero, the efficiency approaches an average (over the levels formed) of one-collision deactivation probabilities for the weak collider. Though this limit is difficult to reach in practice, it indicates that at low pressures the efficiencies are very sensitive to the probabilities of transferring large amounts of energy upon collision.[8] Experiments determining such efficiencies can be used to discriminate between transfer models with broad spreads of probable energy transferred (such as exponential) as opposed to models with narrow spreads (such as step ladder). This has been done by looking at "low-pressure turnup" in some chemical activation systems.[1,8,9] In addition, the low-pressure efficiency should depend strongly upon the excitation energy at which the activated species is formed. This efficiency will decrease rapidly with increasing energy, though it is generally very small (much less than 1) except in systems formed with excitation not much above the critical energy.

High Pressure. Relative Populations. This region, which is experimentally accessible in many external activation systems, is defined when ω is much greater than k_i^{tot} for all populated levels. Since $\beta_\omega^S = 1$ and $\beta_\omega^{ka} = \beta_\omega^D$, we look at the efficiency relative to inhibiting decomposition. At high pressure, the relative steady-state population distribution has an important effect upon this efficiency; the populations resulting from weak collisions are significantly different from those resulting from strong collisions. From eq 3 and 7 where $\omega \to \infty$ we have the relative population of level j resulting from input at level i given by $R_{ji} = (I - P)_{ji}^{-1}$, so at high pressures the relative distribution depends only on the collision model, not the rates. Figure 2 shows the high-pressure relative steady-state populations for two different inputs for a step-ladder model and also for an exponential model of similar efficiency. The relative population of a state below the input is almost independent on how far below the input it is, while the populations fall off rapidly at energies above input. The distributions for the exponential model differ from the step ladder mainly in that the one level where input occurs is more populated than the lower levels, this effect being more extreme in models with higher average energy transferred. This is due to the fact that the exponential models have high probability of no change of energy upon collision. The effect of changing the average energy transferred mainly effects the magnitude of the relative populations, rather than the shape of the distributions.

High Pressure. Excitation Dependence. The effect of changing the excitation (input) energy (*i.e.*, E^+, the excess energy above critical) on the high-pressure efficiencies for various step-ladder models at 300°K (for the butyl-2 decomposition) is shown in Figure 3, where the efficiency resulting from a monoenergetic input is plotted *vs.* the input energy (E^+). The efficiency is very much affected by the step size, the larger step sizes being more efficient; but the shapes of the curves whether for an exponential or step-ladder model at a specified temperature are very similar and thus model distinction can not be made solely by shape. The decrease of the efficiency at high energies is easily rationalized by noting that species formed at higher energies require on the average more collisions to remove all the energy. If this were the only effect, the efficiency would approach unity as the excess energy, E^+, goes to zero.[10] However, due to the law of detailed balancing

$$\frac{p_{ij}}{p_{ji}} = \frac{g_i}{g_j} e^{-(E_i - E_j)/RT} \tag{10}$$

(g_i = density of eigen states when species has energy E_i) which has to be used in constructing the P matrix,[5] there must be a nonzero probability of an "up" transition upon collision if there is a probability for a "down" transition. This is why the levels above the input are populated, and, though this population falls off rapidly with increasing energy above input, it contributes significantly to the total decomposition at low input energies because the unimolecular rate constants rapidly increase with energy in this region. The increasing importance of the more rapid decompositions after an up transition at low energies causes the decrease in the efficiency of inhibiting decomposition in this region.

High Pressure. Temperature Dependence. An example of the effect of the bath gas temperature on the high-pressure efficiency *vs.* E^+ plot is shown in Figure 4. Equation 10 shows that increasing the temperature increases the probability of up transitions at the expense of the down transitions. This results in reduced efficiencies at all E^+ because if down transitions are less probable, more colli-

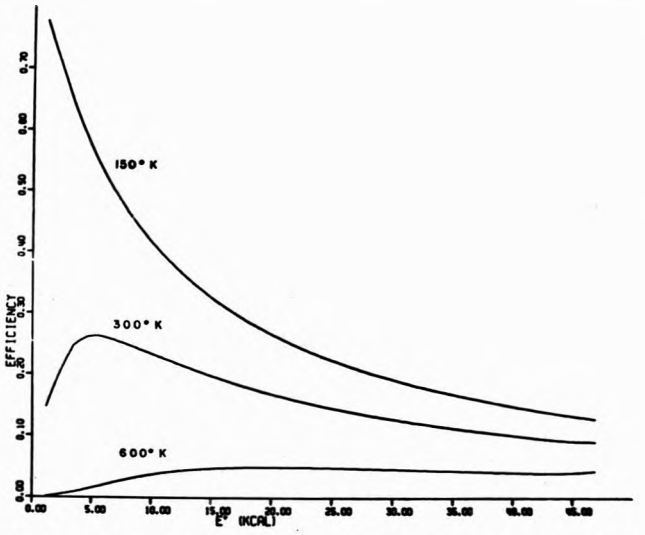

Figure 4. Dependence of $\beta_\infty{}^D$ on E^+ for the butyl-2 system for a step-ladder model with step size of 400 cm^{-1} (1.14 kcal) at various temperatures shown.

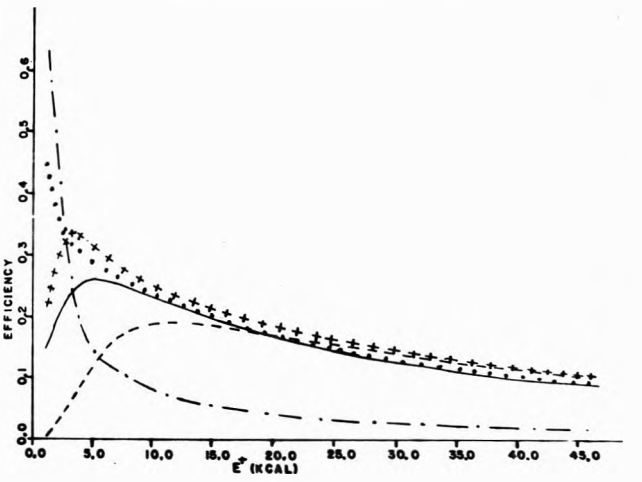

Figure 5. Dependence of $\beta_\infty{}^D$ on E^+ using a step-ladder model (step size = 400 cm^{-1} (1.14 kcal), T = 300°K) for the following chemical activation systems: (——) butyl-2 → propylene + methyl; (- - -) octyl-2 → propylene + pentyl-1; (. . . .) ethyl chloride → HCl + ethylene; (++++) cyclopropane-d_2 structural isomerization *via* H shift; (— · —) $k(E)$ = constant.

sions on the average would be required for stabilization from any level. In addition, the inhibition of efficiencies at lower E^+ is more pronounced at high temperatures because of the importance of the up transitions in causing this effect. As a result, the shape of the efficiency *vs.* E^+ curve changes with temperature as shown, with the maximum efficiency occurring at higher E^+ for higher temperatures.

The importance of up transitions on the efficiencies can be quantitatively assessed by rearranging eq 8

$$\frac{1}{\beta_\infty{}^D} = \left\langle \sum_{j \le i} \frac{k_j}{k_i} R_{ji} \right\rangle_{k_i n_i^{strong}} + \left\langle \sum_{j>i} \frac{k_j}{k_i} R_{ji} \right\rangle_{k_i n_i^{strong}} = \frac{1}{\beta_\infty}\ (\text{low}) + \frac{1}{\beta_\infty}\ (\text{high}) \quad (11)$$

The first term is the contribution to the efficiency due to decompositions from levels lower than those initially formed, and is most important at higher energies. Interestingly, $(1/\beta_\infty)$ (low) appears in most cases we studied to be a nearly linearly increasing function of the input energy. (The only significant deviations were observed in cases with large average energy transferred, high temperature, and rapidly increasing rate constants. Even in those cases, the deviation was mainly in the low E^+ region.) The second term, the contribution to the efficiency due to decompositions from levels higher than input, starts off high and decreases at high inputs. Thus the $(1/\beta_\infty)$ (high) term determines the efficiency at low E^+, while the $(1/\beta_\infty)$ (low) term determines it at high E^+. The apparent linearity of $(1/\beta_\infty)$ (low) suggests that at sufficiently high E^+ or low temperatures, the empirical relationship

$$\beta_\infty{}^D \simeq \frac{1}{C_1 + C_2 E^+} \quad (12)$$

(where C_1 and C_2 depend on the transfer model, the activation system, and the temperature) may be useful. Calculated values of C_1 and C_2 for some of the energy transfer models, temperatures, and chemical activation systems examined are shown in Table I.

High Pressure. Effect of Rate Constants. To examine the importance of the rate constants, the dependence of the high-pressure efficiencies on input level using the same step-ladder energy transfer model for several chemical activation systems was calculated. This is shown in Figure 5. An extreme case is the "constant rate constant" system. Since with this model the rate constants do not increase with energy, up transitions are unimportant in all regions, making $(1/\beta_\infty)$ (high) a small constant. In general, unimolecular rate constants increase with energy; the rate of increase mainly reflects the "tightness" of the activated complex for the reaction. The ethyl chloride[11] decomposition and the cyclopropane[12] isomerization are both examples of reactions with "tight" activated complexes, so their efficiencies most closely resemble those of the "constant rate constant" system. The octyl-2 decomposition[7] (to propylene and pentyl-1) has some loose internal rotations in the activated complex for the decomposition, resulting in rapidly increasing rate constants with energy, which makes up transitions very important. This results in larger $(1/\beta_\infty)$ (high)'s and a much greater depression of the low E^+ efficiencies than found in systems with tighter activated complexes. On the other hand, the $\beta_\infty{}^D$ at high E^+, shown in Figure 5, and the results shown in Table I suggest that the general dependence of the unimolecular decomposition rates on energy have enough in common in a variety of chemical activation systems so that $(1/\beta_\infty)$ (low) (or C_1 and C_2) is relatively insensitive to the system studied. This is seen in Figure 5 by the near agreement at high E^+ of the efficiencies for the several systems (except for the unnatural "constant" system).[3,13]

High Pressure. Model Comparisons. The results shown in Figures 3–5 were for step-ladder models; Figure 6 compares the high-pressure efficiency *vs.* E^+ plot of a step-ladder model with that of an exponential model where the efficiencies are equal when E^+ is 35 kcal/mol. There are no major qualitative differences.[3,14,15] The reduced relative efficiency of the exponential model at lower energies can be explained in terms of the steady-state populations (Figure 2). Because the input level in the exponential case is more populated than the others, there is enhanced decomposition from the level, which results in reduced efficiency of inhibiting decomposition. At higher inputs, this effect becomes less important because of the overshadowing effect of the large number of other populated levels from which decomposition can occur. In fact, the expo-

TABLE I: Calculated Values of C_1 and C_2 (from Eq 12) for Various Energy Transfer Models and Chemical Activation Systems[a]

Energy transfer model			Butyl-2 ↓ propylene + methyl		Octyl-2 ↓ propylene + pentyl-1		Cyclopropane-d_2 ↓ propylene-d_2		Ethyl chloride ↓ HCl + ethylene		$k(E)$ = constant	
Type[b]	$\langle\Delta E\rangle$[c]	Temp, °K	C_1	C_2[d]	C_1	C_2	C_1	C_2	C_1	C_2	C_1	C_2
SL	400	600	4.2	0.40	1.1	0.29	3.6	0.29	3.3	0.35	0	2.0
Exp	550	300	2.9	0.16								
SL	400	300	1.4	0.20	1.5	0.16	1.7	0.16	1.60	0.19	0	1.2
SL	800	300	0.85	0.07	0.93	0.053	0.98	0.058	0.93	0.070	0.27	0.46
SL	1600	300	0.81	0.029	0.85	0.020	0.87	0.024	0.84	0.030	0.40	0.22

[a] Rate constants calculated using the RRKM theory with frequency assignments of molecules and activated complexes given in references shown. [b] SL = step ladder; Exp = exponential. [c] $\langle\Delta E\rangle$ = step size or average energy (in cm^{-1}). [d] C_2 has units of $kcal.^{-1}$

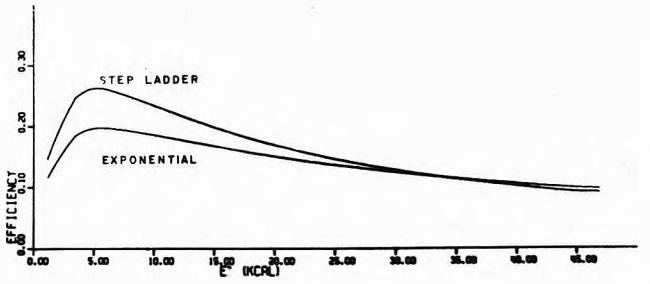

Figure 6. Dependence of $\beta_\omega{}^D$ on E^+ for the butyl-2 system using a step-ladder model (step size = 400 cm^{-1} (1.14 kcal)) and exponential model (average energy = 550 cm^{-1} (1.57 kcal)), both at 300°K. These energies are such that the efficiencies of each model are equal when E^+ = 35 kcal.

nential model becomes more efficient compared to the step-ladder model. In principle, models could be distinguished from experiments in which E^+ is systematically varied. In practice this difference between models loses its significance for broad inputs since an average over many input levels is made, thus smearing out the difference.

Discussion

In external activation experiments, collisions with inert "bath" gases remove excitation energy; but not all gases are equally efficient. The "efficiency" of a weak collider can be defined in three ways: by comparing, (1) apparent rate constants ($\beta_\omega{}^{ka}$); (2) decomposition yields ($\beta_\omega{}^D$); or (3) stabilization yields ($\beta_\omega{}^S$) with what one would obtain if a strong collider were used. $\beta_\omega{}^{ka}$ is conventionally used, but $\beta_\omega{}^D$ and $\beta_\omega{}^S$ (whose product is $\beta_\omega{}^{ka}$) are in several ways more useful concepts.

The efficiency of a weak collider (no matter how defined) depends on more than just the collider–substrate interaction; other factors must be taken into account.

First, the efficiencies depend on the pressure. Both $\beta_\omega{}^D$ and $\beta_\omega{}^S$ decrease monotonically from unity at one extreme in the pressure range to a lower limit (usually nonzero) at the other extreme. $\beta_\omega{}^{ka} = \beta_\omega{}^D$ at high pressure, while $\beta_\omega{}^{ka} = \beta_\omega{}^S$ at low pressure. The intermediate pressure range where $\beta_\omega{}^D$ and $\beta_\omega{}^S$ change most rapidly is where ω is the same order of magnitude as the total decomposition rates of the activated species.

The efficiencies also depend on the energy in excess of the critical energy ($E^+ = E - E_0$) at which the activated species are formed, but the nature of this dependence can vary with pressure. At low pressures an increase of the input energy (*i.e.*, high E^+) drastically decreases the efficiency, while with a decrease of the input energy (*i.e.*, low E^+) the efficiency increases since smaller steps become efficient in stabilization. At high pressures the effect is not so simple. Although $\beta_\omega{}^D$ (= $\beta_\omega{}^{ka}$) decreases at high E^+, as expected, it may also become small at low E^+ when up transitions are significant. This results in the high-pressure efficiency having a maximum at some $E^+ > 0$, the location of that maximum depends upon the temperature and the rate of increase of the rate constants with energy (*i.e.*, the "tightness" of the activated complex).

The bath temperature affects the efficiencies by determining the relative probabilities of up and down transitions through the law of detailed balancing (eq 10). If the temperature is increased, the decreased probability of down transitions causes a relatively uniform reduction of the efficiency in all regions. In the *high-pressure–low* E^+ region, the effect of the temperature is maximized. At low temperatures, the small probability of up transitions permit the high-pressure efficiency to approach unity at low E^+, while at high temperatures, additional decomposition following up transitions can become so important that the high-pressure efficiency may remain very small for small values of E^+.

The rate of change of the rate constants with energy, which reflects the nature of the appropriate activated complex, also affects the efficiencies; but like the temperature, its influence is most important in the *high-pressure–low* E^+ range, where the rate of increase of the rate constant determines just how much additional decomposition occurs after an up transition. The rate constants have little effect on the low-pressure efficiencies; they are only involved in the averaging process for nonmonoenergetic input, so they may be significant only in experiments with very broad spreads of input energies. Interestingly, the efficiencies in the *high-pressure–high* E^+ region seem relatively insensitive to the rates even though the rates are intimately involved in the calculations of these efficiencies. This fact, combined with the observations that at high pressure R_{ji} ($j \leq i$) is approximately constant and that $(1/\beta_\omega)$ (low) *vs.* E^+ is linear (eq 11) implies that the parameter $\Sigma_{j<i}k_j/k_i$ is a linear function of energy (E_i), and is only weakly dependent upon the "tightness" of the activated complex. This may be an artifact of the RRKM rate constant calculational technique used here, but it appears worthy of further investigation.

Conclusion

In order to calculate efficiencies, one needs an energy transfer model. The most important parameter by far for any model is the average energy transferred upon collision; this determines how "efficient" the collider actually is. Details of the models concern the distribution of the

energies transferred; the step-ladder and the exponential models being two very different examples in that respect. Because of the similar results of calculations obtained in the high- (and even moderate) pressure region using the very different step-ladder and exponential models, it appears that low pressure is the only region where such details of the models are important.

The behavior of collisional efficiencies has been interpreted in terms of steady-state populations. Up transitions at high temperature and/or small step size become important and are reflected in the steady-state populations.

Energy transfer is only one of the several aspects of interest in external activation systems. The most sensitive region to obtain energy transfer information is *low-pressure–low* E^+ while the *high-pressure–high* E^+ region is relatively insensitive to the energy transfer model. The importance of energy transfer can thus be minimized or maximized by judicious choice of experimental variables as shown in this paper.

Acknowledgment. One of us (W. P. C.) would like to thank the Lubrizol Corporation for a predoctoral fellowship. A grant for computer time from the Graduate College of the University of Iowa is greatly appreciated.

Appendix. Deactivation Models

The probabilities, p_{ji}'s, in removing energy $\Delta E = E_i - E_j$ from state i are not known *a priori* for systems involving collisions of polyatomics. However, models can be fabricated; shape and $\langle\Delta E\rangle$ are two parameters which grossly characterize the set p_{ij} for all $j \leq i$. The shape describes the spread in the various amounts of energy removed from state i while $\langle\Delta E\rangle$ is the average energy removed, *i.e.*

$$\langle\Delta E\rangle = \sum_{j\leq i} p_{ji}(E_j - E_i)/\sum_{j\leq i} p_{ji}$$

Having the p_{ji}'s for $j \leq i$ the p_{ji}'s for $j > i$ can be determined with the aid of detailed balance and the assumption that $\langle\Delta E\rangle$ is relatively independent of energy. Once the p_{ji}'s are determined for all i and j of interest eq 4 can be solved.

The simplest model is that for an atom with a diatomic molecule in which the p_{ji} are given by selection rules for a harmonic oscillator, *i.e.*

$$p_{ji} = c\delta_{E_j+\langle\Delta E\rangle, E_i}$$

where c is determined from normalization. It is seen that only one specific energy, $\langle\Delta E\rangle$, is transferred per collision. This step-ladder model may or may not hold for polyatomics colliding with other deactivators.

The exponential model has a relatively large number of possible transitions such that the probability for removing energy ΔE decreases as ΔE increases, *i.e.*

$$p_{ji} = ce^{-\Delta E/\langle\Delta E\rangle}$$

where c is determined by normalization.

Other models such as Poisson and Gaussian give efficiency behaviors as calculated from eq 4, which are intermediate between step ladder and exponential so for simplicity only the extreme models (step ladder and exponential) are discussed in this paper.

References and Notes

(1) (a) R. E. Harrington, B. S. Rabinovitch, and M. R. Hoare, *J. Chem. Phys.*, **33**, 744 (1960); (b) G. Kohlmaier and B. S. Rabinovitch, *ibid.*, **38**, 1692, 1709 (1963); (c) *ibid.*, **39**, 490 (1963).
(2) B. S. Rabinovitch and M. C. Flowers, *Quart. Rev., Chem. Soc.*, **18**, 122 (1964); B. S. Rabinovitch and D. W. Setser, *Advan. Photochem.*, **3**, 1 (1964).
(3) D. C. Tardy and B. S. Rabinovitch, *J. Chem. Phys.*, **48**, 5194 (1968).
(4) B. S. Rabinovitch and R. W. Diesen, *J. Chem. Phys.*, **30**, 735 (1959).
(5) D. C. Tardy and B. S. Rabinovitch, *J. Chem. Phys.*, **45**, 3720 (1966); **48**, 5194 (1968).
(6) Reference 1a and M. Hoare, *J. Chem. Phys.*, **38**, 1630 (1963).
(7) M. J. Pearson and B. S. Rabinovitch, *J. Chem. Phys.*, **42**, 1624 (1965).
(8) D. W. Setser, B. S. Rabinovitch, and J. W. Simons, *J. Chem. Phys.*, **40**, 1751 (1964); J. W. Simons, B. S. Rabinovitch, and D. W. Setser, *ibid.*, **41**, 800 (1964); D. W. Setser and J. C. Hassler, *J. Phys. Chem.*, **71**, 1364 (1967).
(9) H. W. Chang, N. L. Craig, and D. W. Setser, *J. Phys. Chem.*, **70**, 954 (1972).
(10) The ethyl system studied by J. H. Current and B. S. Rabinovitch, *J. Chem. Phys.*, **40**, 2742 (1964), does not exhibit this behavior, possibly due to some experimental artifact. The butyl system in ref 1c exhibits the general behavior predicted by our calculations.
(11) K. Dees and D. W. Setser, *J. Chem. Phys.*, **49**, 1193 (1968).
(12) E. W. Waage and B. S. Rabinovitch, *J. Phys. Chem.*, **76**, 1695 (1972).
(13) B. S. Rabinovitch, H. E. Carroll, J. D. Rynbrandt, J. H. Georgakakos, B. A. Thrush, and R. Atkinson, *J. Phys. Chem.*, **75**, 3376 (1971).
(14) J. D. Rynbrandt and B. S. Rabinovitch, *J. Phys. Chem.*, **74**, 1679 (1970).
(15) J. H. Georgakakos and B. S. Rabinovitch, *J. Chem. Phys.*, **56**, 5921 (1972).

Hydrocarbon Surface Species on Cobalt

G. Blyholder* and William V. Wyatt

Department of Chemistry, University of Arkansas, Fayetteville, Arkansas 72701 *(Received August 30, 1973)*

Infrared spectra for ethylene, acetylene, and hydrogen chemisorbed on silica-supported cobalt have been obtained. In the presence of hydrogen, either from gas-phase additions or left on the surface from the reduction procedure, the surface species are mostly saturated hydrocarbons. In the absence of hydrogen many unsaturated species are found. The observation and assignment of a medium intensity band near 1690 cm^{-1} to a carbon–carbon double bond is unique in studies of adsorption on metals in this study of cobalt. A band at 3300 cm^{-1} for a stable surface species formed from acetylene is assigned to a C–H stretch of a surface species containing a carbon–carbon triple bond. The C–H bonds for the absorbed species were found to be labile since evacuation greatly reduced C–H infrared band intensities while hydrogen addition returned it. This effect appears to be more pronounced than previously reported for Ni and Pd. The Co–C bonds are more resistant to hydrogenation than has been reported for Ni–C and Pd–C bonds.

Introduction

Although hydrogenation and dehydrogenation reactions of small hydrocarbons on metal surfaces have been much studied, comparitively little is known about the structure and reactivity of hydrocarbon species while they are actually on the surface. Several infrared investigations of hydrocarbons absorbed on metal surfaces have indicated a variety of surface structures, mostly with C–H stretching frequencies suggesting saturated species.[1,2] The metal-catalyzed exchange of hydrogen and deuterium in hydrocarbons has been used to study C–H bond stability but the relationship of this type of work to the infrared work is not entirely clear. Whereas the infrared work relates mainly to the most stable surface species covering a large fraction of the surface at room temperature, the kinetic exchange experiments may well be pertinent to only a small number of very active sites. This paper will be concerned with the stable species covering an appreciable fraction of a cobalt surface. It is hoped that the insight gained from a knowledge of the most numerous species will aid in understanding the special sites.

Previous infrared studies of adsorbed ethylene and acetylene have yielded the most information about Ni,[3-7] Pd,[5] and Pt[7] which are directly below Ni in the periodic table. A small amount of data has also been reported for Fe[8] and Cu.[5,6] A surprising degree of lability in C–H bonds has been found for hydrocarbon species on Ni and Pd. Since many theories of adsorption on transition metals place strong emphasis on the number of d electrons, the structure and behavior of hydrocarbon species on other transition metals is needed. In this paper the infrared spectra and resulting structural inferences for the surface species formed on silica-supported Co from the interaction of ethylene, acetylene, and hydrogen are presented.

Experimental Section

The experimental technique, cells, and sample preparation were similar to those used previously.[9] The silica-supported Co was prepared from a slurry of the hexahydrate of cobalt nitrate (T. S. Baker, reagent) with Cab-O-Sil (G. L. Cabot Co.) so that an ultimate composition of 15% Co and 85% SiO_2 was produced. The slurry was dried and powdered. Approximately 80 mg of the powder was pressed into a 2.54-cm diameter disk. Reduction of the cobalt nitrate in the disk was carried out in the infrared cell by a flow of dry, oxygen-free H_2 (Airco, dry, 99.9%) at about 400° for 12 hr.

Two distinct cobalt surfaces were produced by the following variation in treatment. The first type was produced by cooling the sample in the presence of hydrogen and then evacuating the sample cells to 10^{-4} Torr. This is expected to produce a hydrogen-covered surface. The second type was produced by evacuation to 10^{-4} Torr while the sample cells were still held at the reduction temperature of 400°. The results indicate that little residual surface hydrogen remained in this case.

The samples transmit infrared radiation over the range from 4000 to 1300 cm^{-1}. Spectra were recorded on either a Perkin-Elmer Model 21 or a Model 337 spectrophotometer.

The ethylene (Matheson Co.) and acetylene (Airco) were purified by subjection to repeated freeze–thaw cycles accompanied by evacuation to 10^{-4} Torr. They were also dried by passing through P_2O_5 at −78°. Hydrogen (Airco) was deoxygenated and dried by passing over Cu turnings at 400° and through a liquid air trap. Each gas was collected in a 1-l. bulb and stored until used.

Spectral Results and Assignments

The spectrum obtained when 10 Torr of ethylene was admitted at room temperature to the sample that had been cooled in H_2 before postreduction evacuation is shown in Figure 1 as well as the spectrum after the ethylene has been evacuated. For this latter spectum infrared frequencies around 2955, 2920, 2880, and 1450 cm^{-1} were obtained. Band assignments for both spectra are listed in Table I. The band at 2955 cm^{-1} was assigned to the asymmetric stretching frequency of a methyl radical while the band at 2920 cm^{-1} was assigned to the asymmetric stretching frequency of a methylene structure. The 2880-cm^{-1} and the 2850-cm^{-1} bands were assigned to the symmetric methyl and methylene stretching frequency, respectively. The band at 1450 cm^{-1} was at best, weak and was tentatively attributed to a methylene deformation mode.

The intensity of the infrared bands resulting from the

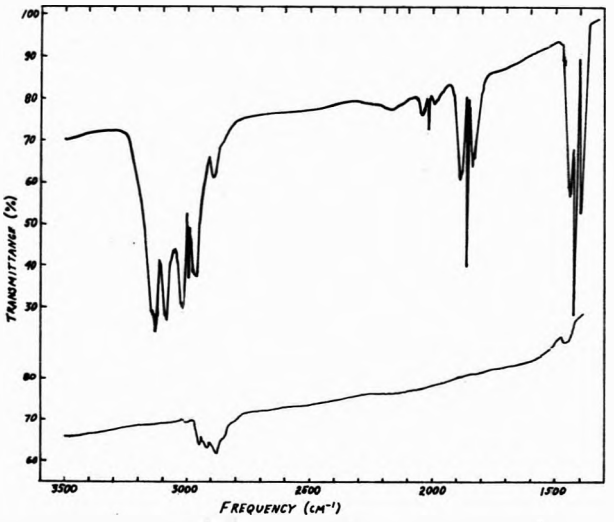

Figure 1. The infrared spectrum of etnylene chemisorbed on silica-supported cobalt (post-reductions evacuation at room temperature): upper spectrum, gas-phase ethylene present (10 Torr); lower spectrum, gas-phase evacuated.

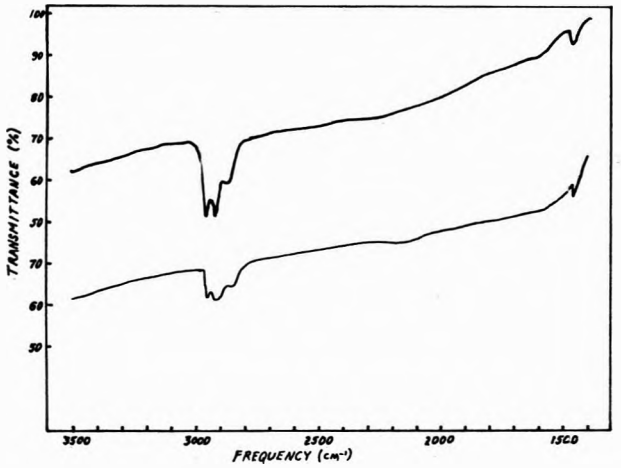

Figure 2. The infrared spectrum of ethylene chemisorbed on silica-supported cobalt showing the result of subsequent hydrogen addition: upper spectrum, hydrogen present (10 Torr); lower spectrum, hydrogen evacuated.

chemisorption of ethylene on cobalt was reduced by extended pumping on the sample cells. When hydrogen gas was added the spectral bands became more intense and indicated an increase in the amount of methyl species present. In fact the C–H band intensity is more intense after H_2 addition as shown in Figure 2 than before H_2 addition as in Figure 1. When hydrogen was admitted to a freshly prepared cobalt surface and ethylene (42 Torr) subsequently added the resulting spectrum was identical with the hydrogenation results of the above processes. Evacuation of the cell produces the reduced C–H band intensity shown in the lower curve of Figure 2. Readmitting fresh hydrogen produced essentially the same intensity bands as were originally present. The intensity increase could not have been due to any condensable gas-phase species produced since no reduction in intensity was observed when a liquid nitrogen cold trap was used to remove any gas-phase species. At no time were completely hydrogenated gaseous alkanes produced in measureable amounts.

When ethylene was admitted to a freshly prepared cobalt sulface in which the post reduction H_2 evacuation was 400°, the observed infrared spectrum indicated more types of surface species than for ethylene on the room temperature evacuated cobalt. After short evacuation of the cell infrared bands were recorded at 2960, 2920, 2890, and 1690 cm^{-1} as shown in Figure 3. A possible weak band above 2960 cm^{-1} was indicated by a leading shoulder and indeed weak bands at 3020 and 3080 cm^{-1} were noted when a sample was run against a silica reference where both sample cells contained gas-phase ethylene. The complete lists of band assignments for Figure 3 are given in Table II.

TABLE I: Frequencies and Band Assignments for Figures 1 and 2

Frequencies, cm^{-1}				
Figure 1		Figure 2		
Upper	Lower	Upper	Lower	Assignment[a]
3130				Gas-phase ethylene
3090				Gas-phase ethylene
3020				Gas-phase ethylene
2995				Gas-phase ethylene
2970				Gas-phase ethylene
	3000	3000		
	2955	2950	2950	Asymmetric CH stretch of CH_3
	2920	2910	2910	Asymmetric CH stretch of CH_2
2890	2880	2870	2880 sh	Symmetric CH stretch of CH_3 or CH
	2850 sh	2850 sh	2840	Symmetric CH stretch of CH_2
2190				Gas-phase ethylene
2060				Gas-phase ethylene
2030				Gas-phase ethylene
2000				Gas-phase ethylene
1900				Gas-phase ethylene
1885				Gas-phase ethylene
1850				Gas-phase ethylene
1450				Gas-phase ethylene
1440				Gas-phase ethylene
1410				Gas-phase ethylene
	1450	1450	1450	CH_2 deformation

[a] References 2, 10, and 11.

The bands at 2960, 2920, and 2890 cm^{-1} were assigned to saturated carbon–hydrogen stretching frequencies. A predominance of methylene groups was indicated by the relative intensities. Band intensity in the C–H region was significantly diminished by evacuation of the reaction cell.

The 1690-cm^{-1} band was not reduced by pumping on the sample. The band was tentatively assigned to a carbon–carbon double bond stretching mode. This assignment would have been stronger if the bands at 3020 and 3080 cm^{-1} could have been confirmed. Other possible causes of this band such as carbon dioxide, water, and surface oxide were eliminated by additional experiments to double check each phase of the procedure. The reaction of acetylene with cobalt surfaces described later strengthens this assignment.

Hydrogenation occurred when hydrogen was admitted to the ethylene-treated cobalt surface described above. The band at 1690 cm^{-1} disappeared slowly and was completely removed after 3 hr (Figure 3). This intensity of the bands assigned to carbon–hydrogen stretching modes changed as expected for hydrogenation of unsaturated and associatively adsorbed ethylene.

TABLE II: Frequencies and Band Assignments for Figure 3

Frequencies, cm^{-1}		
Upper	Lower	Assignment[a]
2960	2970	Asymmetric CH stretch of CH_3
2920	2940 sh	CH stretch of CH_2
2890	2900 sh	Symmetric CH stretch of CH_3 or CH
2830 sh		
1690		C=C stretch
1580		
1450	1460	CH_2 deformation

[a] References 2, 10, and 11.

Hydrogen produced no infrared bands in the region of investigation when admitted to a freshly prepared cobalt surface. The hydrogen-treated surface adsorbed ethylene in a way somewhat intermediate between the hot- and cold-evacuated cobalt surfaces. A band was observed at 1690 cm^{-1} but its intensity was less than that for a hot-evacuated cobalt sample. This indicated that some surface hydrogen had been produced in the preceding treatment.

When acetylene was adsorbed on hot-evacuated cobalt infrared bands were observed at 3300 and 1690 cm^{-1} (Figure 4) as well as those attributed to saturated carbon–hydrogen stretching species as found in the case of ethylene on cobalt.

The band at 3300 cm^{-1} was assigned to an acetylenic carbon–hydrogen stretch and complete assignments for other bands in Figure 4 are listed in Table III. The band at 1690 cm^{-1} was more intense than that of the same band observed when ethylene was adsorbed. On addition of hydrogen to the sample the band at 3300 cm^{-1} was immediately removed and the 1690-cm^{-1} band was more slowly but steadily removed.

The lower spectrum in Figure 4 resulted from the addition of acetylene to a hot-evacuated cobalt surface which had been treated at room temperature for 1 hr with a pressure of 5 cm of hydrogen. A band at 3300 cm^{-1} was initially present. It disappeared rapidly while gas-phase acetylene was present. The intensity of the 1690-cm^{-1} band was slightly less than in the previous case.

The spectrum for acetylene chemisorbed on a cold-evacuated cobalt surface was the same as the lower half of Figure 4. However, the band at 3300 cm^{-1} was not observed.

Discussion

The general features of the surface species that are consistent with the spectra and the assignments are fairly clear but as in the case of most structural assignment based on a limited spectral region there are some ambiguities so the following suggested structure may be regarded as reasonable rather than as completely fixed. The spectra in Figure 1 and the assignments in Table I suggest the presence of I and II.

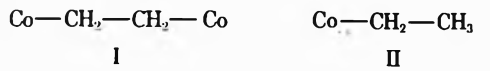

Figure 1 shows the intensity of the methylene stretching frequency (2920 cm^{-1}) to be as great as the methyl-stretching frequency (2955 cm^{-1}). The molar absorptivity of the methylene stretch is less than that of the methyl stretch. Therefore the spectrum indicated a predominance

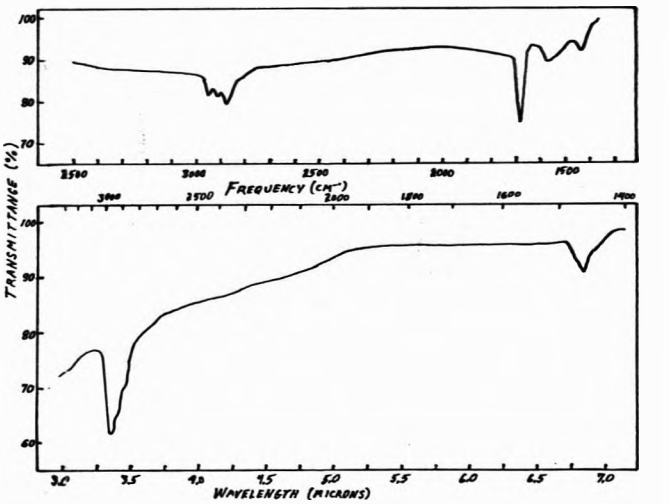

Figure 3. The infrared spectrum of ethylene chemisorbed on silica supported cobalt with a 400° postreduction evacuation and the result of the addition of hydrogen: upper spectrum, after evacuation of the gas-phase ethylene; lower spectrum, hydrogen present (10 Torr).

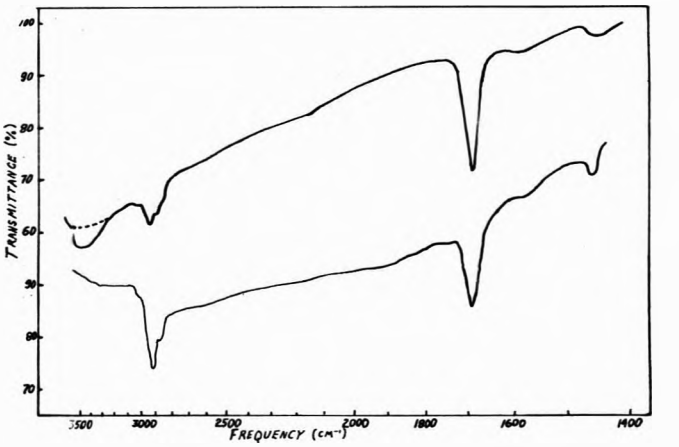

Figure 4. The infrared spectra of acetylene chemisorbed on silica-supported cobalt (postreduction evacuation at 400°): upper spectrum, chemisorbed acetylene; lower spectrum, same except surface previously exposed to hydrogen.

of the associatively adsorbed species (I). The methyl frequency was attributed to the presence of the surface alkyl (II). In view of Peri's interpretation,[4] limited polymerization cannot be eliminated as a possibility. No evidence for unsaturated species is found in Figure 1 since no bands were observed around 3020 cm^{-1} nor were there any that could be assigned to a carbon–carbon double bond stretch.

Evacuation of the gas phase from any of the samples produced a reduction in intensity such as that shown in Figure 2. The reduction was due to the labile nature of the hydrogen to carbon bonds of the surface species. This was confirmed by admitting fresh hydrogen which produced intense C–H bands as shown in the upper curve of Figure 2. The results indicated that a large portion of the cobalt surface was covered with carbon-containing species at all times. The reversibility of intensities with addition and removal of hydrogen alone indicates that the carbon was not removed but remained bonded in some type of "semicarbide" surface species, merely adding or releasing hydrogen as conditions varied.

Since the lower spectrum in Figures 1 clearly indicates the presence of methyl groups when only ethylene has

TABLE III: Frequencies and Band Assignments for Figure 4

Frequencies, cm^{-1}		
Upper	Lower	Assignment[a]
3300		CH stretch of C≡H
3020	3020	
2960	2960	CH stretch of CH_3
2930		CH stretch of CH_2
2890 sh	2900 sh	CH stretch of CH_3
1690	1690	C=C stretch
	1580	
1450	1450	CH_2 deformations

[a] References 2, 10, and 11.

been added, self-hydrogenation or hydrogenation of surface species by hydrogen left on the surface from the reduction process or both must be occurring. The spectra in Figure 3 indicate that rather different results are obtained when ethylene interacts with a cobalt surface for which the postreduction evacuation is at 400° so that little or no hydrogen is left on the surface. The spectral intensity for CH_3 groups is negligible and the medium intensity band at about 1690 cm^{-1} indicates the presence of carbon–carbon double bonds. The presence of the carbon–carbon double bond suggests the presence of structures such as III

$$\underset{\text{III}}{\text{Co—CH—CH}_2} \qquad \underset{\text{IV}}{\text{Co—CH=CH—Co}}$$

and IV. Due to symmetry considerations structure IV would be expected to have a Raman active carbon–carbon vibration as in ethylene. This would leave III as being primarily responsible for the double bond vibration in Figure 3.

The presence of structure IV is also suggested by some other work done in this laboratory.[12] When deuterium gas is added to a sample containing CO and ethylene adsorbed on cobalt, a band appeared at 1680 cm^{-1}, grew, and then decreased in size and finally disappeared. A reasonable explaination for the appearence of this band is that exchange or deuteration of structure IV occurred to produce Co-CH=CD-Co or Co-CH=CHD. The deuterium introduces the necessary asymmetry for the carbon–carbon double bond stretching motion to be infrared active. Further deuteration of these structures gives saturated species so the band at 1680 cm^{-1} disappears. That unsaturated species on the Co surface are readily hydrogenated to saturated species is shown by the lower curve in Figure 3 where hydrogen addition completely removes the band assigned to the carbon–carbon double bond stretch.

Adsorption of acetylene produced even more intense spectra for unsaturated species. The band at 3300 cm^{-1} indicates the presence of a species such as

$$\underset{\text{V}}{\text{Co—C≡C—H}}$$

The presence of C–H stretching bands for CH_2 groups indicated some self-hydrogenation was occurring during acetylene adsorption. The disappearance of the band at 3300 cm^{-1} and reduction in size of the band near 1690 cm^{-1} when hydrogen is admitted to the cell at room temperature shows that the unsaturated species formed from acetylene are readily hydrogenated.

Some of the characteristics of adsorbed hydrocarbon species on cobalt are similar to those for Fe, Ni, Pd, and Cu but there are also some distinct differences. Infrared spectra of ethylene adsorbed on nickel[3,4] show mostly saturated species in the presence of hydrogen and some unsaturated species in the absense of added hydrogen. Similar results have been reported for Pd.[5]

Evacuation of the hydrogenated species on Ni has been reported by Eischens and Pliskin[3] to reduce the C–H band intensity but they did not give the extent of the reduction. This observation indicates that some of the C–H bonds of hydrocarbons adsorbed on Ni are labile. On Pd[5] a reduction of about 30% in the C–H band intensity has been reported to occur upon prolonged evacuation of adsorbed hydrocarbons. For Co Figure 2 indicates about a 70% reduction in the C–H band intensity for extended evacuation. While the comparison is only qualitative these results suggest C–H bonds for hydrocarbon species adsorbed on cobalt are more liable than those on Pd.

In considering the ease of hydrogenation of the metal–carbon bond Eischens and Pliskin note that hydrogen gas treatment of hydrocarbon species on Ni at room temperature removes about 20% of the surface species while Peri[4] observes the production of considerable gas-phase saturated hydrocarbons for similar treatment. Our results for cobalt produce little or no evidence for hydrogen removing surface hydrocarbons at room temperature. Thus it would appear that the Co–C bond is less susceptible to hydrogenation than is the Ni–C bond.

The observation and assignment of the band near 1690 cm^{-1} to a carbon–carbon double bond is unique in studies of adsorption on metals to this study of Co. However it has been reported in homogeneous complexes. Chatt and coworkers[13,14] have observed acetylene complexes of the type $Pt(R(C_6H_5)_3(RC{=}CR'))$ where R and R′ are alkyl groups. These compounds absorb near 1700 cm^{-1} rather than in the free carbon–carbon triple bond region. This was interpreted to indicate a double bond structure existed in the complex. None of the studies of hydrocarbons adsorbed on transition metals other than Co have given a band near 1700 cm^{-1} although many structures containing carbon–carbon double bonds have been proposed. While we have suggested structure III as being responsible for this band clearly other structures in which C–H bonds are replaced by Co–C bonds are possible.

Adsorption of acetylene on Ni,[3,5-7] Pd,[5] and Cu[5,6] gives results similar to those reported here for Co. The most striking difference is that Co gives more unsaturated species as indicated by the presence of a medium intensity band at 3300 cm^{-1} as well as the band at 1690 cm^{-1}. The band at 3300 cm^{-1} was assigned to structure V. For adsorption on Ni and Cu a band was not found in the 3300 cm^{-1} region. For Pd a weak band at 3250 cm^{-1} was found but it could be removed by evacuating the sample in contrast to the 3300-cm^{-1} band on Co which is stable to evacuation.

It has been suggested that ethylene hydrogenation may occur by a mechanism in which gas-phase ethylene abstracts a pair of hydrogen atoms from a surface carbon–hydrogen complex. The lability of the C–H bonds and the resistance of the Co-C bonds to hydrogenation are both factors which are consistant with such a mechanims on a cobalt surface.

References and Notes

(1) M. L. Hair, "Infrared Spectroscopy in Surface Chemistry," Marcel Dekker, New York, N. Y., 1967.
(2) L. H. Little, "Infrared Spectra of Adsorbed Species," Academic Press, New York, N. Y., 1966.
(3) R. P. Eischens and W. A. Pliskin, *Advan. Catal.*, **10**, 1 (1958).
(4) J. B. Peri, *Discuss. Faraday Soc.*, **41**, 121 (1966).
(5) L. H. Little, N. Sheppard, and D. J. C. Yates, *Proc. Roy Soc., Ser. A*, **259**, 242 (1960).

(6) C. P. Nash and R. P. DeSieno, *J. Phys. Chem.*, **69**, 2139 (1965).
(7) N. Sheppard and J. W. Ward, *J. Catal.*, **15**, 50 (1971).
(8) G. Blyholder and A. . Goodsel, *J. Catal.*, **23**, 374 (1971).
(9) G. Blyholder and L. D. Neff, *J. Phys. Chem.*, **66**, 1464 (1962).
(10) L. J. Bellamy, "The nfrared Spectra of Complex Molecules," Wiley, New York, N. Y., 1958.
(11) K. Nakanishi, "Infrared Absorption Spectroscopy," Holden-Day, San Francisco, Calif., 1962.
(12) W. V. Wyatt, Ph.D. Thesis, University of Arkansas, 1971.
(13) J. Chatt, G. A. Rowe, and A. A. Williams, *Proc. Chem. Soc.* (London), 208 (1957).
(14) J. Chatt, R. C. Guy, and L. A. Duncanson, *J. Chem. Soc.*, 827 (1961).

Application of the Polanyi Adsorption Potential Theory to Adsorption from Solution on Activated Carbon. V. Adsorption from Water of Some Solids and Their Melts, and a Comparison of Bulk and Adsorbate Melting Points[1]

Cary C. T. Chiou and Milton Manes*

Department of Chemistry, Kent State University, Kent, Ohio 44242 *(Received July 30, 1973)*

Publication costs assisted by the Office of Research Administration, Kent State University

Adsorption isotherms from water solution onto an activated carbon have been determined, both above and below the underwater melting points, for the following compounds: *o*-, *m*-, and *p*-nitrophenol; 2,5-dichlorophenol; coumarin; phthalide; 3,5-dichlorophenol; *p*-bromophenol; *m*-acetotoluidide; *m*-chloroacetanilide; and 2,2′-bipyridine. Of these compounds, adsorption isosteres on both sides of the underwater melting points have been determined for *o*- and *m*-nitrophenol, phthalide, and coumarin. The isotherms show distinctly higher adsorption on exceeding the melting points. The effect is ascribed to relatively inefficient packing of the solid phases into the carbon pores. The isosteres show first-order transitions at temperatures that are not detectably different from the underwater melting points and that are therefore taken as the melting points of the adsorbates. The identity of the bulk and adsorbate melting points is taken as evidence that the adsorbates are similar in their properties to the corresponding bulk phases. Except for the phenols, the adsorption isotherms of the liquids can be calculated by the previously published modified Polanyi adsorption potential theory, using gas-phase data on the same carbon, together with solute molar volumes and refractive indices. For the phenols (except *o*-nitrophenol), the theory underestimates the adsorption potential by about 20% and requires an empirical factor for each solute to account for the adsorption data.

Introduction

There is good reason to suppose that solids should adsorb onto activated carbon from solution less strongly than the corresponding liquids because the relative inflexibility of the solid structure can make for reduced packing compatibility in fine pores. Manes and Hofer,[2] in applying the Polanyi adsorption potential theory[3] to the adsorption of two dyes from a variety of organic solvents, found the limiting adsorption volumes to be considerably lower than the common limiting volume for the adsorption of gases on the same carbon, and suggested that the discrepancy was due to packing effects. Chiou and Manes,[4] in a study of the adsorption of metal aceylacetonate complexes, found a similar effect. By contrast, studies by Wohleber and Manes[5,6] on the adsorption of organic solvents from water solution, again on the same carbon, showed the limiting adsorption volume to correspond quite closely to the gas-phase limiting volume. However, the observed differences between liquid and solid adsorbates cannot be unequivocally ascribed to the difference in state, since the adsorbates in the cited studies also differed significantly in molecular size, which could affect packing compatibility regardless of state.

We therefore decided to investigate the adsorption behavior, from water solution onto our activated carbon, of a series of organic compounds that melt under water and, for experimental convenience, to limit the investigation to compounds that melt in the approximate range of 30–90°. The approach was as follows: to determine the adsorption isotherms of each compound above and below the bulk melting point; to correlate the resulting data from the point of view of the Polanyi theory (*i.e.*, to plot adsorbed volume against the adsorption potential per unit volume), as in earlier articles in this series;[2,4-6] and to determine whether or not separate correlation curves would be required for the presumed liquid and solid adsorbates.

The investigation promised at the outset to serve two additional purposes. The first was to extend the earlier treatment[5] of the adsorption from water of partially miscible organic liquids to an additional series of partially miscible liquids. The second, which appeared to be even more interesting, was to use adsorption data above and below the bulk melting points to investigate the existence of an adsorbate melting point (or melting range) and possibly to compare the adsorbate and bulk melting points.

Our interest in adsorbate transition temperatures was heightened by the findings of Mattson, *et al.*,[7] that the adsorption of *p*-nitrophenol from water onto an activated

carbon increased anomalously on raising the temperature above 40.3°. They ascribed this anomalous increase to a reversal in sign of the heat of adsorption, which (for reasons to be given later) appeared to be highly unlikely. The fact that their reported temperature for the onset of the anomaly corresponded closely to the *underwater* melting point of their adsorbate strongly suggested that the apparent anomaly could be ascribable to adsorbate melting with a concomitant reduction of the adsorbate volume with improved packing, and led us to the expectation that such anomalies would be more widely observed.

Our findings have been largely in accord with expectations. The adsorption isotherms of a series of 11 compounds, which were selected only on the basis of their melting points and stability, all show significantly lower adsorption below the adsorbate melting points, both on a mass and volume basis. The abrupt increase in adsorption that was reported by Mattson, *et al.*, for *p*-nitrophenol on exceeding the underwater melting point appears to be a general phenomenon for compounds that melt underwater. The limiting adsorbate volumes for the presumed liquid adsorbates are quite close to the values found by Wohleber and Manes[5] for liquids of lower molecular weight, which indicates that molecular size has not yet become a factor in the packing of liquid molecules into the adsorption space. The treatment of Wohleber and Manes[5] for predicting the adsorption of partially miscible liquids from water solution applies to the liquid adsorbates that were here studied, with the exception that the abscissa scale factors calculated for most of the phenols are somewhat below the experimental values. In addition, the adsorbate melting points appear to be true first-order transitions, and the transition temperatures that have been determined for four compounds have in no case been significantly different from the bulk underwater melting points. We take this as suggesting that the adsorbates resemble the bulk phases.

Theoretical

The theory is given in the preceding articles in this series.[2,4,5]

Experimental Section

The activated carbon (Pittsburgh Activated Carbon Division, Calgon Corp., CAL grade activated carbon), apparatus, and experimental techniques were the same as described in previous articles in this series,[2,4-6] except that the high temperature solutions were allowed to settle out for several hours at equilibrium temperatures and the almost clear supernatant solutions were rapidly decanted before final filtration. All solutions were analyzed (after appropriate dilution where necessary) in a Cary 14 (ultraviolet) spectrophotometer. Distilled water was the solvent throughout.

All of the organic compounds were purchased from commercial sources and recrystallized, if necessary, to a minimum purity of 99% as determined by comparison of the molar absorptivities with values from the literature.[8] All compounds used in the determination of the isosteres were recrystallized.

The solubilities (c_s) of the solid solutes at 25° (except for 3,5-dichlorophenol at 22°) and at above-melting temperatures were determined by saturation of water solutions in the shaker bath, followed by spectrophotometric analysis. The densities of the solid solutes were either taken from the literature or determined by a float-and-sink method on individual crystals. Densities of the corresponding pure molten solutes above their melting points were determined to within ±2% by simply weighing measured volumes of the melts; these values were used to convert the weights of liquid adsorbates to volumes. No temperature correction was made for the densities of liquids with underwater melting points well below the normal melting points. The molar volumes, $\bar{V}$, later used in calculating $\epsilon/4.6\bar{V}$ in all cases refer to the molar volumes of the liquid adsorbates.

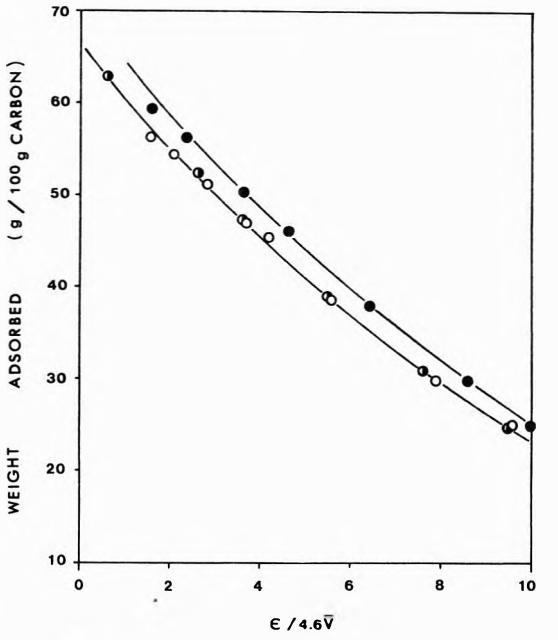

Figure 1. Weight of adsorbed *p*-nitrophenol as a function of $\epsilon/4.6\bar{V}$ (= $(T/\bar{V})\log c_s/c$) at 42 (●), 25 (○), and 42–25° (◑).

The solubilities and densities for each solid and liquid compound at the below-melting and above-melting temperatures are included in Table IV.[9]

In order to show that the observed lower adsorption of solid adsorbates is a true equilibrium effect, the reversibility of six solid-phase adsorption isotherms was tested by first equilibrating the solutions above the melting point for the regular 16 hr, followed by cooling and reequilibration. No hysteresis was observed. Underwater melting points were readily determined as the stationary temperatures on cooling mixtures of the melts with water. Refractive indices of the melts were determined in an Abbé-type refractometer with heated prisms. The data are included in Table III.[9]

Results and Discussion

The adsorption isotherm data are all given in Table I,[9] as weight loading (g/100 g of carbon) *vs.* equilibrium concentration (g/l.). The adsorption isostere data are given in Table II,[9] as equilibrium concentration *vs.* temperature, for loadings as specified; because of the low equilibrium concentrations, the loading on the carbon does not change significantly with changing equilibrium concentration. Figures 1 and 2 show the adsorption isotherm data plotted as weight loading *vs.* $(T/V)\log c_s/c$ (= $\epsilon/4.6\bar{V}$), where ϵ is the adsorption potential, for *p*-nitrophenol and for phthalide, where c and c_s are the respective equilibrium and saturation concentrations. This type of plot has been chosen to show the increase in mass loading for a given relative concentration on raising the temperature above the underwater melting point. All of the determined isotherms

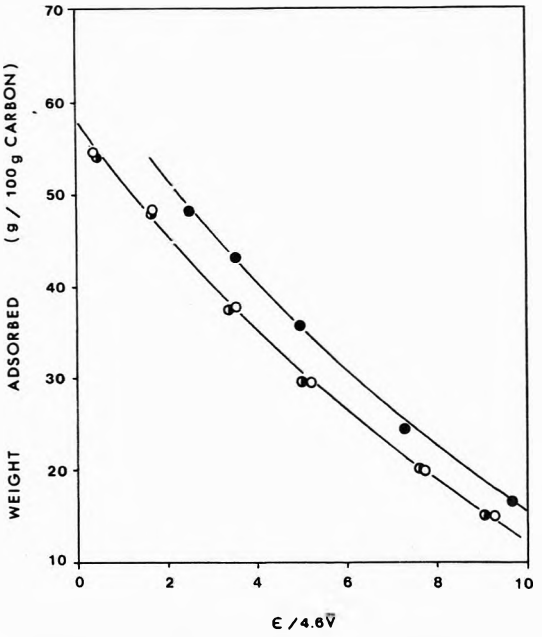

Figure 2. Weight of adsorbed phthalide as a function of $\epsilon/4.6\bar{V}$ at 63 (●), 25 (○), and 63–25° (◑).

show the same effect. We show the plot of *p*-nitrophenol to confirm the experimental findings of Mattson, *et al.*,[7] and the plot of phthalide to show the typical behavior of the nonphenols. Similar plots, which have been omitted to save space, may be readily constructed from the data of Tables I and IV.

Figures 3 and 4 show the data for nitrophenol and for phthalide, this time plotted as correlation curves, *i.e.*, as plots of the log of the adsorbed volume *vs.* $\epsilon/4.6V$, the factor of 1/4.6 being retained for conformity with the notation of earlier publications. In Figure 4, the solid line through the points for the adsorption of solid is simply the best fit through the points; however, the dotted line through the liquid adsorption points is the theoretical curve calculated by the Wohleber–Manes[6] method for correlating the adsorption of partially miscible liquids. This line is essentially the gas-phase hydrocarbon correlation line for the carbon, as determined from gas-phase adsorption (a similar correlation line could have been drawn from the results of Wohleber and Manes on the adsorption of one of their partially miscible liquids from water solution), with an abscissa scale factor calculated from the molar volume, the refractive index, and an empirical scale factor determined by Wohleber and Manes for the adsorption of water. In the calculation of this line there are no adjustable parameters, and its fit to the data illustrates the extent to which the corresponding adsorption isotherms could have been calculated from theory. In Figure 3 the dotted line is again the theoretical line as calculated in Figure 4, and it may be seen to be not nearly as good a fit to the data. The lack of fit appears to be due to the abscissa scale factor; the alternately dotted and dashed line is the same as the dashed line, except for application of an empirical scale factor, which is apparently necessary to fit the data for all of the phenols studied, with the exception of o-nitrophenol. Again, Figure 3 is typical for the phenols (with the exception just noted), and Figure 4 is typical for all of the others. Table III[9] includes the theoretical and experimental scale factors (γ_{sl}) required to bring the points for liquid-phase adsorption into the kind

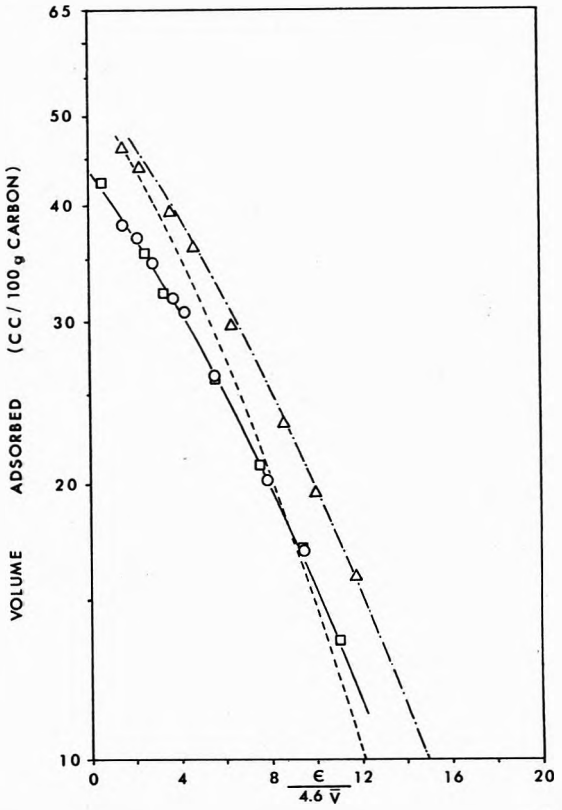

Figure 3. Correlation curves (volume adsorbed *vs.* $\epsilon/4.6\bar{V}$) for *p*-nitrophenol at 42 (△), 25 (○), and 42–25° (□): (- - - -) theoretical curve, no adjustable parameters; (– • –) theoretical curve empirical scale factor (theoretical factor × 1.2); (—) best fit through low-temperature data.

of coincidence that is illustrated in Figures 3 and 4. It should be pointed out that in calculating the adsorbate molar volumes in the ordinates in Figures 3 and 4 we have used the liquid densities to correlate the data above the melting point and the solid densities below the melting point. This could in itself have produced a separation between the correlation curves for liquid and solid, even in the absence of any real packing effects. Figures 1 and 2, and the similar figures that may be drawn from the data of Table I, demonstrate that the presumed packing effect is not merely an artifact of the calculation method. Finally, the low-temperature points of Figures 1–4 contain a number of points representing preequilibration above the melting point and demonstrate the reversibility of the low-temperature isotherms.

Figures 5 and 6 are isostere plots of log c *vs.* $1/T$ for o-nitrophenol, *m*-nitrophenol, phthalide, and coumarin. The intersection of the lines of different slope, or the sawtooth discontinuity between the lines, is taken as locating or bracketing the transition temperature, or adsorbate melting point, which can be localized from the data to about ±1°. The bulk underwater melting points are given in Table III. The estimated transition temperatures for all four isosteres were identical with the corresponding underwater melting points.

We now consider the results exemplified by Figures 1–4. These results first show quite clearly that there is a clear demarcation between the correlation curves, on a mass basis or on a volume basis, for adsorption above and below some fixed temperature for each solute, and that this transition temperature is at least in the region of the underwater melting point. If the temperature is increased

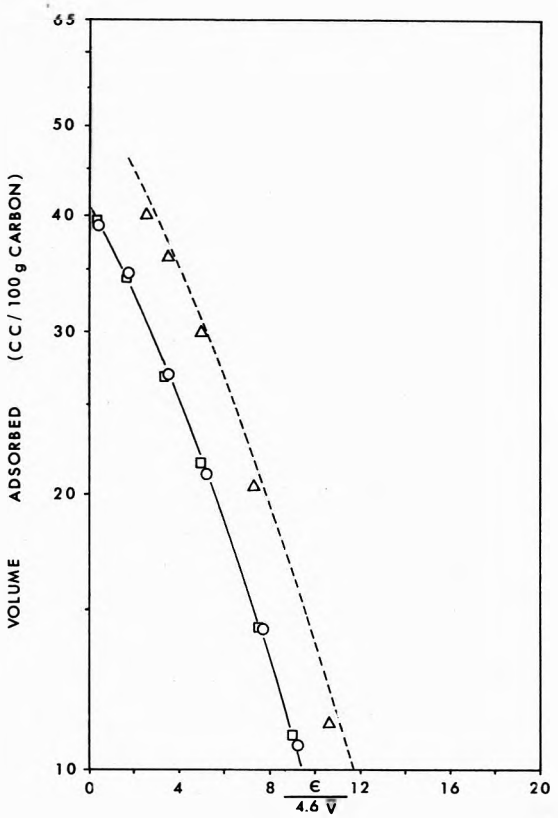

Figure 4. Correlation curves (volume adsorbed *vs.* $\epsilon/4.6\bar{V}$) for phthalide at 63 (△), 25 (○), and 63–25° (□): (- - - -) theoretical correlation curve with no adjustable parameters; (—) best fit to the low-temperature data.

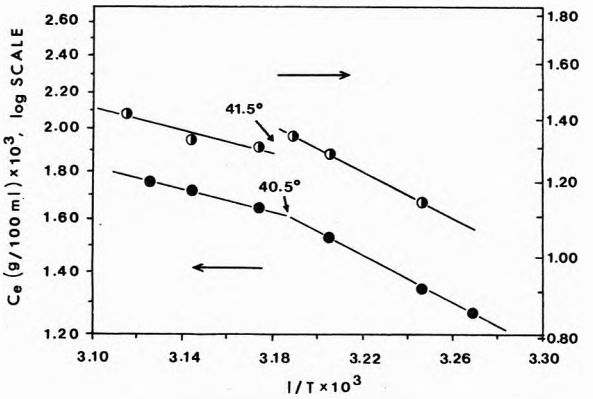

Figure 5. Adsorption isosteres for o-nitrophenol (◑, right scale) and *m*-nitrophenol (●, left scale). Indicated numbers are estimated transition temperatures.

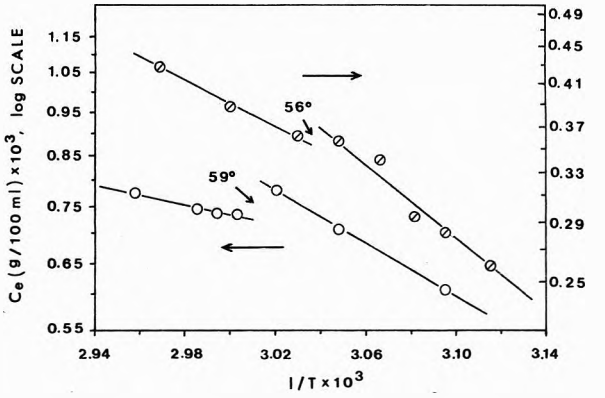

Figure 6. Adsorption isosteres for coumarin (Ø, right scale) and phthalide (○, left scale). Indicated numbers are estimated transition temperatures.

from below to above the transition temperature over a reasonably narrow range, there will be either a reduction in relative concentration at constant loading, or else an increased loading at constant relative concentration. This is the effect that was reported by Mattson, *et al.*,[7] for the adsorption of *p*-nitrophenol on increasing the temperature above 40.3°, and it appears to apply generally to solutes that melt underwater. Mattson, *et al.*, interpreted their observation in terms of steadily increasing adsorption with increasing temperature rather than in terms of a discontinuity, and this interpretation led them to account for their observation on the basis of a reversal of the sign of the heat of adsorption. Since the entropy change on adsorption from dilute solution is negative, it must follow, as pointed out by Brunauer[10] for gas adsorption, that the adsorption must be exothermic, since an endothermic adsorption would be endergonic. The explanation in terms of a reversal of the sign of the heat of adsorption is therefore unacceptable on thermodynamic grounds. If however, we analyze the data from the point of view of the Polanyi theory, we immediately recognize the discontinuity between the two correlation curves (which could otherwise easily be mistaken for a region of increasing adsorption with increasing temperature). We shall see, as a matter of fact (Figures 5 and 6), that on either side of the discontinuity the adsorption continues to decrease continuously in normal fashion with increasing temperature, and that the enthalpy of adsorption is normally exothermic on both sides of the transition temperature. Finally, the demarcation between what we may now presume to be the adsorption of liquid and of solid now allows us to determine with some accuracy the temperature of the transition and to see how close it comes to the underwater melting point. This will be discussed later.

Consider now the magnitudes of the limiting adsorption volumes. As illustrated in Figures 3 and 4, the limiting volumes for the liquid-phase correlation curves are comparable to the corresponding volumes found by Wohleber and Manes[6] in the adsorption of some (room-temperature) organic liquids, which volumes were in turn comparable to limiting volumes for gas-phase adsorption on the same carbon. The present results indicate the absence of any major packing anomalies in the liquid phase for the somewhat larger adsorbate molecules of this investigation.

The reduction in limiting adsorption volume in going from liquid to solid is not exactly constant from compound to compound, but averages to about a 15% reduction relative to the liquid phase. This reduction is interpreted as reflecting relatively inefficient packing of solid crystallites in the adsorption space, the volume of which is assumed to be constant. The limiting volumes observed here are higher than was observed by Manes and Hofer[2] in the adsorption of their two dyes. However, they were of larger molecular size than the compounds studied here, which suggests, as one might expect, that packing inefficiencies in the solid phase increase with increasing molecular size. In the present work the packing effect is clearly distinguishable from molecular sieving, since we compare the solid and liquid phases of the same substances.

We should note in passing that the adsorbate volumes for the liquid phases have been calculated on the assump-

tion that the densities of the liquids are not significantly different at the underwater melting points from their values at the pure melting points where they were determined. Moreover, we have made no correction for the volume of dissolved water in the adsorbed liquid phase. The water content of the bulk liquid phase may be estimated to be about 1% by weight for each 4–5° depression of the melting point. In all cases but two (*p*- and *m*-nitrophenol) the water content was estimated as not more than 5% in the bulk phase; it was therefore neglected in making the calculations.

Before leaving Figures 3 and 4, let us consider their implications for the prediction of adsorption isotherms from water solution. Figure 4 illustrates the extent to which the adsorption data of all of the nonphenolic compounds here investigated could be accounted for by the treatment by Wohleber and Manes[6] of the adsorption of partially miscible liquids. Again we emphasize that there are no adjustable parameters in the calculation of the theoretical curve in Figure 4. The fit of the theoretical curve is not as good in Figure 3, which again is illustrative of our results with phenols (except for *o*-nitrophenol, which is not anomalous). In Figure 3 the Polanyi theory applies, in that one can fit the experimental data with the correlation curve for the carbon that was derived from gas-phase adsorption. However, the calculation of Wohleber and Manes[6] (based on the earlier article by Manes and Hofer[2]) underestimates the abscissa scale factor by about 20%. Anomalously strong adsorption of phenols has been reported, for example by Radke and Prausnitz,[11] who ascribed it to specific interaction of phenols with the carbon surface. It is interesting that *o*-nitrophenol, which is intramolecularly hydrogen bonded, does not show the typical anomalous behavior (from our point of view) of phenols, and it is tempting to associate the anomalous behavior of phenols with intermolecular hydrogen bonding. However, we should expect hydrogen bonding effects of phenols to be swamped out in water solution.

We now consider the determination of the adsorbate melting points and their implication for the state of the adsorbates. Figures 5 and 6 show the transition temperatures to be equal to the underwater melting points within the precision of the measurement, which is about 1°. The plots show discontinuities in the adsorption amounts as well as in the slopes, *i.e.*, there is a sawtooth intersection at the transition temperature. This sawtooth is of course consistent with the existence of separate correlation curves for the liquid and solid adsorbates; it is ascribed to the increase in adsorption potential at the adsorbate–solution interface (Polanyi model) as the newly formed melt shrinks into the adsorption space. The fact that adsorption does not detectably change the transition temperature is in keeping with the Polanyi model, in which the adsorbed and bulk phases have essentially the same properties. Moreover, the similarity in properties implied for the bulk and adsorbed phases is for coverages less than one average monolayer. For example, for *o*-nitrophenol, with an estimated surface area of 52 Å^2 (assumed flat configuration; measured from a molecular model), an average monolayer for our carbon of 1140 m^2/g is approximately 50 g/100 g of carbon. Since the other adsorbates have approximately the same densities, one may estimate the range of coverages in the isosteres at from 60% (o-nitrophenol) to approximately 30% (phthalide) of a monolayer, which were the lowest coverages at which we could measure equilibrium concentrations with sufficient accuracy for isostere plots.

Conclusions

(1) For all 11 compounds studied, exceeding the underwater melting point results in a sharp increase in the adsorption from water solution onto activated carbon. The effect is ascribed to less efficient packing of the solid in the adsorption space.

(2) Adsorption isosteres on four compounds have shown the existence of adsorbate transitions at temperatures that are not detectably different from the bulk underwater melting points, and that may be considered as adsorbate melting points. The identity of bulk and adsorbate melting points suggests similarity between the bulk and adsorbate phases.

(3) Adsorption above the melting point can be accounted for by a modified Polanyi adsorption potential theory. No adjustable parameters are needed for the nonphenolic compounds and o-nitrophenol; an abscissa scale factor about 20% higher than the theoretical factor is needed to account for the adsorption of the phenolic compounds studied.

Supplementary Material Available. Tables I–IV will appear following these pages in the microfilm edition of this volume of the journal. Photocopies of the supplementary material from this paper only or microfiche (105 × 148 mm, 24× reduction, negatives) containing all of the supplementary material for the papers in this issue may be obtained from the Journals Department, American Chemical Society, 1155 16th St., N.W., Washington, D. C. 20036. Remit check or money order for $3.00 for photocopy or $2.00 for microfiche, referring to code number JPC-74-622.

References and Notes

(1) Based on a thesis submitted by C. C. T. Chiou to Kent State University in partial fulfillment of the requirements for the Ph.D. Degree.
(2) M. Manes and L. J. E. Hofer, *J. Phys. Chem.* **73**, 584 (1969).
(3) (a) M. Polanyi, *Verh. Deut. Phys. Ges.*, **16**, 1012 (1914); **18**, 55 (1966); *Z. Elektrochem.*, **26**, 370 (1920); (b) M. Polanyi, *Z. Phys.*, **2**, 111 (1920).
(4) C. C. T. Chiou and M. Manes, *J. Phys. Chem*, **77**, 809 (1973).
(5) D. A. Wohleber and M. Manes, *J. Phys. Chem.*, **75**, 61 (1971).
(6) D. A. Wohleber and M. Manes, *J. Phys. Chem.*, **75**, 3720 (1971).
(7) J. S. Mattson, H. B. Mark, Jr., M. D. Malbin, W. J. Weber, Jr., and J. C. Crittenden, *J. Colloid Interface Sci.*, **31**, 116 (1969).
(8) "Organic Electronic Spectral Data," Vols. 1–6, Interscience, New York, N. Y.
(9) See paragraph at end of paper regarding supplementary material.
(10) S. Brunauer, "Adsorption of Gases and Vapors," Vol. 1, Van Nostrand, Princeton, N. Y., 1943.
(11) C. J. Radke and J. M. Prausnitz, *Ind. Eng. Chem., Fundam.*, **11**, 445 (1972).

Partial Molal Volumes of Ions in Organic Solvents from Ultrasonic Vibration Potential and Density Measurements. I. Methanol

F. Kawaizumi[1] and R. Zana*

C.N.R.S., Centre de Recherches sur les Macromolécules, 67083 Strasbourg, Cedex, France *(Received May 21, 1973; Revised Manuscript Received December 3, 1973)*

The partial molal volumes of monovalent ions in methanol have been obtained from ultrasonic vibration potential and density data for solutions of uni-univalent electrolytes. The ionic partial molal volumes are found to be smaller in methanol than in water. The use of Hepler's equation has permitted us to estimate the geometric and electrostrictive contributions to the partial molal volumes of ions in methanol. The electrostriction appears to be larger for tetraalkylammonium ions than for alkali metal and halide ions. Also, the electrostriction of ions has been found to be larger in methanol than in water. These results are explained in terms of differences in the content of the solvation layer of ions in methanol. The void space around ions appears to be smaller in methanol than in water.

I. Introduction

In the past few years electrochemists have shown increasing interest in ions in organic solvents[2] thereby increasing the necessity for more data on these systems. Among the various quantities which characterize ions in solution, ionic partial molal volumes are of particular importance as they permit quantitative studies of a variety of phenomena.[2a,3,4] This has led some workers to tentative estimates of ionic partial molal volumes in methanol[5-7] by means of two[3,8] of the numerous empirical methods[3,8-12] which have been used in the case of aqueous solutions to split the partial molal volume $\bar{V}_2^0$ of an electrolyte into the individual contributions $\bar{V}_+^0$ and $\bar{V}_-^0$ of the cation and anion. These two methods[3,8] yield two sets of ionic partial molal volume values which are quite similar for aqueous solutions but clearly incompatible for methanol solutions. For instance, values as different as -1[6] and $+9.3$[7] cm^3/mol have been obtained for $\bar{V}^0(Cl^-)$ in methanol.

In view of this situation we have undertaken the determination of the partial molal volumes of ions in organic solvents by means of the still unique experimental method[13] available to obtain these quantities. This method combines ultrasonic vibration potential[14,15] (uvp) and $\bar{V}_2^0$ data of electrolytic solutions. The purpose of this paper is to report $\bar{V}_2^0$ data (obtained from density measurements) and uvp data for a series of uni-univalent electrolytes in methanol from which the partial molal volumes of monovalent ions have been obtained with an accuracy of about ± 2 cm^3/mol, by means of the following equations[13-15]

$$\bar{V}_2^0 = \bar{V}_+^0 + \bar{V}_-^0 \quad (1)$$

$$\Phi = 1.037 \times 10^{-6} v a [t_+(M_+ - d_0\bar{V}_+^0) - t_-(M_- - d_0\bar{V}_-^0)] \quad (2)$$

Φ is the amplitude in μV of the uvp for a moderately dilute solution of uni-univalent electrolyte, v is the velocity of ultrasound (cm/sec) in the solvent, a is the velocity amplitude of a particle in the sound field (cm/sec), t_+ and t_- are the transport numbers of the cation and anion at infinite dilution, M_+ and M_- are their molar masses (g/mol), and d_0 is the density of the solvent (g/cm^3).

II. Experimental Section

Dried freshly distilled methanol and dried salts of reagent grade purity have been used for the preparation of all electrolyte solutions.

1. Density Measurements. The vibrating densitometer[4,16] has been used for this purpose. All solutions have been prepared by weighing-in electrolyte and solvent. The apparent molal volume φ has been calculated according to

$$\varphi = \frac{M}{d_0} - 10^3 \frac{d - d_0}{d_0 c} \quad (3)$$

where d_0 and d are the densities of the solvent and of the solution, M is the molecular weight of the electrolyte, and c the molar concentration.

The densitometer was calibrated prior to the measurements using air and deionized distilled water. The values of d_0 obtained for methanol ranged from 0.786256 to 0.786530 according to the origin of the solvent and its storage time. These differences result very likely from changes in the water content of the various solvent samples. However, they did not matter much as the same solvent sample was used for measuring d_0 and for preparing the electrolytic solutions. The small water content of the solvent (<0.02%) did not affect the values of φ_2 as the apparent molal volume of CsCl was found to be the same in pure methanol and in a 99% methanol–1% H_2O mixture (v/v) as will be seen below. Such a result is likely to hold true for all uni-univalent electrolytes studied in this work. The experiments were reproducible to within 0.00001 g/cm^3. The overall accuracy on φ_2 is thought to be ± 0.2–1 cm^3/mol depending on concentration. This accuracy may appear quite low with respect to that for aqueous solutions. However, it allows $\bar{V}_2^0$ determinations to within ± 1 cm^3/mol and appears to be sufficient for the purpose of this work.

2. Uvp Measurements. Uvp's are generated by pulse-modulated ultrasonic waves at a frequency of 200 kHz. The equipment used in this work is essentially identical with that previously described[13] except for the acoustic cell which is water tight and made of Teflon and glass in order to withstand organic solvents.

Owing to the difference of acoustic impedance between

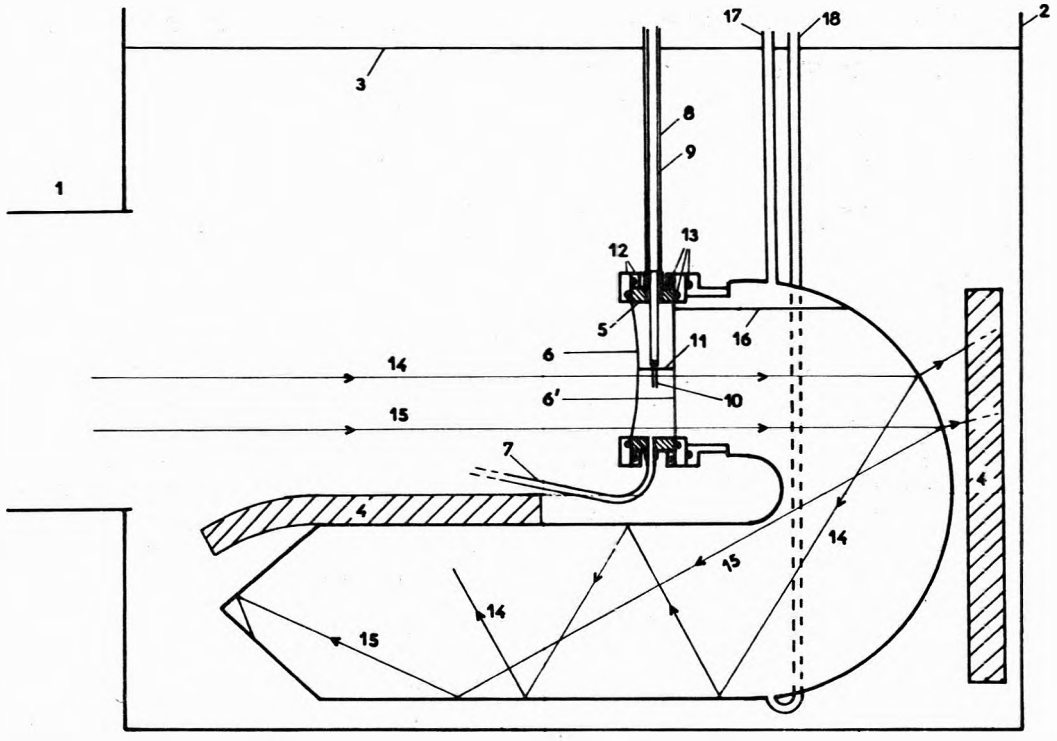

Figure 1. Acoustic cell and its attachment: (1) plastic pipe for the propagation of the ultrasonic beam between the emitter and the acoustic cell; (2) plexiglass tank (60 × 60 × 70 cm); (3) water level in the tank; (4) sheets of butyl rubber acoustically matched to water; (5) acoustic cell (glass cylinder); (6 and 6′) mylar membranes; (7) Teflon draining and filling tube, connected with the cell through a Teflon plug; (8) brass tubing, i.d. 2.9 cm connected with the cell through a Teflon plug; (9) double probe assembly; (10) platinum electrodes (length 15 mm, diameter 0.2 mm); (11) level of solution within the cell; (12) stainless steel rings holding the mylar membranes and ensuring the water tightness of the cell; (13) rubber O rings; (14 and 15) path of the ultrasonic beam in the cell and its attachment; (16) solvent level within the attachment; (17) filling tube; (18) drain.

the organic solvent in the cell and the water in the tank, reflection of the incident beam at the back side of the cell may give rise to standing waves within the cell and perturb considerably uvp measurements. In our set-up standing waves were avoided by assembling to the back side of the cell a hollow brass attachment with a square cross section (15-cm side) and a shape as shown in Figure 1. The connection between cell and attachment is water tight and the solvent filling the attachment is the same as in the cell, thus eliminating reflections. Also, the end of the attachment is shaped in order to enhance interferences between incident beams. Finally, the total path length traveled by the beam within the attachment is about 120 cm thus providing a delay time of 0.8–1.2 msec depending on the solvent. As the pulse duration is about 0.6–0.7 msec no standing waves can occur within the cell. An absorbing sheet of butyl rubber set behind the attachment (see Figure 1) ensures a practically total absorption of the waves which may be transmitted through the attachment wall.

Acoustic cell and attachment are fixed to a mechanical device which allows a precise positioning of the double probe assembly,[13] used for detecting uvp's, in the sound field. The measurements were always performed at the position corresponding to a maximum effect, with the junction between the platinum probes and the double probe Teflon tip out of the solution under study[13] (see Figure 1).

With organic solutions, uvp signals were often fluctuating, likely because of cavitation. These fluctuations were suppressed by reducing the pulse length (0.7 msec as compared to 1.2 msec for measurements in water) and the pulse repetition frequency.

The velocity amplitude a (eq 2) was determined by measuring the uvp of aqueous solutions of RbCl and CsCl for which the values of Φ/a are known.[13] However, when organic solvents replace water the velocity amplitude within the cell is modified as part of the ultrasonic beam is reflected at the front side of the cell. The new velocity amplitude was then obtained as shown in part V.

Additions of water to the electrolyte solutions within the cell did not change the value of Φ, up to a water content of 1%.

III. Apparent Molal Volumes of Electrolytes in Methanol

Density measurements have been performed on ten 1-1 electrolytes (see Table I) and the apparent molal volumes φ calculated using eq 3. The Redlich–Rosenfeld equation[17] has been used to obtain $\bar{V}_2^0$. For electrolytic solutions in methanol, this equation becomes[5]

$$\varphi_2 = \bar{V}_2^0 + 15.77c^{1/2} + hc \qquad (4)$$

$\bar{V}_2^0$ was obtained by plotting $\varphi_2 - 15.77c^{1/2}$ *vs.* c and extrapolating to zero concentration as shown in Figures 2 and 3. The straight lines in Figures 2 and 3 were drawn by hand. The limited solubility of KNO_3 in methanol prevented measurements in a larger concentration range. $\bar{V}^0(KNO_3)$ was obtained by assuming for $h(KNO_3)$ a value close to that for the other electrolytes of Figure 3. The results of Figures 2 and 3 indicate an average error of about ±1 cm³/mol on the values of $\bar{V}_2^0$. For all of the electrolytes studied in this work h was found to be negative. Such a behavior is expected if an extended limiting law is used.[1] The extrapolation procedure using Masson's equation,[18] *i.e.*, the plots of φ_2 *vs.* $c^{1/2}$ yielded $\bar{V}_2^0$ values

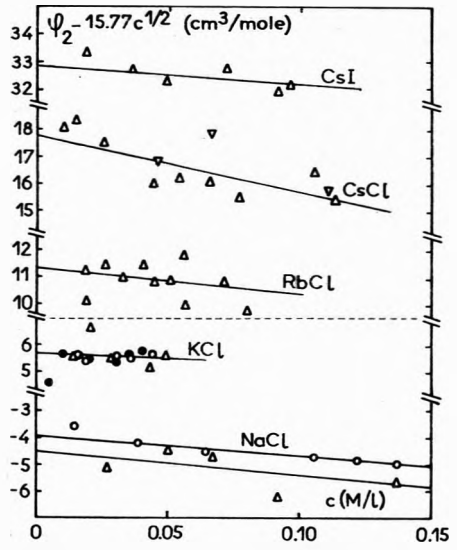

Figure 2. Variation of $\varphi_2 - 15.77c^{1/2}$ *vs.* c for alkali metal chlorides and CsI at 25°: (△) our results in methanol; (▽) results for CsCl in 99% methanol–1% H_2O (v/v); (○) results from ref 20; (●) results from ref 19.

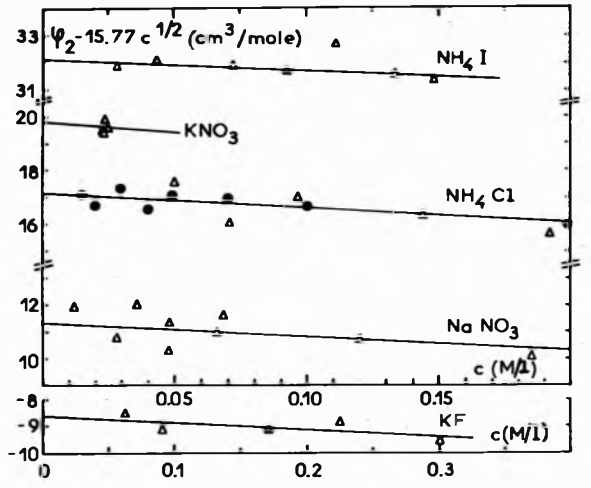

Figure 3. Variation of $\varphi_2 - 15.77c^{1/2}$ *vs.* c for NH_4I, NH_4Cl, KNO_3, $NaNO_3$, and KF at 25°: (△) results obtained in this work; (●) results from ref 19.

slightly above (0.1–0.5 cm³/mol) those obtained by means of eq 4.

Figures 2 and 3 show a satisfactory agreement between our results and those reported by other workers for KCl,[19,20] NH_4Cl,[19] and NaCl.[20]

On the other hand, the results relative to CsCl (Figure 2) show that both φ_2 and $\bar{V}_2^0$ are, within experimental accuracy, not affected by the presence of up to 1% H_2O in the solutions.

The values of $\bar{V}_2^0$ and h obtained from the results of Figures 2 and 3 are listed in Table I where are also given results for other salts obtained by means of eq 3 and 4 and density data from various sources.[19-22] The value $\bar{V}^0(NaBr) = 1$ cm³/mol obtained from the data of Gibson[21] was preferred to the value $\bar{V}^0(NaBr) = 5.1$ cm³/mol reported by Hamann and Lim[23] because these authors did not report any of their density data. Also, the results of Kaurova and Roschina[24] from where Padova[6] obtained $\bar{V}_2^0$ for LiCl, NaCl, and NaBr were discarded as density measurements in this work did not appear to be of sufficient accuracy to allow calculations of φ_2. Moreover the density of the methanol used in these measurements was not given.

TABLE I: Partial Molal Volumes of Uni-Univalent Electrolytes in Methanol at Infinite Dilution and 25°

Electrolyte	$\bar{V}_2^0$, cm³/mol[d] This work	$\bar{V}_2^0$, cm³/mol[d] Other works	h,[d] cm³ l./mol²	t_+[b]	t_-[b]
NaCl	−4.5	−3.9[c,e]	−9	0.463	0.537
NaBr		1.0[f]	−5.3	0.444	0.556
NaI		11.1[e,f]	−6.8	0.418	0.582
$NaNO_3$	11.3		−5	0.425	0.575
KF	−8.6		−2.3	0.557	0.443
KCl	5.7	5.7[e,g]	−4	0.500	0.500
KBr		11.2[g]	−4	0.482	0.518
KI		21.1[e,h,g]	−4.5	0.455	0.545
KNO_3	19.8			0.461	0.539
NH_4Cl	17.1	17.1[g]	−5	0.525	0.475
NH_4I	32.1		−4	0.479	0.521
RbCl	11.3		−9	0.516	0.484
$RbNO_3$	26.1[a]			0.478	0.522
CsCl	17.8		−21	0.538	0.462
$CsNO_3$	32.6[a]			0.499	0.501
CsI	32.9		−7.5	0.492	0.508

[a] Values obtained as explained in the text. [b] Calculated from ref 27–31. [c] The average value −4.1 cm³/mol has been used in the calculations. [d] The average errors on $\bar{V}_2^0$ and h are estimated to be ±1 cm³/mol and ±2 cm³ l./mol², respectively. For CsCl, however, the error on h may be as large as ±5 cm³ l./mol². [e] Reference 20. [f] Reference 21. [g] Reference 19. [h] Reference 22.

The results of Table I show that within experimental error for $\bar{V}_2^0$ (±1 cm³/mol) the additivity of partial molal volumes holds in methanol.

The partial molal volumes of $RbNO_3$ and $CsNO_3$ have been obtained by combining $\bar{V}_2^0$ data relative to other salts (a direct measurement was practically impossible owing to the low solubility of these salts in methanol). For instance, $\bar{V}^0(RbNO_3)$ has been calculated according to

$$\bar{V}^0(RbNO_3) = \bar{V}^0(RbCl) - \bar{V}^0(NaCl) + \bar{V}^0(NaNO_3) = \bar{V}^0(RbCl) - \bar{V}^0(Cl^-) + \bar{V}^0(NO_3^-)$$

In order to diminish the error in $\bar{V}^0(RbNO_3)$ the calculations were carried out using the average value of $\bar{V}^0(NO_3^-) - \bar{V}^0(Cl^-)$ as obtained from the two pairs of nitrates and chlorides with a common cation listed in Table I.

IV. Ultrasonic Vibration Potential Measurements

The results of the measurements performed on 16 uni-univalent electrolytes at concentrations below 3×10^{-2} *M* are listed in Table II. The assignment of a sign to the uvp's is immediate for very asymmetric 1-1 electrolytes. For example, a salt, such as CsCl, constituted by a heavy cation and a rather light anion has a positive uvp, while NaI has a negative uvp.[13] In doubtful cases (as, for example, NH_4Cl, KNO_3, and CsI) the unknown sign has been readily obtained from the variation of the uvp of unknown sign upon addition of a salt with uvp of known sign.[13]

Table II shows that at low concentrations ($c < 3 \times 10^{-4}$ *M*) the magnitude of Φ decreases with c, as expected on the basis of the theoretical treatment of uvp.[14,15] At concentrations above 3×10^{-3} to 10^{-2} *M*, Φ shows a decrease (in algebraic value) whose magnitude depends on the nature of the salt. This decrease which is rather small for chlorides and most nitrates becomes significant with bromides and particularly large with iodides. Such a behavior may be related with the formation of ion pairs or even

TABLE II: Values of Φ in μV as a Function of Concentration at 22°[a]

Electrolyte[b]	Concentration, M						Φ[c]
	10^{-4}	3×10^{-4}	10^{-3}	3×10^{-3}	10^{-2}	3×10^{-2}	
NaCl (3)				5.5	6.5	5	5.5
NaBr (2)		−24	−25.5	−26	−29.5	−33.5	−26
NaI (2)		−52	−55	−57.5	−65	−73.5	−57.5
$NaNO_3$ (2)				−9.5	−11.5	−16	−10
KF (1)	13.5	19.5	22.5	22	15	11	22
KCl (2)				9.5	8.5	8	9.5
KBr (2)				−21	−25.5	−29	−21
KI (2)		−36.5	−46.5	−49	−55	−63.5	−49
KNO_3 (2)				−5.5	−8		−6[d]
NH_4Cl (1)				−4.5	−5.5	−9.5	−4.5[d]
NH_4I (1)		−59	−62.5	−64	−69.5	−72.5	−63.5
RbCl (2)	21.5	40.5	46.5	46	44	43	46
$RbNO_3$ (2)	16.5	24	29	28	26		28.5
CsCl (3)	55	66	79	79	78	79	79
CsI (1)	13	16.5	17	13	6.5	4	16[d]
$CsNO_3$ (2)	47.5	55	63	62.5			62.5

[a] Prior to measurements in methanol, measurements were carried out on aqueous solutions of CsCl and RbCl in order to obtain the value of a_w. The average value of a_w was found to be 10.35 cm/sec and the uvp's measured in methanol have all been multiplied by $10.35/a_w$ to give the values of Φ listed above (a_w is the velocity amplitude in water, determined before each experiment with organic solvents). [b] The numbers in parentheses represent the numbers of independent runs performed on each electrolyte. [c] Values of Φ selected for ionic partial molal volume calculations (see text). [d] Salts for which the sign of the uvp has been obtained as explained in the text.

more complex charged species.[2,25] A small proportion of ion pair (<10%) should not perturb uvp measurements significantly[13] as ion pairs are uncharged and therefore not active as far as uvp's are concerned. However, when this proportion becomes large ion pairs may give rise to a dipole vibration potential[26] and result in a complicated dependence of the measured uvp on concentration as the concentrations of ion pairs and free ions vary with c.

However, Φ varies only slightly with c in the range from 3×10^{-4} to 3×10^{-3} *M* for most of the electrolytes listed in Table II. For this reason, the values of Φ used in ionic partial molal volume calculations have been taken in this range and are listed in the last column of Table II.

V. Calculation of Ionic Partial Molal Volumes

The calculation of $\bar{V}_+^0$ and $\bar{V}_-^0$ by means of eq 1 and 2 involves the values of $\bar{V}_2^0$ (listed in Table I), Φ (listed in Table II), t_+ and t_-, and a.

The transport numbers t_+ and t_- for each of the electrolytes studied in this work have been calculated from the limiting equivalent conductivities of ions in methanol[27-31] and are listed in Table I. As previously noted[32] the fact that the Φ's were obtained at 22° while partial molal volumes and transference numbers are relative to 25° results only in negligible errors.

We had no possibility of directly measuring a when the cell contained solutions in methanol. However, the velocity amplitude in methanol, a_M, can be calculated from the value in water, a_w, using the equation[33]

$$a_M = a_w \frac{2(d_0 v)_w}{(d_0 v)_w + (d_0 v)_M} \qquad (5)$$

where d_0 and v have been already defined (eq 1 and 2). Equation 5 reduces to $a_M = 1.25 a_w$ after replacing d_0 and v by their known values. With $a_w = 10.35$ cm/sec (see Table II) one obtains $a_M = 13.0$ cm/sec. This equation assumes a normal incidence of the ultrasonic beam at the water-methanol interface at the front side of the cell. This condition is not met in our experiments as the mylar membrane is always convex, as shown in Figure 1, because of the difference of hydrostatic pressure between the inside and outside of the cell. On the other hand, eq 5 applies only to plane waves. Owing to these two facts the value of the velocity amplitude obtained from eq 5 must therefore represent a maximum value of a_M. Indeed, calculations carried out with $a_M = 13$ cm/sec and the data of Tables I and II yielded values of the ionic partial molal volumes dependent on the salt for which the calculations were performed: for a series of salts with a common anion X^- the larger the value of Φ, the smaller the calculated value of $\bar{V}^0(X^-)$. The opposite is true for the partial molal volume of a cation calculated from the data relative to salts involving this cation. Such results are expected on the basis of eq 1 and 2 when an overestimated value of a_M is used in the calculations.

This situation led us to adopt another procedure for the determination of ionic partial molal volumes. Equations 1 and 2 have been solved using the data of Tables I and II and taking for a_M a series of values ranging from 10 to 14 cm/sec. For salts with a common cation (or anion) the curves giving the ionic partial molal volume of the cation (or anion) as a function of a_M have been plotted as shown in Figures 4 and 5 for K^+ and Cl^- (similar results have been obtained for Na^+, Cs^+, NO_3^-, and I^-). In an ideal case all of these curves should have crossed each other at a single point. Figures 4 and 5 show that in practice the crossing points are scattered over a certain area. The curves $\bar{V}^0 = f(a_M)$ have then been used to calculate the average value $\langle \bar{V} \rangle$ of the partial molal volume of each ion and the root mean square deviation

$$\sigma = [\Sigma(\bar{V} - \langle \bar{V} \rangle)^2/n]^{1/2}$$

where n is the number of salts, as a function of a_M. The results are shown in Figures 6 and 7. For each ion σ goes through a minimum σ_{min} for a value a_{min} of the velocity amplitude which may be considered as the effective value of a_M. To further minimize the errors the effective values have been averaged according to eq 6 where n_{ion} is the number of ions. These calculations yield

$$\langle a \rangle = 11.75 \text{ cm/sec}$$

$$\langle a \rangle = \frac{1}{n_{ion}} \sum_{\text{all ions}} a_{min} n \sigma_{min}^{-1} / \sum_{\text{all ions}} n \sigma_{min}^{-1} \qquad (6)$$

The values of the ionic partial molal volumes and their

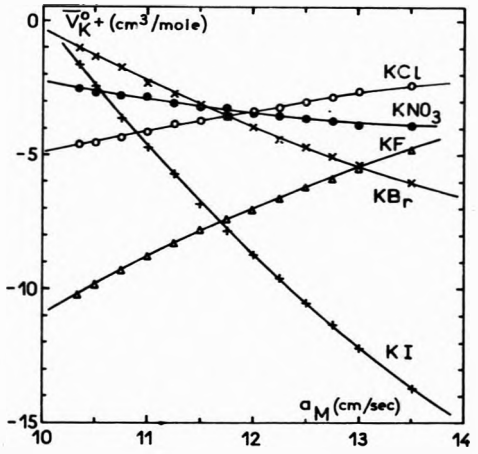

Figure 4. Variation of $\bar{V}^0(K^+)$ as a function of a_M for potassium halides and KNO_3.

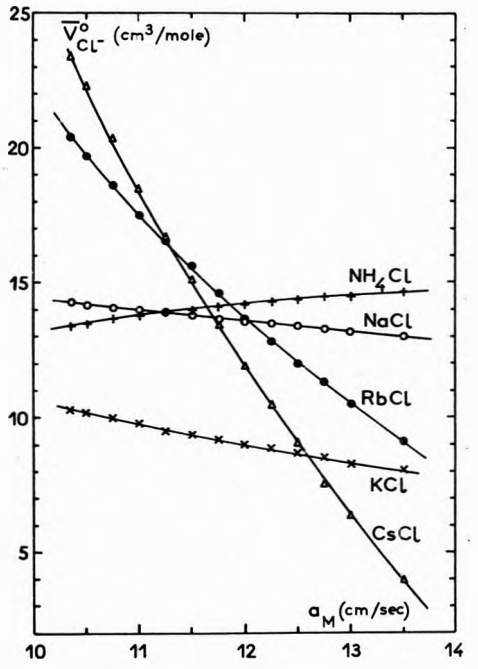

Figure 5. Variation of $\bar{V}^0(Cl^-)$ as a function of a_M for a series of alkali metal and ammonium chlorides.

root mean square deviations (when more than four electrolytes were involved in the averaging procedure) have been obtained from $\langle a \rangle$ and are listed in the first column of Table III.

These results are not always in agreement with the data in Table I. Indeed, if the values of $\bar{V}^0(NO_3^-) - \bar{V}^0(Cl^-)$ calculated from Tables I and III are in good agreement, the two values of $\bar{V}^0(Na^+) - \bar{V}^0(K^+)$ derived in the same manner differ by almost 4 cm³/mol. On the other hand, the values of $\bar{V}^0(NaCl)$ and $\bar{V}^0(NaNO_3)$ calculated from Table III are smaller than those in Table I while the opposite is true for $\bar{V}^0(KCl)$ and $\bar{V}^0(KNO_3)$. These facts seem to indicate that in Table III the values of $\bar{V}^0(Cl^-)$ and $\bar{V}^0(NO_3^-)$ are closer to their real values than $\bar{V}^0(Na^+)$ and $\bar{V}^0(K^+)$. For this reason the values of $\bar{V}^0(Cl^-)$ and $\bar{V}^0(NO_3^-)$ in Table III have been adopted as references and used together with the $\bar{V}_2^0$ data from Table I and from other sources to obtain the ionic partial molal volumes listed in the second column of Table III.

These results have been compared to those obtained by

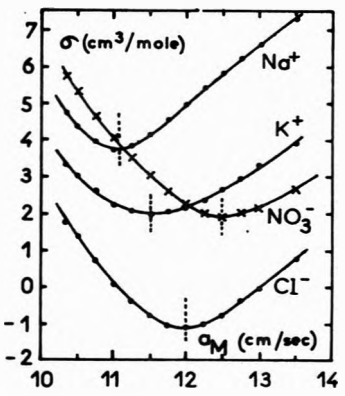

Figure 6. Variation of σ as a function of a_M for Na^+, K^+, NO_3^-, and Cl^-. For the sake of clarity the curves relative to Na^+ and Cl^- have been translated along the σ axis by +3 and −3 cm³/mol, respectively.

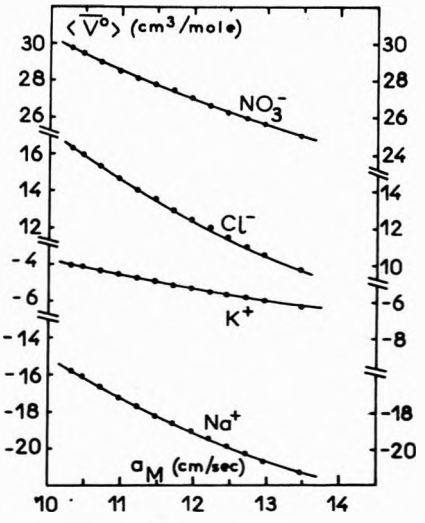

Figure 7. Variation of $\langle \bar{V}^0 \rangle$ as a function of a_M for Na^+, K^+, NO_3^-, and Cl^-.

means of the empirical methods of Mukerjee[3] and of Conway, Verrall, and Desnoyers[8] and the values of $\bar{V}_2^0$ listed in Table I (a direct comparison between the ionic partial molal volumes obtained in this work and those found by Millero[7] and Padova[6] is not possible because of differences in the $\bar{V}_2^0$ values used in these three studies). Within the experimental accuracy the results found using Mukerjee's method in conjunction with Pauling's ionic radii agree with those found in this work. On the contrary the results found by Padova[6] using Conway, Verrall, and Desnoyers extrapolation method[8] are in complete disagreement with the two other sets of data. One is thus led to conclude that this last method[8] is not valid for ions in methanol, in contradistinction with what has been found for ions in water where the two above empirical methods[3,8] yield data in excellent agreement with those obtained by means of uvp.[13]

The correspondence method of Criss and Cobble[34] appears to hold for the results of Table I. Indeed the results of column b and those relative to water obey the equation $(\bar{V}_i^0)_M = a(\bar{V}_i^0)_w + b$ with $a = 0.95$ and $b = -10.4$ cm³/mol. A similar observation has been reported by Millero.[7]

VI. Discussion

Hepler[35] has shown theoretically that the partial molal

TABLE III: Values of the Ionic Partial Molal Volumes and of the Volume Change upon Transfer from Water to Methanol

Ion	$\bar{V}_{ion}^0$ (in Methanol), cm³/mol				$\bar{V}_{ion}^0$ (in water),[f] cm³/mol	ΔV_T, cm³/mol
	This work[a]	This work[b]	d	e		
H^+		−17.0	−4.7		−5.7	−11.3
Li^+		−17.9	−5.6		−6.6	−11.3
Na^+	−18.6 (1.6)	−17.1	−5.0	−16.1	−6.9	−10.2
K^+	−4.9 (2.0)	−7.3	5.0	−6.3	3.3	−10.6
Rb^+	−2.8	−1.7	10.6	−0.7	8.4	−10.1
Cs^+	3.3	4.8	17.1	5.8	15.6	−10.8
NH_4^+	3.1	4.1	17.1	5.1	12.2	8.1
F^-	−1.2	−1.3	−13.6	−2.3	4.5	5.8
Cl^-	13.0 (2.0)	13.0	0.7	12.0	23.5	−10.5
Br^-	17.1	18.3	6.0	17.3	30.4	−12.1
I^-	30.0	28.2	15.9	27.2	41.9	−13.7
NO_3^-	27.5 (2.6)	27.5	15.2		34.7	−7.2
$(CH_3)_4N^+$		70[c]	84.0		83.9	−13.9
$(C_2H_5)_4N^+$		12.9[c]	142.0		143.4	−14.4
$(C_3H_7)_4N^+$		201.7[c]	214.0		208.7	−7.0
$(C_4H_9)_4N^+$		267.9[c]	280.2		271	−3.1

[a] The values in parentheses represent the root mean square deviations obtained from the curves of Figure 6 with a = 11.75 cm./sec. [b] Calculated using $\bar{V}^0(Cl^-)$ = 13 cm³/mol and $\bar{V}^0(NO_3^-)$ = 27.5 cm³/mol, the $\bar{V}_2^0$ values listed in Table I and the values $\bar{V}^0(HCl)$ = −4.0 cm³/mol at 20° (J. Sobkowski and S. Minc, *Rocz. Chem.*, 35, 1127 (1959)) and $\bar{V}^0(LiCl)$ = −4.9 cm³/mol (ref 20). [c] Calculated from the data of ref 5 and the same values of $\bar{V}^0(Cl^-)$ and $\bar{V}^0(Br^-)$ as in *b*. [d] Calculated using the value $\bar{V}^0(Br^-)$ = 6.0 cm³/mol obtained[5,6] by means of the extrapolation method[8] and the $\bar{V}_2^0$ values of Table I. [e] Calculated using Mukerjee's method[3] and the $\bar{V}_2^0$ data of Table I. [f] Calculated from the data tabulated in ref 2a with $V^0(Cl^-)$ = 23.5 cm³/mol.[8,13]

volume of an ion i with a radius r_i is given by

$$\bar{V}_i^0 = Ar_i^3 - B/r_i \qquad (7)$$

In this equation, Ar_i^3 is the geometric contribution which includes the intrinsic volume of the ion and the void space around the ion. On the other hand, $-B/r_i$ is the contribution of electrostriction to $\bar{V}_i^0$. Equation 7 predicts a linear behavior for $\bar{V}_i^0 r_i$ when plotted as a function of r_i^4. Ions in aqueous solutions have been found to verify this prediction;[13] the data for alkali metal and halide ions fall on the same straight line, while those relative to the symmetrical tetraalkylammonium (TAA) ions define a second straight line. Equation 7 has also been found to be valid in methanol, seawater, and *N*-methylpropionamide.[7]

As can be seen on Figure 8, the data relative to ions in methanol also appear to verify eq 7 within experimental accuracy. The results relative to alkali metal and halide ions fall on two parallel straight lines which present a larger slope than the line relative to TAA ions. On the other hand, as to be expected the data of column e of Table II obtained by means of Mukerjee's method, define a single straight line (line 1′) for all of the alkali metal and halides ions, as in the case of water,[13] with the exception of Li^+. It is not possible at the present time to decide whether the difference between lines 1 and 2 and 1′ is real, because of the limited accuracy on uvp measurements. The ionic radii of Pauling for alkali metal and halide ions and of Robinson and Stokes[36] for TAA ions were used for these plots.

The values of A and B have been determined for each series of ions and are listed in Table IV together with the results for ions in water. Our results relative to line 1′ are in excellent agreement with those reported by Millero.[7] The values of A and B will be discussed separately.

(*1*) *Values of A.* The fact that two parallel lines have been found for halide and alkali metal ions indicates that the void space around these ions in methanol is independent of the sign of the ion charge and depends only on r_i. An identical conclusion has been reached for these ions in aqueous solutions.[13]

On the other hand, the values of A show that the void volume around ions is significantly smaller in methanol than in water. On the basis of volume fraction statistics[9,37] similar values of A must be expected for these two solvents, had methanol and water molecules been spherical. Indeed it has been experimentally shown[37] that the void volume in a statistical close packing of two kind of spheres is independent of the ratio of the diameter of the spheres for ratios between 1.7 and 0.6. The radii of water (1.4 Å) and methanol (1.8 Å assuming a spherical molecule) indicate that volume fraction statistics should apply to all halide and alkali metal ions (with the exception of Li^+ which is too small), in both solvents. Indeed for water, whose molecules are symmetrical and quite close to spheres, the experimental value of A (4.75 cm³/mol Å³ [13]) is in good agreement with that calculated from volume fraction statistics (4.35 cm³/mol Å³ [9]) and, as predicted, the result relative to Li^+ clearly departs from the straight line obtained for all small monovalent ions. Methanol molecules however are not spherical. It is then likely that even if volume fraction statistics apply to a mixture of nonspherical and spherical objects, the fraction of void space around spherical ions will differ from the case where a mixture of two types of spheres is considered.

For the large TAA ions the values of A in methanol and water are practically equal and are in both solvents much smaller than for the small monovalent ions. Moreover, in this case the experimental value of A is quite close to that which can be calculated for a hard sphere immersed in a continuous solvent, *i.e.*, $(4/3)\pi N_A$ = 2.52 cm³/mol Å³. The small difference between the experimental slope and its limiting value may simply reflect the accuracy on the values of the radii of TAA ions.[36]

(*2*) *Values of B.* Table IV shows that B is larger in methanol than in water for alkali metal, halide, and TAA ions. The difference is particularly large for TAA ions.

These differences in B values are likely to arise from the chemical anisotropy of the methanol molecule which results in differences of orientation of the methanol dipole in the first coordination layer of the ions, according to the nature of the ion. Ion–methanol contact preferentially occurs at the oxygen atom with alkali metal ions,[38] at the

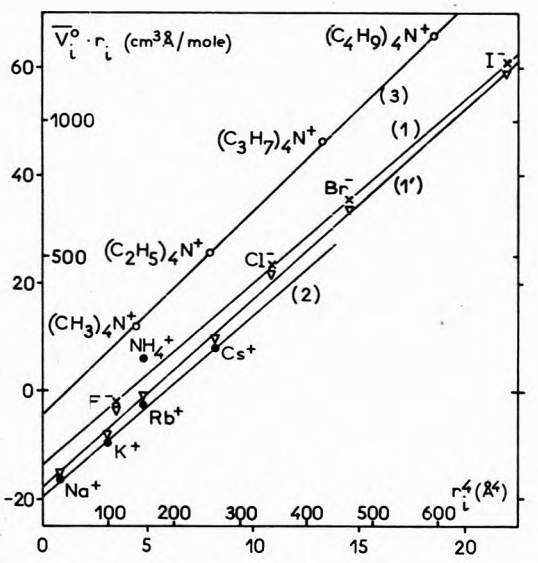

Figure 8. Variation of $\bar{V}_i^0 r_i$ *vs.* r_i^4 for alkali metal ions (line 1), halide ions (line 2), and TAA ions (line 3), using $\bar{V}_i^0$ values of column 2 in Table III, Pauling's ionic radii for alkali metal and halide ions, and TAA ionic radii from ref 36. Line 1′ has been obtained using $\bar{V}_i^0$ values of column e in Table III.

hydrogen atom of the OH groups with halide ions,[38] and at the methyl group with TAA ions. As a result, the immediate neighborhood of alkali metal and halide ions, *i.e.*, the region where electrostriction is very high, should mostly consist of OH groups with a small fraction of CH_3 groups. The reverse should occur with TAA ions.

The Drude–Nernst equation[39] which is based on a continuum model for the solvent leads for monovalent ions to the equation

$$B = \frac{N_A e^2}{2D}\left(\frac{d \ln D}{dP}\right) \qquad (8)$$

where D is the dielectric constant and P the pressure. Equation 8 yields 4.2 and 24.2 cm³ Å/mol for B in water and methanol, respectively.[5-7] It is interesting to note that for ions other than TAA ions the experimental values of B in these two solvents (10 and 17 cm³ Å/mol, respectively) are much closer than the calculated values. This result may be easily understood if one assumes that B is related to the actual properties of the solvation layer and not to the bulk properties of the solvent. As pointed out above the composition of the solvation layers is not very different for alkali metal and halide ions in methanol and water, while the bulk values of D and d ln D/dP differ considerably in these two solvents.

In methanol it is likely that despite a considerable dielectric saturation[5,6] the dielectric constant of the solvation layer of TAA ions, which mostly consists of methyl groups, remains smaller than for other monovalent ions. Also the derivative d ln D/dP has probably a larger value for the solvation layer of TAA ions than for alkali metal and halide ions. Indeed d ln D/dP is approximately equal to the isothermal compressibility K_T[40] which is much larger for alcohols and paraffins than for water.[41] According to eq 8 these two facts should yield for TAA ions a value of B much larger than for alkali metal and halide ions, in agreement with the results of Table IV. The large electrostriction of TAA ions in methanol provides an explanation for the failure of the extrapolation method to yield correct values of ionic partial molal volumes in methanol.[42] Indeed, with such a method, the regular increase of electrostriction with decreasing TAA ion radii (and molecular weight) is expected to yield for the partial molal volume of the halide ion a value significantly smaller than the actual one. This prediction is in agreement with the experimental results; for Br^- the extrapolation method yielded $\bar{V}^0(Br^-)$ = 6 cm³/mol[5,6] while the actual value obtained from uvp data is 18.3 ± 2 cm³/mol.

Table IV: Values of A and B in Methanol and Water

Ions	A, cm³/mol Å³		B, cm³ Å/mol	
	Methanol	Water	Methanol	Water
Halide ions	3.35	4.75[a]	−14	−10[a]
Alkali metal ions	3.35	4.75[a]	−19.5	−10[a]
Line 1′	3.5		−17.5	
Tetraalkylammonium ions	2.37	2.38[b]	−90	−10 to −15[b]

[a] From ref 13. [b] Obtained from the plot of $\bar{V}_i^0 r_i$ *vs.* r_i^4 for TAA ions, using the $\bar{V}_i^0$ values given in ref 13 and the r_i values of ref 36.

(3) *Volume Change ΔV_T upon Transfer of Ions from Water to Methanol.* The values of ΔV_T defined by eq 9 are listed in Table III. For 12 out of the 16 ions in Table III ΔV_T is equal to 11.5 ± 3 cm³/mol. This behavior appears to be the result of the changes of A and B in going from water to methanol

$$\Delta V_{T,i} = (\bar{V}_i^0)_M - (\bar{V}_i^0)_w \qquad (9)$$

Conclusions

The values of the ionic partial molal volumes in methanol have been obtained from the combination of ultrasonic vibration potential and $\bar{V}_2^0$ data for solutions of uni-univalent electrolytes. These values are quite close to those obtained by means of Mukerjee's method.[3] Electrostriction of ions appears to be greater in methanol than in water while void space around ions appears smaller in methanol than in water. The differences between the values of the electrostriction coefficient B for the different types of ions can be qualitatively understood in terms of specific interactions between ions and methanol dipoles.

Acknowledgment. The authors are pleased to thank Dr. J. Francois for her assistance in the density measurements.

References and Notes

(1) On leave of absence from the Department of Chemical Engineering, Faculty of Engineering, Nagoya University, Japan.
(2) (a) F. J. Millero, *Chem. Rev.*, **71**, 147 (1971); (b) J. O. Bockris and A. K. Reddy, "Modern Electrochemistry," Plenum Press, New York, N. Y., 1970, p 450.
(3) P. Mukerjee, *J. Phys. Chem.*, **65**, 740, 744 (1961).
(4) C. Tondre and R. Zana, *J. Phys. Chem.*, **76**, 3451 (1972); C. Tondre, P. Spegt, G. Weill, and R. Zana, *Biophys. Chem.*, **1**, 55 (1973).
(5) J. Padova and I. Abrahamer, *J. Phys. Chem.*, **71**, 2112 (1967).
(6) J. Padova, *J. Chem. Phys.*, **56**, 1606 (1972).
(7) F. J. Millero, *J. Phys. Chem.*, **73**, 2417 (1969).
(8) B. E. Conway, R. E. Verrall, and J. E. Desnoyers, *Trans. Faraday Soc.*, **62**, 2738 (1966); *Z. Phys. Chem. (Leipzig)*, **230**, 157 (1965).
(9) R. H. Stokes and R. A. Robinson, *Trans. Faraday Soc.*, **53**, 301 (1957).
(10) E. J. King, *J. Phys Chem.*, **74**, 4590 (1970).
(11) F. J. Millero, *J. Phys. Chem.*, **75**, 280 (1971).
(12) J. Bernal and R. Fowler, *J. Chem. Phys.*, **1**, 515 (1933).
(13) R. Zana and E. B. Yeager, *J. Phys. Chem.*, **70**, 954 (1966); **71**, 521, 4241 (1967).
(14) P. Debye, *J. Chem. Phys.*, **1**, 13 (1933).
(15) J. Bugosh, E. Yeager, and F. Hovorka, *J. Chem. Phys.*, **15**, 592 (1947).
(16) J. Francois, R. Clément, and E. Franta, *C. R. Acad. Sci., Ser. C*, **273**, 1577 (1971).

(17) O. Redlich and P. Rosenfeld, *Z. Electrochem.*, **37**, 705 (1931).
(18) D. O. Masson, *Phil. Mag.*, **8**, 218 (1929).
(19) G. Jones and H. J. Fornwalt, *J. Amer. Chem. Soc.*, **57**, 2041 (1935).
(20) W. C. Vosburgh, L. C. Connell, and J. Butler, *J. Chem. Soc.*, 993 (1933).
(21) R. E. Gibson, *J. Amer. Chem. Soc.*, **59**, 1521 (1937); R. E. Gibson and J. F. Kincaid, *Ibid.*, **59**, 579 (1937).
(22) D. Mac Innes and M. O. Dayhoff, *J. Amer. Chem. Soc.*, **75**, 5219 (1953).
(23) S. D. Hamann and S. C. Lim, *Aust. J. Chem.*, **7**, 329 (1954).
(24) A. S. Kaurova and G. P. Roschina, *Sov. Phys. Acoustics (Eng. Trans.)*, **12**, 276 (1967).
(25) S. Singh and S. S. Aggarwal, *Z. Phys. Chem. (Frankfurt am Main)*, **81**, 1 (1972).
(26) A. Weinmann, *Proc. Phys. Soc. (London)*, **73**, 345 (1959); **75**, 102 (1960).
(27) A. Unmack, E. Bullock, D. M. Murray-Rust, and H. Hartley, *Proc. Roy. Soc., Ser. A*, **132**, 427 (1931).
(28) J. E. Frazer and H. Hartley, *Proc. Roy. Soc., Ser. A*, **109**, 361 (1925).
(29) B. Kratochvil and H. L. Yeager, *Fortschr. Chem. Forsch.*, **27**, 1 (1972).
(30) R. L. Kay, *J. Amer. Chem. Soc.*, **82**, 2099 (1960).
(31) R. L. Kay, C. Zawoyski, and D. Evans, *J. Phys. Chem.*, **69**, 4208 (1935).
(32) E. B. Yeager and R. Zana, *J. Phys. Chem.*, **76**, 1086 (1972).
(33) J. Blitz, "Fundamentals of Ultrasonics," Butterworths, London, 1963, p 25.
(34) C. Criss and J. W. Cobble, *J. Amer. Chem. Soc.*, **86**, 5385 (1964).
(35) L. G. Hepler, *J. Phys. Chem.*, **61**, 1426 (1957).
(36) R. A. Robinson and R. H. Stokes, "Electrolyte Solutions," Butterworths, London, 2nd ed, 5th printing, 1959, p 125.
(37) B. J. Alder, *J. Chem. Phys.*, **23**, 263 (1955).
(38) G. W. Stockton and J. S. Martin, *J. Amer. Chem. Soc.*, **94**, 6921 (1972).
(39) P. Drude and W. Nernst, *Z. Phys. Chem.*, **15**, 79 (1894).
(40) J. E. Desnoyers, R. E. Verrall, and B. E. Conway, *J. Chem. Phys.*, **43**, 243 (1965); F. Kawaizumi and R. Zana, submitted for publication.
(41) "Handbook of Chemistry and Physics," Chemical Rubber Publishing Co., 44th ed, pp 2212–2218.
(42) I. Lee and J. B. Hyne, *Can. J. Chem.*, **46**, 2333 (1968).

Carbon Disulfide Dissociation in a Thermal Cell[1]

Tzy C. Peng

McDonnell Douglas Research Laboratories, McDonnell Douglas Corporation, St. Louis, Missouri 63166 *(Received June 13, 1974; Revised Manuscript Received October 18, 1973)*

Publication costs assisted by the McDonnell Douglas Corporation

Dissociation products of CS_2 in a vitreous carbon thermal cell are analyzed mass spectrometrically for temperatures up to 1900 K. The reaction products in the cell are observed directly through an effusive flow with a modulated beam sampling technique. CS and S are the only detected products from CS_2 dissociation, indicating $CS_2 \rightarrow CS + S$ is the dominant reaction. The temperature variation of the relative CS and S abundances indicates that $CS_2 + C_{wall} \rightarrow 2CS$ is also a significant reaction in the CS_2 dissociation. The measured relative abundances of CS_2 and CS as a function of temperature agree favorably with those of the equilibrium calculations using the recently obtained CS heat of formation ($\Delta H_f^\circ_0$ = 69.2 kcal/mol at 0 K). On the other hand, the absence of S_2 in our measurements is in support of the CS_2 reaction with the heated vitreous carbon wall mentioned previously.

Introduction

Dissociation of CS_2 yields CS molecules which are important intermediates in CS_2–O CO chemical lasers.[2] The chemistry of CS_2 dissociation has been observed under a high-frequency discharge at 1 Torr,[3] by flash photolysis at 100 Torr,[4] by shock wave heating a CS_2–Ar mixture from 2000 to 3500 K at 1–10 Torr,[5,6] and by passing CS_2 over a heated tungsten ribbon.[7] The high-frequency discharge and flash photolysis studies as well as ac discharge studies[8] concentrated on the generation and lifetime of the CS molecule. CS was also observed in interstellar space,[9] therefore by itself a CS molecule appears stable. The shock wave heating studies produced information on the CS_2 decomposition rate, and the heated tungsten ribbon studies suggest a potential mechanism for CS_2 dissociation. However, the details of the mechanism are not completely understood. This paper present a mass spectrometric analysis of CS_2 dissociation products in a vitreous carbon thermal cell together with new experimental evidence for specific dissociation reactions.

Experimental Section

The experimental arrangement is shown in Figure 1. Major components are (1) the vitreous carbon thermal cell, (2) the beam modulating system—the vibrating fork (Bulova, L-40-P) and the lock-in amplifier (PAR, HR-8), (3) the quadrupole mass spectrometer (EAI Quad 150A), and (4) the vacuum chamber (60 cm diameter and 90 cm long) together with a diffusion pump system. The vitreous carbon thermal cell (17.4 mm diameter 25.4 mm long cylinder) is a high-temperature oven specially fabricated for material–environmental research. The design and performance of this thermal cell has been reported elsewhere.[10]

For CS_2 dissociation studies, a steady flow of 30% CS_2–70% Ar (mole ratio) gas mixture was maintained through the vitreous carbon thermal cell. The input of this flow was at the water-cooled copper electrodes (Figure 1). The input flow rate was controlled by a variable leak (Granville-Phillip series 203) and was measured to be 2.4×10^{-6} g/sec by a mass flow meter (Hasting, ALL-10). The output of this steady flow was through three pin holes

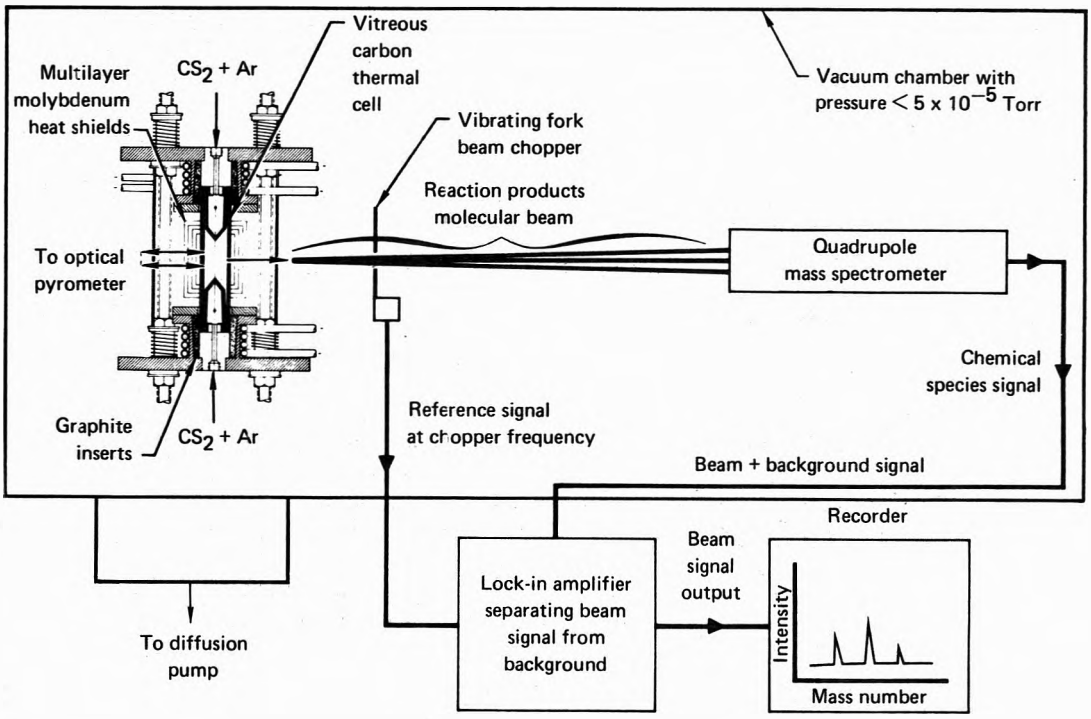

Figure 1. Experimental arrangement for CS_2 thermal dissociation studies.

(0.76 mm diameter) on the wall of the thermal cell. Two of these holes were for temperature measurement of the thermal cell and the third faces the mass spectrometer (Figure 1). The diameter of the holes and the amount of gas flowing through them were such that the condition of an effusion flow holds, *i.e.*, the mean free path within the thermal cell was much greater than the hole diameter. For example, the mean free path at 300 K is 11.3 mm between Ar molecules and is 7.87 mm between CS_2 molecules based on the potential energy data[11] at the gas pressures of 5.2×10^{-3} Torr for Ar and 2.2×10^{-3} Torr for CS_2 within the thermal cell. The mean free path values are also comparable to the diameter (17.4 mm) of the thermal cell indicating that the wall collisions for gas molecules are equally important as the collisions among the molecules themselves. As the gas temperature increases, the mean free path increases. Thus, effusion flow will be maintained at the exit hole over the entire range of temperature reported here (300-1900 K), and the wall collisions have more significance at high temperatures than at room temperature.

Using the effusion flow equation, the total pressure inside the thermal cell at 300 K was calculated to be 7.4×10^{-3} Torr of which the CS_2 partial pressure was 2.2×10^{-3} Torr. At 1900 K, the dissociation of CS_2 was nearly complete, and the total pressure within the thermal cell was calculated to be 25×10^{-3} Torr of which the dissociated products of CS_2 contributed $\sim 12 \times 10^{-3}$ Torr.

The dissociation products of CS_2 and the Ar emerging from the thermal cell were collimated into a molecular beam within a low-pressure ($\sim 3 \times 10^{-5}$) vacuum chamber where residual dissociation products and atmospheric gases were present. Chemical species in both the molecular beam (products from CS_2 dissociation) and the residual gases in the vacuum chamber (background gas) were detected by the quadrupole mass spectrometer. To separate the products from that of the background gas, the molecular beam was chopped at a fixed frequency of 200 Hz and the products in the beam were then synchronously detected using a lock-in amplifier tuned to the same frequency.

The distance between the exit hole at the thermal cell and the ionizer of the mass spectrometer was 8.9 cm and the aperture of the ionizer was 0.318 cm in diameter. Assuming a point source with the inverse square law for beam intensity calculations,[12] the particle concentration in the beam at the ionizer was approximately 10^{11} particle/cm^3. The chopper allowed the beam to pass during $\frac{1}{5}$ of cycle. Hence, the time-averaged particle concentration in the beam at the ionizer is only 2×10^{10} particles/cm^3. By comparison, the particle concentration of the background gas at a vacuum chamber pressure of 3×10^{-5} Torr was about 10^{12} particles/cm^3. Thus, the direct output from the mass spectrometer provided the background gas analysis whereas the output from the mass spectrometer through the lock-in amplifier provided the product analysis from the dissociation of CS_2 in the thermal cell.

Results and Discussions

The mass spectrometrically detected ion signals, representative of the neutral reaction products from CS_2 dissociation, are illustrated in Figures 2a and 2b. The direct mass spectrometer output of the background gas in the vacuum chamber is shown in Figure 2a and the lock-in amplifier output representing the dissociated products of CS_2 in the thermal cell is shown in Figure 2b. CS_2^+, CS^+, and S^+ were the only species observed and were normalized to the Ar^+ intensity to minimize variations within the mass spectrometer. The solid lines are the actual measurements with the range of the data scatter indicated by the vertical bars. The main source of data scatter was from the random electrical noise in the highly sensitive circuit of the lock-in amplifier. The improvement of signal-to-noise ratio for the lock-in amplifier output is thus a continuous process of reducing the ground loop and other electrical noise in the instrumentation system.

Two major problems connected with the analysis of the observed ion data need to be clarified. They are (1) the

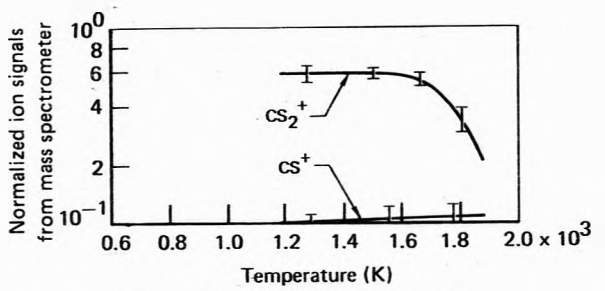

Fig. 2a Background gas analysis

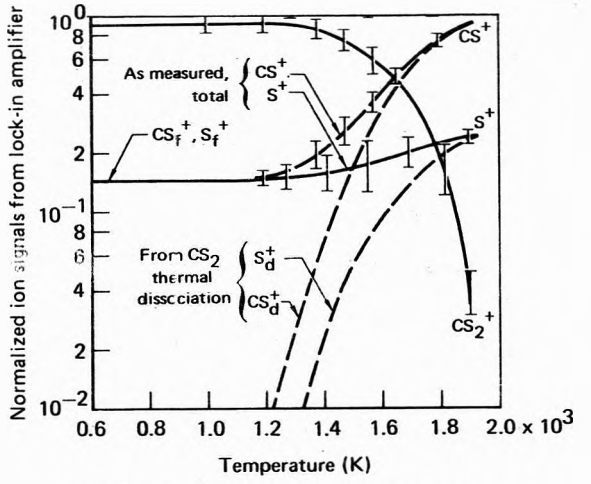

Fig. 2b Dissociated product analysis

Figure 2. Mass spectrometric analysis of CS_2 dissociation from a 70% Ar–30% CS_2 (mole ratio) gas flow through a vitreous carbon thermal cell. Figure 2a shows the direct mass spectrometer output representing the residual background gas analysis in the vacuum chamber. Figure 2b shows the mass spectrometer output through modulated beam sampling representing true CS_2 dissociation analysis in the thermal cell. Solid lines are traces from the measured data with data scatters indicated by vertical bars and dotted lines are obtained by subtracting the fragmentation from the total signals. All ion signal intensities are divided by the Ar^+ intensity at same temperature conditions.

fragmentation of CS_2 molecules upon impact by a 90-eV electron beam within the ionizer and (2) the effect of the cell temperature (up to 1900 K) on this fragmentation pattern.

At temperatures below 600 K and pressures of $\sim 10^{-3}$ Torr, CS_2 does not dissociate. The m/e 44 and 32 ions observed at these low temperatures are produced by electron impact of CS_2 within the ionizer and are denoted by CS_f^+ and S_f^+. As the temperature rises above 1200 K, CS and S ion intensities increase with a corresponding decrease in CS_2 ions. Thus, the additional CS^+ and S^+ intensities above that seen at 600 K are the result of the thermal dissociation of CS_2 and are denoted by CS_d^+ and S_d^+. The appearance of CS_d^+ and S_d^+ and their temperature variation are shown by the dotted lines in Figure 2b.

At temperatures close to 1900 K, the vibrational excitation of CS_2 molecules may change the fragmentation pattern of CS_2 from that at room temperature. However, calculations of vibrational energy distribution indicate that significant redistribution at temperatures close to 1900 K involves mainly vibrational energy levels lying ~85% below the CS_2 dissociation limit. Furthermore, careful examinations of m/e 76(CS_2^+) to m/e 44 (CS^+) and of m/e 76 to m/e 32 (S^+) peak ratios from 300 to 1300 K revealed that the peak ratio decreases were less than 10%. Since CS_2 dissociation was insignificant up to 1300 K based on CS_2^+ data (Figure 2b), the decreases in peak ratios of m/e 76 over m/e 44 and of m/e 76 over m/e 32 are most probably due to internal energies within the CS_2 molecule, including that of vibrational excitation. Thus, errors due to the change of CS_2 fragmentation pattern from high temperature conditions are estimated at 10% for the peak ratios of m/e 76 over m/e 44 and of m/e 76 over m/e 32. For the experimental data reported here, these errors are much less than 10% because of the large amount of CS_2 dissociation near 1900 K. In a similar situation, a 5% error was given by Benson and Spokes[13] in analyzing the isopropyl iodide decomposition at temperatures up to 1300 K.

At pressures of about 5×10^{-3} Torr, CS_2 began to dissociate at 1300 K and the dissociation was nearly complete at 1900 K (*i.e.*, the intensity of CS_2^+ dropped to 4% of the original level). The rate of dissociation as a function of temperature is determined from the CS_2^+ profile and the CS_2 flow (5.7×10^{15} particles/sec) into the thermal cell. A least-square fit to the CS_2^+ profile with 5% deviation yielded the following equation

$$\Delta(CS_2)_{dis}/\Delta t = 5.7 \times 10^{15}[13.1 - 2.59 \times 10^{-2}T + 1.63 \times 10^{-5}T^2 - 3.18 \times 10^{-9}T^3] \text{ particles/sec}$$

where $1250\ K < T \leq 1900\ K$.

The only dissociation products observed using mass spectrometer data were CS and S. This suggests that the principal dissociation reaction is $CS_2 + M \rightarrow CS + S + M$, where M is Ar, another CS_2 molecule, or the vitreous carbon wall. However, $CS_2 + C_{wall} \rightarrow 2CS$ is also possible in view of the large Knudsen number (0.345 at 1900 K) within the thermal cell. These same mechanisms were also suggested by Blanchard and LeGoff in their heated carbonized tungsten ribbon experiment.[7] In Figure 3 the CS_d^+/S_d^+ ratio is plotted as a function of temperature. If $CS_2 + M \rightarrow CS + S + M$ is the sole dissociation reaction, then CS_d^+/S_d^+ will be relatively constant, as was indeed the case up to 1300 K. Above 1300 K, a small but distinct increase in the CS_d^+/S_d^+ ratio occurred signifying additional CS production without the accompanying S production. A reasonable conclusion under our experimental condition is that $CS_2 + C_{wall} \rightarrow 2CS$ is also operative.

Using a mass spectrometer without the modulated beam, Blanchard and LeGoff[7] observed CS and S_2 as dissociated products when CS_2 flowed over a heated carbonized tungsten surface. However, they did not detect any CS_2 dissociation above 2100 K when the carbonized tungsten was replaced by pure carbon. In our experiment, CS_2 dissociated inside a vitreous (pure) carbon thermal cell near 1400 K. However, an analysis of the background gas outside the thermal cell revealed very little dissociation even at 1900 K. The reason for these different results is that CS recombines on the vacuum chamber walls and structural surfaces in the vacuum chambers. Richardson, *et al.*,[14] in their CS loss studies found that CS reacts with the surface carbon releasing about 30 mol % CS_2 back into the gas phase. Thus, the observed CS_2^+ intensity in the background decreases more slowly than CS_2^+ intensity in the beam since CS is constantly returning more CS_2 to the gas phase as it reacts with all surfaces present in our experimental system. In fact, the CS_2^+ temperature profile in the background gas analysis (mass spectrometer output) lags about 300 K behind CS_2^+ profile in the beam gas analysis [lock-in amplifier output (Figure 2)]. Another possible explanation for the observed CS_2^+ data is the fol-

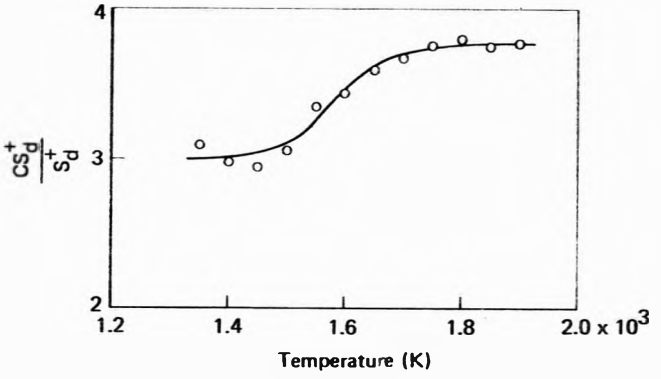

Figure 3. The temperature variation of CS_d^+/S_d^+ intensity ratio from CS_2 dissociation.

lowing: all of the recombined CS_2 stays on the wall, and the decrease of CS_2^+ background is due to the lack of CS_2 molecules in the highly dissociated CS_2 beam. However, this cannot explain the temperature lag of CS_2^+ background intensity behind that of the beam data under steady-state flow conditions.

A quantitative analysis of CS_2 dissociation may be made by assuming that the mass spectrometric sensitivity factors for CS_2 and CS are the same. This assumption is based on an analogy of CO_2 and CO since the chemical changes from CO_2 to CO is similar to that of CS_2 to CS. For CO_2 and CO, the maximum total ionization cross sections at ~100-eV electron energy are 3.4×10^{-16} and 2.7×10^{-16} cm^2, respectively,[15] and their measured mass spectrometric sensitivity factors are 0.8 and 0.77, respectively.[16]

The equal sensitivity factor assumption for CS_2 and CS will introduce a certain amount of error in our data analysis. However, this error is expected to be much less than 50% based on the results by Ames, *et al.*[17] In ref 17, a 50% difference in ionization cross section was recorded between rare earth metals and their metal oxides using a 25-eV electron beam. In our experiments, CS is chemically much more similar to CS_2 than the rare earth metals are to their oxides. Also, the use of a 90-eV electron beam makes the ionization cross section less dependent on the structure of molecules.

Consequently, the measured CS_d^+ intensity represents CS particle flux on the same quantitative terms as the CS_2^+ intensity represents CS_2 particle flux. The particle flux in the effusive flow is given by the product of particle concentration and the average thermal velocity. Since the thermal velocity is inversely proportional to the square root of the molecular weight, on a particle concentration (or mole fraction) basis, the CS^+ intensity must be divided by the square root of the molecular weight ratio (CS_2 to CS) before comparisons with CS_2^+ intensity can be made. In addition, the mole fractions at high temperatures were divided by the CS_2 mole fraction at 300 K, so that analyses for the dissociation of CS_2 with and without the solid carbon wall can be compared with the normalized CS_2 mole fraction which is equal to unity at 300 K. The results for the dissociated species distributions as a function of temperature are plotted in Figure 4 along with the equilibrium values for CS_2 and CS.

The equilibrium products distributions were calculated using 69.2 kcal/mol at 0 K as the heat of formation for CS[18] and a computer program formulated by Gordan and McBride.[19] Two cases were considered: (1) dissociation of CS_2 molecules in a 30% CS_2-70% Ar (mole ratio) gas mix-

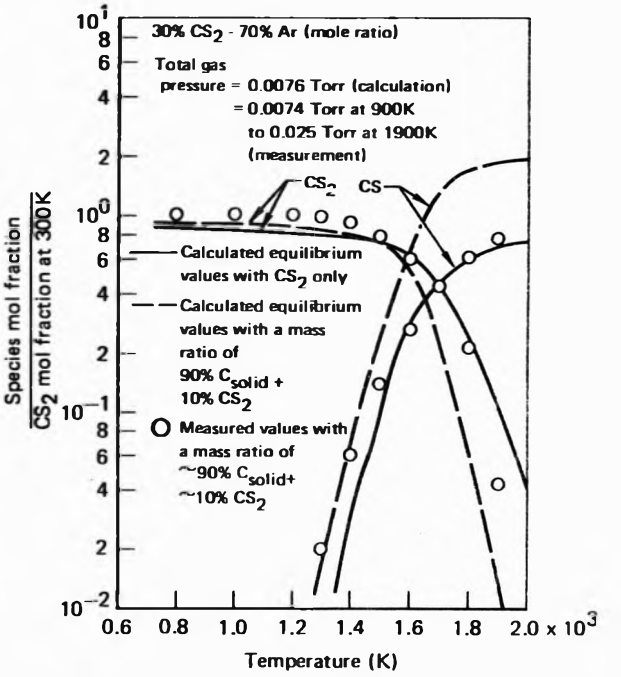

Figure 4. Comparison between calculated and measured values of CS_2 and CS abundance from thermal dissociation of CS_2. Solid line are the calculated equilibrium values with a gas mixture of 70% Ar–30% CS_2 (mole ratio) only. Dotted lines are the calculated equilibrium values including vitreous carbon wall with a 90% C_{solid} + 10% CS_2 mass ratio. Circles are the measured values from CS_2 dissociation within a vitreous carbon thermal cell.

ture; and (2) dissociation of CS_2 in the same gas mixture with the vitreous carbon wall of the thermal cell included as a part of the equilibrium system. For case 2, the vitreous carbon wall is considered as graphite with the same free energy values listed in JANAF tables[20] for graphite. Also, the computer program requires, as a program input, the mass ratio of CS_2 gas and vitreous carbon solid. The mass of the solid carbon was calculated on the basis that only the first layer of carbon atoms on the vitreous carbon surface[21] within the thermal cell were involved in chemical reactions with CS_2 gas molecules. For our experiment, the mass ratio between the solid carbon and the CS_2 gas was 9 to 1. The equilibrium calculations are summarized in Figure 5. The effect of the vitreous carbon wall under equilibrium conditions is to greatly increase the population of CS at the expense of S_2 and S.

According to Figure 4, the measured temperature profiles of CS_2 and CS agree reasonably well with these equilibrium calculations. This general agreement indicates that the thermodynamic conditions in the heated vitreous carbon cell were nearly at equilibrium in spite of a steady CS_2–Ar gas flow of 2.4×10^{-6} g/sec through the thermal cell.

This near equilibrium state within the thermal cell is also anticipated from calculating the average number of wall collisions suffered by each molecule. Using the effusion flow equation together with the conditions of constant mass flow, and of large Knudsen numbers (0.345 at 1900 K) within the thermal cell the average number, N, of wall collisions can be expressed as

$$N = 4V/Ad$$

where V is the volume of the thermal cell, A is the exit area of the effusion flow, and d is the diameter of the cy-

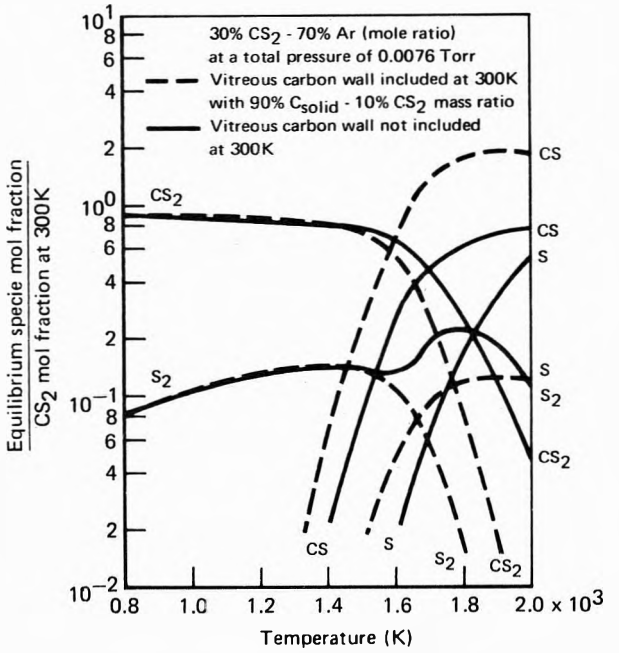

Figure 5. Equilibrium product distribution in gas phase from CS_2 dissociation. Solid lines are the calculated equilibrium values with a gas mixture of 70% Ar–30% CS_2 (mole ratio) only. Dotted lines are the calculated equilibrium values including vitreous carbon wall with a 90% C_{solid} + 10% CS_2 mass ratio.

lindrical thermal cavity. Thus, N is a geometry constant of the thermal cell. For the experimental data reported here, $N \cong 1020$. The CS_2 dissociation energy is 4.68 eV equivalent to $29KT$ at 1900 K. Hence, 30 or $(30)^2$ wall collisions may be required to achieve a dissociation equilibrium. This is adequately met by about 1000 wall collisions for an average CS_2 molecule.

The measured and calculated amount of CS_2 both with and without the vitreous carbon wall are nearly the same for temperatures up to 1500 K. Above 1500 K, the measured amount of CS_2 lies between the two equilibrium values, which are separated by about an order of magnitude at 1900 K. Thus, the experimental evidence suggests that the effect of the vitreous carbon wall is important above 1500 K and that gas-surface reactions should be considered in the chemical kinetic analysis. More precise experimental data are needed before the dissociation process can be defined exactly. Finally, the measured amount of CS below 1500 K coincides with the equilibrium value since the wall effect is apparently large in this region. This suggests that in the initial stage of CS generation, the surface reactions on the vitreous carbon wall play a principal role. However, the confirmation of this suggestion also requires more accurate data than the present measurements provide.

Conclusions

The generation of CS molecules through thermal dissociation of CS_2 in a heated vitreous carbon cell has been demonstrated. In addition, the dissociation of CS_2 begins at 1300 K, and is nearly complete at 1900 K for a partial pressure of CS_2 and its dissociated products of $\sim 10^{-2}$ Torr. The principal dissociation reaction is $CS_2 + M \rightarrow CS + S + M$ where M is a third body. A secondary reaction of the type $CS_2 + C_{wall} \rightarrow 2CS$ is also indicated.

The thermal cell was operated near thermodynamic equilibrium conditions. The effect of the vitreous carbon wall on the dissociation of CS_2 is significant at 1300 K where CS generation is initiated and again at 1900 K where CS_2 dissociation is nearly complete.

References and Notes

(1) This research was supported by the Office of Naval Research.
(2) S. J. Arnold and G. H. Kimbell, *Appl. Phys. Lett.*, **35**, 351 (1969); G. Hancock and I. W. M. Smith, *Chem. Phys. Lett.*, **3**, 573 (1969).
(3) (ε) J. Dewar and H. O. Jones, *Proc. Roy. Soc., Ser. A*, **83**, 526 (1909); (b) M. A. P. Hogg and J. E. Spice, *J. Chem. Soc.*, 4196 (1958).
(4) P. J. Dyne and D. A. Ramsey, *J. Chem. Phys.*, **20**, 1055 (1952).
(5) A. G. Gaydon, G. H. Kimbell, and H. B. Palmer, *Proc. Roy. Soc., Ser. A*, **279**, 313 (1964).
(6) S. J. Arnold, W. G. Brownlee, and G. H. Kimbell, *J. Phys. Chem.*, **74**, 8 (1970).
(7) L. P. Blanchard and P. LeGoff, *Can. J. Chem.*, **35**, 89 (1957).
(8) J. E. Wollrab and R. L. Rasmussen, *J. Chem. Phys.*, **58**, 4702 (1973).
(9) B. E. Turner, *Sci. Amer.*, **228**, 51 (1973).
(10) T. C. Peng, *Rev. Sci. Instrum.*, **44**, 803 (1973).
(11) J. O. Hirschfelder, C. F. Curtiss, and R. B. Bird, "Molecular Theory of Gases and Liquids," Wiley, New York, N. Y., 1954, p 1110.
(12) N. F. Ramsey, "Molecular Beams," Oxford University Press, London, 1956, p 14.
(13) S. W. Benson and G. N. Spokes, *J. Amer. Chem. Soc.*, **89**, 2525 (1967).
(14) R. J. Richardson, H. T. Powell, and J. D. Kelley, *J. Phys. Chem.*, **77**, 2601 (1973).
(15) H. S. W. Massey, E. H. S. Burhop, and H. B. Gilbody, "Electronic and Ionic Impact Phenomena," 2nd ed, Vol. 2, Oxford University Press, London, 1969, pp 1027 and 1046.
(16) A. Cornu and R. Massot, "Compilation of Mass Spectral Data," Haydon and Son, London, 1966.
(17) L. L. Ames, P. N. Walsh, and D. White, *J. Phys. Chem.*, **71**, 2707 (1967).
(18) D. L. Hildenbrand, *Chem. Phys. Lett.*, **15**, 379 (1972).
(19) S. Gordon and B. J. McBride, *NASA Spec. Publ.*, **NASA SP-273** (1971).
(20) D. R. Stull and H. Prophet, *Nat. Stand. Ref. Data Ser., Nat. Bur. Stand.*, **No. 37** (1971).
(21) F. C. Cowlard and J. C. Lewis, *J. Mater. Sci.*, **2**, 507 (1967).

Electrical Relaxation in a Glass-Forming Molten Salt

F. S. Howell, R. A. Bose, P. B. Macedo, and C. T. Moynihan*

Vitreous State Laboratory, Department of Chemical Engineering and Materials Sciences, and Department of Physics, Catholic University of America, Washington, D. C. 20017 *(Received August 27, 1973)*

Publication costs assisted by the Air Force Office of Scientific Research

The dielectric constant ϵ' and electrical conductivity σ of a glass-forming 40 mol % $Ca(NO_3)_2$–60 mol % KNO_3 melt were measured over a frequency range of 0.02 Hz–1 MHz and a temperature range of 25–96°. Measurements were carried out both on the equilibrium liquid above 60° and the nonequilibrium glass below 60°. The observed frequency dispersions in ϵ' and σ were attributed to a nonexponential decay of the electric field *via* the ionic diffusion process and analyzed as such. It was found that the electric field relaxation was well described by the decay function $\phi(t) = \exp[-(t/\tau_0)^\beta]$, $0 < \beta \leq 1$. The mean electric field relaxation time, $\langle\tau_\sigma\rangle$, for the liquid was found to be faster than the mean shear stress relaxation time, $\langle\tau_S\rangle$, by a factor ranging from 10 to 10^4 over the temperature range 96–60°, indicating a solid-like ionic conductivity mechanism in the highly viscous melt. The activation enthalpy for the electrical conductivity dropped from 78 kcal/mol for the equilibrium liquid to 24 kcal/mol for the glass. The difference between liquid and glass activation enthalpies was attributed to thermally induced structural changes in the equilibrium liquid. The width of the spectrum of electric field relaxation times was temperature independent for the glass but broadened with increasing temperature for the liquid. From this it was concluded that the source of the spectrum of relaxation times was the microscopic heterogeneity of the vitreous system and that the temperature dependence of the width of the spectrum for the liquid reflected thermally induced structural changes.

Introduction

In the past decade a large number of anhydrous fused salt mixtures have been found to be glass forming. The most widely studied of these is the $Ca(NO_3)_2$–KNO_3 system which forms glasses over the composition range 25–50 mol % $Ca(NO_3)_2$.[1,2] The resistance to crystallization of supercooled $Ca(NO_3)_2$–KNO_3 melts and the concomitant increase in characteristic relaxation times on supercooling has made possible for this system a number of relaxational studies not feasible with more fluid molten salts. Among these are longitudinal[3] and shear[4,5] ultrasonic relaxational studies and the studies of Angell and coworkers[2,6] of property changes at the glass transition.

Of interest for the present work are the electrical relaxation measurements on a 38 mol % $Ca(NO_3)_2$–62 mol % KNO_3 melt carried out by Rhodes, Smith, and Ubbelohde.[7] They measured the complex electrical permittivity, $\epsilon^* = \epsilon' - i\epsilon'' = \epsilon' - i(\sigma/\omega e_0)$, over the temperature range 84–96° and the frequency range 20 kHz–10 MHz, where ϵ' is the dielectric constant, ϵ'' the dielectric loss, σ the conductivity, ω the angular frequency, and e_0 the permittivity of free space. A dispersion in the dielectric constant ϵ' was observed, the magnitude of which appeared to increase markedly with increasing temperature. Rhodes, *et al.*, analyzed their data in the conventional fashion[8,9] for dielectric relaxation, subtracting from ϵ'' the contribution from the dc conductivity of the melt. The dispersions in ϵ' and in the remaining part of ϵ'' were then tentatively ascribed to oscillation of the Ca^{2-} ions between alternative sites in an ionic cluster.

Analysis of electrical relaxation phenomena in terms of the complex permittivity ϵ^* yields relaxational parameters characteristic of the decay of the displacement vector, **D**, under the constraint of constant electric field, **E**.[10] In a recent series of papers from this laboratory[8,11-13] it has been pointed out that for electrical relaxation in dielectrics containing a substantial concentration of mobile charges it is generally more fruitful to focus attention on the decay of **E** at constant **D**. If surface charges of opposite sign are instantaneously placed on opposite faces of an ionic conductor at time zero and then maintained at a constant value, there will arise inside the material an electric field which in time will decay to zero due to migration of the mobile ions. The decay may be described in the time domain by

$$\mathbf{E}(t) = \mathbf{E}(0)\phi(t) \tag{1}$$

where $\phi(t)$ is a decay function of the general form

$$\phi(t) = \int_0^\infty d\tau_\sigma\ g(\tau_\sigma)\ \exp(-t/\tau_\sigma)$$

τ_σ is an electric field or conductivity relaxation time, and $g(\tau_\sigma)$ is a normalized density function for relaxation times. In the frequency domain this process may be described by[8,11-13]

$$M^*(\omega) \equiv 1/\epsilon^*(\omega) = M' + iM'' = M_s\left[1 - \int_0^\infty dt\ \exp(-i\omega t)(-d\phi(t)/dt)\right] = M_s\int_0^\infty d\tau_\sigma\ g(\tau_\sigma)[i\omega\tau_\sigma/(1 + i\omega\tau_\sigma)] \tag{2}$$

where $M^*(\omega)$ is an inverse complex permittivity or electric modulus and

$$M_s \equiv \lim_{\omega\tau_\sigma \gg 1} M' = 1 \Big/ \lim_{\omega\tau_\sigma \gg 1} \epsilon' \equiv 1/\epsilon_s$$

The limiting low-frequency dielectric constant, ϵ_0, of the conducting dielectric is related to the limiting high-frequency dielectric constant ϵ_s, by [8,11-13]

$$\epsilon_0 \equiv \lim_{\omega\tau_\sigma \ll 1} \epsilon' = \epsilon_s\langle\tau_\sigma^2\rangle/\langle\tau_\sigma\rangle^2 \tag{3}$$

where $\langle\tau_\sigma\rangle$ and $\langle\tau_\sigma^2\rangle$ are respectively the mean and mean

square relaxation times. If the decay function $\phi(t)$ is nonexponential (*i.e.*, if there is a distribution of relaxation times and $g(\tau_\sigma)$ is not a delta function), as is the usual case for relaxation processes in vitreous materials, the $\langle\tau_\sigma^2\rangle/\langle\tau_\sigma\rangle^2$ term in eq 3 will be greater than unity. The decay of the electric field due to migration of mobile ions will then give rise to a nonzero frequency dispersion ($\epsilon_0 - \epsilon_s$) in the dielectric constant ϵ'. Simple physical models for this phenomenon, which differ fundamentally in nature from the type of dielectric relaxation observed in polar nonelectrolytes, have been presented previously[8,12] and are discussed below.

In terms of eq 3 the temperature dependence of the magnitude of the dispersion in ϵ' observed by Rhodes, *et al.*,[7] in a $Ca(NO_3)_2$–KNO_3 melt implies a strong temperature dependence of the distribution of relaxation times for the electric field relaxation. This in turn has very fundamental implications about the nature of the electrical conductivity process in the fused salt, so that an analysis of their data in terms of the electric field relaxation should be highly informative. Their data, however, cover only a short temperature range and too small a frequency range (less than three orders of magnitude) to allow a complete characterization of typical viscous liquid relaxation processes. Hence it was decided to repeat their investigation over an extended temperature and frequency range. The melt composition selected was 40 mol % $Ca(NO_3)_2$–60 mol % KNO_3, for which several previous transport property and relaxational studies have been carried out at this laboratory.[3,4,14,15] The glass transition temperature, T_g (shear viscosity 10^{13} P), is approximately 60°.[4] Since heretofore no detailed characterizations of electrical relaxation in a vitreous ionic conductor both above and below the glass transition temperature have been reported, the present investigation included also a study of electrical relaxation in the $0.4Ca(NO_3)_2$–$0.6KNO_3$ glass.

Experimental Section

Measurements of the equivalent parallel capacitance C and conductance G of a melt or glass sample were carried out over the frequency range 0.02 Hz–1 MHz. In the low-frequency regime (0.02–500 Hz) a three-terminal admittance bridge based on the design of Berberian and Cole[16] was used. At higher frequencies a General Radio 1615A capacitance bridge (0.35–100 kHz) and a three-terminal bridge similar to that described by Cole and Gross[17] (0.5 kHz–1 MHz) were employed.

The dielectric cell was constructed of gold-plated stainless steel with electrical insulators made of Rulon, a filled Teflon with good mechanical stability at high temperatures. In other respects the cell was identical with one described previously.[12] The vacuum capacitance, C_0, was approximately 0.9 pF. The cell was thermostatted in an ethylene glycol–water bath whose temperature could be controlled to ±0.05°. Bath temperatures were measured to an accuracy of ±0.1° either with a calibrated mercury-in-glass thermometer or with a calibrated copper–constantan thermocouple.

Melts were prepared by weight from Fisher Certified Reagent Grade potassium nitrate and from Mallinckrodt AR calcium nitrate tetrahydrate which had been dehydrated by heating in a drying oven at about 160° until no further weight loss occurred. A mixture of the salts of composition 40 mol % $Ca(NO_3)_2$–60 mol % KNO_3 was fused in a beaker on a hot plate and allowed to stand for 1–2 days in the molten state. The lower part of the dielectric cell (a cylindrical cup) was then heated on the same hot plate and melt poured into it to a sufficient height to cover the electrodes. The upper part of the dielectric cell (the electrode assembly) was inserted and bolted to the lower portion. The filled cell was then quenched in hot water at about 60° and transferred to the thermostat bath at about the same temperature.

Two sets of measurements were performed using separately prepared melt samples. In the first of these (equilibrium liquid measurements) the melt was annealed in the cell at 60.1° (approximately T_g) until no further changes were observed in the capacitance C and conductance G readings at a given frequency. C and G were then measured as a function of frequency at this temperature. The temperature was raised by a few degrees and the C and G *vs.* frequency measurements repeated when the melt had come to equilibrium. Measurements were continued in this fashion up to 96.3°.

In the second set of measurements (glass) two preliminary sets of C and G *vs.* frequency data for the equilibrium liquid were collected as described above at two temperatures near T_g to ensure that data obtained in the first set of measurements were reproducible. The melt was then annealed for approximately 3 hr in the cell at 59.5°, followed by a quench in ice water to form the glass. C and G *vs* frequency measurements were then carried out on the glass at five temperatures in ascending order, starting at 25 3° and ending at 54.3°.

Results and Data Analysis

In Figures 1 and 2 are shown plots of the dielectric constant ϵ' and conductivity σ *vs.* frequency for five temperatures above the glass transition. The ϵ' plots of Figure 1 exhibit a frequency dispersion and at the lower temperatures (60.1, 65.3, and 71.4°) a low-frequency plateau corresponding to the limiting low-frequency bulk dielectric constant ϵ_0. At still lower frequencies the ϵ' plots commence a rapid increase with decreasing frequency due to electrode polarization,[8,12] as seen in the curves of Figure 1 for 71.4, 80.7, and 93.2°. At the higher temperatures of Figure 1 (80.7 and 93.2°) the onset of electrode polarization is such that only a low-frequency shoulder rather than a plateau indicates the leveling of the bulk dielectric constant at ϵ_0. The melt conductivities of Figure 2 level off at low frequencies at a value corresponding to the bulk dc conductivity, σ_0.[8,12] Experimental σ_0 values above T_g are listed in Table I and are in excellent agreement with previously measured σ_0 values[14] for this melt.

In Figures 3 and 4 are shown ϵ' and σ *vs.* frequency plots for the $0.4Ca(NO_3)_2$–$0.6KNO_3$ glass. Unlike Figure 1, the ϵ' plots of Figure 3 do not exhibit low-frequency plateaus or shoulders corresponding to the bulk ϵ_0 value, nor do the plots of Figure 4 level out completely at bulk σ_0 values at low frequencies. The preliminary measurements above T_g for this melt before quenching it to form the glass gave ϵ'–f and σ–f plots identical in shape with those of Figures 1 and 2. Hence the most likely explanation for the lack of low-frequency plateaus or shoulders in the ϵ' plots of Figure 3 and the lack of a low-frequency leveling in the σ plots of Figure 4 is that the thermal contraction of the glass on quenching caused it to crack or to pull away slightly from the electrode surfaces, leaving small gaps which act as a large capacitance in series with the sample. Effects of this sort have been discussed in previous publications.[8,12]

TABLE I: Electric Field Relaxational Parameters for $0.4Ca(NO_3)_2$–$0.6KNO_3$ Melt and Glass

T, °C	β	M_s	τ_0(s)	$\langle\tau_\sigma\rangle$(s)	σ_0 (expt), Ω^{-1} cm^{-1}	σ_0 (calcd),[a] Ω^{-1} cm^{-1}	ϵ_0 (calcd)[b]
				Glass			
25.3	0.74	0.138	2.05	2.47		2.60×10^{-13}	10.5
35.3	0.74	0.138	6.0×10^{-1}	7.2×10^{-1}		8.9×10^{-13}	10.5
44.0	0.74	0.138	1.71×10^{-1}	2.06×10^{-1}		3.1×10^{-12}	10.5
50.1	0.74	0.138	9.2×10^{-1}	1.10×10^{-1}		5.8×10^{-12}	10.5
54.3	0.74	0.138	5.6×10^{-1}	6.7×10^{-2}		9.6×10^{-12}	10.5
				Liquid			
60.1	0.72	0.133	1.22×10^{-2}	1.50×10^{-2}	4.3×10^{-11}	4.4×10^{-11}	11.3
62.4	0.70	0.133	6.6×10^{-3}	8.4×10^{-3}	7.9×10^{-11}	7.9×10^{-11}	11.8
65.3	0.69	0.129	2.64×10^{-3}	3.4×10^{-3}	1.97×10^{-10}	2.02×10^{-10}	12.4
68.6	0.67	0.126	8.6×10^{-4}	1.13×10^{-3}	6.0×10^{-10}	6.2×10^{-10}	13.4
71.4	0.64	0.124	3.3×10^{-4}	4.6×10^{-4}	1.51×10^{-9}	1.57×10^{-9}	14.7
74.6	0.61	0.122	1.13×10^{-4}	1.66×10^{-4}	4.3×10^{-9}	4.4×10^{-9}	16.3
77.7	0.59	0.120	4.0×10^{-5}	6.1×10^{-5}	1.22×10^{-8}	1.21×10^{-8}	17.6
80.7	0.58	0.116	1.40×10^{-5}	2.21×10^{-5}	3.46×10^{-8}	3.5×10^{-8}	18.8
83.9	0.55	0.115	4.5×10^{-6}	7.6×10^{-6}	1.03×10^{-7}	1.03×10^{-7}	21.1
86.8	0.53	0.114	1.67×10^{-6}	3.0×10^{-6}	2.52×10^{-7}	2.58×10^{-7}	23.1
89.9	0.53	0.113	7.0×10^{-7}	1.28×10^{-6}	6.0×10^{-7}	6.1×10^{-7}	23.3
93.2	0.52	0.112	2.92×10^{-7}	5.5×10^{-7}	1.46×10^{-6}	1.45×10^{-6}	24.5
96.3					3.10×10^{-6}		

[a] Equation 5. [b] Equation 3.

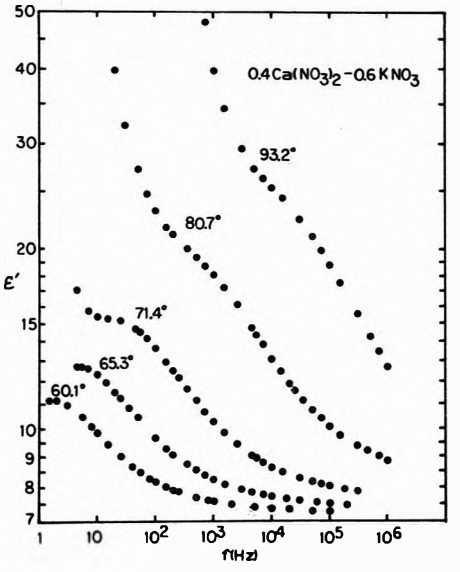

Figure 1. Dielectric constant *vs.* frequency for $0.4Ca(NO_3)_2$–$0.6KNO_3$ melt above the glass transition temperature.

In Figures 5 and 6 are shown plots *vs.* frequency of the real and imaginary parts, M' and M'', of the electric modulus for five temperatures above T_g. These were calculated from the measured ϵ' and ϵ'' *via*[8,11,12]

$$M' = \epsilon'/(\epsilon'^2 + \epsilon''^2)$$
$$M'' = \epsilon''/(\epsilon'^2 + \epsilon''^2)$$

The shapes and heights of the M' and M'' plots of Figures 5 and 6 for the liquid are highly temperature dependent. For the glass, on the other hand, the shapes and heights of the M' and M'' plots were to a good approximation independent of temperature. This is shown in Figure 7 in which a representative selection of M' and M'' data points for the glass at different temperatures is plotted *vs.* a reduced frequency $\omega\tau_0$ (see below for meaning of τ_0). On the scale of the plots of Figures 5 and 7 M' approaches zero at low frequencies. As explained previously,[8,12] this indicates that electrode polarization and sample-electrode

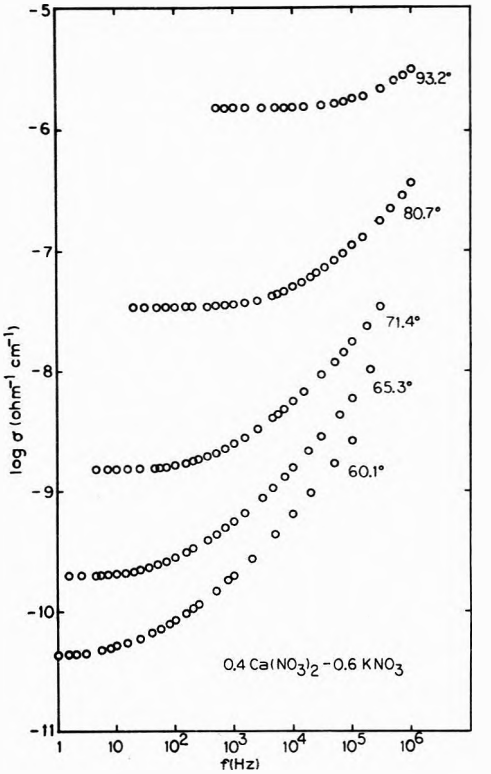

Figure 2. Conductivity *vs.* frequency for $0.4Ca(NO_3)_2$–$0.6KNO_3$ melt above the glass transition temperature.

gaps make a negligible contribution to M^* and may be ignored when the data are analyzed in this form.

The M^* data for the $0.4Ca(NO_3)_2$–$0.6KNO_3$ melt and glass were analyzed in terms of the nonexponential decay function (see eq 1 and 2)

$$\phi(t) = \exp[-(t/\tau_0)^\beta] \quad 0 < \beta \leq 1 \qquad (4)$$

where τ_0 is a characteristic relaxation time and β a relaxational parameter which decreases with an increase in the width of the relaxation time distribution. Analysis techniques have been described elsewhere.[13] The relaxational

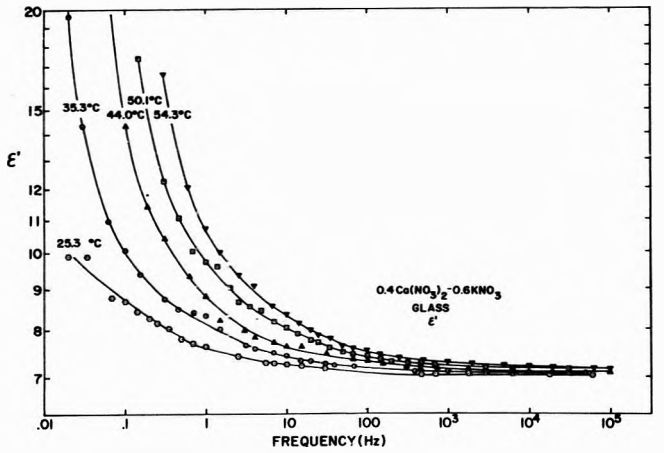

Figure 3. Dielectric constant *vs.* frequency for $0.4Ca(NO_3)_2$–$0.6KNO_3$ glass.

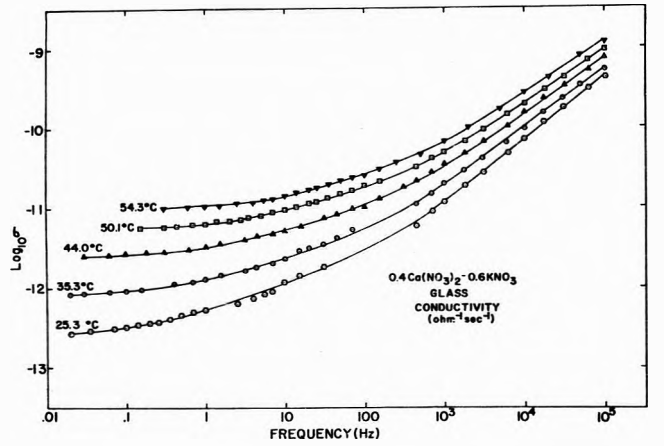

Figure 4. Conductivity *vs.* frequency for $0.4Ca(NO_3)_2$–$0.6KNO_3$ glass.

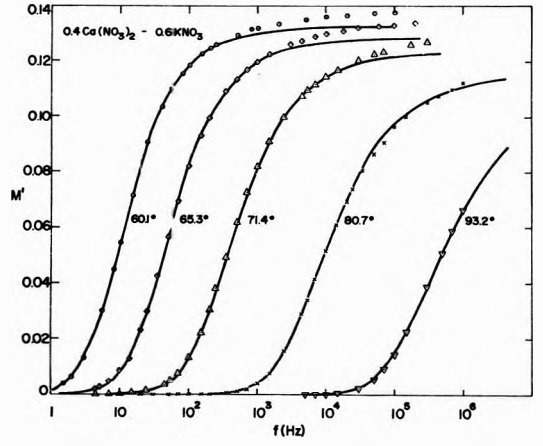

Figure 5. Real part of electric modulus *vs.* frequency for $0.4Ca(NO_3)_2$–$0.6KNO_3$ melt above the glass transition temperature.

parameters β, M_s, and τ_0 for glass and liquid are listed in Table I as a function of temperature. M' and M'' curves calculated from these parameters are shown in Figures 5–7 and are seen to give an excellent fit to the data up to frequencies 1.5 decades beyond the maximum in M'' for the liquid and over an even more extensive frequency range for the glass Also listed in Table I are the mean conductivity relaxation times calculated from[13]

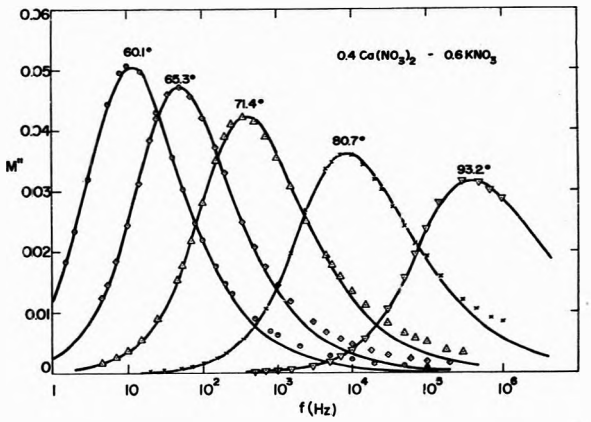

Figure 6. Imaginary part of the electric modulus *vs.* frequency for $0.4Ca(NO_3)_2$–$0.6KNO_3$ melt above the glass transition temperature.

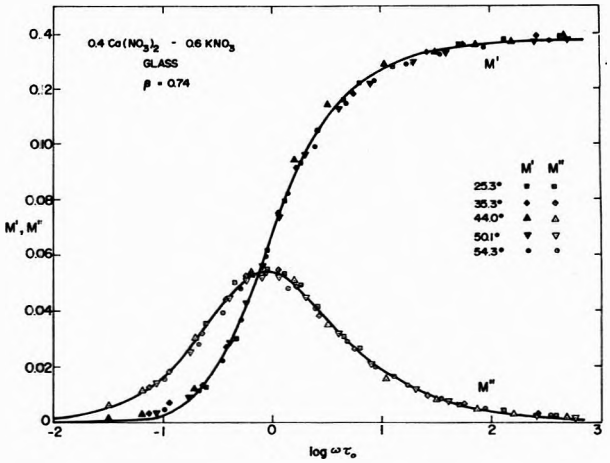

Figure 7. Real and imaginary parts of the electric modulus *vs.* reduced frequency $\omega\tau_0$ for $0.4Ca(NO_3)_2$–$0.6KNO_3$ glass.

$$\langle\tau_\sigma\rangle = (\tau_0/\beta)\Gamma(1/\beta)$$

the dc bulk conductivities calculated from[8,11,12]

$$\sigma_0 = e_0\epsilon_s/\langle\tau_\sigma\rangle = e_0/M_s\langle\tau_\sigma\rangle \quad (5)$$

and the limiting low-frequency dielectric constants ϵ_0 calculated from eq 3 using[13]

$$\langle\tau_\sigma^2\rangle = (\tau_0^2/\beta)\Gamma(2/\beta) \quad (6)$$

where Γ denotes the gamma function. The excellent agreement between measured and calculated ϵ_0 and σ_0 values for the liquid is likewise an indication of the goodness of the fit of the decay function of eq 4 to the observed electric field relaxation data.

Discussion Section

Comparison of Shear and Conductivity Relaxation Times. In Figure 8 is shown an Arrhenius plot of the mean electric field or conductivity relaxation time, $\langle\tau_\sigma\rangle$. At and below 93.2° the $\langle\tau_\sigma\rangle$ data points were taken from Table I; above 93.2° the $\langle\tau_\sigma\rangle$ values were calculated from eq 5 using the conductivity data of Bose, *et al.*,[14] and an M_s value of 0.112. Also plotted in Figure 8 are values of the average shear relaxation time, $\langle\tau_S\rangle$, for the melt calculated from[18] $\langle\tau_S\rangle = \eta_S/G_\infty$, where η_S is the equilibrium liquid shear viscosity and G_∞ the limiting high-frequency or "solid-like" shear modulus. Values of η_S and G_∞ were taken from previous publications.[4,15] The $\langle\tau_S\rangle/\langle\tau_\sigma\rangle$ ratio for the equilibrium liquid is shown as a function of temperature in the inset

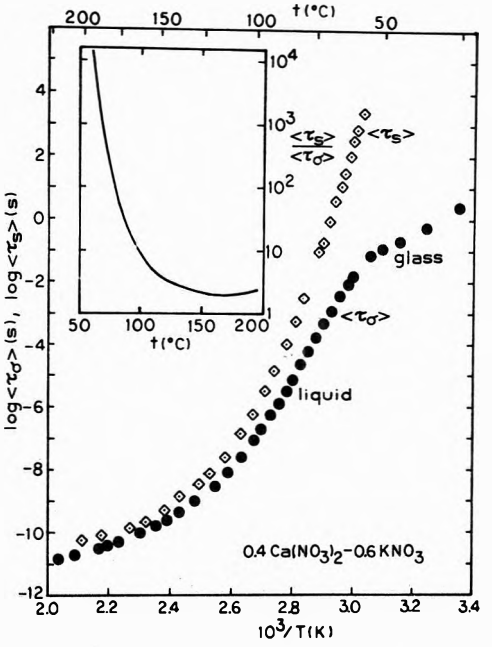

Figure 8. Arrhenius plots of mean conductivity relaxation times $\langle\tau_\sigma\rangle$ and mean shear relaxation times $\langle\tau_S\rangle$ for vitreous $0.4Ca(NO_3)_2$–$0.6KNO_3$. Inset shows $\langle\tau_S\rangle/\langle\tau_\sigma\rangle$ ratio *vs.* temperature.

to Figure 8. M_s values above 93.2° and G_∞ values above 90° are estimated or extrapolated from data at lower temperatures, so that some uncertainty attaches to the high-temperature $\langle\tau_\sigma\rangle$ and $\langle\tau_S\rangle$ values of Figure 8. It is unlikely, however, that at the high-temperature extreme of Figure 8 the $\langle\tau_\sigma\rangle$ and $\langle\tau_S\rangle$ values are in error by more than a factor of 2, which is unimportant for the qualitative conclusions of the present paper.

$\langle\tau_S\rangle$ is the average time constant for decay of a shear stress at constant strain in the liquid *via* the viscous flow mechanism. As such it approximates the time constant for overall rearrangement of the liquid structure and can be considered to be the kinetic parameter controlling the ordinary glass transition. As seen in Figure 8, $\langle\tau_\sigma\rangle$ and $\langle\tau_S\rangle$ for the $0.4Ca(NO_3)_2$–$0.6KNO_3$ melt are of comparable magnitude at high temperatures, so that ionic electrical migration and diffusion are accompanied by simultaneous rearrangement of the local liquid structure. This is to be expected from the approximate validity of the Stokes–Einstein and Nernst–Einstein equations for fluid melts.[19] Below 150°, however, the $\langle\tau_S\rangle/\langle\tau_\sigma\rangle$ ratio of the liquid commences an accelerated increase with decreasing temperature, attaining a value of around 10^4 in the glass transition region. $\langle\tau_\sigma\rangle$ is related *via* eq 5 to the dc conductivity σ_0 and hence to the mobilities of the most mobile ions in the system. Hence this result implies that at low fluidities and temperatures where $\langle\tau_S\rangle \gg \langle\tau_\sigma\rangle$ a solid-like electrical conduction mechanism prevails in the equlibrium $0.4Ca(NO_3)_2$–$0.6KNO_3$ melt. The mobile ions migrate through a quasilattice structure which is "frozen" on the time scale of the elementary diffusive motions of the mobile ions in a fashion similar qualitatively to alkali ion diffusion in silicate glasses or to vacancy diffusion in alkali halide crystals.

As noted in previous papers[20-22] this sort of phenomenon ($\langle\tau_S\rangle \sim \langle\tau_\sigma\rangle$ at high fluidities, $\langle\tau_S\rangle \gg \langle\tau_\sigma\rangle$ at low fluidities near T_g) seems to be a common property of a wide variety of ionic liquids. The $\langle\tau_S\rangle - \langle\tau_\sigma\rangle$ discrepancy near

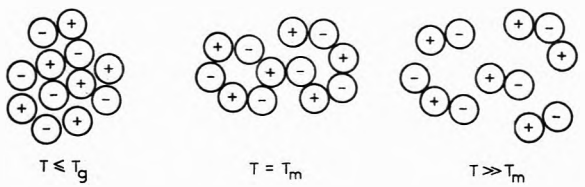

Figure 9. Two-dimensional representations of fused salt structure in different temperature regions. T_m is the melting point.

T_g is manifested in the extreme in alkali network oxide melts, where at 10^{13} P equilibrium melt conductivities are of the order of 10^{-4} to 10^{-3} ohm^{-1} cm^{-1},[23] corresponding to $\langle\tau_S\rangle/\langle\tau_\sigma\rangle$ ratios of the order of 10^{10}–10^{11}.[20] On the other hand, for concentrated aqueous LiCl solutions the $\langle\tau_S\rangle/\langle\tau_\sigma\rangle$ ratio near T_g is only around 5–10.[20] The $\langle\tau_S\rangle/\langle\tau_\sigma\rangle$ ratios near T_g for the $0.4Ca(NO_3)_2$–$0.6KNO_3$ fused salt and for concentrated aqueous calcium nitrate solutions[21,22] appear to be intermediate between those for the alkali network oxide melts and those for the LiCl solutions.

It has been suggested previously[20-22] that $\langle\tau_S\rangle/\langle\tau_\sigma\rangle$ ratios greater than unity at low temperatures may arise from a substantial mobility difference between the component ions of an ionic liquid, the faster moving ions determining $\langle\tau_\sigma\rangle$ and the slower moving ions, which control the rate of rearrangement of the overall liquid structure, determining $\langle\tau_S\rangle$. In the present case it may be that the strong coulombic interactions of the divalent Ca^{2+} ions with NO_3^- ions lead to local structural elements whose characteristic rearrangement times are long compared to the times characteristic of diffusional motions of the monovalent K^+ ions with respect to neighboring nitrates.

It appears, then, that there are three somewhat different isobaric conductivity mechanisms for a typical equilibrium ionic melt which manifest themselves in different temperature regions. The structures characteristic of these three regions are suggested in the idealized two-dimensional representations of a fused salt of Figure 9.

Typical fused salts melt with a substantial increase in volume and a decrease in both nearest-neighbor coordination numbers and interionic distances.[24] In the region near the melting point, characterized usually by viscosities of the order of 0.01–0.1 P, the molten salt exhibits what might be termed an *ionic liquid* type of conductivity. $\langle\tau_S\rangle$ and $\langle\tau_\sigma\rangle$ are of comparable magnitude, as are the mobilities of all the component ions, and the electrical conductivity shows a positive temperature coefficient. The conductivity mechanism in this region (if the term "mechanism" is at all applicable) is a small biased drift of anions and cations in opposite directions superimposed upon a rapid and continual rearrangement of the local liquid structure. In this region any sort of transition state or activated jump theory of ionic transport is quite inappropriate, as pointed out by Goldstein.[19,25]

As the fused salt is cooled below the ionic liquid region, the density of the salt increases, presumably accompanied by an increase in nearest-neighbor coordination numbers, and eventually a high viscosity region in which $\langle\tau_S\rangle \gg \langle\tau_\sigma\rangle$ is reached. In this region the melt exhibits the *ionic solid* type of conductivity which has been described above, and transition state or activated jump theories of ionic conductivity are appropriate.[19,25]

If the salt temperature is raised isobarically far above the melting point a region is reached in which the conductivity passes through a maximum and then decreases with further temperature increases, although the viscosity continues to decrease with increasing temperature.[19,26,27]

Here the volume of the salt has increased to a point that it is energetically unfavorable for the system to maintain a fairly uniform particle density on a microscopic level. Rather the system has begun to take on gas-like properties with extensive association of ions into "clusters," accompanied by a net decrease in the number of "free" charged particles.[19] In this region above the conductivity maximum the system may be said to exhibit a *weak electrolyte* type of conductivity, and it is likely that $\langle\tau_\sigma\rangle$ will become smaller than $\langle\tau_S\rangle$.

Temperature Dependence of Conductivity above and below the Glass Transition Temperature. As shown in Figures 8 and 10, the Arrhenius plots of $\langle\tau_\sigma\rangle$ and σ_0 exhibit abrupt changes in slope at the glass transition around 60°. Between T_g and about 95° the liquid σ_0 values of Table I show an Arrhenius temperature dependence with an activation enthalpy, $\Delta H^* = -R\ \mathrm{d}\ \ln\ \sigma_0/\mathrm{d}(1/T)$, of 78 kcal/mol, where R is the ideal gas constant. This is in good agreement with the results of a previous study.[14] The glass below T_g also exhibits an Arrhenius temperature dependence, but with a much smaller activation enthalpy, 24 kcal/mol. Similarly large conductivity activation enthalpy differences between liquid and glass have been reported for alkali network oxide systems.[23]

Qualitatively, the explanation of the decrease in ΔH^* at the glass transition is as follows. Above T_g the structural relaxation times for the liquid are short compared to the time taken to thermostat the sample and to perform the permittivity measurements. (The magnitude of the structural relaxation time can be approximated roughly by $\langle\tau_S\rangle$.) Hence above T_g the temperature coefficient of σ_0 or $\langle\tau_\sigma\rangle$, as manifested in the activation enthalpy, reflects both changes in the actual temperature and thermally induced changes in the equilibrium liquid structure. Well below T_g the structural relaxation times are very long compared to the time needed to thermostat the sample and to perform the permittivity measurements, so that the liquid structure is frozen on the time scale of the experiment. ΔH^* for the glass thus lacks any contribution from changes in the structure of the system and is correspondingly smaller than ΔH^* for the equilibrium liquid. Fused salt structures above and below T_g are suggested pictorially in Figure 9. For the present system changes in the equilibrium structure of the liquid account for some two-thirds of the conductivity activation enthalpy in the temperature region just above T_g.

It is instructive to note that this explanation is somewhat analogous to that used to account for the increase in conductivity activation enthalpy in alkali halide crystals in passing from the low-temperature extrinsic conduction region to the high-temperature intrinsic conduction region.[28] In the extrinsic region the number of vacancies is temperature independent and equal to the number quenched into the crystal from higher temperatures or associated with impurities. In the intrinsic region the number of vacancies is controlled by the equilibrium thermodynamics of vacancy formation and becomes highly temperature dependent, giving rise to an additional contribution to the conductivity temperature coefficient.

The simplest one-parameter characterization of the structure of a vitreous system is in terms of a fictive (or structural or configurational) temperature, T_f.[29-31] In the most approximate sense T_f may be thought of as the temperature at which the structure of the system would be the equilibrium structure. Hence T_f and the actual temperature T are identical for an equilibrium liquid, but for a nonequilibrium glass, depending on its previous thermal history, T_f may be greater or less than T. An isobaric transport property w, such as conductivity, inverse relaxation time, etc., might then be expressed functionally in the form

$$w = w(T, T_f) \tag{7}$$

The corresponding activation enthalpy is

$$\Delta H^* \equiv -R\frac{\mathrm{d}\ \ln\ w}{\mathrm{d}(1/T)} = -R\left[\frac{\partial\ \ln\ w}{\partial(1/T)}\right]_{T_f} - R\left[\frac{T^2}{T_f^2}\right]\left[\frac{\partial\ \ln\ w}{\partial(1/T_f)}\right]_T \frac{\mathrm{d}T_f}{\mathrm{d}T} \tag{8}$$

For the equilibrium liquid above T_g, $T_f = T$, $\mathrm{d}T_f/\mathrm{d}T = 1$, and both terms on the right-hand side of eq 8 contribute to ΔH^*, provided that $(\partial\ \ln\ w/\partial(1/T_f))_T$ is not zero. For the glass well below T_g, where the structure is frozen on the experimental time scale, T_f is a constant, $\mathrm{d}T_f/\mathrm{d}T = 0$, and only the first term on the right-hand side of eq 8 contributes to ΔH^*. Thus ΔH^* for the equilibrium liquid is different from ΔH^* for the glass.

Equations 7 and 8 imply that experimentally observable effects associated with the glass transition are of a purely relaxational character, although the magnitude of the kinetic parameters may depend in turn upon thermodynamic quantities such as free volume,[32] configurational entropy,[33] or degree of bonding.[34] The experimental evidence for the dependence of liquid and glass transport properties such as bulk viscosity, shear viscosity, and ionic conductivity upon the structure of the system is incontrovertible.[23,29-31,35-38] Rather the main problem with regard to eq 7 and 8 is the presumption that, in addition to temperature T, a single structure-dependent ordering parameter, which we have termed T_f, is sufficient to specify a given transport property w for a vitreous system. There is some experimental evidence that this is not too bad as a first approximation. Narayanaswamy[31] has shown recently that the mean relaxation time controlling isobaric volume or shear compliance relaxation during annealing of oxide glasses could be expressed in the form

$$\langle\tau\rangle = \langle\tau\rangle_0 \exp\left[\frac{X\Delta E}{RT} + \frac{(1-X)\Delta E}{RT_f}\right]$$

where $\langle\tau\rangle_0$, ΔE, and X are constants, $0 \le X \le 1$, and T_f is assessed from the specific volume or refractive index of the glass. Saad and Moynihan[38] have recently confirmed Narayanaswamy's conclusions for evolution of both volume and electrical conductivity during isothermal annealing of alkali silicate glasses.

We hasten to add here that for a given glass a fictive temperature assessed from one property, such as specific volume, is not necessarily the appropriate ordering parameter for specifying a different property, such as the electrical conductivity. This was shown by Ritland[36] and confirmed by Boesch and Moynihan,[37] who found that an annealed and quenched glass and a rate-cooled glass which had the same refractive indices had different values of the dc conductivity. Hence it would seem that the ordering parameter T_f for a transport property must be defined in some nonredundant fashion appropriate to the property itself. If eq 7 and 8 are valid, both the property $w(T, T_f)$ and its temperature coefficient are functions of T_f. Thus a useful internal consistency condition for the use of a single parameter T_f is that the activation enthalpy ΔH^* for a glass should be a single monotonic function of the corresponding transport property $w(T, T_f)$ at a fixed

temperature T. A test of this sort is shown in Figure 11 for the conductivity of three alkali network oxide glasses.[36,37] As predicted if a single ordering parameter T_f is to a first approximation sufficient to specify σ_0 at a fixed temperature, the ΔH^*–σ_0 points for both rate-cooled and annealed-and-quenched glasses fall on the same curve for a given system within the experimental error in ΔH^* (conservatively estimated at ±0.1 kcal/mol).

Acceptance of eq 7 and 8 implies an important criterion which must be met by any theory which leads to an expression for the isobaric dependence of transport properties of liquids and glasses. The theory must allow for the dependence of the transport property on the fictive temperature, T_f, or on some other structure-dependent property (*e.g.*, free volume, configurational entropy or enthalpy, degree of bonding, number of "holes," etc.) related to it. More specifically, a single functional form must account for the temperature dependence of the transport property in both the liquid and the glass.

Consider for instance the Adam–Gibbs expression for the transport property w[33]

$$w = w_0 \exp[-b/RTS_c(T_f)] \tag{9}$$

where w_0 and b are constants. $S_c(T_f)$ is the configurational entropy and depends only on the fictive temperature. From eq 8 the activation enthalpy is

$$\Delta H^* = \frac{b}{S_c(T_f)} + \frac{bT}{S_c^2(T_f)}\left[\frac{dS_c(T_f)}{dT_f}\right]\frac{dT_f}{dT} \tag{10}$$

Recalling that for the equilibrium liquid $dT_f/dT = 1$, while for the glass $dT_f/dT = 0$, the liquid activation enthalpy is

$$\Delta H_{liq}^* = \frac{b}{S_c(T_f)} + \frac{bT}{S_c^2(T_f)}\left[\frac{dS_c(T_f)}{dT_f}\right] \tag{11}$$

and the glass activation enthalpy is

$$\Delta H_{gl}^* = b/S_c(T_f) \tag{12}$$

All the quantities in the second term of the right side of eq 11 are positive, so that the Adam–Gibbs theory predicts that $\Delta H_{liq}^* > \Delta H_{gl}^*$, in accord with experiment. Interestingly, since $dS_c(T_f)/dT_f$ is positive, eq 12 also predicts that ΔH_{gl}^* should decrease with increasing fictive temperature. This is in accord with the data of Figure 11 and with the observations of Kaneko and Isard[23] on the conductivities of alkali silicate glasses.

If one assumes that $S_c(T_f)$ is given by[33]

$$S_c(T_f) = \Delta C_p \ln (T_f/T_0)$$

where ΔC_p is a temperature-independent configurational heat capacity and T_0 the temperature at which the configurational entropy vanishes at equilibrium, eq 9 may be written

$$w = w_0 \exp[-(b/\Delta C_p)/RT \ln (T_f/T_0)] \tag{13}$$

and corresponding modifications made in eq 10–12. Plazek and Magill[35] found that the temperature dependence of the relaxation time for the recoverable part of the shear compliance for tri-α-naphthylbenzene could be described by eq 13. More important, they found that having assessed the parameters $(b/\Delta C_p)$ and T_0 from the data for the *liquid*, they were able to predict quantitatively the activation enthalpy for the *glass*.

The foregoing is not intended as a defense of the Adam–Gibbs theory, either with respect to the microscopic model on which it is based or with respect to the general functional form it predicts for the temperature dependence of liquid and glass transport properties. There are many liquids whose transport properties in the highly viscous temperature regime do not conform to the predictions of the Adam–Gibbs theory, the present $0.4Ca(NO_3)_2$–$0.6KNO_3$ fused salt system being one case in point.[4,14,15] Rather it is intended as an example of a transport theory that in its most primitive functional form (*i.e.*, eq 13) handles the problem of structure and fictive temperature in a manner in accord with the criterion set forth above and in cases in which it gives an adequate description of liquid transport properties gives also, with the introduction of no additional parameters, an accurate account of the glass transport properties. The latter is not true of either the simple free volume theory[32] or of the bond-lattice theory of Angell and coworkers.[34] In these cases it would be necessary in order to account for glass transport properties to introduce additional parameters (the temperature dependence of the free volume or degree of bonding in the glass) which cannot be assessed from measurements on the equilibrium liquid.

To describe the electrical transport properties of the $0.4Ca(NO_3)_2$–$0.6KNO_3$ liquid and glass we propose a transition state theory type of expression

$$w = w_0 \exp(-\Delta G^*(T,T_f)/RT) \tag{14}$$

where $\Delta G^*(T,T_f)$ is the activation free energy and w_0 a constant. We further propose an empirical expression for $\Delta G^*(T,T_f)$ which is a sum of thermal and structural terms

$$\Delta G^*(T,T_f) = A - BT + C/T_f + D/T_f^2 + E/T_f^3 + \ldots \tag{15}$$

where A, B, C, D, E, ... are constants. The first two terms on the right side of eq 15 represent the thermal contribution to $\Delta G^*(T,T_f)$ in the ordinary "ΔH–$T\Delta S$" form; the remaining terms on the right-hand side represent the structural contribution in terms of a power series in $1/T_f$. Combining eq 14 and 15 and taking the logarithm we obtain

$$\ln w = \ln w_0' - \frac{A}{RT} - \frac{C}{RTT_f} - \frac{D}{RTT_f^2} - \frac{E}{RTT_f^3} - \ldots \tag{16}$$

where $\ln w_0' = \ln w_0 + B/R$. The activation enthalpy from eq 8 is

$$\Delta H^* = \left(A + \frac{C}{T_f} + \frac{D}{T_f^2} + \frac{E}{T_f^3} + \ldots\right) + \left(\frac{CT}{T_f^2} + \frac{2DT}{T_f^3} + \frac{3ET}{T_f^4} + \ldots\right)\frac{dT_f}{dT} \tag{17}$$

For the liquid ($T = T_f$, $dT_f/dT = 1$) this gives

$$\Delta H_{liq}^* = A + \frac{2C}{T_f} + \frac{3D}{T_f^2} + \frac{4E}{T_f^3} + \ldots \tag{18}$$

and for the glass (T_f = constant, $dT_f/dT = 0$)

$$\Delta H_{gl}^* = A + \frac{C}{T_f} + \frac{D}{T_f^2} + \frac{E}{T_f^3} + \ldots \tag{19}$$

so that our empirical expression for $\Delta G^*(T,T_f)$ leads to the expected activation enthalpy difference between liquid and glass.

The dc conductivity data of Figure 10 were fitted to eq 16 ($w = \sigma_0$) using a least-squares procedure and including terms up to the third power of $1/T_f$. T_f for the glass was

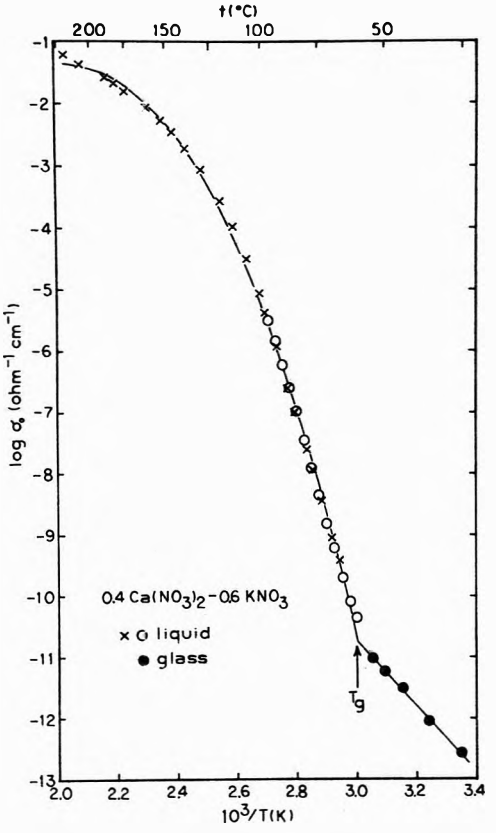

Figure 10. Arrhenius plot of dc conductivity for $0.4Ca(NO_3)_2$–$0.6KNO_3$ glass and liquid: (O) equilibrium liquid, present experimental results; (×) equilibrium liquid, ref 14; (●) glass, present results, σ_0 calculated from eq 5. Curve represents a least-squares fit of data to eq 16. The fictive temperature for the glass is indicated as "T_g."

taken to be the experimental annealing temperature prior to quenching the glass, 59.5° (= 332.7 K), and is indicated as "T_g" in Figure 10. The least-squares analysis gave, with R in cal/mol deg and σ_0 in ohm^{-1} cm^{-1}, ln w_0' = 12.35, $A = 1.3131 \times 10^5$, $C = -1.16687 \times 10^8$, $D = 3.4093 \times 10^{10}$, $E = -2.359 \times 10^{12}$, and standard deviation ln σ_0 = 0.26. The curve calculated from these parameters is shown in Figure 10. The fit is not within the precision of the experimental data, but must nonetheless be counted fairly good overall, since the standard deviation (0.26) of the experimental values of ln σ_0 from the calculated values is only about 1% of the range in ln σ_0 (25.8) covered by the data. Hence we have shown in this case, in accord with our criterion, that it is possible to account for both liquid and glass transport data with a single function which allows for the dependence of the transport property on T_f and which contains no more adjustable parameters[14,39] than are needed to give a good description of the liquid data alone.

There is one deficiency in the detailed functional form of our empirical eq 15 for ΔG^* which should be pointed out. Equation 15 predicts that the activation entropy for the glass should be independent of fictive temperature T_f

$$\Delta S_{gl}^* = -(\partial \Delta G^*/\partial T)_{T_f} = B$$

Analysis of recent experiments[37] on alkali silicate glasses has revealed, however, that ΔS_{gl}^* does show a substantial dependence on T_f. It would not be unreasonable to expect that a suitable modification of the functional form of eq 15 without the introduction of any additional empirical parameters should be able to account for this. Just what modifications are needed, however, cannot be known unless conductivity data on the same system both for the equilibrium liquid and for several glasses of different, but extremely well-defined, thermal histories are available. Such data do not appear to exist at the present, and their acquisition may be counted an experimental undertaking of some importance.

Temperature Dependence of the Distribution of Conductivity Relaxation Times. For the equilibrium liquid $0.4Ca(NO_3)_2$–$0.6KNO_3$ above the glass transition the magnitude of the dispersion in ϵ', $(\epsilon_0 - \epsilon_s)$ (Figure 1) and the width at half-height of the M'' *vs.* frequency plots (Figure 6) both increase with increasing temperature. In terms of our analysis of the electrical relaxation these two observations are accounted for by the same phenomenological explanation, an increase in the width of the distribution of conductivity or electric field relaxation times with increasing temperature, as manifested in the decrease in the liquid β parameter of Table I with increasing temperature. For the glass, on the other hand, the widths at half-height of the M'' *vs.* frequency plots (Figure 7) and the corresponding β parameters of Table I are temperature independent, indicating a similar temperature independence of the distribution of conductivity relaxation times.

In the temperature range investigated here, in which $\langle \tau_S \rangle \gg \langle \tau_\sigma \rangle$, the structure of the system is effectively frozen on the time scale of the electrical relaxation. The glass and liquid are different only insofar as the average liquid structure changes from temperature to temperature ($T_f = T$), while the glass structure is temperature independent (T_f is constant). Hence it would appear that the distribution of conductivity relaxation times is determined strictly by the structure or fictive temperature T_f of the system.

In previous publications[8,12] we have speculated that the explanation for the nonsingle distribution of conductivity relaxation times and the corresponding dispersion in ϵ' in vitreous ionic conductors was one proposed by Stevels,[40] Taylor,[41] and Isard,[42] namely, a lack of translational invariance of the free-energy barriers impeding ionic diffusion. To put it another way, the ionic diffusion and conductivity mechanism for vitreous ionic conductors in the range studied here is quite likely an ionic "hop" from one site of local free-energy minimum to another and covering at most a distance of a few atomic diameters. On a distance range of this size a vitreous material is heterogeneous, so that on the scale of the elementary ionic diffusion motions the local electrical conductivity appears to vary from site to site. The greater this microscopic heterogeneity, the broader will be the distribution of conductivity relaxation times and the greater the corresponding magnitude of the dispersion in ϵ'.

In these terms the decrease in the β parameter of Table I for the liquid with increasing temperature indicates a substantial increase[43] in the microscopic heterogeneity of the equilibrium fused salt with increasing temperature in the 33° range just above T_g covered by our experiment. The increase in heterogeneity with increasing temperature is in accord with the ideas regarding fused salt structure described in a previous section and depicted in Figure 9. It is also in accord with the suggestion of Angell[44] that, because of the nondirectional character of the bonding in an ionic melt, a fused salt may approach at low temperatures and high packing densities a state approximating the highly ordered random-close-packed liquid structure.[45] With the thermal expansion accompanying tem-

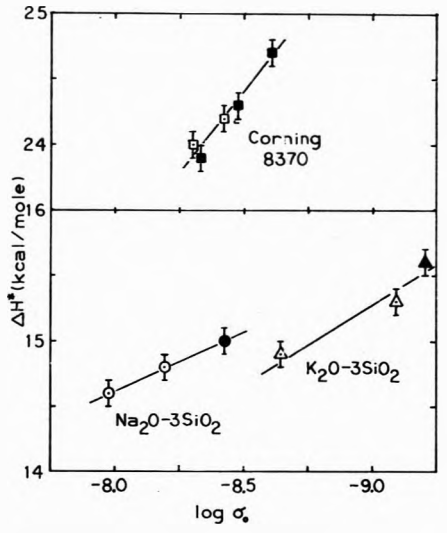

Figure 11. Conductivity activation enthalpy *vs.* dc conductivity at constant temperature for alkali network oxide glasses. Data for Corning 8370 glass at 250° from ref 36; data for sodium and potassium silicate glasses at 50° from ref 37: open symbols, annealed-and-quenched glasses; filled symbols, rate-cooled glasses.

perature increases this low-temperature geometric order decreases.

It should be noted that our findings here for the liquid contradict the predictions of the environmental relaxation model[39] proposed by one of us to account for the temperature dependence of the conductivity of this melt (see Figure 10). In this model it was suggested that the non-Arrhenius temperature dependence of σ_0 observed at intermediate temperatures was correlated with a growth in the size of the local liquid microstructure and that this in turn manifested itself as an increase in the width of the distribution of relaxation times with decreasing temperature. At sufficiently low temperatures, however, the size of the liquid microstructure was predicted to exceed the spatial range over which a transport was sensitive to the microstructure. In this low temperature range σ_0 was expected to return to an Arrhenius temperature dependence and the width of the distribution of relaxation times to saturate at a constant value. We find, however, in the low-temperature Arrhenius range for σ_0 studied here that the width of the relaxation time distribution not only fails to become temperature independent, but actually decreases with decreasing temperature.

A final point worthy of mention is a small but significant difference between the character of the distribution of conductivity relaxation times observed for the equilibrium liquid and that for the glass. This is most easily perceived by comparing the M'' *vs.* frequency curves of Figure 6 with that of Figure 7. For the equilibrium liquid the decay function of eq 4 gives an excellent fit to the data over the important low- and intermediate-frequency ranges, but at high frequencies above some 1.5 decades beyond the maximum in the M'' plots the calculated curves begin to fall significantly below the experimental data points. For the glass, however, the experimental data points and calculated curve are in good agreement at frequencies well beyond 1.5 decades past the maximum in M''. The effect is such that the spectrum of conductivity relaxation times for the glass has the appearance of having narrowed considerably on the fast relaxation time side in relation to the corresponding spectrum for the liquid.

In terms of our discussion relating the distribution of conductivity relaxation times to the structure of the system, one would expect that if an equilibrium liquid were quenched to form a glass at a sufficiently high rate that no structural changes took place during the quench the distribution for the glass should be identical with that of the equilibrium liquid. This condition is most likely not fulfilled in our experiment. Because of the large thermal mass of the conductivity cell and the poor thermal conductivity of the melt, it is probable that the initial rate of temperature change of the salt between the electrodes in the center of the cell was slow enough that during the quench a small amount of structural relaxation took place, even though the liquid had been equilibrated at a temperature (59.5°) corresponding to a viscosity of about 10^{13} P. Studies on alkali network oxide systems in the annealing range[31,36] have generally shown that the structure of partially relaxed or rate-cooled glasses does not correspond to an equilibrium structure at any temperature. Consequently it is not surprising that we find a slight discrepancy between the shapes of the glass and equilibrium liquid spectra of relaxation times. This discrepancy, of course, implies that the use of a single ordering parameter T_f is not sufficient to specify completely the electrical relaxation process in the glass. The differences in the M'' plots for liquid and glass, however, appear at high frequencies, while the dc conductivity σ_0 is determined primarily by the long relaxation times which contribute most strongly to the mean relaxation time $\langle\tau_\sigma\rangle$ and to the shapes of the M'' plots at low frequencies. Hence our conclusion that the dc conductivity can to a first approximation be accounted for by a single ordering parameter T_f remains unaffected.

Summary and Conclusions

It is unfortunate that due to their high liquidus temperatures and corresponding lack of substantial kinetic barriers to nucleation and crystallization below the liquidus simpler fused salts such as the alkali halides cannot withstand the degree of supercooling required for studies of the sort conducted here on a $0.4Ca(NO_3)_2$-$0.6KNO_3$ melt and glass. The behavior of this system at higher temperatures, however, suggests that, aside from its glass-forming ability, it is in no way atypical of other ionic melts. Consequently, we speculate that the characteristics of the $0.4Ca(NO_3)_2$-$0.6KNO_3$ melt revealed in the present study are in the qualitative sense general features of all molten salts. Of these characteristics the most significant are the following.

(a) As an equilibrium fused salt passes with decreasing temperature into the high viscosity region the electrical conductivity process changes gradually from a liquid-like mechanism, in which ionic migration and structural rearrangement occur on the same time scale, to a solid-like mechanism, in which the elementary diffusive motions of the more mobile ions take place in the context of a frozen structure.

(b) Thermally induced changes in the liquid structure are of equal or greater importance in changing the magnitude of the isobaric electrical conductivity than is the increase in the average kinetic energy of the ions. This is indicated in the low-temperature regime by the large decrease in activation enthalpy in passing from liquid to glass and in the high-temperature regime by the existence of a conductivity maximum.

(c) The nonexponential character of the electric field

decay and the corresponding frequency dispersion in the dielectric constant are a result of the microscopic heterogeneity of the system. In the equilibrium melt this microscopic heterogeneity increases with increasing temperature at constant pressure.

Acknowledgment. This research was supported by Contract No. AFOSR 72-2203 from the Air Force Office of Scientific Research. The authors are indebted to L. P. Boesch for his assistance in numerous aspects of this project.

References and Notes

(1) H. Rawson, "Inorganic Glass Forming Systems," Academic Press, London, 1967, pp 213–223.
(2) K. J. Rao, D. B. Helphrey, and C. A. Angell, *Phys. Chem. Glasses*, **14**, 26 (1973).
(3) R. Weiler, R. Bose, and P. B. Macedo, *J. Chem. Phys.*, **53**, 1258 (1970).
(4) H. Tweer, N. Laberge, and P. B. Macedo, *J. Amer. Ceram. Soc.*, **54**, 121 (1971).
(5) G. M. Glover and A. J. Matheson, *Trans. Faraday Soc.*, **67**, 1960 (1971).
(6) J. Wong and C. A. Angell, *J. Non-Cryst. Solids*, **7**, 109 (1972).
(7) E. Rhodes, W. E. Smith, and A. R. Ubbelohde, *Trans. Faraday Soc.*, **63**, 1943 (1967); *Rev Int. Hautes Temp. Refract.*, **4**, 231 (1967).
(8) P. B. Macedo, C. T. Moynihan, and R. Bose, *Phys. Chem. Glasses*, **13**, 171 (1972).
(9) C. T. Moynihan, R. D. Bressel, and C. A. Angell, *J. Phys. Chem.*, **55**, 4414 (1971).
(10) N. G. McCrum, B. E. Read, and G. Williams, "Anelastic and Dielectric Effects in Polymeric Solids," Wiley, New York, N. Y., 1967.
(11) V. Provenzano, L. P. Boesch, V. Volterra, C. T. Moynihan, and P. B. Macedo, *J. Amer. Ceram. Soc.*, **55**, 492 (1972).
(12) J. H. Ambrus, C. T. Moynihan, and P. B. Macedo, *J. Phys. Chem.*, **76**, 3287 (1972).
(13) C. T. Moynihan, L. P. Boesch, and N. L. Laberge, *Phys. Chem. Glasses*, in press.
(14) R. Bose, R. Weiler, and P. B. Macedo, *Phys. Chem. Glasses*, **11**, 117 (1970).
(15) R. Weiler, S. Blaser, and P. B. Macedo, *J. Phys. Chem.*, **73**, 4147 (1969).
(16) J. G. Berberian and F. H. Cole, *Rev. Sci. Instrum.*, **40**, 811 (1969).
(17) R. H. Cole and P. M. Gross, *Rev. Sci. Instrum.*, **20**, 252 (1949).
(18) T. A. Litovitz and C. M. Davis, "Physical Acoustics," Vol. IIA, W. P. Mason, Ed., Academic Press, New York, N. Y., 1965, pp 281–349.
(19) C. T. Moynihan, "Ionic Interactions," Vol. I, S. Petrucci, Ed., Academic Press, New York, N. Y., 1971, pp 261–384.
(20) C. T. Moynihan, N. Balitactac, L. Boone, and T. A. Litovitz, *J. Chem. Phys.*, **55**, 3013 (1971).
(21) J. H. Ambrus, C. T. Moynihan, and P. B. Macedo, *J. Electrochem. Soc.*, **119**, 192 (1972).
(22) J. H. Ambrus, H. Dardy, and C. T. Moynihan, *J. Phys. Chem.*, **76**, 3495 (1972).
(23) H. Kaneko and J. O. Isard, *Phys. Chem. Glasses*, **9**, 84 (1968).
(24) H. A. Levy and M. D. Danford, "Molten Salt Chemistry," M. Blander, Ed., Wiley, New York, N. Y., 1964, pp 109–125.
(25) M. Goldstein, *J. Chem. Phys.*, **51**, 3728 (1969).
(26) L. F. Grantham and S. J. Yosim, *J. Chem. Phys.*, **45**, 1192 (1966).
(27) J. D. Kellner, *J. Phys. Chem.*, **72**, 1737 (1968).
(28) L. W. Barr and A. B. Lidiard, "Physical Chemistry, An Advanced Treatise," Vol. X, W. Jost, Ed., Academic Press, New York, N. Y., 1970, pp 151–228.
(29) A. Q. Tool, *J. Amer. Ceram. Soc.*, **29**, 240 (1946).
(30) M. Goldstein, "Modern Aspects of the Vitreous State," Vol. 3, J. D. MacKenzie, Ed., Butterworths, Washington, D. C., 1964, pp 90–125.
(31) O. S. Narayanaswamy, *J. Amer. Ceram. Soc.*, **54**, 491 (1971).
(32) (a) M. H. Cohen and D. Turnbull, *J. Chem. Phys.*, **31**, 1164 (1959); (b) A. K. Doolittle, *J. Appl. Phys.*, **22**, 1471 (1951); **23**, 236 (1952).
(33) G. Adam and J. H. Gibbs, *J. Chem. Phys.*, **43**, 139 (1965).
(34) (a) C. A. Angell, *J. Phys. Chem.*, **75**, 3698 (1971); (b) C. A. Angell and K. J. Rao, *J. Chem. Phys.*, **57**, 470 (1972); (c) C. A. Angell and R. D. Bressel, *J. Phys. Chem.*, **76**, 3244 (1972).
(35) D. J. Plazek and J. H. Magill, *J. Chem. Phys.*, **45**, 3038 (1966).
(36) H. N. Ritland, *J. Amer. Ceram. Soc.*, **39**, 403 (1956).
(37) L. P. Boesch and C. T. Moynihan, *J. Non-Cryst. Solids*, submitted for publication.
(38) N. Saad and C. T. Moynihan, paper presented at Glass Division Meeting, American Ceramic Society, Bedford, Pa., Oct 12, 1973 (see abstract in *Amer. Ceram. Soc. Bull.*, **52**, 705 (1973)).
(39) H. Tweer, J. H. Simmons, and P. B. Macedo, *J. Chem. Phys.*, **54**, 1952 (1971).
(40) J. M. Stevels, "Handbuch der Physik," Vol. 20, S. Flügge, Ed., Springer-Verlag, Berlin, 1957, p 372.
(41) H. E. Taylor, *J. Soc. Glass Technol.*, **41**, 350 T (1957); **43**, 124 T (1959).
(42) J. O. Isard, *Proc. Inst. Elec. Eng., Part B., Suppl.*, **22**, 440 (1962).
(43) A somewhat better "feel" for the large variation with temperature of the distribution of conductivity relaxation times for the liquid may be had if this is described in terms of the standard deviation of $\ln \tau_\sigma$ from its mean rather than in terms of the β parameter.[13] At 60.1° the value $\beta = 0.72$ corresponds to a standard deviation of 1.24, while at 93.2° the value $\beta = 0.52$ corresponds to a standard deviation of 2.11.
(44) C. A. Angell, *J. Amer. Ceram. Soc.*, **51**, 117, 125 (1968).
(45) (a) J. D. Bernal, *Nature (London)*, **183**, 141 (1959); (b) J. D. Bernal and J. Mason, *ibid.*, **188**, 910 (1960).

An Electron Paramagnetic Resonance Study of SO_2^- and SO_4^- Ions on Vanadium Oxide Supported on Silica Gel

K. V. S. Rao and J. H. Lunsford*

Department of Chemistry, Texas A & M University, College Station, Texas 77840 *(Received August 13, 1973)*

Publication costs assisted by the Environmental Protection Agency

When SO_2 was adsorbed on partially reduced vanadium(V) oxide deposited on silica gel, two SO_2^- species were formed. The principal values of the g tensors are $g_{xx} = 2.002$, $g_{yy} = 2.008$, and $g_{zz} = 2.004$ for SO_2^-(A) and $g_{xx} = 2.001$, $g_{yy} = 2.010$, and $g_{zz} = 2.002$ for SO_2^-(B). Species A was predominant in the spectrum recorded at 298°K, whereas species B was predominant at 77°K. When 5 Torr of oxygen was added to the sample with adsorbed SO_2^- and the sample was heated to 373°K, SO_2^- was oxidized to SO_4^-. The g values of SO_4^- are $g_\perp = 2.030$ and $g_\parallel = 2.002$.

Introduction

The electron paramagnetic resonance (epr) spectra of SO_2^- [1-3] and of its oxidation products[4] on surfaces have been studied in detail in recent years. Sulfur dioxide reacts rapidly with partially reduced oxides of molybdenum, titanium, zinc, and magnesium oxide containing trapped electrons to form its anion radical SO_2^-.[1-3] On magnesium oxide SO_2^- reacts with molecular oxygen to form SO_3^-;[4] however, on the partially reduced oxides of molybdenum and titanium SO_2^- reacts with O_2 forming O_2^- plus diamagnetic ions.[5,6]

Vanadium(V) oxide deposited on silica gel is a widely used catalyst for the oxidation of SO_2 to SO_3. Van Reijen and Cossee[7] studied supported vanadium on silica catalyst by epr spectroscopy and showed that reduction of vanadium(V) is accompanied by the formation of tetrahedrally coordinated surface ions of tetravalent vanadium. The epr spectra of vanadium catalysts for SO_2 oxidation[8] and the activation energy for SO_2 activation[9] have been investigated recently.

Kazanskii and coworkers[10-12] studied the radicals formed by adsorption of different gases on reduced vanadium oxide supported on silica gel. The adsorption of oxygen resulted in the formation of O_2^- and O^- radicals.[10,11] When nitrous oxide was added at room temperature, it decomposed forming O^- radicals. However, the adsorption of nitrous oxide at 195°K, nitrogen at either 77°K or at room temperature, or sulfur dioxide at room temperature lead to the appearance of intense narrow signals against a background of the epr spectrum from tetrahedrally coordinated vanadium(IV) ions.[12] The intense lines have been attributed to the extra lines that can be expected for certain values of the nuclear quantum number because of the nonmonotonic variations of the magnetic field with the angle between the symmetry axis of the molecule and the magnetic field.[12-14] In view of the larger electronegativity of SO_2 compared to O_2 and the behavior of similar catalysts such as molybdenum supported on silica gel, it is surprising that sulfur dioxide did not form its anion radical when adsorbed on vanadium(IV).

The present work is devoted to a further study of the radicals formed upon adsorption of sulfur dioxide on supported vanadium, and also to an investigation of the oxidation products of the adsorbed sulfur oxide radical.

Experimental Section

The samples of vanadium on silica gel were prepared by saturating silica gel with an aqueous solution of ammonium vanadate with subsequent drying at 353°K and decomposition in air at 773°K for 12 hr. The vanadium content was approximately 2 wt %.

The samples were heated in 150 Torr of oxygen at 773°K to remove possible organic contaminants and then reduced with 25 Torr of H_2 at 773°K for 30 min. During the reduction step, water vapor was removed from the system by using a trap at 77°K. The samples were evacuated for about 2 hr at the same temperature. Sulfur dioxide (5 Torr) was then admitted to the sample at room temperature.

Sulfur-33 enriched SO_2 was prepared by treating 5 mg of sulfur containing 10 or 25% ^{33}S with 50 Torr of pure O_2 at 673°K for about 6 hr. The SO_2 was purified by the conventional freeze–pump technique.

The epr spectra were usually recorded at X-band, with the sample either at room temperature or at 77°K by using a Varian E-6S spectrometer. A Varian 4502 spectrometer was employed to determine Q band spectra. The g values were determined relative to a phosphorus doped silicon standard with $g = 1.9987$ or DPPH with $g = 2.0036$.

Results and Discussion

The epr spectrum of partially reduced vanadium on silica gel was similar to the spectrum observed by Shvets, *et al.*[11] This has been attributed to the V(IV) ions in the tetrahedral environment. After adsorption of about 5 Torr of SO_2 at room temperature the initial spectrum was somewhat modified, and in the central region a new intense signal was observed. The saturation behavior of this spectrum and its shape were different from that of the background vanadium spectrum.

As shown in Figure 1 the spectrum of the new species is somewhat different at 298 and at 77°K. The spectrum is characteristic of a radical with axial symmetry, or it may be attributed to the poorly resolved spectrum of a radical with lower symmetry. Assuming the latter case, since SO_2^- has C_{2v} symmetry, the g values of this new radical, along with the g values of SO_2^- on different catalyst surfaces, are given in Table I. The Q band and X band spec-

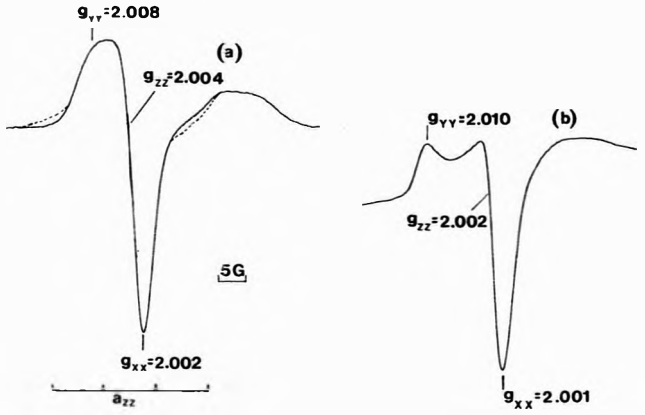

Figure 1. Epr spectrum of SO_2^- on vanadium oxide supported on silica gel (a) recorded at 298°K (b) recorded at 77°K.

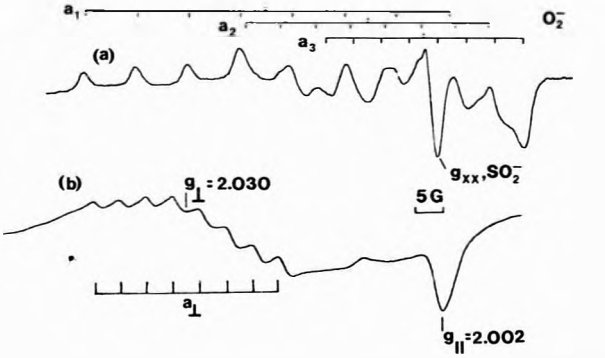

Figure 2. (a) Epr spectrum of O_2^- and SO_2^- on vanadium supported on silica gel, recorded at 298°K; (b) epr spectrum of SO_4^- on vanadium supported on silica gel recorded at 77°K. $a_\perp$ represents the hyperfine splitting of vanadium.

TABLE I: g Values of SO_2^- on Different Catalyst Surfaces

Catalyst		g_{xx}	g_{yy}	g_{zz}	Ref
MgO	(A)	2.0028	2.0097	2.0052	1
	(B)	2.0014	2.0078	2.0033	
Mo/SiO_2		2.003	2.011	2.003	3
TiO_2		2.001	2.005	2.001	2
ZnO		2.002	2.007	2.004	2
V/SiO_2	(A) X band	2.002	2.008	2.004	This
	Q band	2.002	2.007	2.003	work
	(B)	2.001	2.010	2.002	

tra are in good agreement, which confirms that the spectra are not the result of angular anomalies of vanadium(IV). It can be seen from Table I that the g values of the radical formed on vanadium supported on silica gel are in the same range as the g values observed for SO_2^- on other catalyst surfaces; hence, it is likely that sulfur dioxide adsorbed on reduced vanadium oxide on silica gel forms its anion radical SO_2^-. The slightly different spectra observed at room temperature and at 77°K may be attributed to SO_2^- ions in different environments on the surface. The presence of two adsorption sites for SO_2^- on MgO has been clearly demonstrated.[1] The high- and low-temperature spectra are labeled SO_2^-(A) and SO_2^-(B), respectively.

To determine the hyperfine splittings of sulfur in SO_2^-, SO_2 enriched with 10 and 25% ^{33}S(I = 3/2) was adsorbed on the supported vanadium. The regions where the $^{33}SO_2^-$ spectrum differs from $^{32}SO_2^-$ are indicated with dotted lines in Figure 1a. None of the hyperfine structure is clearly resolved; however, the absorption indicated by the dotted portion of the spectrum is attributed to the outer pair of lines centered on g_{zz}. These were the strongest hyperfine lines observed for SO_2^- on MgO when SO_2 enriched to 44% ^{33}S was used.[1] Efforts to identify other hyperfine lines have failed, probably because of their low intensity against the background due to V(IV) ions. From the two outer lines of the quartet centered on g_{zz} it was determined that the value of the hyperfine constant along the z direction, a_{zz}, is approximately 10 G. This value is almost the same as that observed[1] for $^{33}SO_2^-$ on MgO; hence, the evidence is reasonably strong that the SO_2^- ion is formed on reduced vanadium on silica gel upon adsorption of sulfur dioxide.

It is very likely that SO_2^- is adsorbed near vanadium ions, although no hyperfine structure of vanadium has been observed in the SO_2^- spectrum. This is consistent with the conclusion, based upon the hyperfine structure for SO_2^- on MgO, that the unpaired electron is totally transferred to SO_2, resulting in binding forces which are purely electrostatic.

Upon addition of 2 Torr of oxygen to the sample of vanadium on silica gel containing SO_2^-, the signal attributed to O_2^- appeared in addition to the SO_2^- signal. The epr spectrum of O_2^- and SO_2^- recorded at 298°K is shown in Figure 2a. The analysis of the O_2^- spectrum follows that of Kazanskii, *et al.*,[11] and the magnetic parameters are the same within experimental error: g_1 = 2.022, g_2 = 2.011, g_3 = 2.005; a_1 = 9.5 G, a_2 = 6.4 G, a_3 = 5.1 G. After heating the sample containing O_2^- and SO_2^- at 373°K for about 30 min, both the O_2^- and SO_2^- spectra decreased in amplitude, and a new spectrum characteristic of a radical with axial symmetry appeared. The new species did not form in the absence of either SO_2^- or O_2^-; therefore it probably forms as a result of the reaction between SO_2^- and O_2^-. According to reaction 1 the most likely radical is SO_4^-.

$$SO_2^- + O_2^- \longrightarrow SO_4^- + e \qquad (1)$$

The epr spectrum of the new species recorded at 77°K is depicted in Figure 2b. The weak maximum at g = 2.010 is due to a small amount of SO_2^-(B) which did not react with the superoxide ion. The minimum at $g_{\parallel}$ = 2.002 also overlaps with the minimum at g_{xx} = 2.001 from the spectrum of SO_2^-(B). Since the area above the baseline in a derivative spectrum must equal the area below the baseline, it is evident that only about 30% of the minimum in Figure 2b is due to the spectrum of SO_2^-(B) and the remainder must be attributed to the new species.

The g values of the new radical, along with the g values of SO_4^- in other environments are given in Table II. The principal axes of SO_4^- in γ-irradiated K_2SO_4 are along the two oxygen–oxygen directions and along the bisector of the OSO angle. If SO_4^- is formed on the surface of vanadium oxide supported on silica gel it is more likely that one of the oxygens of SO_4^- comes from the lattice oxide ion which is bonded to vanadium. The SO_4^- ion would have axial symmetry in this type of environment. Hence, the principal axis system for SO_4^- in γ-irradiated K_2SO_4 and for SO_4^- on vanadium on silica gel are different. When the g values of SO_4^- in γ-irradiated K_2SO_4[15] are transformed assuming C_{3v} symmetry they become 2.03, 2.03, and 2.008. Then the g values are essentially in agreement with the g values observed for the radical on vanadium on silica gel as given in Table II.

TABLE II: g Values of SO_4^- in Different Matrices

	g_{xx}	g_{yy}	g_{zz}	Ref
$K_2S_2O_8$	2.0327	2.0084	2.0035	22
K_2SO_4	2.0486	2.0082	2.0037	15
K_2SO_4[a]	2.057	2.009	2.003	23
	2.048	2.009	2.004	
V/SiO_2	2.030	2.030	2.002	This work

[a] Two sites have been observed for SO_4^-.

Attempts to detect ^{33}S hyperfine structure in the spectrum of 25% enriched $^{33}SO_4^-$ were unsuccessful. This is not surprising since the observed ^{33}S splitting in SO_4^- is about 3.5 G.[15] This splitting would not be resolved in the present case.

The eight-line hyperfine spectrum centered on $g_\perp$ is due to the interaction of SO_4^- with the vanadium nucleus. A vanadium splitting of $a_\perp$ = 5 G may be compared with splittings of $a_\perp$ = 14 G for O^- and a_{xx} = 6.8 G, a_{yy} = 5.9 G, and a_{zz} = 9.7 G for O_2^- on this catalyst.[10] The splitting in the parallel direction was not resolved, and it is assumed to be <2 G. A spin density of about 0.5% in the s orbital and about 2% in the d orbital of vanadium has been calculated[16] by taking the theoretical a_{iso} value to be 950 G[17] and the anisotropic value to be −105 G.[18] The negligible spin densities on both sulfur and vanadium nuclei in SO_4^- bonded to vanadium is in agreement with the suggestion that in 31 electron radicals of XO_4 structure the unpaired electron is largely confined to the nonbonding orbital on the oxygens.[19]

Attempts to determine ^{17}O hyperfine splittings for SO_4^- were unsuccessful, probably because of the exchange of the ^{17}O in molecular oxygen with lattice oxide ions. The isotopic exchange reaction between molecular oxygen and oxide ions of vanadium oxide supported on silica gel has been observed at low temperatures by Nikisha, *et al.*[20] The exchange between $^{17}O^-$ and lattice oxide ions has also been noted for O^- on molybdenum supported on silica gel.[21] The exchange rate increases with temperature, and at 373°K the exchange is probably complete, making it impossible to observe any ^{17}O splitting.

SO_4^- on vanadium supported on silica gel was stable up to 473°K. The amount of oxygen necessary to oxidize SO_2^- to SO_4^- seems to be critical. When an excess of oxygen was added, the O_2^- spectrum remained, though less intense upon heating the sample to 373°K, and no SO_4^- spectrum was observed.

The radical $S_2O_3^-$ is isoelectronic with SO_4^- and has similar g values,[15] but the ^{33}S hyperfine splittings for one of the sulfur atoms of $S_2O_3^-$ are about 117 and 136 G. The failure to observe any ^{33}S splittings for SO_4^- on the surface rules out the possibility of the radical being $S_2O_3^-$.

Acknowledgment. This investigation was supported by research Grant No. 801136, Air Pollution Control Office, Environmental Protection Agency.

References and Notes

(1) R. A. Schoonheydt and J. H. Lunsford, *J. Phys. Chem.*, **76**, 323 (1972).
(2) A. I. Maschenko, G. B. Pariiskii, and V. B. Kazanskii, *Kinet. Katal.*, **8**, 704 (1967).
(3) V. M. Vorotyntsev, V. A. Shvets, and V. B. Kazanskii, *Kinet. Katal.*, **12**, 1249 (1971).
(4) Y. Ben Taarit and J. H. Lunsford, *J. Phys. Chem.*, **77**, 1365 (1973).
(5) K. V. S. Rao and J. H. Lunsford, unpublished results.
(6) A. I. Maschenko, G. B. Pariiskii, and V. B. Kazanskii, *Kinet. Katal.*, **9**, 151 (1968).
(7) L. L. Van Reijen and P. Cossee, *Discuss. Faraday Soc.*, **41**, 277 (1966).
(8) V. M. Mastikhin, Ya. Zyulkovski, and G. M. Polyakova, *Teor. Eksp. Khim.*, **5**, 705 (1969).
(9) V. M. Mastikhin, G. M. Polyakova, Ya. Zyulkovski, and G. K. Boreskov, *Kinet. Katal.*, **11**, 1463 (1970).
(10) V. A. Shvets, M. E. Sarichev, and V. B. Kazanskii, *J. Catal.*, **11**, 378 (1968).
(11) V. A. Shvets, V. M. Vorotyntsev, and V. B. Kazanskii, *Kinet. Katal.*, **10**, 356 (1969).
(12) V. M. Vorotyntsev, V. A. Shvets, and V. B. Kazanskii, *Kinet. Katal.*, **12**, 678 (1971).
(13) R. Neiman and D. Kivelson, *J. Chem. Phys.*, **35**, 156 (1961).
(14) H. K. Gersman and J. D. Swalen, *J. Chem. Phys.*, **36**, 3221 (1962).
(15) J. R. Morton, D. M. Bishop, and M. Randic, *J. Chem. Phys.*, **45**, 1885 (1966).
(16) P. W. Atkins and M. C. R. Symons, "The Structure of Inorganic Radicals," Elsevier, Amsterdam, 1967, p 20.
(17) J. E. Wertz and J. R. Bolton, "Electron Spin Resonance," McGraw-Hill, New York, N. Y., 1972.
(18) B. A. Goodman and J. B. Raynor, *Advan. Inorg. Radiochem.*, **13**, 135 (1970).
(19) Reference 16, p 174.
(20) V. V. Nikisha, B. N. Shelimov, V. A. Shvets, A. P. Griva, and V. B. Kazanskii, *J. Catal.*, **28**, 230 (1973).
(21) Y. Ben Taarit and J. H. Lunsford, *Chem. Phys. Lett.*, **19**, 348 (1973).
(22) P. W. Atkins, J. A. Brivati, A. Horsfield, M. C. R. Symons, and P. A. Tevalion, *Int. Symp. Free Radicals, 6th*, (1963).
(23) K. Aiki and K. Hukuda, *J. Phys. Soc. Jap.*, **22**, 663 (1967).

COMMUNICATIONS TO THE EDITOR

Dielectric Constants of 1-Pentanol–Water Mixtures at 25°

Publication costs assisted by the Office of Saline Water

Sir: Additivity rules predict that the addition of a substance of higher dielectric constant to one of lower permittivity would give a mixture with a higher dielectric constant than that of the second component. Herewith is reported a striking exception to expectation: initial addition of water (D = 78.35) to *n*-amyl alcohol (1-pentanol, D = 15.14) *lowers* the dielectric constant. A minimum appears in the D *vs.* wt % curve at about 3.5% water.

The D *vs.* wt % curve for methanol–water mixtures is nearly linear over the whole range of compositions; for ethanol–water, it is slightly concave upward. The curvature increases on going to propanol (normal and iso) and still more with *tert*-butyl alcohol.[1] These results, together with our observation on 1-pentanol–water mixtures, suggest that the branch points which appear when water enters the hydrogen-bonded alcohol chains have a lower net dipole moment than that corresponding to the vector sum of the components previous to mixing, and that the decrease becomes greater as the number of carbon atoms in the alkyl group increases. Work on other mixtures is in progress; we hope to find a correlation between the structure of the components and the magnitude and sign of $(\partial D_{12}/\partial x_2)_0$, where x_2 is a measure of the water concentration, and thereby to learn something about short-range interactions between polar compounds. Below is an account of the behavior of the pentanol–water mixtures.

As part of a study of the conductance of a series of quaternary ammonium salts in mixed solvents, 1-pentanol was chosen as one of the components. Our values for the physical constants at 25° (dielectric constant, D = 15.14; viscosity, 0.0353 P; density, 0.8117 g/ml) did not agree with the literature values. Viscosities[2,3] of 0.03476 and 0.03347 and densities[2,4] of 0.81096 and 0.8095 have been reported. The greatest discrepancies appear in the dielectric constants, for which the values 15.04,[2] 14.5,[5] 13.77,[4] and 13.18[6] are given. Evans and Gardam[2] dried their amyl alcohol by refluxing over calcium oxide; Larson and Hunt[4] used metallic calcium; no information on the purification of the other materials is available. The method of measurement used by Evans and Gardam is completely reliable; the methods used by the earlier workers are susceptible to errors if the conductance of the test liquid is not negligible.

TABLE I: Dielectric Constants of 1-Pentanol–Water Mixtures at 25°

Wt % H_2O	0.00	0.75	1.16	1.80	2.47
D	15.14	14.97	14.91	14.80	14.71
Wt % H_2O	3.13	3.76	4.14	5.15	
D	14.63	14.65	14.68	14.74	

Our 1-pentanol (Fisher's Certified Grade) was dried by refluxing over calcium hydride; water content, as determined by a Perkin-Elmer 880 gas chromatograph, was 0.010 ± 0.001%. The chromatograph showed only the pentanol peak and the water blip. Dielectric constants were measured at 1 MHz, using the General Radio 716-CS1 bridge, and a Lind-Fuoss[7] cell. The results are given in Table I for 1-pentanol and for several mixtures with water. (The solubility of water, 2.19%, as reported by Gimmings and Baum,[8] is too low; our highest water concentration is just short of saturation.) The presence of a minimum near 3.5% water is distinctly visible. We conclude that the lower values of the dielectric constant previously reported were due to the presence of water in the samples measured.

Acknowledgment. This work was supported by the Office of Saline Water, U. S. Department of the Interior, under Contract No. 14-01-0001-1308.

References and Notes

(1) H. S. Harned and B. B. Owen, "The Physical Chemistry of Electrolytic Solutions," 3rd ed, Reinhold, New York, N. Y., 1958, Table 5-1-4, p 161.
(2) D. F. Evans and P. Gardam, *J. Phys. Chem.*, **73**, 158 (1969).
(3) W. J. Jones, S. T. Bowden, W. W. Yarnold, and W. H. Jones, *J. Phys. Colloid. Chem.*, **52**, 753 (1948).
(4) R. G. Larson and H. Hunt, *J. Phys. Chem.*, **43**, 417 (1939).
(5) P. Girard, *Trans. Faraday Soc.*, **30**, 763 (1934).
(6) H. R. Sarna and P. N. Trenhan, *Curr. Sci. (India)*, **21**, 306 (1952); *Chem. Abstr.*, **47**, 4153a (1953).
(7) J. E. Lind, Jr., and R. M. Fuoss, *J. Phys. Chem.*, **65**, 999 (1961).
(8) P. M. Gimmings and R. Baum, *J. Amer. Chem. Soc.*, **59**, 1111 (1937).

Sterling Chemistry Laboratory **Alessandro D'Aprano**
Yale University
New Haven, Connecticut 06520

Received January 21, 1974

AMERICAN CHEMICAL SOCIETY PUBLICATIONS IN MICROFORM

- Well over a million pages of chemistry's premier publications
- Back volumes and current subscriptions available in 35- or 16-mm microfilm and various cartridges
- Unlimited copying privileges built into microfilm subscriptions
- Current availability of nonprint materials in microfiche
- For full details of the ACS microform program, write or call:

Mr. Kenneth Phillips
Special Issues Sales
American Chemical Society
1155 16th St., N.W.
Washington, D. C. 20036
Tel: (202) 872-4364

and ask for your free copy of the informative booklet on the "Information Implosion!"

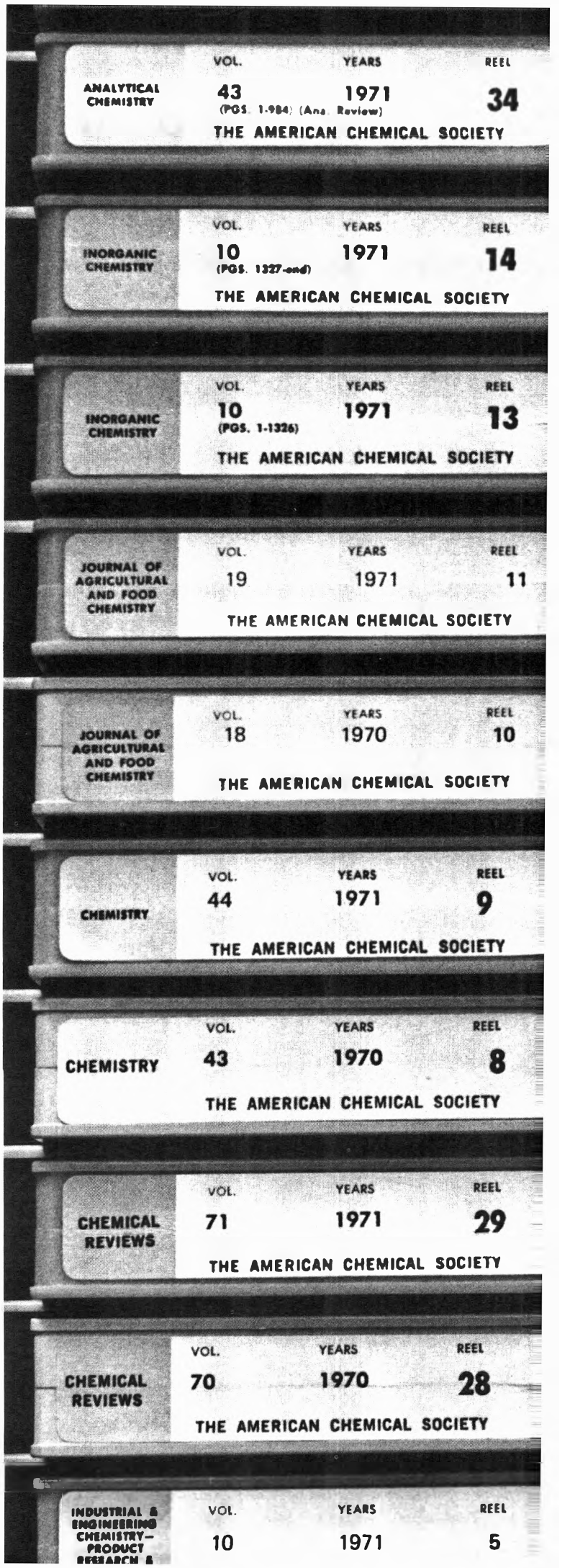

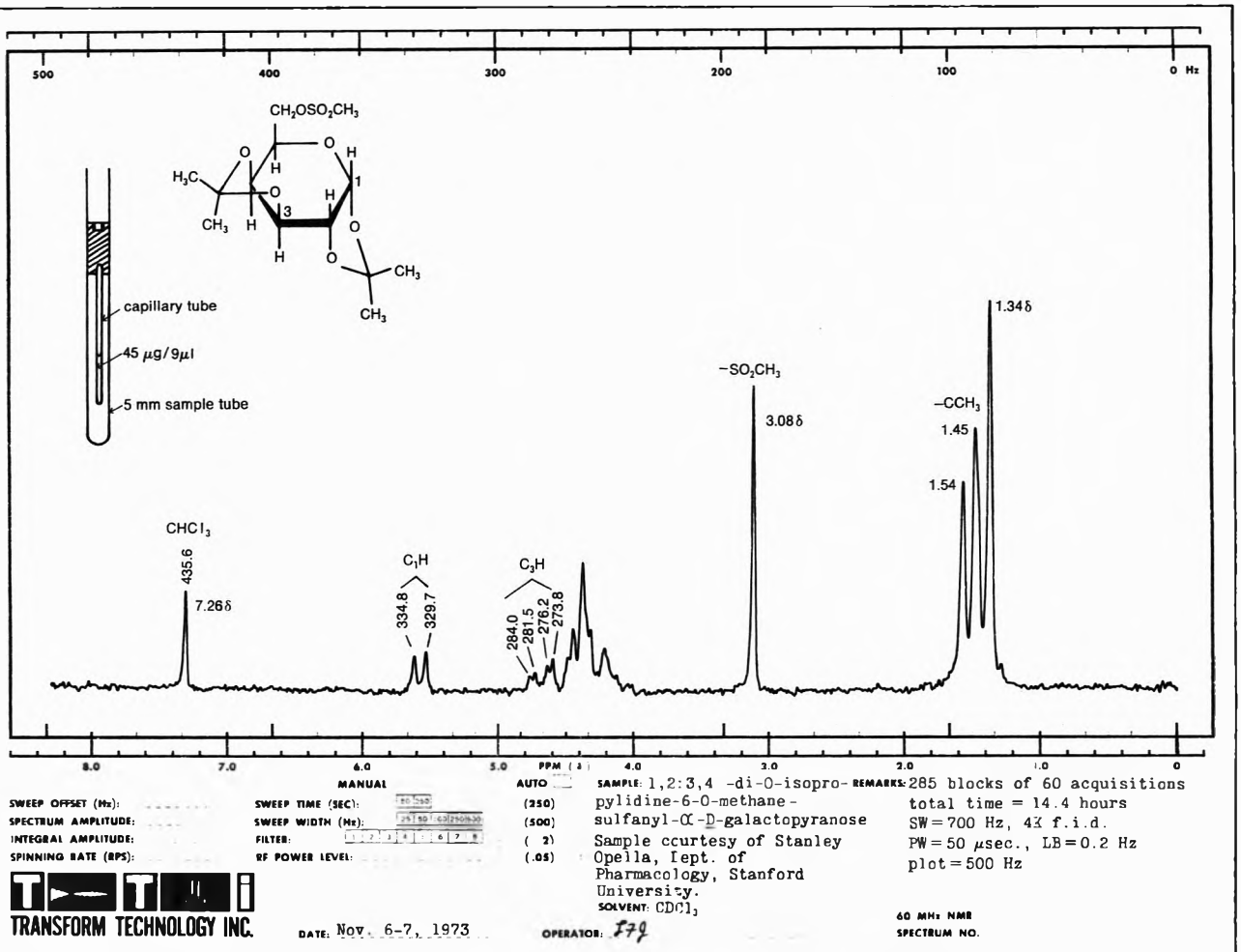

Analysis of very small samples is best done using a microcell approach. Here, 45 micrograms of a compound with molecular weight 338 was contained in a capillary tube of 1.0 mm I.D. The peak at 3.08δ, although weak after one block of acquisitions, served adequately for the peak register method, which effectively cancels long-term field drift. Signal frequencies and chemical shifts were copied from an oscilloscope display of peak positions using an assigned value of 435.6 Hz for the chloroform peak. The spectrum is very well defined, and demonstrates that overnight FT operation with a T-60A/TT-7 system is quite feasible and very useful for microsample analysis.

MICROSAMPLE ANALYSIS with a TT-7/T-60A System

The TT-7 pulsed RF Fourier transform accessory benefits NMR operation by dramatically increasing sensitivity over that obtained in the normal CW mode of operation. Typically, samples five to ten times smaller than those now being handled can be run in the same amount of analysis time. Signal input, accumulated free induction decay, or transformed spectra can be displayed on the TT-7's cathode ray tube for visual monitoring. The spectra can be plotted using the T-60 recorder. Digital integrations of spectra can be viewed or plotted as well.

Not only will the TT-7 enhance the sensitivity and increase sample throughput of your T-60 but it will also provide an excellent Fourier transform training facility. Its ease of use is incomparable. In addition, spin-lattice relaxation times can be determined from a series of runs using the progressive saturation technique. Optional automatic T_1 measurements are available using the inversion-recovery technique as well as other multi-pulse experiments. In addition to sensitivity improvement and T_1 measurement applications, the basic TT-7 system will provide computer calculations of theoretical NMR spectra of up to six spins (seven spins with 12K core memory and disk memory system).

Phone or write for more details.

NICOLET INSTRUMENT CORPORATION

5225 Verona Road, Madison, Wisconsin 53711
Phone: 608/271-3333